Structure formation and identification in geometrically driven soft matter systems

Tobias Martin Hain

kumulative Dissertation

zur Erlangung des akademischen Grades
"doctor rerum naturalium" (Dr. rer. nat.)
in der Wissenschaftsdisziplin "Mathematische Physik"

eingereicht an der
Mathematisch-Naturwissenschaftlichen Fakultät
Institut für Mathematik
der Universität Potsdam

Diese Arbeit ist Teil eines Co-tutelle Verfahrens

zwischen der
Mathematisch-Naturwissenschaftlichen Fakultät
der Universität Potsdam
und des College of Science, Health, Engineering and Education
der Murdoch University, Perth

Abstract

Subdividing space through interfaces leads to many space partitions that are relevant to soft matter self-assembly. Prominent examples include cellular media, e.g. soap froths, which are bubbles of air separated by interfaces of soap and water, but also more complex partitions such as bicontinuous minimal surfaces.

Using computer simulations, this thesis analyses soft matter systems in terms of the relationship between the physical forces between the system's constituents and the structure of the resulting interfaces or partitions. The focus is on two systems, copolymeric self-assembly and the so-called Quantizer problem, where the driving force of structure formation, the minimisation of the free-energy, is an interplay of surface area minimisation and stretching contributions, favouring cells of uniform thickness.

In the first part of the thesis we address copolymeric phase formation with sharp interfaces. We analyse a columnar copolymer system "forced" to assemble on a spherical surface, where the perfect solution, the hexagonal tiling, is topologically prohibited. For a system of three-armed copolymers, the resulting structure is described by solutions of the so-called *Thomson problem*, the search of minimal energy configurations of repelling charges on a sphere. We find three intertwined Thomson problem solutions on a single sphere, occurring at a probability depending on the radius of the substrate.

We then investigate the formation of amorphous and crystalline structures in the Quantizer system, a particulate model with an energy functional without surface tension that favours spherical cells of equal size. We find that quasi-static equilibrium cooling allows the Quantizer system to crystallise into a BCC ground state, whereas quenching and non-equilibrium cooling, i.e. cooling at slower rates then quenching, leads to an approximately hyperuniform, amorphous state. The assumed universality of the latter, i.e. independence of energy minimisation method or initial configuration, is strengthened by our results. We expand the Quantizer system by introducing interface tension, creating a model that we find to mimic polymeric micelle systems: An order-disorder phase transition is observed with a stable Frank-Caspar phase.

The second part considers bicontinuous partitions of space into two network-like domains, and introduces an open-source tool for the identification of structures in electron microscopy images. We expand a method of matching experimentally accessible projections with computed projections of potential structures, introduced by Deng and Mieczkowski (1998). The computed structures are modelled using nodal representations of constant-mean-curvature surfaces. A case study conducted on etioplast cell

membranes in chloroplast precursors establishes the double Diamond surface structure to be dominant in these plant cells. We automate the matching process employing deep-learning methods, which manage to identify structures with excellent accuracy.

Zusammenfassung

Die Unterteilung eines Raums durch Grenzflächen führt zu Raumaufteilungen, die für die Selbstorganisation weicher Materie relevant sind. Bekannte Beispiele sind zelluläre Medien, wie z.B. Seifenschaum, der aus Luftblasen besteht, getrennt durch Wände aus Wasser und Seife, und komplexere Partitionen, wie sie z.B. durch bikontinuierliche Minimalflächen erzeugt werden.

In dieser Arbeit werden mit Hilfe von Computersimulationen Systeme weicher Materie in Bezug auf den Zusammenhang zwischen dem im System vorherrschenden, physikalischen Kräften und der Struktur der resultierenden Grenzflächen oder Partitionen untersucht.

Der Schwerpunkt liegt hierbei auf zwei Systemen, eine Copolymerschmelze und das sogenannte Quantizer Problem, bei denen der treibende Faktor der Strukturbildung, nämlich die Minimierung der freien Energie, aus einem Zusammenspiel der Minimierung der Oberfläche der Grenzflächen und der gleichzeitigen Minimierung der Elastizitätsenergie besteht. Unter diesen Gegebenheiten bevorzugen solche Systeme Zellen gleichmäßiger Größe.

Im ersten Teil der Arbeit befassen wir uns mit der Bildung von scharfen Grenzflächen in Systemen von Copolymeren. Wir analysieren die zylindrische Phase eines Copolymersystems, das gezwungen wird, sich auf einer kugelförmigen Oberfläche zu organisieren. Die Topologie dieser Oberfläche erlaubt es der optimalen Konfiguration, dem Sechseckgitter, nicht, sich zu bilden.

Für dreiarmige Copolymere wird die entstehende Struktur durch Lösungen des sogenannten *Thomson Problems* beschrieben. Letzteres sucht nach der Konfigurationen von abstoßenden Ladungen auf einer Kugeloberfläche mit minimaler Energie. Auf einem Substrat haben wir eine Kombination aus drei ineinandergreifende Lösungen des Thomson Problems gefunden, wobei der Typ der Lösungen statistisch von dem Radius des Substrates abhängt.

Anschließend untersuchen wir die Bildung von amorphen und kristallinen Strukturen im Quantizersystem, einem teilchenbasierenden Modell, dessen Energiefunktional keine Oberflächenspannung enthält und möglichst kugelförmige Zellen gleicher Größe begünstigt. Wird das System quasistatisch im thermodynamischen Gleichgewicht abgekühlt, kristallisiert das Quantizersystem in den geordneten BCC Grundzustand. Wird das System allerdings zu schnell abgekühlt, sodass es sich nicht mehr im thermodynamischen Gleichgewicht befindet, bildet sich eine amorphe, annähernd hyperuniforme

Struktur aus. Wir konnten zeigen, dass diese Struktur bemerkenswert unabhängig von den Ausganszuständen, sowie der Art der Energieminimierung zu sein scheint. Im Ausblick erweitern wir das Quantizersystem, indem wir Oberflächenspannung einführen. Unsere Ergebnisse deutet darauf hin, dass dieses so erweiterte Modell Mizellenphasen in Polymersystem modellieren kann. Wir beobachten einen Phasenübergang von einer ungeordneten, flüssigen Phase hin zu einer festen Frank-Caspar-Phase.

Der zweite Teil der Arbeit behandelt bikontinuierliche Grenzflächen, die den Raum in zwei netzwerkartige Domänen aufteilen. Wir führen eine Open-Source Software ein, das die Identifizierung von Strukturen anhand derer Mikroskopaufnahmen ermöglicht. Hierzu erweitern und verbessern wir eine Methode, die durch den Abgleich experimentell zugänglicher Projektionen in Mikroskopaufnahmen mit berechneten Projektionen potenzieller Strukturen basiert. Dieses Verfahren wurde erstmal von Deng und Mieczkowski (1998) eingeführt. Die simulierten Strukturen basieren auf einer Nodalflächenmodellierung von dreifach-periodischen Flächen konstanter mittlerer Krümmung. Wir führen eine Fallstudie an Zellmembranen von Etioplasten, den Vorläufern von Chloroplasten, durch. Wir konnten die Struktur dieser Etioplasten als die Diamond-Struktur identifizieren. Als Ausblick automatisieren wir den Identifizierungsproyess mit Hilfe von Deep-Learning-Methoden. Erste Ergebnisse zeigen, dass mit diesem Ansatz die Identifizierung von Strukturen mit ausgezeichneter Genauigkeit gelingt.

Erklärung

Diese Arbeit ist im Zuge einer binationalen Promotion, wie im Kooperationsvertrag geregelt, an der Universität Potsdam und der Murdoch University, Perth eingereicht und wurde sonst bisher an keiner weiteren Hochschule eingereicht.

Sie wurde selbstständig verfasst und keine anderen als die angegebenen Quellen und Hilfsmittel wurden benutzt. Dies versichere ich hiermit an Eides statt.

T. Hain
(Tobias Hain)

x

Contents

List of Figures

Authorship contributions

This thesis contains co-authored work that has been published. This chapter provides an overview of the contributions of each author.

Publication 1

Details of work

Location:	chapter 2.
Title:	Patchy particles by self-assembly of star copolymers on a spherical substrate: Thomson solutions in a geometric problem with a color constraint
Published as:	Hain, T. M., Schröder-Turk, G. E. & Kirkensgaard, J. J. K. Patchy particles by self-assembly of star copolymers on a spherical substrate: Thomson solutions in a geometric problem with a color constraint. Soft Matter 15, 9394–9404 (2019)

	Tobias M. Hain	Gerd Schröder-Turk	Jacob J. K. Kirkensgaard
Contribution (%)	70	15	15
Concept Development	x	x	x
Data Collection	x		
Data Analyses	x		
Drafting of Manuscript	x		
Reviewed Manuscript	x	x	x

T. Hain
Candidate

G. Schröder-Turk
Principal Supervisor
Murdoch

M. Evans
Principal Supervisor
Potsdam

Publication 2

Details of work

Location:	chapter 3.
Title:	Low-temperature statistical mechanics of the Quantizer problem: Fast quenching and equilibrium cooling of the three-dimensional Voronoi liquid
Published as:	Hain, T. M., Klatt, M. A. & Schröder-Turk, G. E. Low-temperature statistical mechanics of the Quantizer problem: Fast quenching and equilibrium cooling of the three-dimensional Voronoi liquid. J. Chem. Phys. 153, 234505 (2020)

	Tobias M. Hain	Michael A. Klatt	Gerd Schröder-Turk
Contribution (%)	75	10	15
Concept Development	x	x	x
Data Collection	x		
Data Analyses	x		
Drafting of Manuscript	x	x	x
Reviewed Manuscript	x	x	x

T. Hain	G. Schröder-Turk	M. Evans
Candidate	Principal Supervisor	Principal Supervisor
	Murdoch	Potsdam

Publication 3

<u>Details of work</u>

Location:	chapter 4.
Title:	SPIRE—a software tool for bicontinuous phase recognition: application for plastid cubic membranes
Published as:	Hain, T. M. et al. SPIRE—a software tool for bicontinuous phase recognition: application for plastid cubic membranes. Plant Physiology (2021) doi:10.1093/plphys/kiab476.

	T. M. Hain	M. Bykowski	M. Saba	M. E. Evans
Contribution (%)	50	15	5	5
Concept Development	x	x	x	
Data Collection		x		
Data Analyses	x	x		
Drafting of Manuscript	x	x		
Reviewed Manuscript	x	x	x	x

	G. E. Schröder-Turk	L. Kowalewska
Contribution (%)	15	10
Concept Development	x	x
Data Collection		x
Data Analyses		
Drafting of Manuscript		x
Reviewed Manuscript	x	x

T. Hain	G. Schröder-Turk	M. Evans
Candidate	Principal Supervisor	Principal Supervisor
	Murdoch	Potsdam

Optimal partitions as model systems for cellular media

This thesis addresses structure formation in soft matter, with a focus on geometrically *optimal* cellular media. In this case, geometrically optimal means that cellular structures assemble, driven by an optimization of a purely geometric quantity. We will investigate this geometrical optimization process with the aim of gaining an understanding about how and why the resulting structures are built.

This introductory chapter provides a broad introduction to cellular partitions in soft matter, pointing out where each of the chapters of this thesis are placed in the field. The following chapters then provide more specific and detailed introductions to their respective content.

To describe cellular media and define a notion of "optimality" a quantitative description is needed. For this purpose we will use partitions and tilings. Partitions and tilings are a mathematical model of how to divide space into smaller subvolumes. A wide array of practical applications of such partitions exists in e.g. geography, chemistry, biology and physics. Several examples will be given in this introduction.

1.1   Planar tilings

A well-known example for a planar tiling is the honeycomb structure bees build in their hives, as shown in fig. (1.1). The honeycomb structure subdivides a planar surface into hexagons, which do not leave any gaps in between them. This pattern has been of interest for over 2000 years, when scholars in ancient Rome have been fascinated by this regular structure and were wondering why bees build them as they do [Varro, 1934]. The beehive's hexagonal structure, like any planar tiling, can be described using vertices (points), edges (lines) and faces (polygons). The vertices mark the start and end points of edges, whereas a face is determined by its enclosing edges. In the case of the honeycomb structures, the vertices lie at the six corners of the hexagons and are connected by edges, where three edges always meet at each vertex at an angle of $120°$. The faces of this particular tiling are regular hexagons.

The honeycomb structure has several compelling properties. First, it is part of a special subclass of tilings, called regular tilings [Grünbaum and Shephard, 2013]. These are tilings which only consists of one type of regular polyhedra. Only three of these tilings exist in the plane, using a regular triangle, square and hexagon as tile respectively. A larger subgroup of tilings are so-called *Archimedian tilings*, which consist of multiple types of regular polygons. An example of an Archimedian tiling consisting of regular octagons and squares is shown in fig. (1.3c). A key aspect of tilings is symmetry [Horne, 2000, Grünbaum and Shephard, 2013, Conway et al., 2016]. Not all tilings (or partitions) are symmetric, as we will see throughout this thesis. We first need to introduce an isometry, which is a transformation $\sigma : \mathbb{E}^2 \to \mathbb{E}^2$ which preserves distances. An isometry is also called a congruent transformation since it does not distort objects. There are four possible isometries in the euclidean plane $\mathbb{E}^2$: (1) rotations around a point, (2)
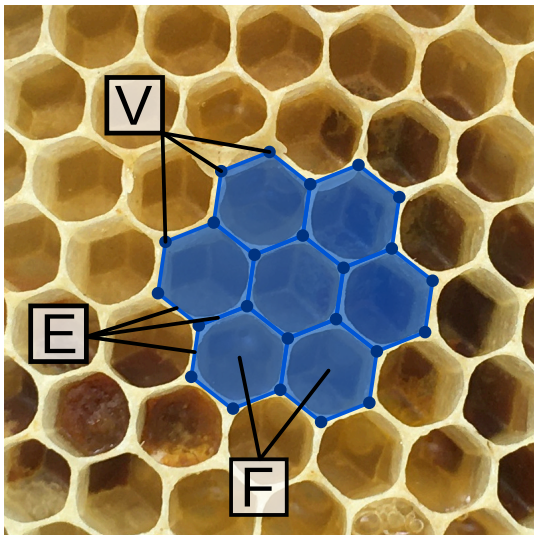
Figure 1.1: A honeycomb as an example of a planar tiling. A planar surface is subdivided into smaller domains, called faces (F). Such faces are bounded by edges (E), which connects vertices (V). Here, the plane is tiled by hexagons, each with six vertices. Image credits Matthias Beutke.
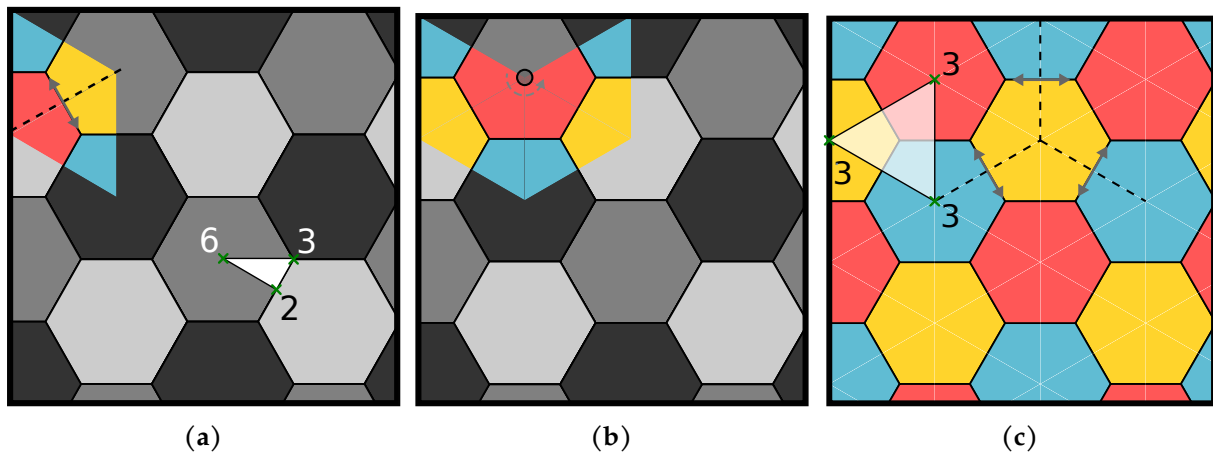
Figure 1.2: A three colored, regular tiling of hexagons. This so-called honeycomb pattern is highly symmetric and can be reconstructed from its smallest, asymmetric unit cell, marked with white triangles for the single colored hexagonal tiling (a) and the three-colored tiling (c). The green crosses indicate kaleidoscopic points, i.e. rotation centers where mirror lines meet. The number indicates the number of mirror lines meeting at the according point. By repeatedly applying the symmetry operations of the tiling onto the unit cell, here rotations and mirroring, the entire tiling pattern can be created.

translations along a vector (3) reflections in a line and (4) glide reflections in a line [Grünbaum and Shephard, 2013, Conway et al., 2016]. A symmetry of a tiling is then an isometry - or a combination of several isometries - which maps a set S onto itself, i.e. $\sigma S = S$, where the set S represents the tiling. A symmetric tiling can then be described using the smallest, asymmetric patch, called the fundamental region, and the symmetries of the tiling. The entire tiling can be reconstructed by repeatedly applying the symmetry operations to the fundamental region as illustrated in fig. (1.2). Symmetric tilings are thus infinite.

The symmetries of planar tilings can be labelled using the so-called *orbifold* notation. For a full description we refer to Conway et al. [2016], here we just indicate the basics. Each symmetry operation is given a different symbol: ● for a rotation center, ∗ for a mirror line, × for a glide reflection and ○ for a translation. By adding numbers to the symbols, the symmetries can be specified more: ∗6 denotes that 6 mirror lines meet in a single point in the tiling. The hexagonal tiling has thus an orbifold notation of ∗632. An important aspect of the orbifold notation is that it directly describes the topology of a tiling. More details on the topology of tilings will be provided in chapter 2. Other popular notations for symmetries include the Hermann-Mauguin or the Schönfliess notations [Hahn, 2005, Graef and McHenry, 2012], which are popular in crystallography.

Crystallography studies the symmetries and structure of ordered solid materials and is a well established area of physics with many textbooks available [Ashcroft et al., 1976, Sands, 1993, Kittel, 2004, Graef and McHenry, 2012, Szwacki and Szwacka, 2016]. A
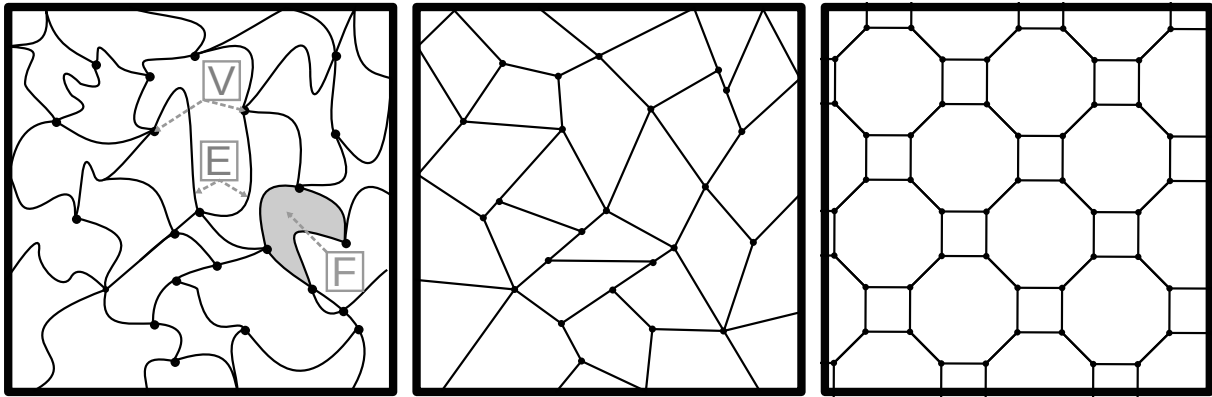
(**a**) Tiling no symmetries and curved egdes

(**b**) Arbitrary tiling with no symmetries but straight edges.

(**c**) Periodic, symmetric tiling

Figure 1.3: Examples of planar tilings. Tilings are subdivisions of the plane into non-overlapping cells leaving no gaps. Tilings can be described in terms of vertices (V), i.e. points where two or more edges meet, edges (E) connecting vertices and faces (F), which are bounded by edges.

key aspect of crystals is their symmetry: all crystals are built from a so-called translational unit cell, consisting of one or more atoms, and a lattice on which points the unit cell is placed. The lattice is given by a set of three unit vectors $\mathbf{b}_i$. As such, crystals are a natural partition of space with the shape of the unit cell determining the partition. Thus, by definition, any crystal has at least translational symmetry and is thus periodic, but may have several more symmetries like rotations or inversions, depending on the type of lattice and choice of unit cell. There exist only a finite number of possible symmetries for a crystal, these are labelled using so-called plane (two dimensions) and space groups (three dimensions) [Hahn, 2005]. These play an important role for the identification of structures, since the symmetry groups can be experimentally determined using scattering methods [Hahn, 2005, Als-Nielsen and McMorrow, 2011a, Szwacki and Szwacka, 2016]. For completely disordered and asymmetric tilings, edges and faces are of arbitrary shape, an example is shown in fig. (1.3a). This leaves us with the formal definition of a tiling: a covering of space by a set of non-overlapping shapes, which do not leave any gaps [Grünbaum and Shephard, 2013]. Due to their lack of symmetries, these tilings can be difficult to handle. Contrary to symmetric tilings, where providing a unit cell or fundamental region together with its symmetries is enough to describe the entire tiling, the positions of vertices, edges and faces have to be provided to completely describe disordered tilings.

An additional layer of complexity can be added by introducing color to tilings [Grünbaum and Shephard, 2013, Conway et al., 2016]. Here, each face is then assigned a color. Colored tilings are for example the subject of the famous *four-color problem* [Barnette, 1983]. This problem conjectures that for any planar tiling, four colors are enough to color the entire tiling so that no edge is adjacent to two tiles with the same color.

Figure 1.4: A tiling of the sphere consisting of six four-sided polygons. The rod indicates a rotational symmetry axis. Note that, due to the curved surface of the sphere, three squares meet at each vertex (b), instead of four as is the case in the planar tiling consisting of squares (a).
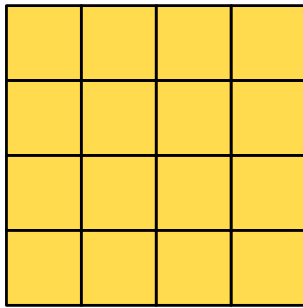
(**a**) planar tiling by squares
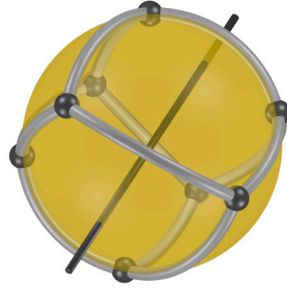
(**b**) spherical tiling by four-sided polygons

This conjecture has been proven by Appel and Haken [1977], Appel et al. [1977]. Colors allow to differentiate between two otherwise identical shapes, as shown in fig. (1.2). Here the hexagonal pattern is expanded by using three colors and as such has three different tiles instead of only one tile. By introducing color, the symmetry and the unit cell of the tiling change. The orbifold notation, for example, of the three-colored hexagonal tiling is ∗333, with a fundamental region indicated in fig. (1.2), instead of ∗632 of the single-colored version.

1.2 Tilings on curved surfaces

Tilings can be generalised to any kind of surface, such as the surface of a sphere. The main difference to planar tilings is that the tiled surface is now curved. Curvature measures the bending, i.e. how much a curve or surface deviates from its flat counter part [Millman and Parker, 1977]. That is the more a surface bends away from a flat plane, the higher is its curvature.

The study of spherical tilings is closely connected with the study of polyhedra with regular polygons as faces: by projecting the vertices and edges onto a sphere, spherical tilings can be generated, where the edges of the polyhedra becomes great circles [Coxeter et al., 1954, Grünbaum and Shephard, 1981]. The polyhedra and the spherical tiling then share the same symmetries and order. An example is presented in fig. (1.4b), where a cube is projected on the surface of a sphere. Spherical tilings has been successful in describing the surface structure of spheres. A successful example is virus capsids [Flint et al., 2015]. These are the spherical shells containing the genetic information of viruses. This shell is self-assembled, i.e. constructed without external forces with only very little help from cellular machinery, from one or a few types of identical building proteins [Berger et al., 1994, Konevtsova et al., 2012]. Caspar and Klug [1962] laid out basic design principles of the arrangements of these protein building

blocks and found that many virus capsids show icosahedral symmetry, where the proteins prefer a local hexagonal symmetry with few pentagonal defects. Mannige and Brooks [2008] found that for many virus families the surface structure of these capsids can be represented as a tiling of the sphere, where the basic building blocks (proteins) are represented by a tile each. These tilings then reflect the order and symmetries of the protein assemblies. The rules and orderings of possible virus surface structures can thus be translated to a mathematical problem of how spheres can be tiled.

Further applications of spherical tilings include the modelling of two dimensional foams [Roth et al., 2012] or bubbles [Mughal et al., 2017a,b] in spherical confinement, or the description of spherical molecules such as the Buckminster fullerene, a sphere consisting of 12 pentagons and 20 hexagons [Hebard, 1993].

The general definition of spherical tilings differs little from the one of planar tilings: a spherical tiling is a covering of $\mathbb{S}^2$ by sets T_i (the tiles) without gaps [Grünbaum and Shephard, 1981]. However, due to the intrinsic curvature of the sphere, or any curved surface, the combinatorics of the tiling changes. Where as in the plane the sum of all angles around a vertex add up to 2π, this is not the case on curved surfaces any more, as visualised in fig. (1.4). This concept is called geometric frustration: a preferred structure can not be arranged due to geometric constraints. This concept will be the main focus of chapter 2 of this thesis with more details provided there.

1.3 Optimal tilings

To introduce optimal tilings, we will reconsider the honeycomb pattern and the old question why bees build their hives in this specific pattern (see fig. (1.1)). This question dates back as early as 36 B.C., when addressed by the scholar Varro in Ancient Rome. His answer to that question, without giving proof, was that this shape either is most suitable for the six legs of the bees, or - the more geometrical approach - that this shape, i.e. a hexagonal tiling of the plane, encloses the biggest amount of space given a fixed perimeter length in between cells [Varro, 1934, Hales, 2001]. The latter hypothesis became to be known as the *honeycomb conjecture*. When reformulated, this conjecture states that the hexagonal tiling uses the least edge length among all planar tilings with tiles of the same area. Considering the energy consumption needed to produce wax [Coggshall and Morse, 1984], a hexagonal honeycomb would be optimal in a way that it saves building material, however, the reality is slightly more complex. See references [Tóth, 1964, Weaire and Aste, 2008, Mughal et al., 2017b] for more details.

The question of the honeycomb tiling being optimal in minimising its edge length is very similar to the isoperimetric problem: which shape of a given perimeter length encloses the largest area? The answer to this question in the $\mathbb{E}^2$ plane is the circle [Blåsjö, 2005]. However, since disks do not tile the plane without gaps in between them, this can not be the solution to the question behind the honeycomb conjecture. Such an arrangement of disks with gaps in between them is called a packing [Conway and Sloane, 1999, Weaire and Aste, 2008]. The honeycomb conjecture states that the "next best" shape which tiles space is the hexagon. Partitions can be induced by using a point
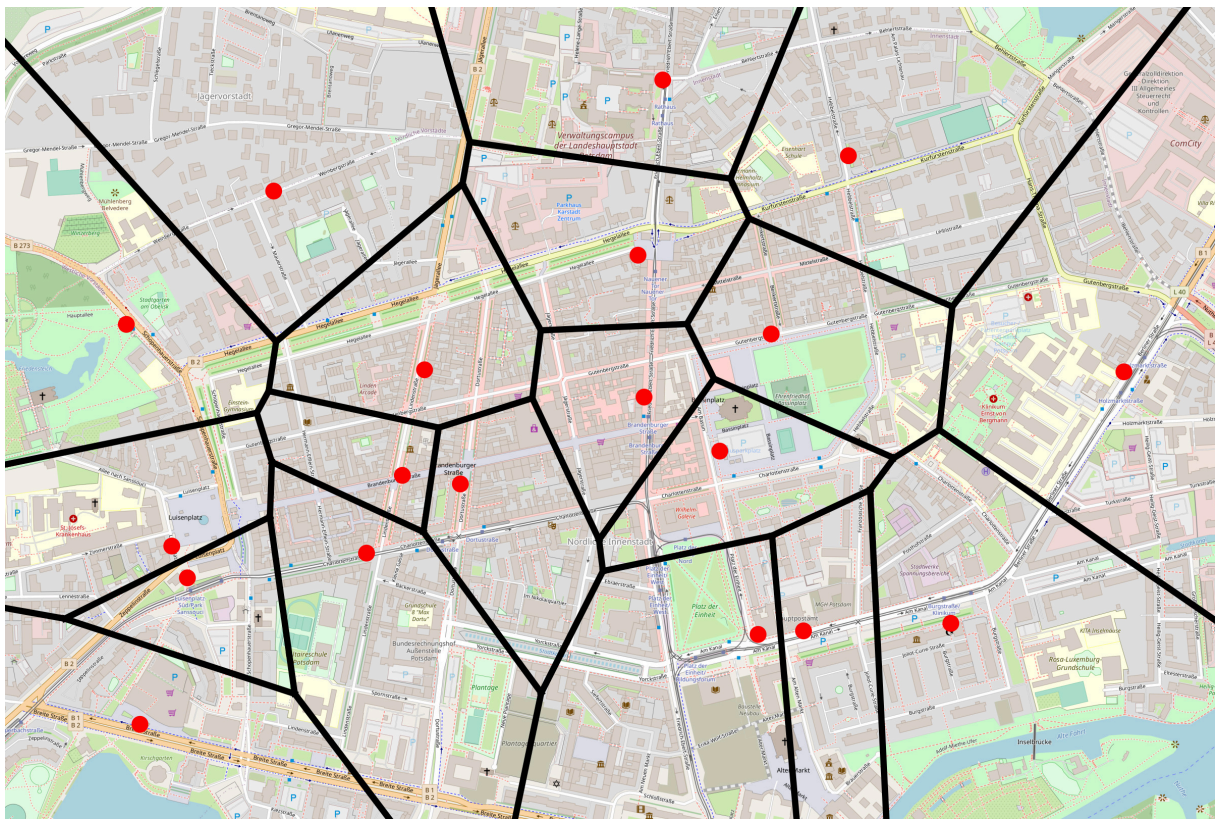
Figure 1.5: City plan of Potsdam, Germany, with postboxes marked with red dots. The positions of the postboxes induce a partition (tiling) of the city: each postbox is assigned a tile, representing the "catchment area", i.e. the area of inhabitants using this postbox, based on the assumption each inhabitant uses the closest (measured in Euclidean distance) postbox. This point set induced tiling is called Voronoi tessellation and assigns each point a cell containing all locations in space closest to the point. Map data from OpenStreetMap, ©OpenStreetMap

set, for example the centers of a disk packing. We will illustrate this process using an example: assuming the inhabitants of a town are lazy and will only use the postbox closest to their home (measured in Euclidean distance), the distribution of the latter assigns each postbox a "catchment area" of inhabitants using said postbox, as shown in fig. (1.5). Each catchment area then is a tile in a partition of the city. The shape of each tile is purely determined by the positioning of the points (postboxes), i.e. the shapes and areas of the tiles change when the points (respectively postboxes) are moved around the map. This way of assigning each point the area closer to itself than any other

point is called the *Voronoi tessellation*. Using this technique, some tiling problems can be expressed in terms of the arrangement of points instead of providing information for all vertices, edges and faces of a partition.

Voronoi diagrams are an important concept of how to create tessellations based on point sets and is used throughout this thesis. Its origin dates back to Dirichlet [Dirichlet, 1850] and Voronoi [Voronoi, 1908]. We will provide a brief introduction, however, refer to relevant textbooks and reviews for more details [Aurenhammer, 1991, Okabe et al., 2000, Aurenhammer et al., 2013]

The Voronoi diagram assigns to each point $\mathbf{p}_i$, also called site, of a set S a cell V_i [Aurenhammer, 1991, Okabe et al., 2000]. The latter is defined as

$$V_i = \{\mathbf{x} \mid ||\mathbf{x} - \mathbf{p}_i|| \leq ||\mathbf{x} - \mathbf{p}_j|| \text{ for } j \neq i, j \in I_n\}, \tag{1.1}$$

where I_n is the set of all site indices. Graphically speaking, the Voronoi cell V_i associated to the site $\mathbf{p}_i$ is the region containing all points closer to the site $\mathbf{i}$ than to any other site. Each region is bounded by edges, at the end of edges vertices are placed. With the regions as tiles, the Voronoi diagram creates a partition of space based on a point set. This Voronoi graph is the dual graph of the Delauny triangulation [Okabe et al., 2000].

Voronoi tessellations or diagrams have an extensive number of applications, as reviewed in [Aurenhammer, 1991], and include nearest neighbor search, structure analysis in crystallography or local optimisation problems [Okabe et al., 2000]. Further examples will be introduced throughout this thesis.

A popular method to compute the Voronoi diagram is to compute the Delauny triangulation using convex hulls first, and then compute the Voronoi diagram as the dual graph of the Delauny triangulation [O'Rourke et al., 1998]. However, also a cell-based algorithm has been developed Rycroft [2009], providing more algorithmic flexibility.

Generalisations to the Voronoi diagram exists, for example the weighted Voronoi diagram, also called Laguerre diagram [Okabe et al., 2000]. Here each site has a weight, and the edges of the tessellation are not placed in the middle between two points, but shifted reflecting the weights of the two sites. These tessellations are thus useful in describing systems of extended bodies, such as polydisperse sphere packings.

Whereas Laguerre Tessellations have straight edges, tessellations with curved edges exist, namely the set-Voronoi diagrams [Schaller et al., 2013] and so-called navigation maps [Richard et al., 2001]. These have the advantage that tessellations of convex bodies of arbitrary shapes can be described in more detail than the Laguerre or Voronoi
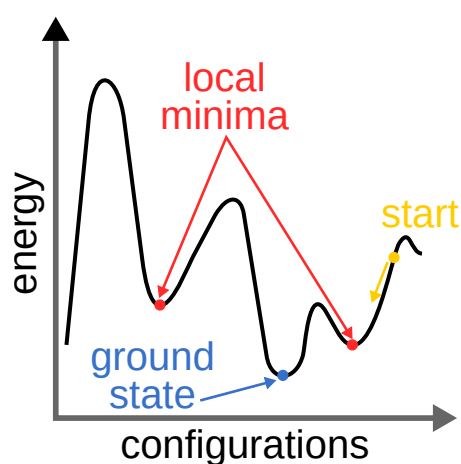
Figure 1.6: A schematic energy functional, assigning an energy, such as the total edge length of a tiling to a configuration of a system, for example a tiling given as a collection of vertices and edges. The configuration with the globally lowest energy is called ground state (blue dot), other minima are called local minima (red dots), which can be stable, i.e. a system in such a state will not evolve to further reach states of lower energy. The process of energy minimisation would be equivalent to evolve an initial configuration so that its energy (yellow dot) finds the global minima. This complex task might get stuck in local minima.

tessellation would allow. In general, the neighborhoods deducted from the Laguerre tessellation differ to the ones from the navigational maps. We found set-Voronoi diagrams to reconstruct the "correct" neighborhood relations - compared to visual analysis - more robust than a Voronoi or Laguerre tessellation. For a in-depth discussion, we refer to existing literature, such as [Richard et al., 2001, Katgert and van Hecke, 2010, Clusel et al., 2009].

We now circle back to the question, as to what constitutes an optimal tiling? The purpose of the above introduced tiling would be to measure how un/evenly postboxes are distributed over a city, i.e. a tiling containing cells of strongly varying area indicates an homogeneous distribution [Du et al., 1999]. To express this quantitatively we define a function

$$E(\mathbf{P}) = \sum_{i}^{N} \left(A(V_i) - \rho^{-1} \right)^2 \tag{1.2}$$

with $\mathbf{P} = (p_1^x, p_1^y, p_2^x, p_2^y, ..., p_n^x, p_n^y)$ being a vector containing all N positions of postboxes, $A()$ is the function computing the area of a Voronoi cell V_i and $\rho = \frac{N}{F}$ where F being the area of the city. As defined in eq. (1.2), E measures the total deviation of a perfectly distributed mailbox placement. The larger the value E gets, the less optimal is the mailbox placement and thus the partition. In physics, the quantity E is often called *energy* and the function which assigns an energy to a configuration of cells or points is called *energy functional*, or more generally *fitness function*. Since energy functionals usually take as input many parameters, a graphical visualisation of the function defined in eq. (1.2) is impossible. Thus we will introduce some aspects of energy functionals with the help of a simple, schematic energy functional shown in fig. (1.6). The ground state of an energy functional is the configuration of a system, which among all possible configurations, has the lowest energy (blue dot in fig. (1.6)) [Wales and Wales, 2003]. Moving the locations of the postboxes around in the example thus changes the value of the energy functional (eq. (1.2)) of the tiling and therefore its energy. The optimal

position of the postboxes for a given energy functional is then found, if the system is at its global minimum, thus the post boxes are perfectly spread out. This process of finding the optimal locations is called *energy minimization*. In fig. (1.6), this process is depicted as an initial configuration (yellow dot) being rearranged so its energy is decreased and moves towards the global minima. Depending on the exact procedure, a system might get stuck in stable local minima (marked as red dots in fig. (1.6)). That is the system can no longer reduce its energy and will remain in a locally optimal configuration, although the ground state as the globally optimal configuration, is not reached yet.

There exist many different types of energy minimisation methods, each with its own strengths and weaknesses. Which type to chose depends on the exact problem to be solved. The implementations of these processes can become arbitrarily complex, and efficiently designing such a process is beyond the scope of this thesis. However, the methods used for this thesis will be presented at the appropriate locations in later chapters.

The energy functional driving the honeycomb conjecture would be the total length of all edges in the tiling, with a constraint that all faces must have the same area. But are the bees right and is the honeycomb conjecture true? That is, is the hexagonal structure indeed the ground state of said energy functional? Many tried to proof the honeycomb conjecture, as is reviewed by Szpiro [2003]. Although not successful in proving the conjecture, Tóth [1972] formulated the remarkable equivalency of the honeycomb conjecture and the question of the densest disk packing in the plane [Tóth, 1972]. This means that the Voronoi diagram of the most dense disk packing in the plane would also solve the honeycomb conjecture. This relation again highlights the close connection of tilings and packings. In 1999, Hales [2001] - almost 2000 years after its formulation - finally proved the honeycomb conjecture. Since this prove shows that the hexagonal tiling has the least interface length among all regular tilings, all systems which are driven by an edge length minimisation will aim to adapt a honeycomb pattern, as we will see throughout this thesis.

1.4 Partitions of space and packings

We just introduced the hexagonal tiling as the optimal tiling to minimise the total edge length for a given tile area. This structure is ordered and highly symmetric. In this section, we will introduce structures which are asymmetric and disordered, but nevertheless optimal, given some energy functional. The given examples are three dimensional partitions, subdividing space into cells, which are separated by faces. A face is again

bounded by edges, which are connected by vertices. Due to their occurrence in everyday
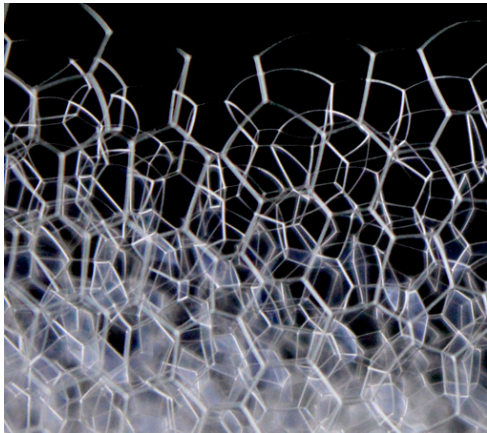
Figure 1.7: A dry foam, consisting of polyhedral cells, filled with air, separated by interfaces of water and surfactants. Due to its chemical and physical nature, the foam arranges to minimise the total area of its interfaces. (Photo credit Wiebke Drenckhan-Andreatta)

live, foams (see fig. 1.7) are an excellent example for a cellular material: space is divided into polyhedral cells filled with air, which are separated by interfaces made up by water and surfactants [Weaire and Hutzler, 2001, Stevenson, 2012, Wilson, 2014, Perkowitz and Perkowitz, 2000, Isenberg, 1992]. That is, the foam provides a disordered, random partition of space into single foam cells with a specific geometry and structure. Foams have been of long interest, with Plateau [1873] publishing his research about foams in 1873. Since then this subject has attracted much attention. Among others, structural properties [Matzke, 1946, Kraynik et al., 2004, Drenckhan and Langevin, 2010], the aging (coarsening) of foams [Ryan et al., 2016, Evans et al., 2012, 2017] and rheological properties [Evans et al., 2013b, 2017, Drenckhan et al., 2005] were investigated.

The driving force in foams is the surface tension: a large interface area is energetically less favourable, i.e. the cells deform and arrange in order to minimise the surface tension in the foam while not being able to exchange air. The air trapped inside the cells can not be exchanged, so the final structure of a foam is a compromise between minimal interface area and air pressure inside the cells [Weaire and Hutzler, 2001]. This again is a cellular optimization problem, similar to the honeycomb conjecture: which space-tiling cell minimises its surface area given a fixed cell volume? This problem was introduced by Lord Kelvin in 1887 [Sir William Thomson, 1887, Weaire, 1997] and thus named after him: the Kelvin problem. Lord Kelvin proposed the truncated octahedron as a solution. However, over 100 years later, Weaire and R. Phelan [1994] were able to give a counter example, with a structure consisting of two different cells with equal volume, which was has in total about 0.3% less surface area than the truncated octahedron [Weaire and R. Phelan, 1994]. While this is so far the most optimal solution, a conclusive proof is yet outstanding.

A fascinating property of soap-films is that they solve Plateau's problem [Harrison and Pugh, 2016]. This originally mathematical problem was introduced by Lagrange

in 1760 [Plateau, 1873] and searches for the surface with a fixed boundary which min-
imises its surface area. Due to the surface tension of soap-films, the latter naturally
solve Plateau's problem and thus form so-called minimal surfaces. This concept is not
constraint to soap-films and will be discussed in detail in chapter (4).

In the presentation of the honeycomb conjecture, the close connection - sometimes
equivalency - of packing and partition problems has been shown. A three dimensional
analogon for packing problems is the so-called Kepler problem [Szpiro, 2003, Hales,
2006, Torquato and Stillinger, 2010]. The latter searches for the densest sphere packing in
three dimensions. This question dates back to around 1600, and in 1611 Kepler proposed
the now called Kepler conjecture: the densest way of packing spheres in space is to place
the centers on the grid points of a face centered (FCC) cubic grid, visualised in fig. (1.9).
The grid points of a FCC grid sit at the corners of a cube as well as at the centers of its
faces.

An equivalent structure with identical packing density as the FCC packing is
the so-called hexagonal close packing (HCP). Like the packing, it consists of layers of
densely packed spheres, however, the arrangement of the layers differs from the FCC
packing. Since both FCC and HCP packings are built from the same layers of planar
packings, structures with mixed "layers" of FCC and HCP are possible.

Although the Kepler problem is strictly speaking a packing problem, this problem
can be reformulated as a partition problem: using the Voronoi diagram, each sphere
is assigned a cell. Due to its definition, these cell form covering of the space. The

(a) Kelvin cell   (b) Weaire-Phelan cells
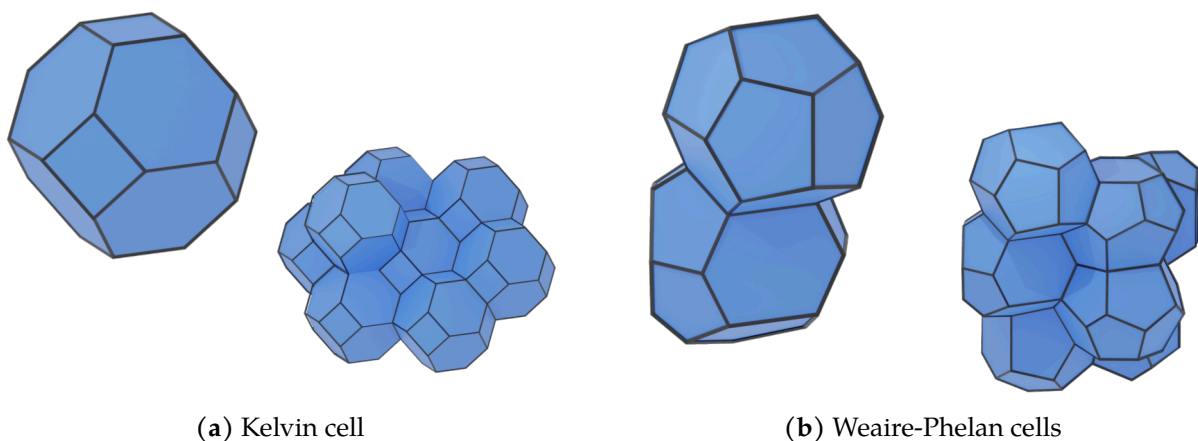
Figure 1.8: A single cell and a packing of several unit cells of the Kelvin (a) and the Weaire-
Phelan (b) foams. Whereas the Kelvin cell partitions space in equal cells minimising the interface
area, the Weaire-Phelan structure is the presently best partition of space minimising interface
area, however, using two different cells both of the same volume. The Kelvin cell consists of 14
faces, with six squares and eight hexagons. The Weaire-Phelan structure consists of a 14-sided
polyhedron, with 12 pentagonal and two hexagonal faces, and a 12-sided polyhedra with 12
pentagonal faces.

most dense sphere packing is then reached for the smallest possible Voronoi cell which contains the entire sphere. If the search is constrained to regular partitions, i.e. partitions made up of only a single type of cell, the Kepler problem reduces to the search for the smallest possible Voronoi cell which can cover space without gaps and overlap.

Similar to the honeycomb conjecture, it took many years and attempts until a proof of this conjecture was found [Szpiro, 2003]. It was again Hales [2005] who was able to prove this conjecture, using a computer-assisted proof.

The above optimisation problems with their respecting energy functionals are excellent models for real world cellular materials. These are driven by very similar or even identical energy functionals [Weaire and Aste, 2008]: when poured in a container, granular materials, such as sand, forced by the weights of the grains, compact into jammed, dense packings [de Gennes, 1999, Weaire and Aste, 2008, Mehta, 2012] and as such are attempts to solve the Kepler problem. Such packings have been studied intensively [Conway and Sloane, 1999, Cohn and Elkies, 2003, Torquato and Stillinger, 2010, Torquato, 2002].

Dry foams and froths, driven by minimization of the surface tension energy as discussed above, minimise the surface area of their cells and bubbles [Weaire and Hutzler, 2001].

The analytical approach of proving that a structure may or may not be the optimal solution to an optimization problem has the disadvantage that the structure has to be known beforehand. Using real world systems, such as grain packings, or model systems implementing the physical behavior, provides the opportunity to find new solutions to

(a) A FCC sphere packing   (b) Voronoi diagram of a FCC sphere packing   (c) Single FCC Voronoi cell
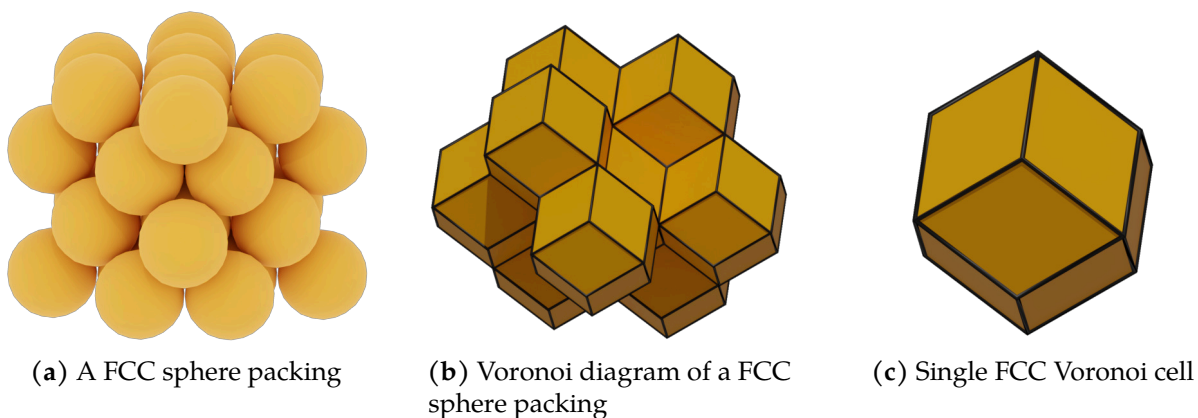
Figure 1.9: (a) A face-centered-cubic (FCC) sphere packing. A sphere is positioned at each corner and at the centers of each face of a cube. This arrangement has the highest density ($\approx 74\,\%$) among all sphere packings. (b) The Voronoi tessellation of a FCC point pattern, partitioning space into equal cells, each made up of 12 diamond shaped faces. (c) A close up of a single FCC Voronoi cell.

said optimisation problems and vice versa.

For example, with the FCC packing being the densest, i.e. optimal packing, i.e. densest, packing, one might expect spheres poured into a container to arrange in said structure. Analog foam cells would be expected to take the shape of the Weaire-Phelan structure, as they are (at least currently) the energetically most favourable configurations. Experimental experience already shows us that this is not the case: instead of adopting the optimal solution, disordered states emerge, both for the spheres in a container, as well as foams. Although these disordered states have a higher energy, i.e. lower density than the FCC or higher surface area than Weaire-Phelan foam, these disordered configurations are still stable and do not equilibrate into the respective ground states.

Although these states are disordered, they still are characteristic for their respective energy functional. Bernal's random close packing (RCP) [Bernal and Mason, 1960, Finney, 2013, Schaertl and Sillescu, 1994] as a disordered solution for the Kepler problem for example shows a characteristic upper bound ($\approx 64\,\%$) for its density and a characteristic average coordination number, i.e. the average number of how many spheres touch each other.

Even more strict rules, called Plateau's Laws, apply to the disordered configurations solving the Kelvin problem [Kraynik, 2006, Weaire and Hutzler, 2001]: (1) the faces of each bubble are spherical caps (2) exactly three faces meet at each edge at an angle of $120°$ (3) exactly four edges meet at each vertex at an tetrahedral angle of $\approx 109.47°$.

The concept of disordered, but stable local minima being favored over the respective ground states is the focus of chapter 3. There, a system will be investigated of which the ground state is known to be a body centered cubic (BCC) lattice. However, recent research found a stable, disordered state, analog to the random close packing for the Kepler problem or Plateau's foam to the Kelvin problem. The chapter will investigate the stability of this disordered state.

1.5   Infinite structures

In this last section, we introduce several infinite partitions of space with intriguing geometry, the so-called triply periodic minimal surfaces (TPMS).

Minimal surfaces minimise their surface area for a given fixed boundary and as a result have a vanishing mean curvature [Nitsche, 2011]. The previously discussed

(a) Gyroid   **(b)** Diamond   **(c)** Primitive
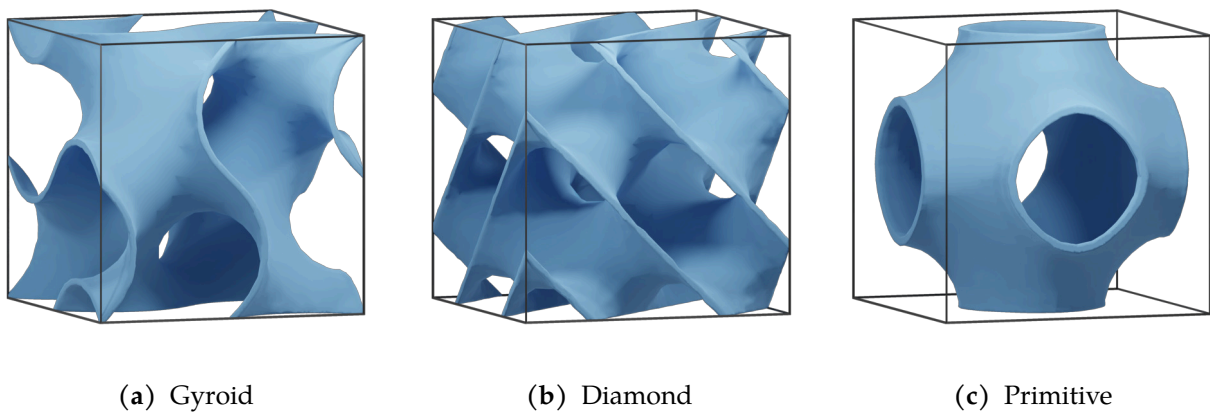
Figure 1.10: Three examples of triply periodic minimal surfaces (TPMS). These surface are usually highly symmetric and periodic in all three spatial dimensions. As minimal surfaces, i.e. they minimise their surface area given a fixed boundary, they have a vanishing mean curvature. The surface divides space in two intertwined but separated channels of equal volume, also see fig. (4.3) for a visualisation of the channel networks. Such surfaces often occur in soft-matter systems, where they are build by e.g. polymers or lipids, see also fig. (4.4).

soap films are examples of minimal surfaces. Triply periodic means that the surfaces are periodic in all three spatial dimensions. TPMSs have the important property that they divide space into two intertwined, but separate channels. Due to this property, these structures are also referred to as bicontinuous phases.

Research on TPMSs began as early as 1865, when Schwarz discovered the first TPMS, which was called the primitive (P) (fig. (1.10c) and diamond (D) surface (fig. (1.10b). Years later, Schoen [1970] found a number of new of these surfaces, among them the Gyroid (G) surface (fig. (1.10a). Many interfaces and structures have been found to assemble into the P, D or G surfaces. These structures have been found to act as a photonic crystals [Michelson, 1911, Wynberg et al., 1980, Jewell et al., 2007, Berthier et al., 2014, Sharma et al., 2014, Arwin et al., 2012, Vukusic and Sambles, 2003, Joannopoulos et al., 2011]: due to their geometry, the structure can exhibit photonic band gaps at certain wavelengths, causing light with said wavelength to be reflected. This phenomenon has been observed for a Gyroid structure, where one channel is filled solid with chitin, in the wing scale of a butterfly [Wilts et al., 2017], providing a bright green color. A Diamond structure with the same purpose is found in a beetle [Wilts et al., 2012b].

A complex membrane-like structure is also found in the prolamellar bodies (PLB) of the precursors of chloroplasts [Gunning, 1965]. The exact structure of these PLBs, however, has been long debated. In chapter 4 we are able to identify this structure as a Diamond surface [Hain et al., 2021]. TPMSs are also found as self-assembled structures in soft-matter systems, such as polymer melts or ampiphilic lipid systems. Analogous to foams, these molecules in solution assemble into films minimising their surface area

while trying to keep the molecular arrangement as little stretched or compressed as possible (for details, see chapter 2). As a result, the molecules arrange along minimal surface, see fig. (4.4). Further details on these processes, structures and their references will be given in chapters 2 and 4.

As the example of the PLB illustrates, the identification of these complex structures is challenging. Methods include X-ray scattering, but also direct imaging using e.g. transition electron microscopes. The latter, however, only provides a planar cross section or projection of a three dimensional structure, making a direct identification challenging. This problem will be addressed in this thesis in chapter 4

1.6   Outline and structure of this thesis

This chapter aims to provide a general introduction to cellular media, driven by geometrical optimisation, which is the topic of this thesis. More specifically, we investigate self-assembly in geometrically driven cellular media. Here three particular aspects are considered. Two of them are related to self-assembly, namely the effect of geometric frustration and the stability of disordered phases as local minima of energy functionals. The third aspect addresses the identification of TPMS in soft-matter systems.

The further structure of this thesis is as follows: each chapter is based on one publication, presented in full, which is prefaced by a introduction to the corresponding topic. This introduction provides a literature overview for each publication and connects the different chapters of this thesis. The last chapter of this thesis provides a coherent discussion, with a focus on the connection of our results to other research in the field, of the results from each publication and provides an outlook on future research. The thesis consists of three publications.

- Chapter 2 is based on [Hain et al., 2019] and will investigate a polymer melt assembling into planar tiling patterns, minimising its interface length. As discussed above, its ground state is thus the honeycomb pattern. To tweak this structure, we will force this polymer melt onto a spherical substrate. This spherical geometry is incompatible with the honeycomb pattern, which as a result will have to adapt. Here Molecular Dynamics simulation will be employed to compute the self-assembly process. We find that the structure of the tilings is closely related to the Thomson problem of placing electrons on a sphere.

- Chapter 3 is based on [Hain et al., 2020] and considers the Quantizer problem, a geometric optimization problem defined on the Voronoi diagram of a point

set. The Quantizer problem is then the search for the arrangements, where all cells are of equal volume and as "spherical" as possible. Similar to established optimization problems, the ground state is known to be the body-centered-cubic structure, however, recently a disordered but stable structure has been found [Klatt et al., 2019]. In this chapter we will test the stability of this disordered structure over its ground state.

- Chapter 4 is based on [Hain et al., 2021] and will present a new open-source software tool developed by us, called SPIRE: Surface Projection Image Recognition Environment. This tool is based on so-called direct template correlative matching (DTC): a planar projection of a three dimensional structure, for example obtained from electron microscope images, is compared to a library of artificial projections of potential structures. This method has been first introduced by Deng and Mieczkowski [1998]. With SPIRE, we improve the functionality and usability of this approach, facilitating faster and more exact structure identification and analysis.

- Chapter 5 contains a conclusion, synthesis and outlook of this thesis. Here, our results are presented coherently in the context of relevant work in corresponding fields. An extensive outlook on our ongoing research and future projects is given.

Effect of geometric frustration on polymeric self-assembly

This chapter investigates how the self-assembly process and the resulting structure are influenced by geometric frustration. The topological defects in a three-colored honeycomb tiling are analysed for systems forced onto a spherical substrate. The honeycomb tiling is self-assembled by a polymer melt of triblock star copolymers confined to a spherical shell. The self-assembly process is simulated using Dissipative Particle Simulation (DPD) code.

The core of this chapter is our publication [Hain et al., 2019] which contains methods, results and a discussion of the latter. The following first section will provide a general introduction to the background of this article, starting with general polymeric self-assembly and more specifically self-assembly of tiling patterns using star copolymers. The concept of topological defects in ordered arrangements caused by curvature is introduced before the publication is presented in full. A conclusion and outlook is given in chapter 5.
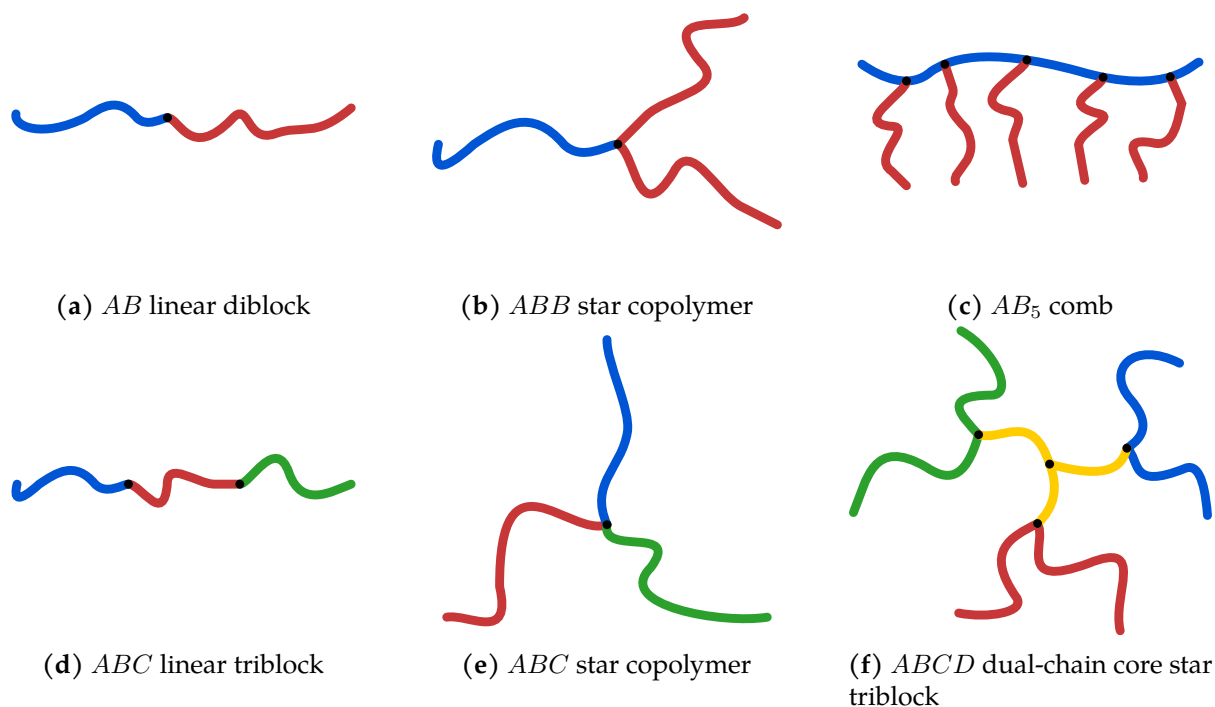
2.1   Polymeric self-assembly

2.1.1   Foundations of polymeric self-assembly

Self-assembly is the ability of components to arrange into structures without external influence [Isaacs et al., 1999, Whitesides and Grzybowski, 2002]. A wide variety of structures are self-assembled, for example molecular [Philp and Stoddart, 1996], liquid [Mezzenga et al., 2019] or colloidal [Dijkstra and van Roij, 2005, Ellison et al., 2006, Schönhöfer et al., 2017, Loudet et al., 2000] crystals, biological membranes [Almsherqi et al., 2009] and cell organelles[Garab, 2016]. Block copolymers have been studied for over 50 years, since they offer a wide variety of molecular architectures with a well understood theoretical foundation based on only a few parameters [Reddy et al., 2021]. Due to these properties, block copolymers has been used as a model system to study and understand the self-assembly of a variety of morphologies in soft-matter, as for example reviewed by Bates and Frederickson [1999], Bates and Bates [2017], Polymeropoulos et al. [2017], Reddy et al. [2021]

Block copolymers are macromolecules consisting of at least two different species of monomers (in here visualised by different colors) combined into chain-like blocks, that is sections of identical monomers. An arbitrary number of blocks of different species are joint at so-called grafting points to form a macromolecule. This allows for various architectures, such as stars, combs or linear triblocks, as shown in fig. (2.1)[Matsen, 2007, Fischer et al., 2014]. The foundation of polymeric self-assembly lies in the chemical incompatibility of different block types [Bates and Frederickson, 1999]. This incompatibility is manifested in repulsive forces between two monomers of different types. Contacts of different block types are thus avoided, however, can not be avoided completely since different blocks are joined at grafting points. This results in the polymers organising into morphologies minimising the interface area between different block types. This process is called self-assembly. Depending on the chemical composition, i.e. the strength of the incompatibility, of the polymers and the length of the different blocks, various different morphologies form.

To introduce some morphologies of block polymers, we present the different self-assembled structures of a melt of the simplest copolymer, the linear AB diblock. A polymer melt is a liquid consisting solely of polymer molecules, without a solvent. AB linear diblocks are copolymer chains, consisting of two linked blocks of types A and B. The length of the A block as a fraction of the entire chain is given as f_A whereas the strength of the chemical incompatibility of the different block types is given as the so-called interaction parameter χ_{AB} [Matsen and Schick, 1994, Matsen and Bates, 1996,

(a) AB linear diblock   **(b)** ABB star copolymer   **(c)** AB_5 comb

(d) ABC linear triblock   **(e)** ABC star copolymer   **(f)** $ABCD$ dual-chain core star triblock

Figure 2.1: Different architectures of block copolymers. Block copolymers are molecules where blocks, i.e. sections of identical species, are joined together into a macromolecule. Different species are here visualised by different colors and denoted by letters, here 'A', 'B' and 'C'. The points (black dots) where different blocks are joint are called grafting points. Block polymers show a rich morphology of self-assembled structures, see e.g. fig (2.2) for morphologies of AB linear diblock copolymers.

Bates et al., 1994, Bates and Frederickson, 1999]. A phase diagram as a function of f_A and χ_{AB}, as well as visual presentations of the common phases is shown in fig. (2.2).

In the following section we will summarise the theoretical foundations of polymeric self-assembly following the reviews by Matsen [2002, 2007], Bates and Fredrickson [1990] unless stated otherwise. More details can be found in the cited literature throughout this introduction or in text books on the topic [Hamley, 1998, Jones and Richards, 1999, Enders and Wolf, 2011, Gedde, 2013].

In the *de-facto* standard theoretical model, called Gaussian chains, polymers are treated as continuous curves in space $\mathbf{r}_\alpha(s)$, where α numerates each polymer chain. However, an exact knowledge of the position of each molecule is not important, instead, the quantity considered here is the ensemble average density $\Phi(\mathbf{r})_X = \left\langle \hat{\Phi}(\mathbf{r})_X \right\rangle$ of a monomer species X at a position $\mathbf{r}$ with

$$\hat{\Phi}_X(\mathbf{r}) = \frac{N}{\rho_0} \sum_\alpha^n \int_0^{f_X} \delta\left(\mathbf{r} - \mathbf{r}_\alpha(s)\right) \mathrm{d}s$$
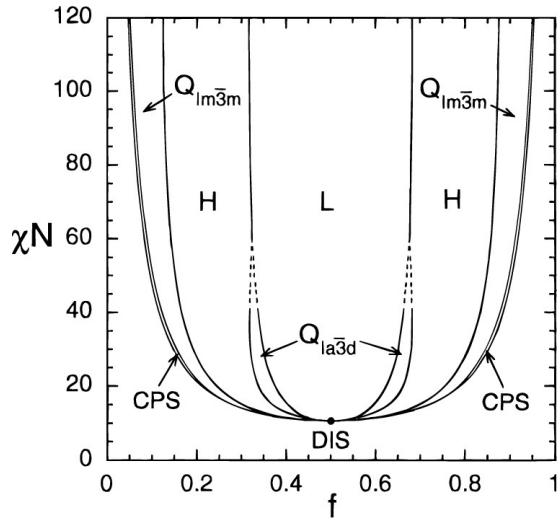
(a) Self-Consistent Field Theory (SCFT) computed phase diagram of AB diblock copolymers. Ordered phases include micelles ($Q_{Im\bar{3}m}$), hexagonal cylinders (H), Gyroid network ($Q_{Ia\bar{3}d}$) and lamellas (L). Reprinted with permission from [Matsen and Bates, 1996]. Copyright 1996 American Chemical Society.
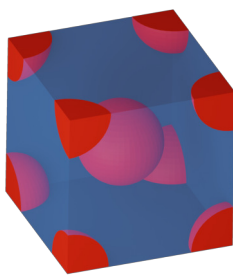
(b) Micelles
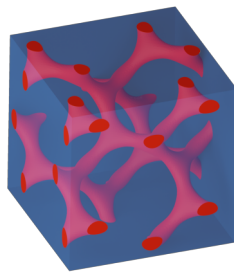
(c) Gyroid (G)
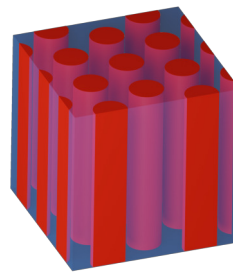
(d) Hexagonal Cylinders (H)
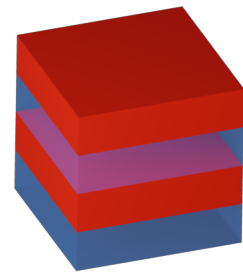
(e) Lamella (L)

Figure 2.2: Phase diagram (a) and visualisation of the most common phases of AB diblock copolymers (b-e). For weak interactions of $\chi_{AB}N < 20$ the melt is entropy driven and well mixed, i.e. no microphase separation takes place. For a strong enough interaction strength $\chi_{AB}N > 20$, the polymer melt undergoes microphase separation and assembles into ordered structures. We describe the morphologies with increasing f_A. **Micelles** (b): The short A type blocks congregate into a spherical domain, called micelles. These micelles float in a matrix made up of the B tails of the polymer chains. The centers of the micelles has been found to sit on lattice positions of periodic lattices, such as the cubic body-centered-cubic (BCC) or face-centered-cubic (FCC), but also the A15 Frank-Caspar phase. **Gyroid** (c): The A type tails here form an infinite, triply periodic network, called srs-net, surrounded by a B-typed matrix. See also fig. (4.4c). **Cylinders** (d) : A domains are parallel cylinders arranged in a hexagonal order of infinite length, surrounded by a B-typed matrix. **Lamella** (e): Alternating layers of A and B type sheets form, a cross section is shown in fig. (2.3b). Further increasing f_A does not generate new structures, but due to the symmetry of the linear diblocks, identical structures where A and B type domains are switched form.

(**a**) Mixed polymer melt

(**b**) Micro-phase separated lamella morphology

(**c**) Micro-phase separated micelle
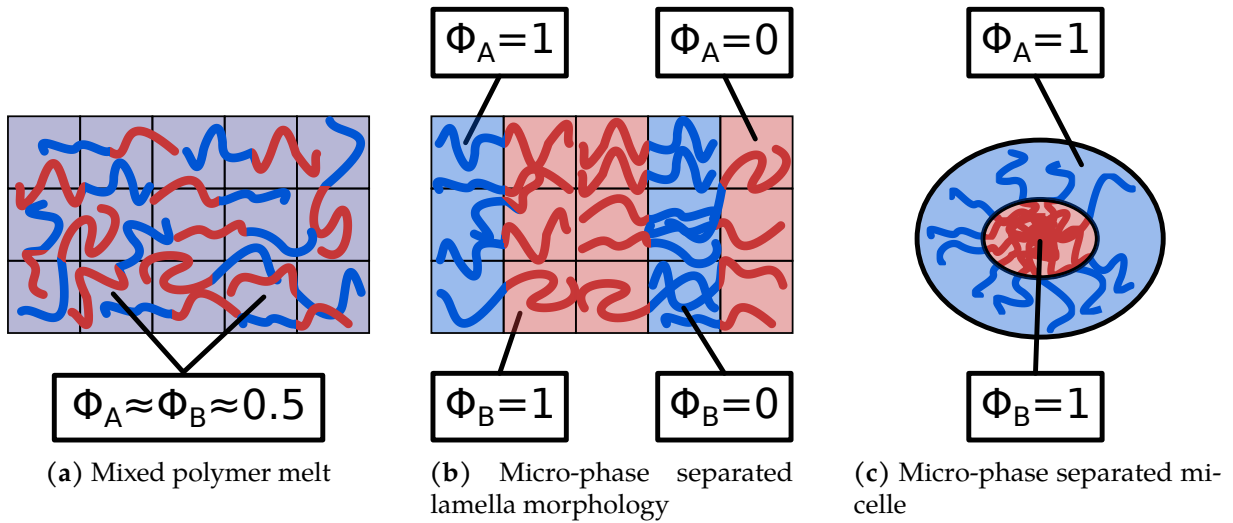
Figure 2.3: Example of a mixed (a) and microphase separated (b,c) polymer melts.

where ρ_0^{-1} is the volume of a chain segment, N is the number of segments in a polymer chain (see fig (2.4)) and f_X is the fraction of the block of type X in the polymer. Since polymer melts can be assumed as almost incompressible liquids, the sum of the densities of all monomer species must add up to 1. In regions where the polymer species are well mixed, the densities of different species are about equal, as shown in fig. (2.3a). Regions with an excess of one monomer species then show a high density of a species. If the density is close to 1, such a region herein is considered to be a domain of the type of this species, as depicted in fig. (2.3). Where as in fig. (2.3) the average density of rectangular regions is computed, domains of purely one monomer species can be of any shape, e.g. as shown in fig. (2.3c). A full thermodynamical treatment of polymer melts is out of scope for this thesis, but we will provide a phenomenological approach to the statistical mechanics of polymer melts.

A system in statistical mechanics is driven by the extremisation of a thermodynamical potential, in the case of polymer melts this is the free energy $F = U - TS$, where U is the internal energy of the system due to its interactions, T is its temperature and S is its entropy. As can be seen, for high temperatures the system is entropically driven and prefers a uniform mixing, as shown in fig. (2.3a), where as for low temperatures the system is driven by the internal energy. This is the regime where self-assembled structures form, such as the lamella phase shown in fig. (2.3b).

To model the interactions of polymers, a so-called coarse grained model is employed. Here, a section of the polymer chain, e.g. a single monomer unit or more, is treated as a single unit called segment, depicted as a disk in fig. (2.4). Since its internal structure is consisting of many atoms, a segment has only a statistical length which can be stretched and compressed. The energy contribution to the free energy of such a chain
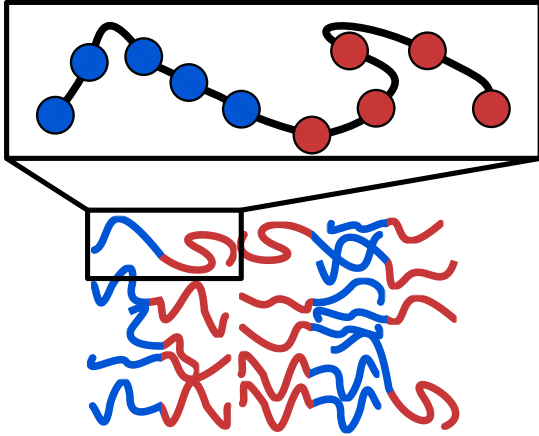
Figure 2.4: The continuous chains modelling polymers in the standard Gaussian chain model are discretised into a coarse grained model for theoretical and numerical treatment. Here, one or more monomer units are grouped into a so-called segment, here depicted by a disk. The color of the disk visualises the type of the segment. Shown are AB diblock copolymers. Coarse grained models are also employed when using computer simulations.

is consisting of two parts: (1) the energy of the interactions between the segments and (2) the internal energy of the chain due to stretching and compression of the segments.

The internal energy of the chain in an interval $[s_1, s_2]$ is given as

$$\frac{E_{st}}{k_B T} = \frac{3}{2Na^2} \int_{s1}^{s2} |\mathbf{r}_\alpha(s)|^2 \, \mathrm{d}s \tag{2.1}$$

where $\mathbf{r}_\alpha(s)$ is a space curve describing the polymer chain, N is the number of segments in the polymer, a is the statistical segment length, and $k_B T$ is the temperature of the melt. The internal energy penalises configurations where segments are strongly stressed or compressed, thus perturbed from their favourite segment length a. This is the case for configurations where the polymer chain is relatively straight or strongly curled into a blob.

The interaction between two segments is modelled as a single contact force. Here, contact force means an interaction potential which only interacts with direct neighbouring particles. The strength and energy content of the interactions between two segments of species A and B is modelled by the so-called Flory-Huggins parameter χ_{AB} [Flory, 1942, Huggins, 1942, Flory, 1944], where a parameter for each pairwise interaction between monomer species is used. The total energy from interactions U is given as

$$\frac{U}{k_B T} = \chi_{AB} \rho_0 \int \phi_A(\mathbf{r}) \phi_B(\mathbf{r}) \mathrm{d}\mathbf{r} \tag{2.2}$$

where ρ_0^{-1} is the volume taken by a single segment.

To model insoluble, that is chemical incompatible, monomer species, the interaction parameter between the latter are chosen higher then the interaction parameter between identical monomers thus $\chi_{AB} > \chi_{AA}$. This results in an energy penalty if two monomers of different species are in contact. Due to the urge of the system to reduce its energy, the molecules will rearrange to avoid contacts of different monomer species,

resulting in a separation of the latter.

The strength of this separation process is dependent on the interaction strength and temperature, as mentioned above. At high temperatures and low interaction forces, the system will be entropically driven and prefer a thoroughly mixed system. Reducing the temperature and increasing the interaction strength will then lead to a regime called *weak segregation limit* (WSL). In this regime areas with an excess of one monomer types will form. Further reducing the temperature and increasing the interaction strength will finally result in the *strong segregation limit* (SSL). In this limit, different types of polymer blocks are completely separated and the densities of the polymers are described by step functions. Sharp interfaces form in between the boundaries.

In the SSL, a mixed system of polymers of solely type A or B will undergo what is called macrophase separation[Bates and Fredrickson, 1990, Bates et al., 1994, Bates and Frederickson, 1999]: two domains will form, where each domain will contain only a single type of monomers. A more complex behavior show block copolymers: since blocks of different species are joined, contacts of the latter can never be avoided, but only reduced as much as possible. Instead of two large, separated domains, many small domains will form. The larger the interfaces are, the more unfavourable contacts between different monomer species occur. By the minimisation of the free energy the system arranges to a morphology reducing the interface area as much as possible. This phenomenon of unfavored contacts and interface area minimisation is referred to as surface tension.

The grafting points of the polymers will sit on the interfaces in between domains and the arms extend in the respective domain, as depicted in fig. (2.3b). If the domains are getting too stretched out, the polymer arms are getting elongated, resulting in a penalty in the internal energy of the chain. Microphase separation is thus dominated by the competition of minimising unfavored segment contacts, thus minimising the interface area, and minimising the stretching penalty.

The SSL theory has been extensively treated analytically [Helfand and Wasserman, 1976, Olmsted and Milner, 1994, 1998, Semenov, 1985] and is important in this chapter, since the polymer melts considered in our publication of this chapter (sec. 2.3) are in the SSL. In this limit, where pure domains of one type of monomer are divided by sharp interfaces, the free energy of a polymer melt can conveniently be written purely in terms of the geometry of the macroscopic structure[Likhtman and Semenov, 1994, Helfand and Tagami, 1972, Semenov, 1985]:

$$F = F_{\text{int}} + F_{\text{st}}$$

with

$$F_{\text{int}} = a\chi^{\frac{1}{2}} S \tag{2.3}$$

$$F_{\text{st}} = \frac{\pi^2}{16} \frac{1}{N_A^2 a^2} \int_{[A]} z^2\left(\mathbf{r}\right) \mathrm{d}^3\mathbf{r} \tag{2.4}$$

where S is the total interface area, a is the statistical segment length, N is the number of segments in each polymer chain and z is the shortest path from any point to the nearest interface [Likhtman and Semenov, 1994]. The free energy F is expressed in two terms: an interfacial term, F_{int}, contributing the surface tension penalties and a entropic term, F_{st}, contributing the chain stretching penalties. This is a key concept for this thesis: in the SSL, the self-assembled equilibrium structures of a polymer melt can be expressed as a macroscopic, cellular optimisation problem.

2.1.2   Equilibrium structures and tilings from polymeric self-assembly

Stable, microphase separated equilibrium structures in copolymer melts in the SSL have been predicted theoretically as well as found experimentally. A successful theory to predict stable, equilibrium phases is the so-called Self-Consistent-Field-Theory (SCFT): Helfand and Tagami [1971] first introduced a theory about the interfaces between different monomer species in AB diblock copolymer melts. This theory is later extended by the employment of a mean field theory by the same authors [Helfand and Tagami, 1972]. A connection between the mean field theory and more fundamental statistical dynamics is made by Helfand [1975]. Helfand and Sapse [1975] extended the theory to unsymmetrical polymers using Gaussian random-walk statistics to describe the polymers. Helfand and Wasserman [1976] introduces a narrow interface approximation. Leibler [1980] introduced an analytical approximation for melts in the WSL, where earlier theories could not be applied due to assumptions made, such as narrow interfaces. Semenov [1985] presents a theory for melts in the SSL and studies the interactions of micelles in polymer melts. Matsen and Schick [1994] computes the phase diagram of AB diblock copolymers using SCFT. Matsen and Bates [1996] finally unifies theories for polymers in the WSL and SSL lifting traditional approximations. A number of articles and reviews exists for this popular theory, also considering more complex morphologies [Schmid, 1998b, Likhtman and Semenov, 1994, Fredrickson et al., 2002, Ceniceros and Fredrickson, 2004, Schmid, 1998a, Whitmore and Vavasour, 1995, Matsen, 2002, 2007, Arora et al., 2016].

SCFT assumes the space curves modelling the polymer chains to be random walks and thus have Brownian motion statistics [Matsen, 2002]. Instead of considering

the segment-segment interactions of all molecules, the segments only interact with a field, which is generated by the segments of the polymer melt and computed from the species densities Φ_X. A set of modified diffusion equations describes the evolution of the fields [Matsen, 2002, Arora et al., 2016]. Given an initial, educated guess for the polymer configurations, and thus fields, SCFT then provides a framework to compute the stable equilibrium configuration, i.e. the free energy minimum [Matsen, 2002].

Another approach is to model polymer segments as particles, which are linked to chains by harmonic springs, as shown in fig. (2.4). Based on these models established particle based simulation methods, namely Monte Carlo (MC) [Verdier and Stockmayer, 1962, Haliloğlu and Mattice, 1996, Dotera and Hatano, 1996, Larson, 1989, Micka and Binder, 1995, Ko and Mattice, 1995, Gemma et al., 2002, Hoffmann et al., 1997, Lü and Kindt, 2004] and Dissipative Particle Dynamics simulations (DPD) [Groot and Madden, 1998, Kirkensgaard, 2012a, Wang et al., 2021, Español and Warren, 2017, Huang and Yu, 2007] have been applied and adapted to simulate polymeric self-assembly.

Dissipative Particle Dynamics [Hoogerbrugge and Koelman, 1992, Español and Warren, 1995, 2017] is a type of coarsed grained Molecular Dynamics simulation. In this model multiple segments of a polymer are combined into a single bead which interaction is described by a soft, repulsive potential. Groot and Madden [1998] found a expression to write these forces in terms of the Flory-Huggins interaction parameter χ and thus linking it to existing polymer theories. A simulation starts with an initial configuration, then Newton's equations of motion $\mathbf{F} = m\mathbf{a}$ are used to simulate the time evolution of each particle of the system [Groot and Madden, 1998]. After an appropriate amount of time the polymer melt is in equilibrium and the self-assembled structure has formed. DPD simulations has been used extensively to simulate polymeric self-assembly [Groot and Madden, 1998, Kirkensgaard, 2012a, Wang et al., 2021, Español and Warren, 2017, Huang and Yu, 2007]. We use DPD simulations in our work; more details about this technique and its implementation can be found in the *Methods* section of our publication [Hain et al., 2019].

With advances in the field of polymer synthesis a vast variety of polymer architectures can be created experimentally [Polymeropoulos et al., 2017] and thus many theoretically predicted structures have been confirmed experimentally [Foerster et al., 1994, Bates et al., 1994, Khandpur et al., 1995, Zhao et al., 1996]. The number of possible polymer architectures and thus resulting structures is countless [Bates and Frederickson, 1999, Bates, 2005, Guo et al., 2008, Grason et al., 2003, Grason and Kamien, 2004, Grason, 2006, Ye et al., 2005, Olmsted and Milner, 1998, Polymeropoulos et al., 2017].

In experiments, structures can be identified using scattering techniques, such

as small-angle X-ray scattering (SAXS)[Als-Nielsen and McMorrow, 2011b]. But also direct imaging technologies such as transmission electron microscopy are employed [Foerster et al., 1994]. Here, a three dimensional structure has to be identified based on an planar cross section or projection of the latter. This is a challenging task, and not limited to polymer melts, and is in-parts addressed by chapter 4 of this thesis.

Here, we will address the phase behavior of the ABC and ABB star copolymers (see fig. (2.1e)), since these polymers are used in this thesis as model system. The self-assembly of star copolymer melts has been studied, both theoretically [Olvera de la Cruz and Sanchez, 1986, Gemma et al., 2002, Grason and Kamien, 2004, Han et al., 2008, Huang and Yu, 2007, Kirkensgaard, 2012b,a, Kirkensgaard et al., 2014, Zhang et al., 2010, Tang et al., 2004] and experimentally [Okamoto et al., 1997, Takano et al., 2004, 2005, de Campo et al., 2011]. For ABB stars, possible morphologies include micelle, lamellar and cylindrical phases analog to diblock copolymers. Due to the increased complexity of ABC star copolymers (there are 3 types of domains instead of 2), the phase space is more complex than for e.g. AB linear diblocks. To produce simple, clear phase diagrams, only a few parameters can be changed. In the listed literature, for example, phase diagrams are presented, where the fraction of only one arm is altered, with the two remaining arms being chosen at same length, i.e $f_A \neq f_B = f_C$, and the interactions are symmetrical, i.e. $\chi_{AB} = \chi_{AC} = \chi_{BC}$. In this case, further phases are found: lamellar with spheres, perforated lamella, lamella with cylinders, lamella in micelles, columnar piled disks as well as a bicontinuous, intertwined diamond phase. We will refrain from going into further details here, but focus on the phase relevant for this work, the columnar phase.

This phase has already been found for linear diblocks and consists of infinitely long cylinders which arrange in a certain pattern. In case of the ABB system, A-typed cylinders are packed in a B-typed matrix, as shown in fig. (2.5b). In ABC systems, these cylinders are tightly packed, however, since a melt does not allow for gaps the polymer arms extend beyond the cylinders to fill the gaps, creating a hexagonal shape for the cylinders [Grason, 2006]. This is also the case for the ABB system, as indicated in fig. (2.5d), however, since all tiles have identical color, this effect is not visible as compared to the ABC system.

A cross section perpendicular to these cylinders, both for ABC and ABB systems as shown in fig. (2.5c) and (2.5d), thus yields a planar tiling, where each domain of polymers is considered a tile. Each tile has a "color" associated, determined by the monomer species. That is tiles of identical shape but different color can still be differentiated.
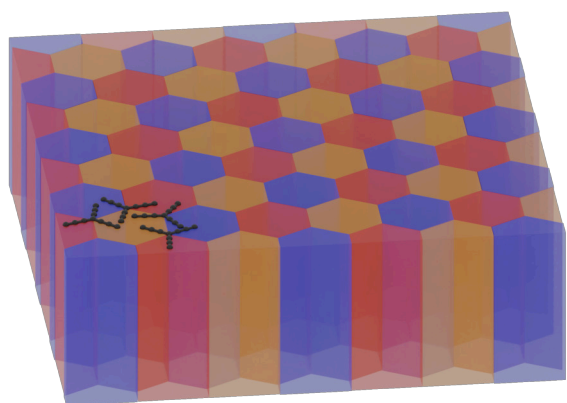
(**a**) 3D render of the hexagonal columnar phase in an ABC star copolymer melt.
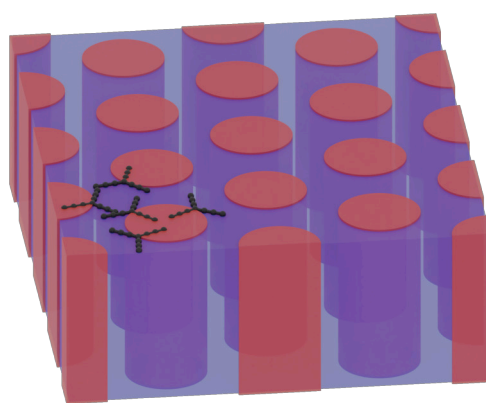
(**b**) 3D render of the hexagonal columnar phase in an ABB star copolymer melt.
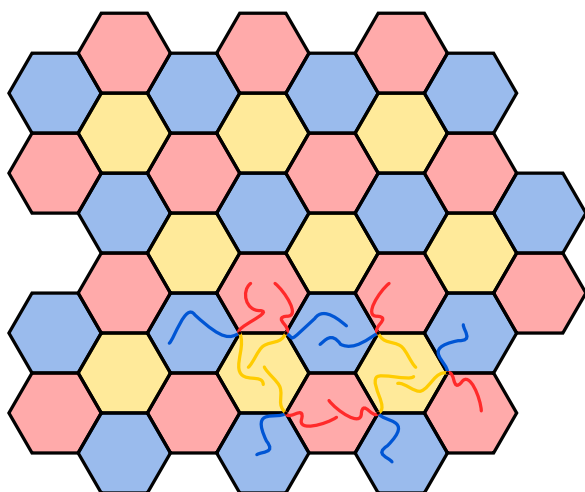
(**c**) Three colored hexagonal tiling obtained by a perpendicular cross section of the columnar phase for symmetric ABC star copolymers. Each color denominates a different monomer species. The grafting points of the stars can only sit at the vertices of the tilings.
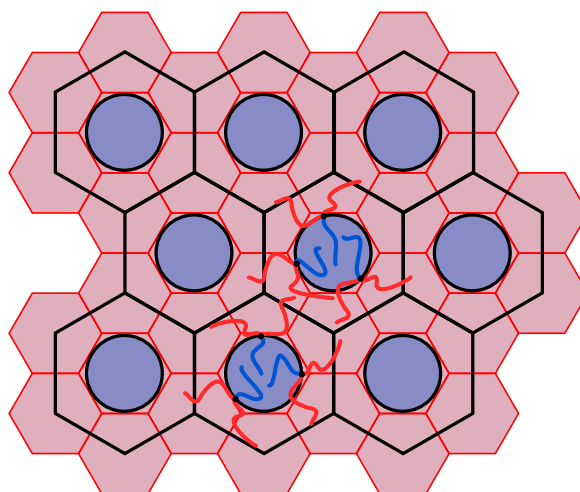
(**d**) Hexagonal columnar phase for symmetric ABB star copolymers. The grafting points of the polymers can sit anywhere on the surface of the cylinder.

Figure 2.5: Hexagonal, planar tiling patterns created through self-assembly of ABC and ABB star copolymers. For symmetrical arm lengths and interactions, that is $f_A = f_B = f_C$ and $\chi_{AB} = \chi_{AC} = \chi_{CB}$ a cylindrical phase assembles. Cross sections perpendicular to the cylinder axis are planar tiling patterns, in this case a hexagonal tiling.

The size of the tiles are determined by the length of the polymer arms of each species f_X. For symmetric star polymers, that is $f_A = f_B = f_C$ and $f_A = f_{B_1} = f_{B_2}$ respectively, all tiles are of equal size and a honeycomb tiling is formed for both ABC (see fig. (2.5c)) and ABB (see fig. (2.5d)) stars. For different fractions, different sized tiles assemble and the tiling changes from a honeycomb pattern to different tilings. A vast amount of different tilings have been predicted theoretically [Kirkensgaard, 2012b,a, Kirkensgaard et al., 2014, Zhang et al., 2010, Gemma et al., 2002] and also been visualised directly using transmission electron microscopy [Hayashida et al., 2006, 2007, Okamoto
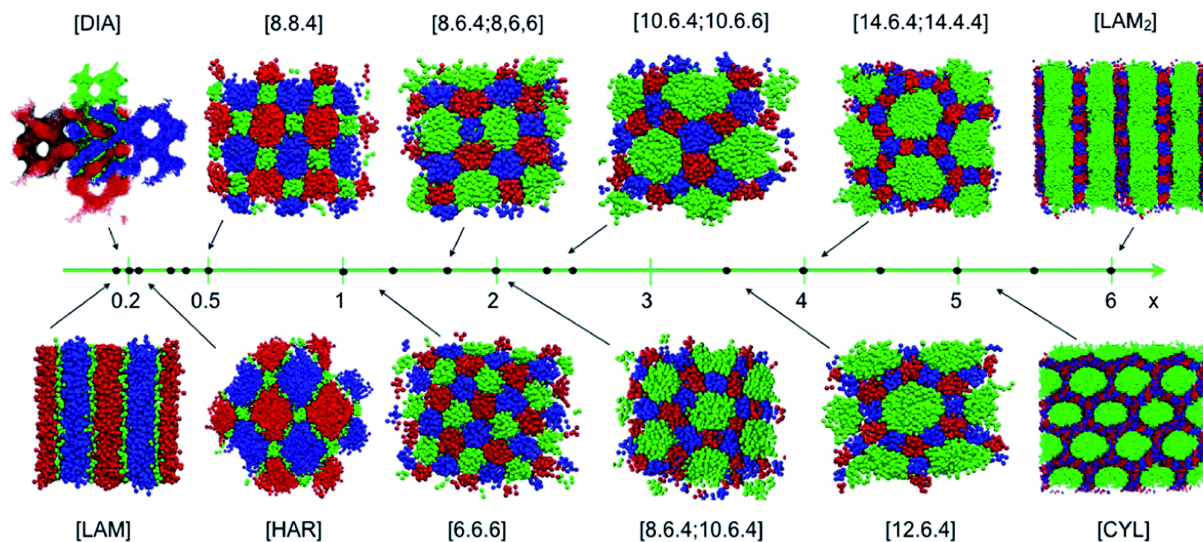
Figure 2.6: Tiling patterns formed as cross section of the cylindrical phase in ABC star copolymers with symmetric interactions. Different patterns are assembled by altering the length of one arm of the star, tuning the size of the tiles created by the latter. Republished with permission of Royal Society of Chemistry, from [Kirkensgaard et al., 2014]; permission conveyed through Copyright Clearance Center, Inc.

et al., 1997, Takano et al., 2004, 2005, de Campo et al., 2011]. Some tilings generated by keeping two arms at constant length while alternating the length of the third arm are shown in fig. (2.6). Here we can see the optimization aspect of polymeric self-assembly. As stated earlier the polymer melt tries to minimise the interface area between domains of different species while keeping all domains as spherical as possible to minimise the chain stretching penalty. It is known that the honeycomb structure, and thus the hexagonal arrangement of the cylinders, minimises the total edge length and as such is the prime candidate to form.

A key aspect of the three-colored tilings generated by the ABC systems, is that the grafting points, that is the centers of the stars, have to sit at the vertices of the tilings. Only at these positions each arm can extend into a domain of its corresponding species. This has two important implications: (1) the tiling consists only of vertices of order three [de Campo et al., 2011] and (2) only tiles with an even number of adjacent tiles are allowed [Gemma et al., 2002]. We will refer to the second implication as *color constraint*. The latter is a key aspect in our publication and will thus be discussed in its *Introduction* section in more detail, but is also addressed throughout the article.

All of the presented tilings have been found as cylindrical phases in bulk simulations, i.e. a polymer melt in a 3D volume. Several authors addressed the question, if confining a polymer melt to a certain geometry alters the assembled structures compared to the bulk case [Han et al., 2008, Lin et al., 2010, Lv et al., 2016]. A melt of ABC star copolymers was confined to a thin film and a cylinder, with the result that previously

existing morphologies are altered and entirely new morphologies assemble. However, it was argued that a surface field, i.e. an attractive substrate, had a stronger influence on altering the morphology than the geometric confinement. Xu et al. [2009] addressed an ABC star copolymer system confined into a cylinder and found new morphologies and a more complex phase diagram than compared to the bulk case. Li et al. [2013] studied the morphology of ABC star polymers confined to a spherical cavity using SCFT. A number of previously unknown morphologies are found and known structures found to be altered by the confinement.

Extensive work, however, was put towards the self-assembly of diblock copolymers on a sphere or spherical substrate [Tang et al., 2005, Yu et al., 2007, Chantawansri et al., 2007, Vorselaars et al., 2011, Zhang et al., 2014]. On the two dimensional surface of a substrate or spherical volume, the cylinders collapse into a flat patch, which we will refer to as micelle. The lamella and micelle/cylindrical phases are compared to the bulk case. In the latter the micelles (respectively cylinders) arrange on a hexagonal grid, i.e. each micelle has six direct neighbors. On the sphere, however, micelles with five or seven neighbors appear, which are called topological defects. These occur either isolated or as so called grain scars, where many defects are linked together. While Li et al. [2013] briefly studied the tiling patterns of ABC star copolymers in a spherical cavity, it is only reported that the hexagonal pattern is disturbed, but no further analysis was performed. This open question of the exact structure is addressed in our publication [Hain et al., 2019] in sec. 2.3

The origin of the topological defects lie in the curved surface of the sphere, which renders a hexagonal pattern incompatible. This effect, where a locally preferred pattern can not be propagated globally, is called geometrical frustration [Sadoc and Mosseri, 1999, Grason, 2016]. This important aspect and its relation to polymeric self-assemblies and tilings will be discussed in the next section.

2.2 Geometric frustration - topological defects in crystalline order

We will approach the subject of geometric frustration using the honeycomb shown in fig. (2.7). As already stated above, the perfect honeycomb pattern is a tiling of a planar surface, consisting of only hexagonal faces, as shown in fig. (2.7a). The honeycomb presented, however, is not planar, but exhibits a "wavy" surface, i.e. there are some sections which are flat and some which are bend and thus curved. This is indicated in the height profile at the bottom of fig. (2.7a). Being curved, or curvature, in this

case means that the flat structure bends out of its two dimensional plane into the three dimensional space (see also fig. (2.8)). A closer look at different locations, marked with rectangles in the figure, illustrates two aspects: fig. (2.7b) contains a flat area, here, a perfect hexagonal tiling is found, as indicated in the figure. Figure (2.7c) shows a section of the honeycomb, which is curved, as indicated in the height profile. In this area, the perfect hexagonal structures is disrupted by defects: heptagons and pentagons. These defects are called topological defects, and their origin lies in the curvature of the honeycomb. This concept is best explained by considering it "backwards", as illustrated in fig (2.8). Panel (a) shows a perfect hexagonal tiling. The angles of the edges align perfectly with each other, so no gaps occur in the pattern and as such a valid tiling exists. Panel (b) introduces defects in the hexagonal order in the form of two pentagons. The angles of the edges do not align and gaps occur. These are, however, not permitted in a tiling and the only way - apart from deforming the tiles - is to curve the tiles in or out of the plane, as shown in fig. (2.8c). That is by choosing the tiles of a tiling, its curvature, thus how the tiling will bend, can be determined. This is an important phenomenon: the topological features of a tiling, that is the number and order of faces, are connected to its curvature. This relation is rooted in the Gauss-Bonnet-theorem [Kamien, 2002, Millman, 1977]:

$$\iint_M K dS = 2\pi\chi \tag{2.5}$$

where the integral is carried over the entire surface of a manifold M, $K = \kappa_1\kappa_2$ is the Gaussian curvature given as the product of the two principal curvatures κ_1, κ_2 (see fig. (4.2) for a definition) and χ is the Euler characteristic. The Euler characteristic is a topological invariant of a structure. This theorem establishes a connection between the curvature, and thus geometry, of a surface and its topology given as the Euler characteristic χ. More specifically, it states that the total amount of curvature in a surface is a topological invariant. In relation to the example in fig. (2.8) this means, that changing the topology of the tiling, for example by introducing pentagons instead of hexagons, induces curvature in the tiling.

In the case of the honeycomb in the bee hive (fig. (2.7)), this statement is "reversed": if a curved surface needs to be tiled, one has to introduce non-hexagonal tiles to cope with the curvature. This constraint applies to the polymer melt confined onto a spherical, thus curved, surface. That is the hexagonal structure can not be assembled. The analysis of the resulting defects, especially in regards to the color-constraint, is the key finding of our publication [Hain et al., 2019].

The Euler-Characteristic of a tiling can be computed using Euler's Formula [Kamien, 2002]

$$V - E + F = \chi \tag{2.6}$$
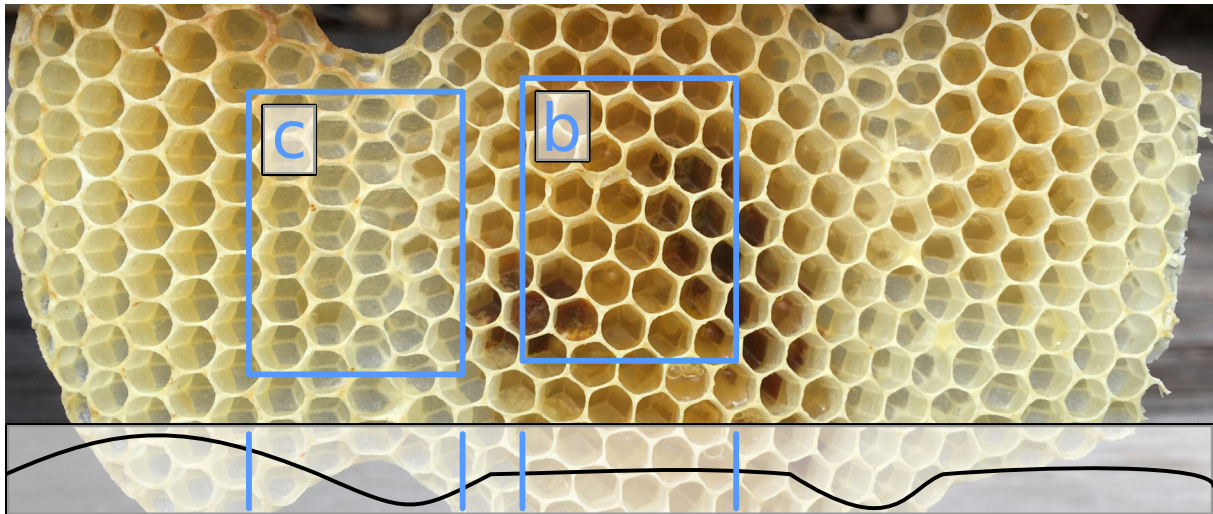
(a) A honeycomb from a beehive grown naturally without a frame to force planar construction. The bottom graph indicates a height profile of the honeycomb showing flat and curved sections.
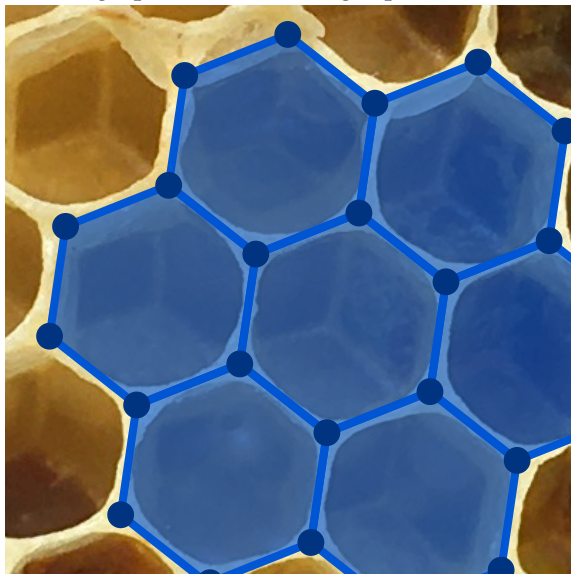
(b) A regular hexagonal structure inside the honeycombs, extract from fig. (2.7a). Hexagons tile a planar surface without leaving gaps, while minimising the interface area in between cells.
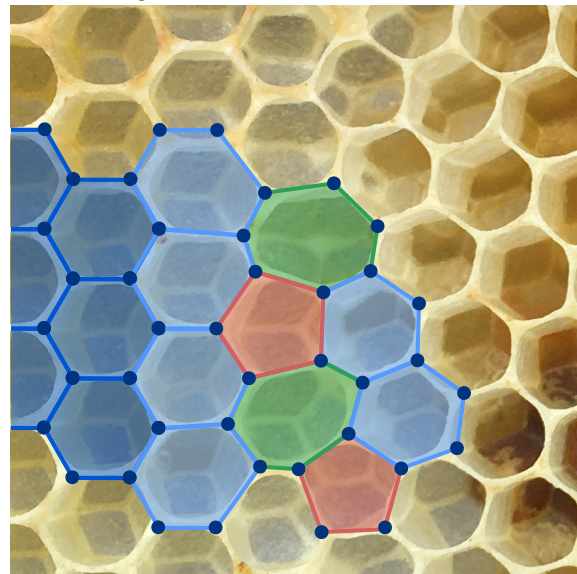
(c) Extract from fig. (2.7a). The bees build a curved structure which, due to its curvature, can not be tiled by hexagons (dark blue). As a result a scar of pentagons (red) and heptagons (green) are included in the tiling to cope with the curvature. Also hexagons close to the scar are deformed (light blue)

Figure 2.7: Wax honeycomb inside a bee hive. The predominant order is a hexagonal tiling, as indicated in (b). However, due to the wavy structure (see caption of (b)) and the thus induced curvature, defects in the form of pentagons and heptagons occur, as indicated in (c). (Photo credit Matthias Beutke)

(**a**) A planar, hexagonal tiling

(**b**) An arrangement of hexagons and polygons, not a tiling since gaps exists in between tiles

(**c**) Hexagons and pentagons bend out of the plane to close the gaps
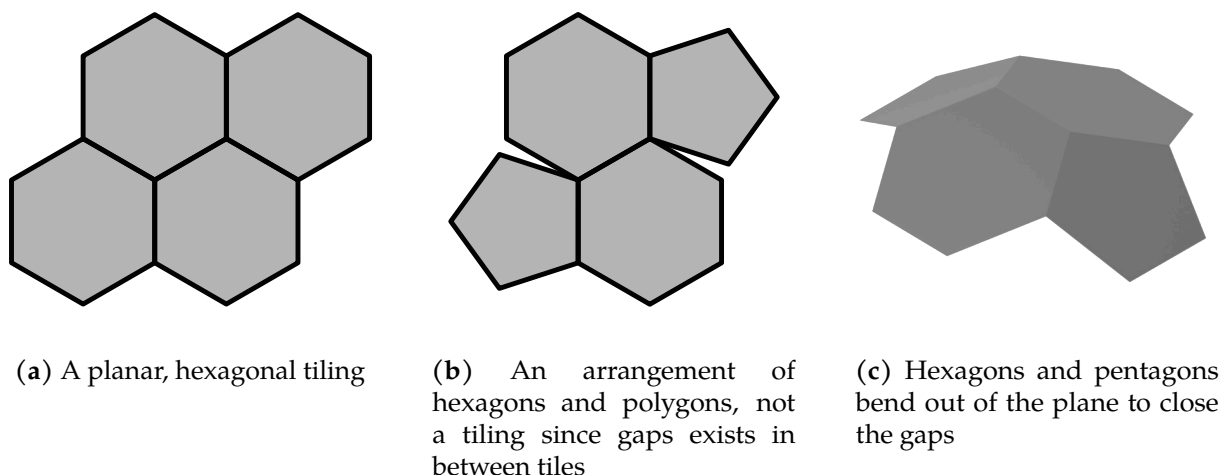
Figure 2.8: Topology induced curvature. (a) The topology of a hexagonal tiling allows to cover flat surfaces without leaving gaps. (b) By introducing pentagons into the tiling, its topology changes as described by Euler's equation, see eq. (2.6). Gaps occur between the tiles, since the sum of angles at each vertex does not add up to 2π. (c) To close the gaps, the polygons bend out of the plane initially covered by the hexagons. Thus curvature is introduced in the tiling by changing its topology, as stated by the Gauss-Bonnet theorem, see eq. (2.5)

where V is the number of vertices, E the number of edges and F the number of faces in a tiling. For an infinite, periodic hexagonal grid eq. (2.6) yields $\chi_{\text{hex}} = 0$. Evaluating the left side of eq. (2.5) for a torus yields $\chi_{\text{torus}} = 0$, where as for a sphere $\chi_{\text{sphere}} = 2$ holds. This means the total amount of curvature in a periodic hexagonal tiling is compatible with the surface of a torus, but incompatible with the the surface of a sphere. A hexagonal tiling thus can never curve in a way to fit the surface of a sphere, thus defects, e.g. pentagons, need to be introduced. These pentagons would then be called topological defects, caused by the geometric frustration. The Gauss-Bonnet theorem also explains why deforming the pentagons and hexagons in the example in fig. (2.8) would not help to fill the gaps: the topology and thus the total amount of curvature would not change and thus not help to fill the gaps.

We now arrived at the core question of this chapter's publication: what topological defects will assemble in a polymer melt of ABC star copolymers confined to a spherical shell? This is analog to the question which topological defects occur if a hexagonal tiling is forced onto a spherical shell. This is a question which has been addressed already by several authors.

Diblock copolymers introduce pentagons and heptagons in their hexagonal order to cope with the curvature [Tang et al., 2005, Yu et al., 2007, Chantawansri et al., 2007, Vorselaars et al., 2011, Zhang et al., 2014]. Similar investigations were made using repulsive, colloidal particle packings freezing on a sphere. On a plane these particles would arrange in a hexagonal order with 6 direct neighbors. When computing the

Voronoi diagram, this order is equivalent to a honeycomb tiling. Bausch et al. [2003], Lipowsky et al. [2005], Einert et al. [2005] report links of 5-fold and 7-fold defects, termed scars. That is particles with 5 or 7 direct neighbours, equivalent to pentagons and heptagons in the tiling, occur in the otherwise hexagonal order. Irvine et al. [2010] expanded the setup to geometries beyond the sphere and found similar, topologically neutral scars, that is scars that as such do not contribute to the total amount of curvature. However, they allow to act like fabric pleats, in the same way as the honeycomb in fig. (2.7a) curves but *in total* is flat. Guerra et al. [2018] suggest in a similar system that clusters of defects arrange in an icosahedral order. Bowick et al. [2006], Kusumaatmaja and Wales [2013] confirm these experimental results using energy minimisation of electrostatically charged particles on curved surfaces. Further theoretical treatment was undertaken by Vitelli et al. [2006].

A historical problem concerning orderings on the sphere is the Thomson problem [Thomson, 1904]. Proposed in course of his atomic model, Thomson asked what the arrangement of repulsive electrons confined onto a spherical surface is. This problem has been addressed extensively, with many different methods being employed to find solutions [Robinson et al., 2013, Erber and Hockney, 1991, Bondarenko et al., 2015, Altschuler et al., 1994, 1997, Wales and Ulker, 2006]. Alternative Thomson problems with generalised potentials have been considered as well [Bowick et al., 2002, Mughal, 2014, Miller and Cacciuto, 2011a].

Robinson et al. [2013] reports that solutions of the Thomson problems form triangulated polyhedra from which the dual lattice can be constructed. This dual lattice is equivalent to the Voronoi tessellation of the electron positions. Therefore, finding Thomson solutions is a way to generate tilings of a sphere and investigate defects in line with the colloid systems. Altschuler et al. [1997] found for configurations with $12 < N < 100$ charges that most solutions consisted of a majority of hexagons, combined with a combination of pentagons, heptagons, squares and quadrilaterals. For configurations with $100 < N < 327$ charges Wales and Ulker [2006] found that most configurations consist of 12 pentagons and otherwise only hexagons. For configurations with $N > 327$ additional heptagons occur with more than 12 pentagons. However, multiple studies [Erber and Hockney, 1991, Bondarenko et al., 2015] report an increasing number of local minima for high values of $N > 50$, where the ground state might have low statistical weight.

In conclusion the defect structure of a hexagonal order on a sphere seems to be reasonably well studied, however, no attempts to investigate the defect structure of a three colored tiling pattern has been undertaken.

2.3 Patchy particles by self-assembly of star copolymers on a spherical substrate: Thomson solutions in a geometric problem with a color constraint

With the following publication, we aim to fill this gap by studying the self-assembly of star polymers onto a spherical shell. Our research contributes several novel aspects, however, the main aspect is the color constraint, introduced by the ABC star copolymers. That is we investigate the defects in three-colored hexagonal tiling forced onto a spherical surface. The color constraint forbids 5-fold and 7-fold declinations to form, which are the dominant topological defects to form in a hexagonal lattice on a spherical surface to cope with the curvature. The article is now reproduced in full from [Hain et al., 2019] with permission from the Royal Society of Chemistry.

Patchy particles by self-assembly of star copolymers on a spherical substrate: Thomson solutions in a geometric problem with a color constraint†

Tobias M. Hain, [ab] Gerd E. Schröder-Turk [*abc] and Jacob J. K. Kirkensgaard [*c]

Confinement or geometric frustration is known to alter the structure of soft matter, including copolymeric melts, and can consequently be used to tune structure and properties. Here we investigate the self-assembly of ABC and ABB 3-miktoarm star copolymers confined to a spherical shell using coarse-grained dissipative particle dynamics simulations. In bulk and flat geometries the ABC stars form hexagonal tilings, but this is topologically prohibited in a spherical geometry which normally is alleviated by forming pentagonal tiles. However, the molecular architecture of the ABC stars implies an additional 'color constraint' which only allows even tilings (where all polygons have an even number of edges) and we study the effect of these simultaneous constraints. We find that both ABC and ABB systems form spherical tiling patterns, the type of which depends on the radius of the spherical substrate. For small spherical substrates, all solutions correspond to patterns solving the Thomson problem of placing mobile repulsive electric charges on a sphere. In ABC systems we find three coexisting, possibly different tilings, one in each color, each of them solving the Thomson problem simultaneously. For all except the smallest substrates, we find competing solutions with seemingly degenerate free energies that occur with different probabilities. Statistically, an observer who is blind to the differences between B and C can tell from the structure of the A domains if the system is an ABC or an ABB star copolymer system.

1 Introduction

The self-assembly of linear diblock copolymers and their phase diagram is nowadays well understood.[1–3] By contrast, the study of the phase behaviour of more complex copolymer architectures, like grafts or stars,[4] remain incomplete, due to the larger parameter space and, hence, a larger variety of possible structures.[2,3,5–7] Here we consider ABC 3-miktoarm star terpolymers, henceforth called ABC star copolymers. These are copolymers which consist of three linear chains connected at a central grafting point,[3,4,8,9] as shown in Fig. 1 or Fig. 2. These star copolymers can be synthesized so that the three arms are immiscible; herein we refer to the three polymeric species as colors: blue, yellow and red. When this immiscibility drives the
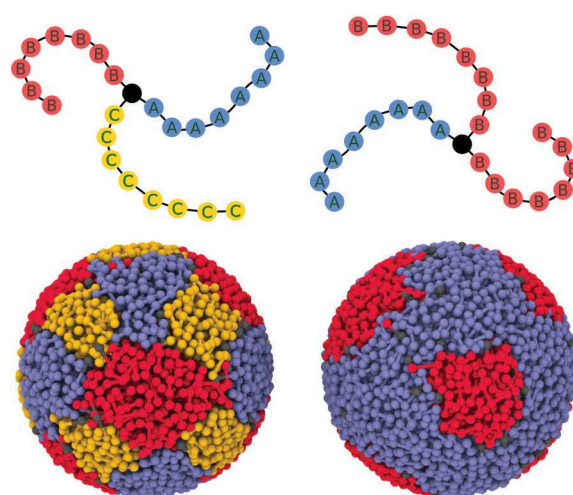
Fig. 1 Polymeric self-assembly of ABC and ABB star copolymers on a spherical substrate. Top panel: Schematic visualization of coarse grained models of ABC and ABB star copolymers used for the DPD simulations. Bottom panel: Snapshots of simulations comprising ABC and ABB star copolymers. Polymer arms of identical color agglomerate into patches. The ABC system creates a three colored tiling of the sphere, whereas the ABB system builds a single tiling made up of only A-type patches in a B-type matrix.

[a] College of Science, Health, Engineering and Education, Mathematics and Statistics, Murdoch University, 90 South Street, 6150 Murdoch, Western Australia, Australia. E-mail: G.Schroeder-Turk@murdoch.edu.au

[b] Physical Chemistry, Department of Chemistry, Lund University, P.O. Box 124, 221 00 Lund, Sweden

[c] Department of Food Science, University of Copenhagen, Rolighedsvej 26, 1958 Frederiksberg, Copenhagen, Denmark. E-mail: jjkk@food.ku.dk

† Electronic supplementary information (ESI) available. See DOI: 10.1039/c9sm01460h
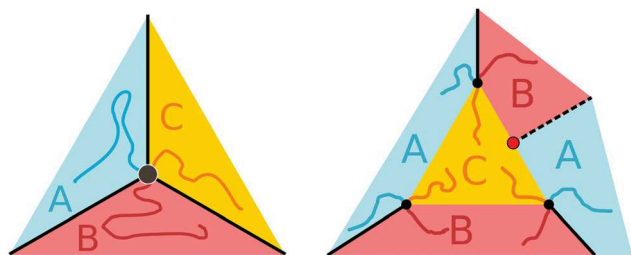
Fig. 2 Structural constraints imposed by polymer architecture: the color constraint. Left panel: Since the three different polymer arms making up domains are bonded at a central junction bead (grafting point), the latter must sit on points or lines where three different domains meet so that each arm may extend in a domain of its species. Right panel: For tiling patterns, this results in the so-called color constraint: only polygons with an even number of edges are allowed, where the types of all adjacent polygons alternate. The figure illustrates this: if a polygon with an uneven number of edges is attempted to be formed, a new interface (dashed line) and grafting point (red point) is introduced by the architecture of the stars, resulting in an even polygon.

moieties to micro-phase separation, the arms of equal species will agglomerate into domains, which will self-assemble into complex structures. Considerable amount of work has been put towards the investigation of one type of these structures: columnar phases whose cross-sections are planar tiling patterns.[10–20]

A distinguished and important feature of ABC star copolymers is that all structures arising from these molecules must be compatible with the special architecture of the latter:

1. The grafting points form triple lines[13] where three different domains meet, which, in cross-section, corresponds to vertices of the tiling pattern.

2. Any given patch of a given color (*e.g.* yellow), must be surrounded by an alternating sequence of patches of the other colors (*e.g.* blue and red). The number of these surrounding patches must then be even.[12]

For more details see Fig. 2. In this article we will refer to constraint 2 as the color constraint.

If the star copolymers are chosen symmetrically, *i.e.* all arms have equal length, and with equal interaction strength between the arms, a hexagonal columnar phase is formed where a cross section perpendicular to the columns yields a planar 3-colored honeycomb pattern which we here consider as the 'ground state' of the system.[10–13,16,19,21] The hexagonal tiling can be tuned into a large variety of tilings by varying the length of one of the three arms.[10,12,19] However, all these tilings consist of vertices of order three only, which is enforced by the molecular architecture of the star copolymers.

Apart from changing the chemical composition or interactions of the polymers, another way to tune structures is by geometric confinement. A simple analogy illustrates this fundamental geometric concept: the peel of an orange for example cannot be confined to a flat plane, without tearing or deforming it. This also applies for the star polymers: the optimal free energy configuration they form in the plane, the regular honeycomb, cannot be fitted on a spherical substrate without distorting the planar pattern.

Unlike the restriction of polymers to a thin film, the confinement to curved geometries, like spheres, does not only impose the constraint of physical confinement onto the polymers,

but also introduces curvature to the system. This alters the shape and structure of the space available to the polymer melt which can enforce or prohibit some structures to form. Such curvature-related effects have been described for multiple self-assembly systems.

Several articles report on the influence of curvature on hexagonal particle orders on surfaces with positive and negative curvature, both using experiments[22–27] and simulations.[24,28,29] Two dimensional tilings can be created from these particle assemblies by assigning each particle a polygon where the number of edges coincides with its coordination number, which is the number of neighbouring particles. This process is equivalent to computing a Voronoi diagram of the particles. While these particles would arrange in a hexagonal order in a plane, and therefore, form a perfect hexagonal tiling, defects in this patterns were found after the particles self-assembled on curved surfaces.

Zhang *et al.*[30] found similar defects in the self-assembly of AB diblock copolymers confined to a spherical substrate using numerical methods to solve the Landau–Brazovskii theory. For cylinder forming diblocks, the cylinders distributed over the surface of the sphere in a generally hexagonal order, however, 5-fold defects were found. For larger systems, scars of connected 5- and 7-fold defects occur. These scars were previously found by Chantawansri *et al.*[31] in their studies about AB diblock copolymers on spherical substrates using SCFT. They furthermore found that the number of cylinders depends on the radius of the spherical substrate.

These defects have a fundamental mathematical origin: the different topologies of the confining surface. Each tiling and polyhedra (and topological equivalents) have an intrinsic property, the Euler characteristic χ, describing its topological type.[32–34] An Euler characteristic of $\chi = 2$ corresponds to an object that is a single component without any handles or cavities, such as the sphere. A given tiling can only tessellate a surface of the same topological space, therefore surfaces having the same Euler characteristic as the tiling.[33] A planar, periodic hexagonal tiling has $\chi = 0$, as does a torus. Therefore the hexagonal tiling can be mapped onto the latter. When a hexagonal lattice is forced onto an incompatible curved surface, as for example a sphere with $\chi = 2$, the mismatch leads to 'geometric frustration': the hexagonal lattice is incompatible with the topology of the substrate. To cope with this incompatibility defects occur in the hexagonal order.

To check if a tiling is compatible with a sphere, Euler's formula can be used, which reads in case of a sphere:[32,34]

$$\chi = V - E + F = 2 \qquad (1)$$

where V, E, F is the number of vertices, edges and facets in the tiling. If a tiling fulfills this condition, it can be mapped onto a sphere without defects. In our case, where tilings are generated by ABC star copolymers, the color constraint can be incorporated into eqn (1). Since only vertices where three edges meet are allowed, each edge is shared by two and each vertex by three facets (see also Fig. 2). In this case, eqn (1) can then be expressed in terms of the number of polygons in the tiling:

$$\chi = \sum_i \left(\frac{i \cdot n_i}{3} - \frac{i \cdot n_i}{2} + n_i \right) = \sum_i \left(1 - \frac{i}{6} \right) n_i = 2 \qquad (2)$$

38
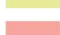
where n_i is the number of polygons with i edges in the tiling. This equation easily shows that a hexagonal tiling is incompatible, since the term in the brackets equals zero for $i = 6$. Therefore polygons with a different number of edges need to be introduced to fulfil the equation. One solution to eqn (1) for the sphere is the arrangement of 12 pentagons to an icosahedron. Since the left side of eqn (1) vanishes for hexagons, an arbitrary number of the latter can be added to the 12 pentagons and the topology will not change. A well-known configuration is the soccer ball, consisting of 12 pentagons and 20 hexagons. Apart from investigations of particles from polymer systems, abstract systems with topological defects were investigated analytically.[33,35–37] Here the behavior of abstract disclinations from the crystalline state, for example particles with 5 neighbours in an otherwise hexagonal lattice, was investigated using free energy calculations. The results agree with the results found in the physical particle and polymer systems: the favoured state are 12 5-fold disclinations, also the above mentioned scars (connected disclinations) are found.

A very prominent problem of ordering on a sphere is the so-called Thomson problem. It was formulated by J. J. Thomson in 1904 in the context of his atomic model. The Thomson problem is the search for the minimal energy configuration of n repelling electrons, all of the same negative charge $-e$, on a spherical surface.[38] The resulting arrangement of electrons and their symmetries[39–43] has been found in many seemingly unconnected problems, as for example in the design of protein virus capsides,[44–46] the construction of fullerens and nano-tubes,[47] in more generalized Thomson problem versions,[48] but also in connection with polymeric self-assembly where it was stated that the cylinders in the cylindrical phase of AB diblock copolymers on a spherical substrate arrange on the sphere as particles in the Thomson problem would.[31] To reach the minimal energy solution, the optimal coordination number of a single electron is six, however, due to the geometric frustration defects in the hexagonal order must occur, as explained above.[49] For our system, it is useful to interpret the electron positions of the Thomson problem solutions as vertices of a polyhedra. The graph of its dual polyhedron is a tiling of the sphere, where each electron is assigned a tile whose number of edges is equivalent to the coordination number of the corresponding electron. A solution of the Thomson problem, henceforth called a Thomson solution, can therefore be described and labeled by its dual lattice, see Table 1.

In conclusion, using ABC star copolymers confined to a spherical shell as a model system enables the simultaneous study of two different constraints: geometric frustration and the influence of the color constraint. To investigate the effects of each on their own, a strategy is needed to switch one of them on and off. This is accomplished by using two different kind of star molecules, the aforementioned ABC stars and ABB star molecules, see right panel in Fig. 1. These only differ to the ABC stars in that two arms are of the same species. Thus the color constraint can be eliminated, since the grafting points of the ABB stars can move freely across the interface between A and B type domains. The A type domains, which are the tiles in the resulting tiling, can then freely move around in a B type matrix.

Table 1 Solutions of the Thomson problem for systems with up to 12 electrons described as spherical tilings. The table shows the number of n-gons and the Schläfli symbol for the dual lattice of a solution of a N-electron Thomson problem. A Schläfli symbol[12,69,70] is a set of l numbers $[k_1,k_2,\ldots k_l]$ denoting that a vertex is adjacent to l tiles with k_l edges respectively (see also right pane in Fig. 5). The Schläfli symbol for an entire tiling just lists all different types of occurring vertices, see Fig. 5. The symbols to the left relates to the textures in Fig. 6

	N	Schläfli symbol	1 Edges	2	3	4	5	6
			Number of tiles with					
■	2	[1.1]	2					
■	3	[2.2.2]		3				
■	4	[3.3.3]			4			
■	5	[3.4.4]			2	3		
■	6	[4.4.4]				6		
■	7	[4.4.5]				5	2	
■	8	[[4.4.5], [4.5.5]]				4	4	
■	9	[[4.5.5], [5.5.5]]				3	6	
■	10	[[4.5.5], [5.5.5]]				2	8	
■	11	[[4.5.5], [4.5.6], [5.5.5], [5.5.6]]				2	8	1
■	12	[5.5.5]					12	
■		Non-Thomson						
■		Invalid						

2 Methods

2.1 Dissipative particle dynamics of star copolymers

Dissipative Particle Dynamic (DPD) simulations are used to find equilibrium configurations of the polymer systems. DPD simulations[50,51] are a type of molecular dynamic simulations designed for coarse grained models of molecules, which makes it a natural fit for polymer melts.[11,21,52,53] As all molecular dynamics simulations, the DPD method is based on the forward integration of Newton's equation of motion in time for each particle i:

$$\frac{d^2\mathbf{x}_i}{dt^2} = \frac{1}{m} \cdot \mathbf{F}_i$$

In our case, a particle is a single bead in the polymer arms (see Fig. 1), where each bead may represent many atoms. A symmetric star copolymer then consists of a center particle with three connected arms, each consisting of a chain of bonded particles. A schematic representation of such a coarse grained polymer is shown in Fig. 1.

We use the simulation package HOOMD-BLUE[54–56] to perform our simulations. We will only briefly discuss the parameters used at this point, for details on the implementation we refer to ref. 57 and the documentation of the HOOMD-BLUE package.[58] In this simulation package all units are given based on three reference units (distance $\mathscr{D}$, energy $\mathscr{E}$ and mass $\mathscr{M}$) which can be chosen arbitrarily. All other units, for example a force, can be derived from these units, for more details we refer to the HOOMD-BLUE manual.[58] In the course of this article, all given values are given in

terms of these reference units unless stated otherwise. The package implements the DPD method following the formulation of ref. 51 and 57. Here the force on particle i is given as

$$\mathbf{F}_i = \sum_{i \neq j} \left(\mathbf{F}_{ij}^{\mathrm{C}} + \mathbf{F}_{ij}^{\mathrm{D}} + \mathbf{F}_{ij}^{\mathrm{R}} \right)$$

where the sum is over all particle pairs within a cutoff radius $r_{\mathrm{c}} = 1$ around the i-th particle. The force consists of three contributions: a conservative force $\mathbf{F}_{ij}^{\mathrm{C}}$ representing the repulsive interactions between the particles, a dissipative force $\mathbf{F}_{ij}^{\mathrm{D}}$ and a random force $\mathbf{F}_{ij}^{\mathrm{R}}$. The latter two act as a thermostat to keep the temperature of the system constant. Since a thermostat is a built-in feature of the DPD interactions, the system is technically advanced as a *NVE* ensemble using a standard velocity-Verlet step algorithm, although it is effectively a *NVT* ensemble. The conservative force is 0 only for $r_{ij} \geq r_{\mathrm{c}}$ and is otherwise given by

$$\mathbf{F}_{ij}^{\mathrm{C}} = a_{ij} \left(1 - \frac{r_{ij}}{r_{\mathrm{c}}} \right) \hat{\mathbf{r}}_{ij} \qquad (3)$$

where a_{ij} is the maximum repulsion between two particles and therefore a measure of the interactions strength, $\mathbf{r}_{ij} = \mathbf{r}_i - \mathbf{r}_j$ and $\hat{\mathbf{r}}_{ij} = \mathbf{r}_{ij}/|\mathbf{r}_{ij}|$. The interactions between two particles of the same species is given as $a_{ii} = 75 \frac{k_{\mathrm{B}}T}{\rho}$, where ρ is the number density and $k_{\mathrm{B}}T$ the temperature in the polymer melt. The interaction parameters can be mapped onto the well established Flory–Huggins interaction parameter χ_{ij}[59,60] used in polymer science using $a_{ij} = a_{ii} + 3.268\chi_{ij}$.[61] We use values of $a_{ii} = 25$ and $a_{ij} = 40$ that, at a temperature of $k_{\mathrm{B}}T = 1$ and a particle density of $\rho = 3$, corresponds to $\chi_{ij} \approx 4.6$. With an armlength of 8 beads per arm, this gives $\chi N \approx 74$. Due to the many parameters and complexity of a star copolymer melt, parameters for an order–disorder transition are barely existent in the literature. However, a value of $\chi N \approx 74$ is well above the order–disorder transition for diblock copolymers[2] and as high as values used in other studies of ABC star copolymers[5,19] and thus in the strong segregation limit. As a measure of the stretching of the polymer molecules the radius of gyration[62] is provided in the ESI.†

The single beads of the polymer chains are bonded by a harmonic potential, given as $V_{\mathrm{H}}(r) = \frac{1}{2}k(r - r_0)^2$, where k measures the strength of the bond and r_0 the bond rest length. In our system we chose $k = 4\frac{\mathscr{E}}{\mathscr{D}^2}$ and $r_0 = 0.88\mathscr{D}$ as the position of the first peak of the pair correlation function in a system of unbonded, identical particles with the given interaction parameters. Each arm in the polymers consists of 8 beads.

The confinement of the system to a spherical substrate is modelled as follows: the simulation volume is a spherical shell bounded by two repulsive spherical walls interacting with the polymers with a purely repulsive Lennard-Jones potential:

$$V_{\mathrm{LJ}}(r) = 4\varepsilon \left[\left(\frac{\sigma}{r} \right)^{12} - \left(\frac{\sigma}{r} \right)^6 \right] + \Delta V$$

where r in this case is the length of the vector from the particle perpendicular to the wall, not to be confused with r_{ij}, the
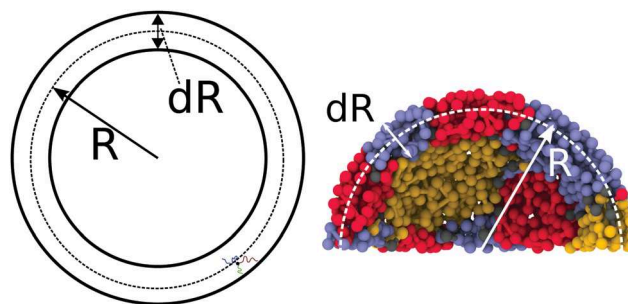
Fig. 3 Simulation setup and substrate model. Left panel: Schematic sketch of a cross section of the simulation setup. The two black, bold circles represent spherical, repulsive 'Lennard-Jones walls' with radii of $R + \frac{\mathrm{d}R}{2} + \sigma$ and $R - \frac{\mathrm{d}R}{2} - \sigma$. As shown, the outer wall exerts a LJ-force on a particle along a vector perpendicular to the wall towards its center. The force of the inner shell acts outwards. Together these walls confine the polymers to a shell of thickness dR. Right panel: Cross section through a simulation snapshot with radius $R = 8\mathscr{D}$ with the same quantities marked. The image shows the homogeneity of structure in the radial direction of the shell and gives an idea for the scale of the system.

pairwise distance between two particles, see Fig. 3. $\Delta V = -(r - r_{\mathrm{cut}})\frac{\partial V}{\partial r}(r_{\mathrm{c}}) - V_{\mathrm{LJ}}(r_{\mathrm{c}})$ and σ is the range of the repulsive potential, ε would be the strength of the attractive part of the Lennard-Jones potential, however, is of no relevance in the purely repulsive version used here. While the outer wall exerts a force towards its center, the forces of the inner wall acts outwards. Hence, the wall keeps all particle inside the spherical shell they enclose. We choose $\sigma = 1\mathscr{D}$ and set the cutoff of the wall potential to $r_{\mathrm{c}} = 2^{\frac{1}{6}}\sigma$ to cut the attractive tail.

The spherical walls are concentric around the origin with radii of $R_{\mathrm{i}} = R - \mathrm{d}R/2 - \sigma$ and $R_{\mathrm{o}} = R + \mathrm{d}R/2 + \sigma$, the shell therefore has a thickness of dR, as shown in Fig. 3. The amount of curvature forced onto the system can then be tuned by varying the radius of the spherical shell. The initial position of the centers of the stars are chosen inside the simulation volume from a uniform distribution. The arms are then placed at random positions around the center. In order to achieve a well mixed configuration the system runs 5.5×10^5 time steps where the interaction parameter between any species of particles is set to $a_{ii} = a_{ij} = 25\frac{\mathscr{E}}{\mathscr{D}}$. After this warmup phase the parameters are set as stated above according to their species. The temperature of the system was kept constant at $k_{\mathrm{B}}T = 1$ for the entire run. All simulations have been run with time steps of $\Delta t = 0.005$ and ran at least 3×10^8 time steps, larger systems with $R > 8\mathscr{D}$ ran 5×10^8 time steps. After these long runs we assume that an equilibrium is reached, which is confirmed visually in random samples. The radius R of the spherical shell was varied with $R = 4, 5, 6, 7, 8, 9, 10\mathscr{D}$ with a shell width of d$R = 2$. Alternating the radius has two effects: (1) due to constant a number density of $\rho = 3\frac{1}{\mathscr{D}^3}$ the number of molecules increase with a larger shell volume; (2) the curvature of the shell decreases with increasing radius. For each radius 20 configurations for each ABC and ABB systems were simulated with different random initialisations for statistical significance.

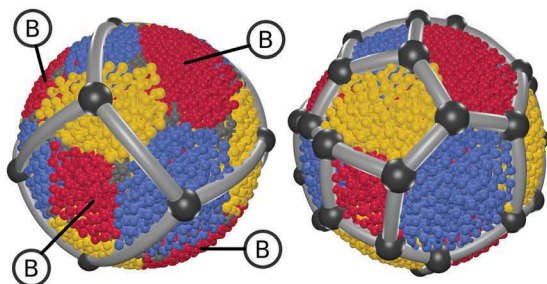**Fig. 4** Two different methods for the analysis of tiling patterns in an ABC system using Set-Voronoi diagrams. Right: Patches of all colors are used to generate a single, three-colored, spherical tiling for a single ABC system. Here the vertices are located at triple lines where three different colors meet and the edges correspond to inter-domain interfaces. The color constraint applies directly to the tiling. Left: Only the patches corresponding to a particular polymeric type X (= A, B, or C) are considered in the tiling analysis, creating a single colored tiling (the image is for X = B, red). The same could be done with the other two colors, yielding in total three single-colored tiling for each ABC system. Note that the color constraint does not apply directly onto this single-colored tiling, *i.e.* uneven numbers of edges are possible, however the frustration on the polymer system still applies. This single-color analysis allows direct comparison to tilings generated in ABB systems, see *e.g.* Fig. 5.

2.2 Structure analysis of tiling patterns

When the simulation is deemed to be equilibrated, the resulting spherical tilings are recovered from the polymer configurations using Set-Voronoi diagrams[63] as implemented in pomelo.[64] The aim is to substitute a domain in the system with a polygon, representing a tile, where the number of edges of the latter is equal to the number of neighboring domains.

In the ABB systems we characterize the structure of the A beads, considering the B particles as a matrix. We use a cluster algorithm (implemented in the trajectory analysis package freud[65]) to identify all A domains. This provides a list of N clusters, one for each A type domain, each with a list of which particles it is made from. Then the Voronoi diagram of all A

type particles is computed, where all cells of particles belonging to the same cluster are merged, leaving one cell per cluster. The number of neighbors for each domain are determined from the number of adjacent cells sharing a common edge. The spherical tiling is recovered by representing each domain by a polygon which number of edges equals the number of neighbors.

For the visualizations of the tiling shown in Fig. 5 and 7, the vertices of a tiling are placed at the vertices of the Voronoi cells of the patches. The edges connecting vertices are great circle segments. Fig. 5 shows a simulation snapshot on the left and a representation of the spherical tiling in the middle. We obtain 2D topological representations of the tilings through the Mercator projection as used in.[30] Each point on the sphere given in spherical coordinate angles (θ, ϕ) with $\theta \in [-\pi/2, \pi/2]$ and $\phi \in [0, 2\pi]$ is mapped in the Cartesian plane by $x = R\phi$ and $y = R \ln\left(\tan\left(\frac{\pi}{4} + \frac{2}{5}\theta\right)\right)$. An example of such a projection is shown on the right hand panel of Fig. 5. In these representations, the plot has periodic boundary conditions in the x direction, however, not in y direction. The top and bottom tiles therefore are not adjacent, but represent the tiles at the poles of the sphere. The purpose of the planar projections is to correctly capture the topology and neighbor relations, not the geometry, which is deformed in the projection.

In order to make direct comparison to the single-colored tilings from ABB systems to tilings from the ABC systems possible, instead of constructing a three-colored tiling were edges would follow the inter-domain interfaces (see right panel in Fig. 4), we analyse each of the three species in the latter individually, treating the respective other two domains as the matrix, and apply the same analysis as above. That is, to analyse A, we consider B and C indistinguishable and to represent the matrix and so on. From each ABC system three single-colored tilings from the A, B and C type domains are obtained, as can be seen in Fig. 7. In these single-colored tilings the vertices are not restricted to triple-lines and the edges do not correspond to inter-domain interfaces as is
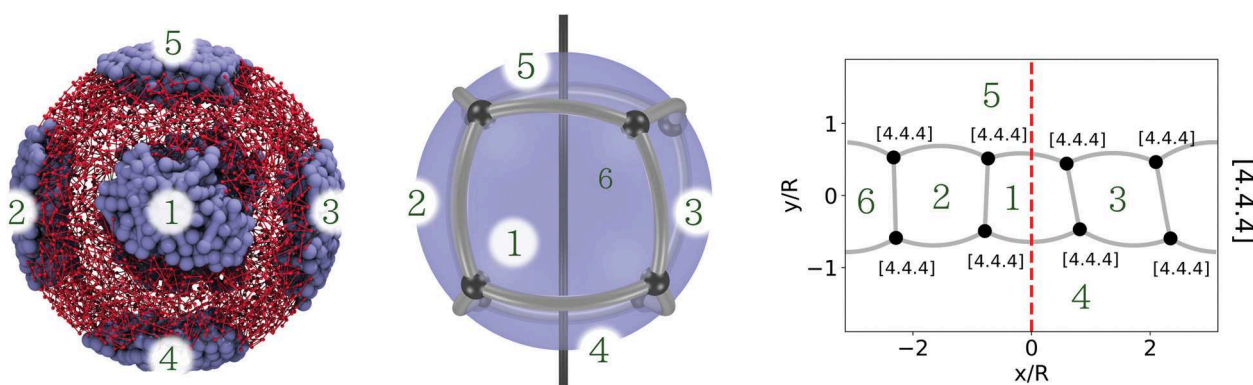
Fig. 5 Spherical tilings from polymeric self-assembly on a spherical substrate. Left panel: A simulation snapshot of an equilibrated ABB star copolymer melt confined to a spherical shell. The A-type arms have assembled into six domains, which arranged in a cuboidal symmetry in the B-type matrix. Middle panel: The spherical tiling recovered from the polymer system. Each face in the tiling corresponds to a blue domain in the simulation snapshot as labeled. Right panel: A modified Mercator projection of the spherical tiling, labeled with the corresponding tiles on the sphere and the domain in the simulation snapshot. Each vertex is labeled with its Schläfli symbol, the union of all types of distinctive vertex labels gives the Schläfli symbol of the entire tiling, as shown vertically on the far right. In order to be comparable, all tilings are rotated so all tilings of a type have the same orientation. The gray axis in the middle panel indicates the orientation of the red, dashed line in the projection in 3D.

41

the case in ABB systems, see Fig. 4. Although this single-color analysis seems to lift the color constraint of these tilings, *i.e.* polygons with an uneven number of edges are possible, this is a purely virtual aspect of the analysis and the frustration still applies on the polymer systems.

Tilings are labeled using Schläfli Symbols, see caption of Table 1 for details. All simulation screenshots were made using the Tachyon render[66] in VMD,[67] the renderings of the tilings were created using a custom script in BLENDER.[68]

Every 1×10^6 simulation step, a snapshot of all particles was made, which results in 300 frames over the simulation time. The statistics shown in the result section include all tilings from the latest 15 frames of the simulation to account for invalid simulation frames. Since 20 independent runs were made for each radius, 300 frames were analysed for both the ABC and ABB systems. In the ABB system, this provides 300 spherical tilings, in the ABC system 900 tilings, since there are three colors in each frame. Note, however, that the "real" statistics are only based on 20 different runs for each polymer type and radius, since the tiling in the last 15 frames of each run are assumed to be equilibrated and therefore is not expected to change.‡

Fig. 6 Equilibrium configurations of self-assembly of star copolymers on a spherical substrate. Results of multiple runs of the self-assembly of ABB (top) and ABC (bottom) star copolymers on a spherical substrate of radius *R*. Each color denotes one type of tiling, as labeled in Table 1. The plot shows the fraction of simulation snapshots found with the respective tiling for each radius. In general, multiple tilings are found as solutions for a single radius, where the results for ABB and ABC systems differ. The exact data in text form in a table can be found in the ESI.†

3 Results and discussion

We find the following key features:

• For spherical substrates with $R < 8$ all tilings generated by both the ABB and ABC systems are identical to tilings generated from Thomson solutions, see Fig. 6. Only for radii $R \geq 8$, we observed simulations of ABC systems which were not Thomson-type solutions (see below). In ABB systems we only found Thomson solutions.

• For $R > 4$, instead of a single equilibrium solution, we find a spectrum of configurations, see Fig. 6. Within our analysis, these appear as degenerate (or nearly degenerate) configurations that occur with statistical frequencies.

• The analysis of the three single-colored tilings of an ABC system shows that they each individually form Thomson solutions, but not necessarily of the same tessellation type, see Fig. 7.

• The resulting tilings can be tuned by varying the radius of the sphere where the ABC star copolymer system shows a different behaviour in the frequencies of the tilings than the ABB star copolymer systems, see Fig. 6.

To start our discussion we single out the $R = 8$ systems to illustrate the key results. Out of the 300 frames in the ABB

systems with $R = 8$, we find the majority of frames (about 95%) to have 6 tiles in a [4.4.4] configuration, only a very small proportions of 5% has 5 tiles in a [3.4.4] tiling. Both of the configurations are identical to tilings generated by Thomson solutions. The ABC case is slightly more complex: out of the 900 analysed tilings, we find only about 14% of the configuration with 6 tiles in a [4.4.4] tiling, 47% with 7 tiles in a [4.4.5] tiling, about 31% with 8 tiles in a [4.4.5, 4.5.5] tiling and 6% with 9 tiles as a [4.5.5, 5.5.5] configuration. As in the ABB systems, all of these are identical to tilings from Thomson solutions. Only about 1% of the tilings were found to differ from the Thomson solution tilings.

While for $R = 8$ the ABB system overwhelmingly forms the same type of tiling, the ABC misses this feature. We find this behaviour across most of the other systems on different radii: all of the ABB systems form at least two different tilings for each radius, the $R = 9$ system even three, however, all are Thomson solutions. All ABC systems show at least three different tilings for each radius, again almost all of them are Thomson solutions. We find exceptions for the $R = 4$ spheres, where for both systems only a single type of tiling is found and the ABC system for $R = 7$, where although three different tilings are found, the majority (86%) of analysed frames forms only one type. Another exception are larger ABC systems, where we find an increasing number ($\approx 1\%$ for $R = 8$, $\approx 12\%$ for $R = 9$, $\approx 44\%$ for $R = 10$) of tilings not connected to the Thomson problem. However, we do see these percentages go down as the simulations are running for longer times so we conjecture that eventually all non-Thomson solutions might anneal out.

Since the free energy levels of different tilings is a function of the sphere radius, as will be discussed later, this may allow the conclusion that the energy levels are almost degenerate for the majority of the combinations of the chosen star copolymers

---

‡ In general the presented analysis method using Voronoi diagrams works well and is robust. In some rare cases, however, we find it to produce invalid results. These cases are, when very short edges appear in the Voronoi diagram, which means two vertices are very close together. In these cases the neighborhood relations are not clear for the algorithm and small displacements of a single particle can alter the resulting tiling. The other weak point is the cluster analysis. Since all systems are run at finite temperature, there might be particles moving outside their domain in the vicinity of another domains. The cluster algorithm then can mistake both clusters as a single one. Most of these invalid frames can be identified and then ignored by checking if $\chi \neq 2$. A neglectable number of $\approx 1.5\%$ frames were found to be invalid in the sense as discussed.
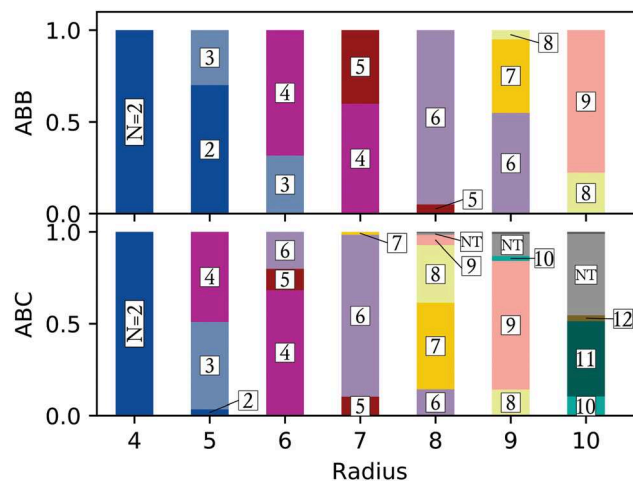
42

Fig. 7 The three spherical tilings representing the structure of the A, B and C domains. The figure shows three single-colored tilings, generated by the self-assembly of ABC star copolymers, in each of the colors on the same sphere. Left panel: Rendering of the simulation snapshot where the patches creating the tiling are emphasized while showing the others simultaneously. Middle panel: The single-colored tiling derived from the emphasized patch configuration on the left. Note that only patches of the emphasized colors are considered for the computation of the tiling, which allows for direct comparison with single-colored tilings from ABB systems. The axis shows the orientation of the axis with the highest symmetry. Right panel: A 2D projection of the tiling. The black axis in the middle column indicates the position of the red line in the projection plots. The label of the tiling is given on the far right side.

and simulation volume geometry. The finite temperature of our simulation then allows the system to jump into local minima instead of the energetic ground state, which results in the spectrum of tilings found here. For some systems though ($R = 4$, ABB on $R = 7$, ABC on $R = 8$) the energy level of certain configurations seems to be deep enough to prevent other structures to assemble.

For all of the ABB system and ABC systems with $R < 8$ we find that all tilings are of Thomson-type solutions, as seen in Fig. 6. This means that the N A-type (and respectively B- and C-type) patches will sit at the same positions as the electrons would in a N-electron Thomson solution, which we checked by visual observation. This is a remarkable result since although

the polymers only have short range interactions a structure of long range order is formed. Such long range interactions in a similar system of interacting micelles formed by diblock copolymers has been predicted by ref. 71.

For ABC systems, with increasing radii beginning at $R \geq 8$ an increasing number of configurations, up to $\approx 40\%$, are not of the Thomson-type. These are shown in Fig. S2–S9 in the ESI.† An analysis of the patch shapes in Thomson and non-Thomson solutions did not show statistical significant differences. Hence, a correlation between patch shape and being a Thomson or non-Thomson solution could not be found. For more information on the methodology and the data see Fig. S1 in the ESI.† We rather argue that these systems are stuck in local minima.

The Thomson problem in general is known for its high probability of being stuck in local minima.[40] Already for $N = 32$ electrons the probability of finding the global minimum drops significantly, which roughly coincides with the threshold where our results show local minima. Using polymer melts instead of point-like particles adds even more complexity to the energy landscape. The fact that the ABB systems – somewhat simpler than the ABC system, due to the missing color constraint for example – do not show any non-Thomson solutions and that the proportion of non-Thomson solutions increase with increasing radius, and thus number of patches, supports this.

Based on the observation that the simulations only show Thomson solutions up to systems with $R = 7$, all of those ABC systems must consist of three different tilings, each of which solves the Thomson problem on its own while coexisting with two others on the same sphere. We will elaborate on this again using an example system from the $R = 8$ runs using Fig. 7, however, all systems of various sizes share the same behaviour.

Fig. 7 shows how three different Thomson solutions can coexist on a single sphere. When only considering the blue patches, while red and yellow act as a matrix, the resulting tiling is of type [4.4.4]. Analogue type [4.4.5] and [4.4.4] tilings are formed in the red and yellow patches respectively. The tilings have a different orientation on the sphere as can be seen on the orientation of the axis of highest symmetry.

In the case of the $R = 8$ tilings, the overwhelming number of ABC systems were found to be a combination of three Thomson solutions, where the most prominent combinations are (7/8/8) with 19%, (7/7/8) with 15%, (7/7/7) with 15% and (6/7/7) with 14%. The number denotes the number of patches in the tiling, the tiling label can be found using Table 1. Only a small number of 1% of the systems contained tilings which are not Thomson solutions. The same holds for systems with smaller radius: since no tilings were found not to solve the Thomson problem, all combinations there consist of Thomson solutions. For larger systems the number of non-Thomson configuration increases. Therefore, the amount of configurations containing non-Thomson solutions increases as well, however, we cannot say if that is caused by increasingly difficult equilibration or due to other reasons, for example the color constraint preventing some combinations to be assembled.

In the $R = 8$ case we found the (7/7/7) combination formed in two different ways: once with only Thomson solutions, and once with one Thomson solution and two non-Thomson tilings. In this case we clearly see that it is possible to build this (7/7/7) combination using only Thomson solutions, thus proving that the color constraint does not prohibit the Thomson solutions to form. This hints towards our guess that combinations with non-Thomson solutions are not caused by the color constraint but equilibration issues. Apart from this observation we could not find any regularities in the frequencies of the different combinations of the tilings for any radius.

It is important to note that although the simulation data of ABB systems for $R = 8$ clearly shows the type [4.4.4] tiling as the minimal energy configuration, we could only find one out of 300 combinations being a $3 \times [4.4.4]$ tiling on a single sphere in the ABC systems of the same radius. This observation is found as general behaviour across all runs: there are statistically significant differences in the frequency with which single-colored tilings occur in ABB and ABC systems. This circumstance shows that while the general behavior – forming Thomson solutions – seems untouched by the color constraint, it does affect the self-assembly process: there are differences between ABB and ABC systems that are manifested in the topology of the adopted structures, or at least in the statistical properties of the latter. This observation enables us to answer the following question: if one is only able to see one kind of color, for example by looking through colored filters, is it possible to determine if the observed structure is assembled by an ABB or an ABC system? The answer depends on the circumstances: if only one configuration is available, the answer is no, since each configuration found in this article is assembled by both the ABB and the ABC systems. However, if multiple samples are available, the answer is yes. The different statistics of frequencies of the tilings in the different systems as shown in Fig. 7 enables us to determine the type of systems of the given samples.

To understand why ABC systems behave differently we need to look at the free energy functional determining the resulting structures. When assuming that all equilibrium solutions are Thomson solutions, the resulting tiling type is determined by the number of patches assembled in the melt. As can be seen in the data, this number is a function of the radius: with increasing sphere size the number of patches increases. This follows from the energy functional of polymer melts in the strong segregation limit:

$$F = F_{conf} + F_{int}$$

where F_{conf} is the entropic contribution determined by the domain shape and F_{int} is the enthalpic contribution and measures the interface area.[71] The entropic contribution favours most spherical patch shapes and penalises domains, where the polymer chains have to be stretched. Consider an exemplary ABB system with two A-type patches located at the north and south pole of the sphere. The interfaces, on which the grafting points of the star copolymers must sit, are then disk segments centred around the poles. From there the B type arms stretch to cover the entire sphere. Since the arm length is kept constant, the arms must stretch increasingly with increasing sphere radius to cover the surface of the sphere. This comes with an entropic penalty. At some point it becomes energetically more favorable to change to a three patch configuration which, despite the increasing interface energy, relaxes the polymer arms and reduces the entropic energy contribution. This interplay between minimising the interface area and entropic energy contribution determines the number of domains and, thus, the resulting structure in these systems.

The differences in the frequencies of tilings in ABB and ABC systems are caused by a modification of the energy functional. While in the ABB systems only A–B interfaces exist, the ABC systems also develop A–C and B–C interfaces, thus, increasing the enthalpic energy contribution. The entropic contribution changes since the grafting points of the star copolymers are not allowed to move freely along the A–B interface but are constrained to ABC triple lines, resulting in more constrained polymer paths leading, presumably, to an entropic penalty.
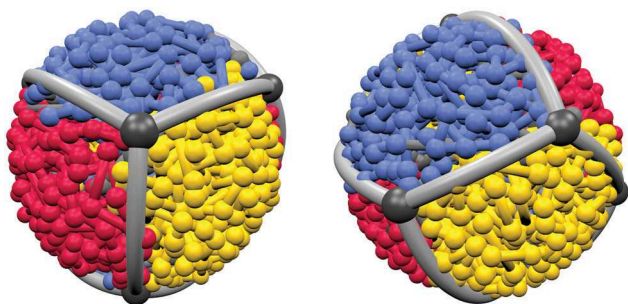
Fig. 8 Rendering and three-colored tiling of a three-colored Thomson solution. The figure shows a three-colored tiling, where each patch of any color corresponds to a Thomson particle. Each color on its own in terms as described above solves the Thomson problem, but also the three-colored tiling solves the Thomson problem. This configuration with $N = 6$ is one of only two where this is possible since the tiling in this case only consists of squares which are allowed with the color constraint.

Apart from the more subtle influences of the color constraint on single-colored tilings in ABC systems, the effect of the color constraint can be directly seen when looking at the three-colored tilings constructed from patches of all colors. In these tilings the vertices and edges of the Voronoi cells coincide with the triple lines and inter-domain interfaces of the polymer structure, see right panel in Fig. 4 or Fig. 8. Note that unlike the single-colored tilings used so far, each patch of any color corresponds to a Thomson particle at once. Here the color constraint can be directly applied to these three-colored tilings. As can be seen in the references in this article, all Thomson solutions for $N \geq 12$ contain tiles with an uneven number of polygons, which means these solutions can not be formed by the polymer melt due to the color constraint. This is backed by our data, where we did not find any of the Thomson solutions for systems with $N \geq 12$, where $N = N_A + N_B + N_C$ is the total number of patches in all colors respectively Thomson particles. For systems with $R \leq 7$ tilings consisting of 6 squares plus $N - 6$ hexagons are found, for system sizes with $R \geq 8$ also octagons occur in tilings with $N \geq 25$. For each octagon an additional square must be introduced to fulfil Eulers equation with $\chi = 2$.

As can be seen in Table 1, the only Thomson solutions for $N < 12$ which only contain polygons with an even number of edges are $N = 3$ and $N = 6$. While the $N = 3$ case proved difficult to equilibrate to a cylindrical phase due to very small system sizes and does not allow for any conclusions, the $N = 6$ case is equivalent to a cube with alternating colored faces and is found for $R = 4$ in ABC systems (see Fig. 8). While each color solves the Thomson problem on its own as single-colored $N = 2$ tilings, the combination of all three colors also forms a three-colored Thomson solution unlike any other configuration in our data. This observation gives rise to the assumption that also for the three-colored tilings the Thomson solutions would be the optimal state, however, the frustration imposed by the color constraint keeps the system in a metastable state.

4 Conclusion and outlook

In this article the self-assembly of ABC and ABB star copolymers confined to a spherical shell was simulated using DPD molecular dynamics simulations in order to investigate the combined influence of geometric frustration and the color constraint inherent in the ABC system. In bulk simulations, these polymers form columnar phases whose cross sections are 3-colored, planar, hexagonal tiling patterns. The architecture of ABC stars imposes the color constraint onto the resulting structures: only tiles with an even number of edges are allowed where the color of all adjacent tiles must alternate. To differentiate between the influence of the color constraint and the curvature ABB systems were simulated as reference, where the color constraint does not apply.

We can summarise our findings into four core results: (1) apart from kinetically stuck configurations in large ABC systems ($R \geq 8$), we find all single-colored tilings in both ABB and ABC systems to be Thomson solutions. (2) In ABC systems we find three possibly different tilings on each sphere, one in each color while neglecting the other two, all of which solve the Thomson problem for small radii individually. We find some non-Thomson solutions for larger radii ($R \geq 8$) but believe this is due to equilibration issues as discussed above.

(3) A spectrum of configurations dominates the ensemble, rather than a single structure. This leads to the occurrence of a small number of different tilings in both ABB and ABC systems, with varying probability. (4) The latter can be tuned by varying the sphere radius, which means we can switch between Thomson solutions of different numbers of particles. While we could not find any combination of three tilings on the same sphere which the color constraint does not allow, the frequencies of the tilings in the ABC compared to the ABB system show statistically significant differences. This provides the possibility to differentiate between the two systems: statistically speaking we can determine if a tiling was formed by an ABB or and ABC system by only being able to see a single color.

A direct comparison of our work to the presented results of frozen particles on a sphere[35] or the diblock copolymers on a spherical substrate[30] is somewhat difficult: while in these systems the number of particles is in the order of 100 (which is equivalent to one patch in our systems), our largest system consists of a maximum of 12 domains in a single tiling. At these system sizes the tilings are missing the regularity to define "defects" in their structure. Taking the entire ABC system with all of its colors into account, however, we have a system consisting of up to 37 patches. Here we can see the influence of the color constraint: instead of finding isolated pentagonal defects or scars of pentagons and heptagons, we find either six squares or a combination of squares and octagons to cope with the geometrical constraint.

A promising and interesting application of this work can be found in the field of patchy particles: discrete particles with patches on their surface which can couple and form bonds to other patches, *e.g.* Janus-particles.[72,73] A mechanism to assemble such particles and tune their coordination number include self-assembly of monolayers of surfactants on spherical substrates.[74,75] Our work presents an example how such a self-assembly could be realised. Instead of using two repulsive walls to model a spherical substrate, the architecture and composition of the polymer can be modified, so that spherical droplets will form in solution, as seen

45

in previous work.[76–79] Preliminary simulations showed that adding a fourth arm, immiscible with the already existing arms, would form the core of such a droplet, on which surface the ABC arms assemble as presented in this work. By tuning the length of this fourth arm, the radius of the droplets can be changed. As shown in this article, the number of patches would change and therefore the coordination number of the droplet as a patchy particle. Further, instead of using symmetric star copolymers, the length of one arm can be varied to generate different, 'asymmetric' tilings, analogue to.[10,12]

Conflicts of interest

The authors declare no conflict of interest.

Acknowledgements

References

1 F. S. Bates, *MRS Bull.*, 2005, **30**, 525–532.
2 M. W. Matsen, *Self Consistent Field Theory and Its Applications*, Wiley-Blackwell, 2007, ch. 2, pp. 87–178.
3 G. M. Grason and R. D. Kamien, *Macromolecules*, 2004, **37**, 7371–7380.
4 G. Polymeropoulos, G. Zapsas, K. Ntetsikas, P. Bilalis, Y. Gnanou and N. Hadjichristidis, *Macromolecules*, 2017, **50**, 1253–1290.
5 Z. Guo, G. Zhang, F. Qiu, H. Zhang, Y. Yang and A.-C. Shi, *Phys. Rev. Lett.*, 2008, **101**, 028301.
6 C. A. Tyler, J. Qin, F. S. Bates and D. C. Morse, *Macromolecules*, 2007, **40**, 4654–4668.
7 M. G. Fischer, L. de Campo, J. J. K. Kirkensgaard, S. T. Hyde and G. E. Schröder-Turk, *Macromolecules*, 2014, **47**, 7424–7430.
8 S. Okamoto, H. Hasegawa, T. Hashimoto, T. Fujimoto, H. Zhang, T. Kazama, A. Takano and Y. Isono, *Polymer*, 1997, **38**, 5275–5281.
9 J. J. K. Kirkensgaard and S. Hyde, *Phys. Chem. Chem. Phys.*, 2009, **11**, 2016–2022.
10 J. J. K. Kirkensgaard, M. C. Pedersen and S. T. Hyde, *Soft Matter*, 2014, **10**, 7182–7194.
11 J. J. K. Kirkensgaard, *Interface Focus*, 2012, **2**, 602–607.
12 T. Gemma, A. Hatano and T. Dotera, *Macromolecules*, 2002, **35**, 3225–3237.
13 L. de Campo, T. Varslot, M. J. Moghaddam, J. J. K. Kirkensgaard, K. Mortensen and S. T. Hyde, *Phys. Chem. Chem. Phys.*, 2011, **13**, 3139–3152.
14 K. Hayashida, T. Dotera, A. Takano and Y. Matsushita, *Phys. Rev. Lett.*, 2007, **98**, 195502.
15 K. Hayashida, W. Kawashima, A. Takano, Y. Shinohara, Y. Amemiya, Y. Nozue and Y. Matsushita, *Macromolecules*, 2006, **39**, 4869–4872.
16 A. Takano, S. Wada, S. Sato, T. Araki, K. Hirahara, T. Kazama, S. Kawahara, Y. Isono, A. Ohno, N. Tanaka and Y. Matsushita, *Macromolecules*, 2004, **37**, 9941–9946.
17 A. Takano, W. Kawashima, A. Noro, Y. Isono, N. Tanaka, T. Dotera and Y. Matsushita, *J. Polym. Sci., Part B: Polym. Phys.*, 2005, **43**, 2427–2432.
18 P. Tang, F. Qiu, H. Zhang and Y. Yang, *J. Phys. Chem. B*, 2004, **108**, 8434–8438.
19 G. Zhang, F. Qiu, H. Zhang, Y. Yang and A.-C. Shi, *Macromolecules*, 2010, **43**, 2981–2989.
20 Y. Matsushita, *Macromolecules*, 2007, **40**, 771–776.
21 J. J. K. Kirkensgaard, *Phys. Rev. E: Stat., Nonlinear, Soft Matter Phys.*, 2012, **85**, 031802.
22 W. T. M. Irvine, V. Vitelli and P. M. Chaikin, *Nature*, 2010, **468**, 947.
23 W. T. M. Irvine, M. J. Bowick and P. M. Chaikin, *Nat. Mater.*, 2012, **11**, 948–951.
24 R. E. Guerra, C. P. Kelleher, A. D. Hollingsworth and P. M. Chaikin, *Nature*, 2018, **554**, 346.
25 P. Lipowsky, M. J. Bowick, J. H. Meinke, D. R. Nelson and A. R. Bausch, *Nat. Mater.*, 2005, **4**, 407–411.
26 T. Einert, P. Lipowsky, J. Schilling, M. J. Bowick and A. R. Bausch, *Langmuir*, 2005, **21**, 12076–12079.
27 A. R. Bausch, M. J. Bowick, A. Cacciuto, A. D. Dinsmore, M. F. Hsu, D. R. Nelson, M. G. Nikolaides, A. Travesset and D. A. Weitz, *Science*, 2003, **299**, 1716–1718.
28 S. P. Giarritta, M. Ferrario and P. Giaquinta, *Phys. A*, 1992, **187**, 456–474.
29 S. Giarritta, M. Ferrario and P. Giaquinta, *Phys. A*, 1993, **201**, 649–665.
30 L. Zhang, L. Wang and J. Lin, *Soft Matter*, 2014, **10**, 6713–6721.
31 T. L. Chantawansri, A. W. Bosse, A. Hexemer, H. D. Ceniceros, C. J. García-Cervera, E. J. Kramer and G. H. Fredrickson, *Phys. Rev. E: Stat., Nonlinear, Soft Matter Phys.*, 2007, **75**, 031802.
32 R. D. Kamien, *Rev. Mod. Phys.*, 2002, **74**, 953–971.
33 M. J. Bowick and L. Giomi, *Adv. Phys.*, 2009, **58**, 449–563.
34 J. Conway, H. Burgiel and C. Goodman-Strauss, *The Symmetries of Things*, CRC Press, 2016.
35 M. J. Bowick, D. R. Nelson and A. Travesset, *Phys. Rev. B: Condens. Matter Mater. Phys.*, 2000, **62**, 8738–8751.
36 M. Bowick, A. Cacciuto, D. R. Nelson and A. Travesset, *Phys. Rev. Lett.*, 2002, **89**, 185502.
37 M. J. Bowick and Z. Yao, *EPL*, 2011, **93**, 36001.
38 J. J. Thomson, *London, Edinburgh Dublin Philos. Mag. J. Sci.*, 1904, **7**, 237–265.
39 T. Erber and G. M. Hockney, *J. Phys. A: Math. Gen.*, 1991, **24**, L1369.
40 A. N. Bondarenko, M. N. Karchevskiy and L. A. Kozinkin, *J. Phys.: Conf. Ser.*, 2015, **643**, 012103.
41 E. L. Altschuler, T. J. Williams, E. R. Ratner, R. Tipton, R. Stong, F. Dowla and F. Wooten, *Phys. Rev. Lett.*, 1997, **78**, 2681–2685.

42 D. J. Wales and S. Ulker, *Phys. Rev. B: Condens. Matter Mater. Phys.*, 2006, **74**, 212101.

43 D. J. Wales, H. McKay and E. L. Altschuler, *Phys. Rev. B: Condens. Matter Mater. Phys.*, 2009, **79**, 224115.

44 D. L. D. Caspar and A. Klug, *Cold Spring Harbor Symp. Quant. Biol.*, 1962, **27**, 1–24.

45 R. V. Mannige and C. L. Brooks, *Phys. Rev. E: Stat., Nonlinear, Soft Matter Phys.*, 2008, **77**, 051902.

46 S. B. Rochal, O. V. Konevtsova, A. E. Myasnikova and V. L. Lorman, *Nanoscale*, 2016, **8**, 16976–16988.

47 M. Robinson, I. Suarez-Martinez and N. A. Marks, *Phys. Rev. B: Condens. Matter Mater. Phys.*, 2013, **87**, 155430.

48 A. Mughal, *Forma*, 2014, **29**, 13–19.

49 A. Pérez-Garrido, M. J. W. Dodgson and M. A. Moore, *Phys. Rev. B: Condens. Matter Mater. Phys.*, 1997, **56**, 3640–3643.

50 P. J. Hoogerbrugge and J. M. V. A. Koelman, *EPL*, 1992, **19**, 155.

51 P. Español and P. Warren, *EPL*, 1995, **30**, 191.

52 J. J. K. Kirkensgaard, *Soft Matter*, 2010, **6**, 6102.

53 J. J. K. Kirkensgaard, *Soft Matter*, 2011, **7**, 10756.

54 J. A. Anderson, C. D. Lorenz and A. Travesset, *J. Comput. Phys.*, 2008, **227**, 5342–5359.

55 J. Glaser, T. D. Nguyen, J. A. Anderson, P. Lui, F. Spiga, J. A. Millan, D. C. Morse and S. C. Glotzer, *Comput. Phys. Commun.*, 2015, **192**, 97–107.

56 C. L. Phillips, J. A. Anderson and S. C. Glotzer, *J. Comput. Phys.*, 2011, **230**, 7191–7201.

57 R. D. Groot and P. B. Warren, *J. Chem. Phys.*, 1997, **107**, 4423–4435.

58 https://hoomd-blue.readthedocs.io/en/stable/index.html.

59 P. J. Flory, *J. Chem. Phys.*, 1942, **10**, 51–61.

60 M. L. Huggins, *Ann. N. Y. Acad. Sci.*, 1942, **43**, 1–32.

61 R. D. Groot and T. J. Madden, *J. Chem. Phys.*, 1998, **108**, 8713–8724.

62 M. Fixman, *J. Chem. Phys.*, 1962, **36**, 306–310.

63 F. M. Schaller, S. C. Kapfer, M. E. Evans, M. J. Hoffmann, T. Aste, M. Saadatfar, K. Mecke, G. W. Delaney and G. E. Schröder-Turk, *Philos. Mag.*, 2013, **93**, 3993–4017.

64 S. Weis, P. W. A. Schönhöfer, F. M. Schaller, M. Schröter and G. E. Schröder-Turk, *EPJ Web Conf.*, 2017, **140**, 06007.

65 freud, https://freud.readthedocs.io/en/stable/index.html, Accessed: 2019-01-17.

66 J. Stone, MSc thesis, Computer Science Department, University of Missouri-Rolla, 1998.

67 W. Humphrey, A. Dalke and K. Schulten, *J. Mol. Graphics*, 1996, **14**, 33–38.

68 blender, https://www.blender.org/.

69 J. J. K. Kirkensgaard, M. E. Evans, L. de Campo and S. T. Hyde, *Proc. Natl. Acad. Sci. U. S. A.*, 2014, **111**, 1271–1276.

70 B. Grünbaum and G. Shephard, *Tilings and Patterns*, Dover Publications, Incorporated, 2013.

71 A. Semenov, *J. Exp. Theor. Phys.*, 1985, **61**, 744.

72 Z. Zhang and S. C. Glotzer, *Nano Lett.*, 2004, **4**, 1407–1413.

73 C. Casagrande, P. Fabre, E. Raphaël and M. Veyssié, *Europhys. Lett.*, 1989, **9**, 251–255.

74 I. C. Pons-Siepermann and S. C. Glotzer, *Soft Matter*, 2012, **8**, 6226–6231.

75 I. C. Pons-Siepermann and S. C. Glotzer, *ACS Nano*, 2012, **6**, 3919–3924.

76 T. Higuchi, A. Tajima, K. Motoyoshi, H. Yabu and M. Shimomura, *Angew. Chem., Int. Ed.*, 2008, **47**, 8044–8046.

77 T. Higuchi, A. Tajima, H. Yabu and M. Shimomura, *Soft Matter*, 2008, **4**, 1302–1305.

78 S.-J. Jeon, G.-R. Yi, C. M. Koo and S.-M. Yang, *Macromolecules*, 2007, **40**, 8430–8439.

79 K. H. Ku, Y. J. Lee, Y. Kim and B. J. Kim, *Macromolecules*, 2019, **52**, 1150–1157.

47

Supplementary Material:
Patchy particles by self-assembly of star copolymers on a spherical substrate: Thomson solutions in a geometric problem with a color constraint

Tobias M. Hain,[a,c], Gerd E. Schröder-Turk[*a,b,c] and Jacob J. K. Kirkensgaard[*b]

[a] College of Science, Health, Engineering and Education, Mathematics and Statistics, Murdoch University, 90 South Street, 6150 Murdoch, Western Australia, Australia
[b] Department of Food Science, University of Copenhagen, Rolighedsvej 26, 1958 Frederiksberg, Copenhagen, Denmark
[c] Physical Chemistry, Department of Chemistry, Lund University, P.O. Box 124, 221 00 Lund, Sweden
[*] G.Schroeder-Turk@murdoch.edu.au, jjkk@food.ku.dk

1 Frequency of Thomson solutions in simulation runs

Left table (ABB system):

R	N	frames found	Proportion [%]
4	2	300	100
5	2	210	70
5	3	90	30
6	3	95	31.7
6	4	205	68.3
7	4	180	60
7	5	120	40
8	5	15	5
8	6	285	95
9	6	165	55
9	7	120	40
9	8	15	5
10	8	67	22.3
10	9	233	77.7

Right table (ABC system):

R	N	frames found	Proportion [%]
4	2	900	100
5	2	31	3.4
5	3	428	47.6
5	4	441	49
6	3	1	0.1
6	4	614	68.2
6	5	105	11.7
6	6	180	20
7	5	92	10.2
7	6	794	88.2
7	7	14	1.6
8	6	128	14.2
8	7	425	47.2
8	8	282	31.3
8	9	50	5.5
8	NT	9	1
8	INV	6	0,7
9	8	129	14.3
9	9	626	69.5
9	10	27	3
9	NT	104	11.5
9	INV	14	1.5
10	10	93	10.3
10	11	370	41.1
10	12	29	3.2
10	NT	398	44.2
10	INV	10	1.1

Table 1 Frequencies and numbers of equilibrium solutions for ABB (left table) and ABC (right table) systems The table lists the values fig. (6) in the main article is generated from. Shown are the absolute numbers and the frequencies of which equilibrium solutions are found in multiple runs of the simulations.

2

2   Characterization of Non-Thomson solutions
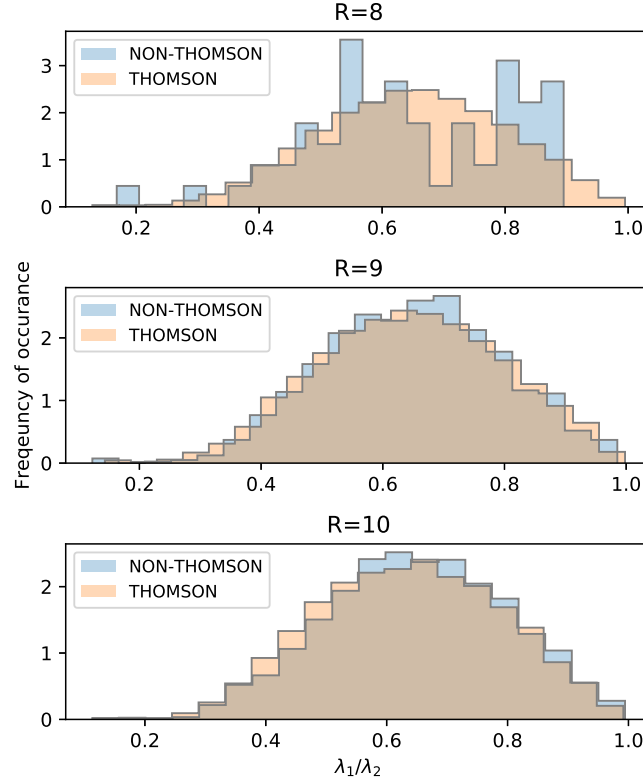
Figure 1 Shape metrics describing the anisotropy of the patches Shown is the distribution of the dimensionless ratio of the two smaller eigenvalues $\frac{\lambda_1}{\lambda_2}$ of the tensor of inertia $I_{ij} = \sum_l^{N_k} \left(||\mathbf{x}_l||^2 \delta_{ij} - x_i x_j \right)$ computed for each patch k. Here $\mathbf{x}_l$ is the position of particle l in the cluster k and N_k is the number of particles associated with the cluster. The tensor of inertia can be represented by a 3×3 matrix and provides information about the mass distribution of a body in 3D space. Its eigenvalues equal to the moments of inerta around its principal axes. In case of sphere caps the largest eigenvalue corrseponds to the principal axis in radial direction, where as the two smaller eigenvalues correspond to the two tangential directions. For a spherical cap these are degenerate and their ratio $\frac{\lambda_1}{\lambda_2}$ equals to one. If the cap is distorted to a ellipsoidal shape one of the eigenvalues will increase, resulting in a decreasing ratio $\frac{\lambda_1}{\lambda_2}$. Hence, the smaller the ratio of the smaller eigenvalues, the more distorted the cap is from a spherical shape. The slight differences which can be seen in the distributions of eigenvalue fractions of Thomson and non-Thomson solutions in the figure of our preliminary analysis are too small to be of statistical significance. Therefore we can find no correllation between the patch shape and the type of the tiling.

3

2.1 List of Non-Thomson solutions found in our analysis
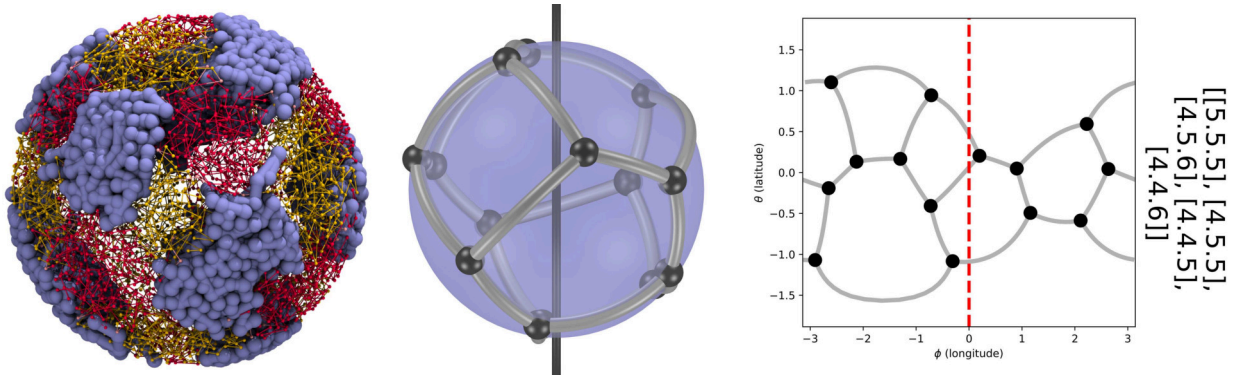
Figure 2 Non-Thomson solution for $N = 9$ patches with 4 squares, 4 pentagons and 1 hexagon.
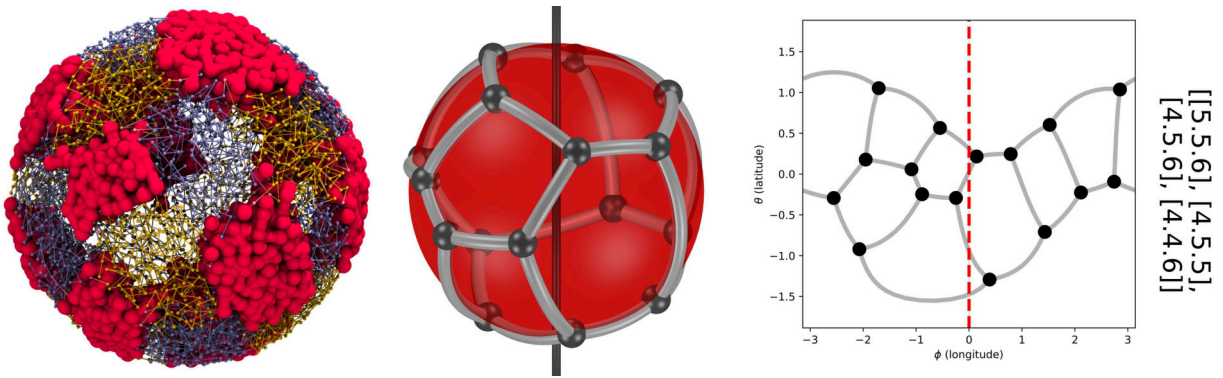
Figure 3 Non-Thomson solution for $N = 10$ patches with 4 squares, 4 pentagons and 2 hexagon.
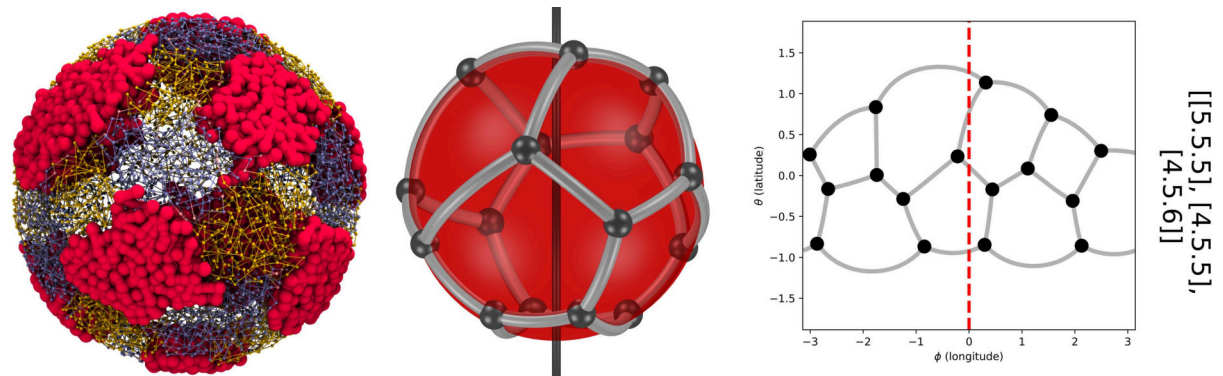
Figure 4 Non-Thomson solution for $N = 10$ patches with 3 squares, 6 pentagons and 1 hexagon.

4
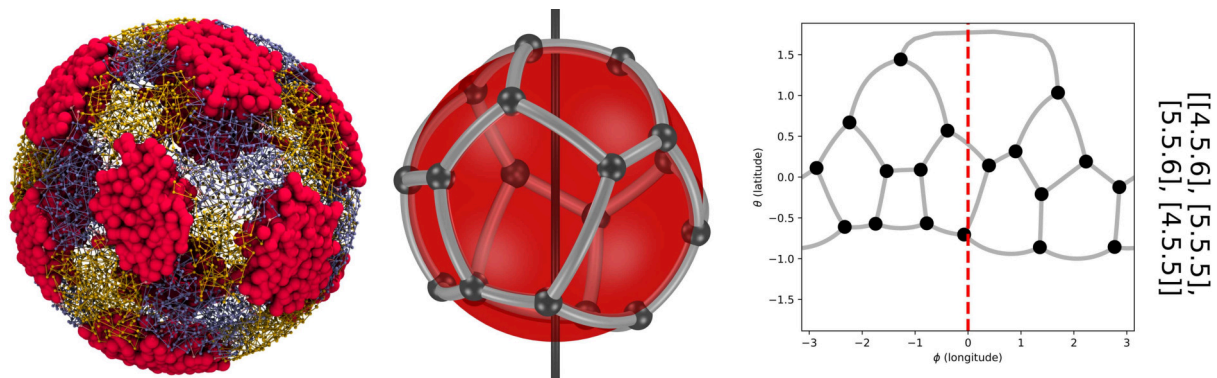
Figure 5 Non-Thomson solution for $N = 11$ patches with 3 squares, 6 pentagons and 2 hexagon.
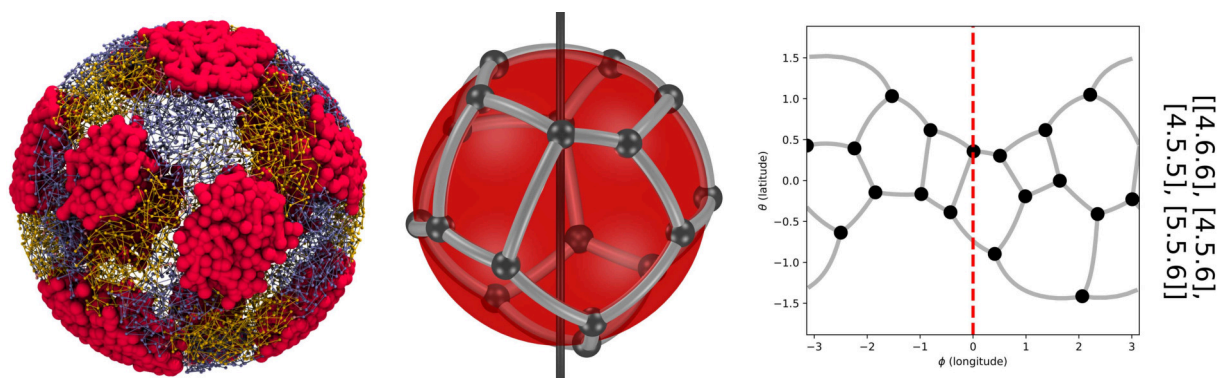
Figure 6 Non-Thomson solution for $N = 11$ patches with 4 squares, 4 pentagons and 3 hexagon.
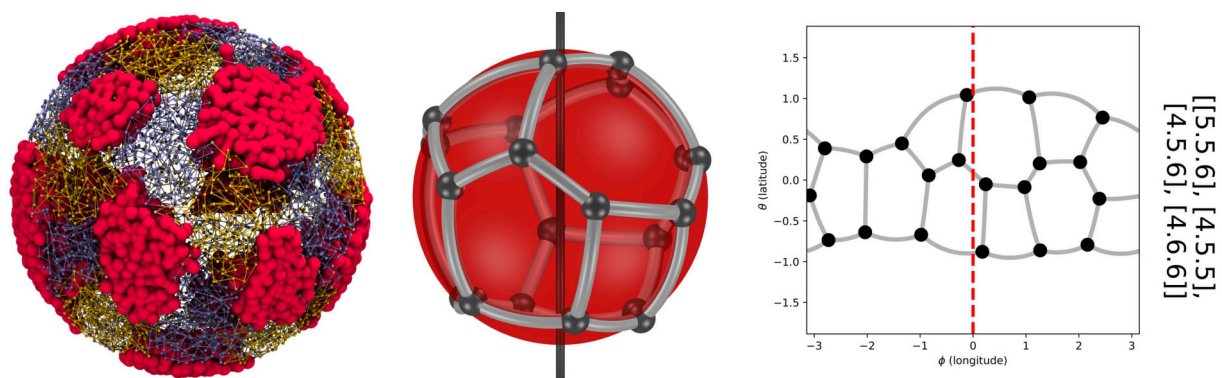
Figure 7 Non-Thomson solution for $N = 12$ patches with 4 squares, 4 pentagons and 4 hexagon.

5
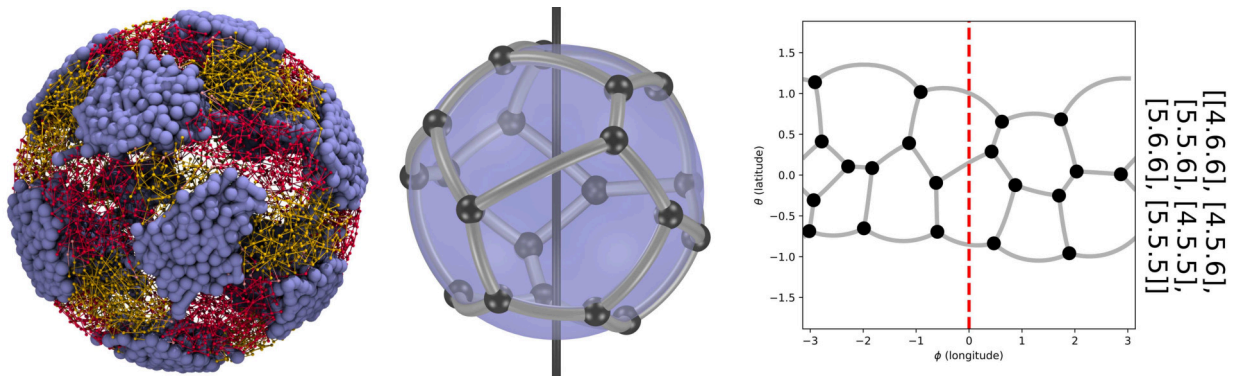
Figure 8 Non-Thomson solution for $N = 12$ patches with 3 squares, 6 pentagons and 3 hexagon.
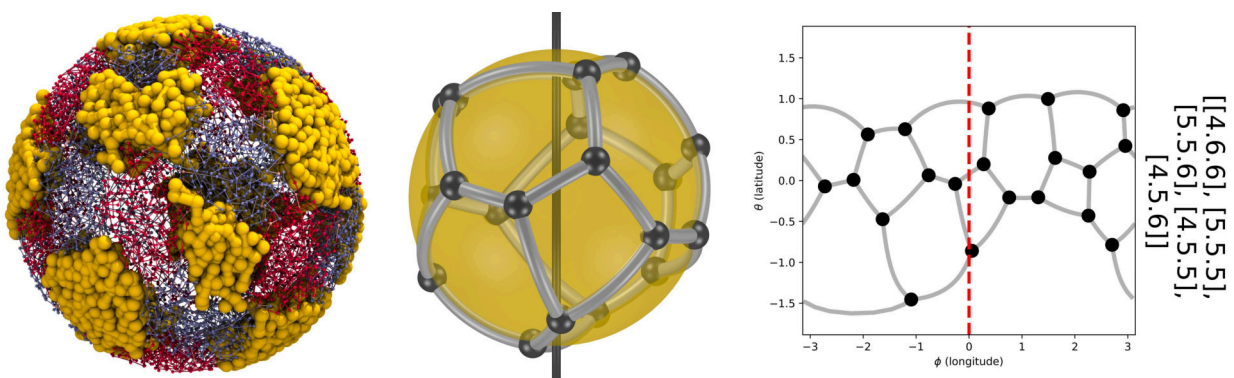
Figure 9 Non-Thomson solution for $N = 12$ patches with 2 squares, 8 pentagons and 2 hexagons.

6

3 Radius of gyration of *ABB* and *ABC* star copolymers
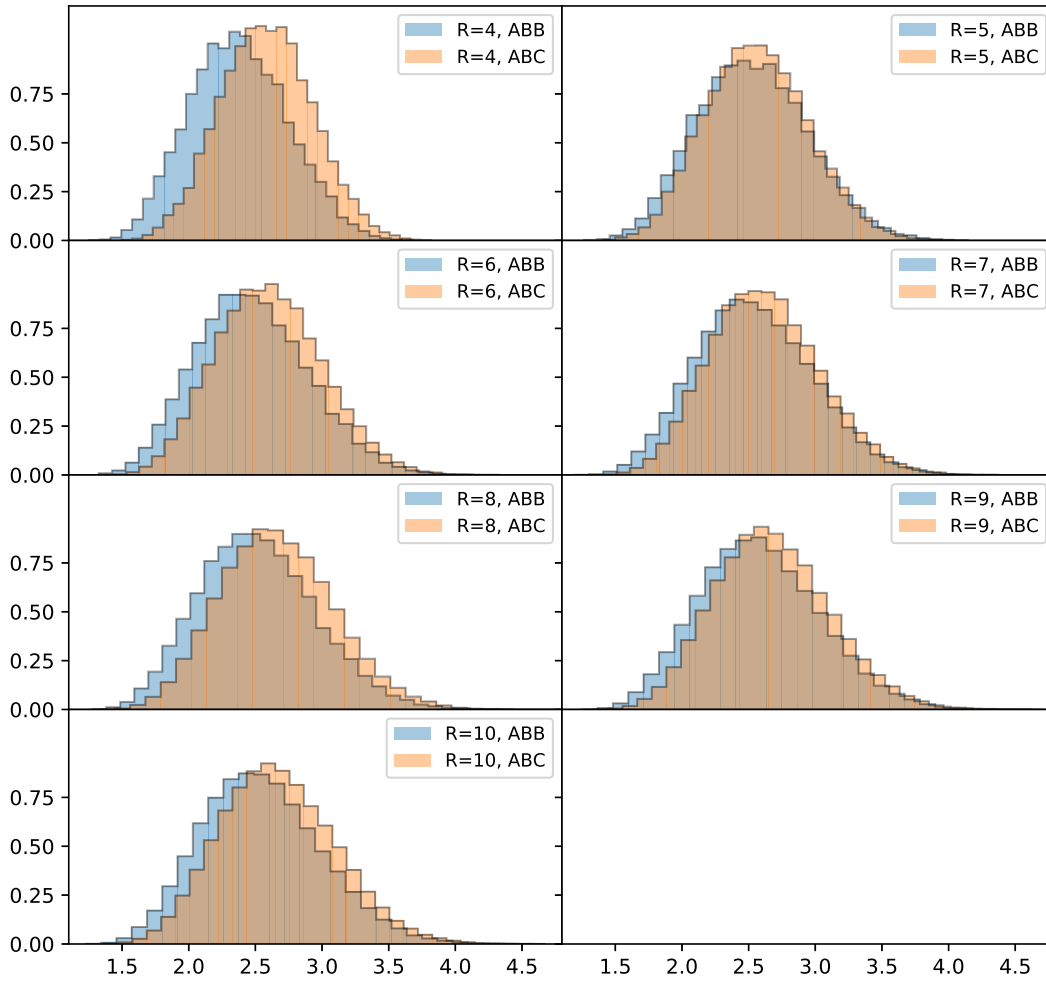
Figure 10 Distribution of radii of gyration of *ABC* star copolymers confined to a spherical shell The figure shows the radius of gyration $R_G = \sqrt{\frac{1}{N} \Sigma_i^N \mathbf{r}_i^2}$, where the sum runs over all beads in the polymer and $\mathbf{r}_i$ is the vector from the i-th bead to the center of mass of the polymer[1], for all polymers in the analyzed frames in terms of the length unit $\mathscr{D}$. All data is shown for a shell width of $dR = 2\mathscr{D}$. The figure shows that polymers in the *ABB* system are slightly more compact than in an *ABC* system.

References

[1] M. Fixman, *The Journal of Chemical Physics*, 1962, **36**, 306–310.

Jamming and crystallisation in cellular media: the Quantizer problem

In the previous chapter, planar tilings in polymer melts in the strong segregation limit (SSL) were investigated. These can be considered as cellular media, however, with deformable cells. In this chapter we will address a Voronoi-based cellular optimisation problem, the Quantizer problem, as a statistical mechanics problems of interacting particles at finite temperatures. This model is relevant for the behavior of cellular materials.

We start by introducing the Quantizer problem as an geometrical optimisation problem, especially in regards to well established geometric optimisation problems. As a cellular system, the Quantizer problem is connected to other cellular media, thus an introduction to the latter and how they are modelled using Voronoi tessellations and Centroidal Voronoi tessellations (CVT) is provided. The Quantizer problem is formally introduced, as well as its reformulation as a system of interacting particles, before presenting our publication [Hain et al., 2020]. The connections and parallels between the Quantizer problem and cellular media, especially polymer melts in the SSL is addressed later in chapter 5.

	Ground state	stable, disordered state
Kepler Problem	HCP/FCC	Bernal's RCP
Kelvin Problem	Weaire-Phelan	Plateau foams
Quantizer Problem	BCC	Klatt (?)

Figure 3.1: An overview of previously introduced optimisation problems. Each problem has a ground state, i.e. a configuration globally minimising the energy functional. Due to the complex energy landscapes of these problems, local minima in form of disordered states exists for the Kelvin and Kepler problem.

3.1 The Quantizer problem: a geometric optimisation problem as model for cellular media

In the introduction of this thesis we introduced two cellular optimisation problems: the Kelvin problem [Sir William Thomson, 1887, Weaire, 1997] and the Kepler problem [Szpiro, 2003, Hales, 2006]. For both of these systems crystalline ground states are known, however, stable disordered states in form of local minima exists, as shown in fig. (3.1). Both of these stable minima occur in physical systems, e.g. as random foams [Matzke, 1946, Kraynik, 2006, Weaire and Hutzler, 2001] or in bead packings [Bernal and Mason, 1960, Finney, 2013, Schaertl and Sillescu, 1994, Conway and Sloane, 1999, Cohn and Elkies, 2003]. In the context of these established global and local minima of established optimisation problems, we will address a reported universal, amorphous but hyperuniform state recently found for the Quantizer system [Klatt et al., 2019], herein called *Klatt structure*. Amorphous and hyperuniform point sets, or particles, are systems with no apparent order, however, a suppression of density fluctuations on large length scales [Torquato and Stillinger, 2003, Torquato, 2016, 2018]. We want to highlight two possible implications of the reported *Klatt structure*.

The first aspect considers the *Klatt structure* as a geometric optimisation problem. The best known minimiser of the Quantizer in three dimensions is the crystalline body centered cubic (BCC) lattice [Gersho, 1979, Conway and Sloane, 1999]. Klatt et al. [2019] put forward the hypothesis that the newly found structure could be the characteristic disordered, but stable structure for the Quantizer system, as is the random close packing (RCP) for the Kepler and Plateau's foams for the Kelvin problem. This chapter's publication [Hain et al., 2020] addresses this hypothesis by investigating the stability of this disordered state under in and out of equilibrium cooling.

The second aspect addresses the Quantizer problem as a model system for cellular

material. On the one hand it is closely connected, and thus might act as a (partial) model system to polymer melts, on the other hand insights from the Quantizer system, such as why the hyperuniform *Klatt structure* is stable, may advance the understanding of other cellular material such as systems modelling skin cells [Bi et al., 2016, Merkel and Manning, 2018] (also see sec. (3.4)). Both aspects are addressed in detail in chapter 5.

3.2 The Quantizer problem

The Quantizer problem is an optimization problem originating in computer science [Gersho, 1979, Lloyd, 1982, Conway and Sloane, 1999, Okabe et al., 2000, Du and Wang, 2005, Du et al., 2010, Gray and Neuhoff, 1998]. Gersho [1979] addressed it as a problem of how to quantify, i.e. discretise, signals with least amount of error. For this purpose consider a set of output points $\mathbf{z}_1, \mathbf{z}_2, ..., \mathbf{z}_n$, called generators, in a k dimensional space. Each point $\mathbf{z}_i$ is assigned its Voronoi cell. An input vector $\mathbf{X}$ located in the cell of the point $\mathbf{z}_j$ is discretised to the latter. Lloyd [1982] noted that an optimal Quantizer, i.e. a Quantizer minimising the discretisation error, is achieved if the Voronoi diagram is most central, that is if the $\mathbf{z}$ are positioned at the centers of their respective Voronoi cell, see fig. 3.2.
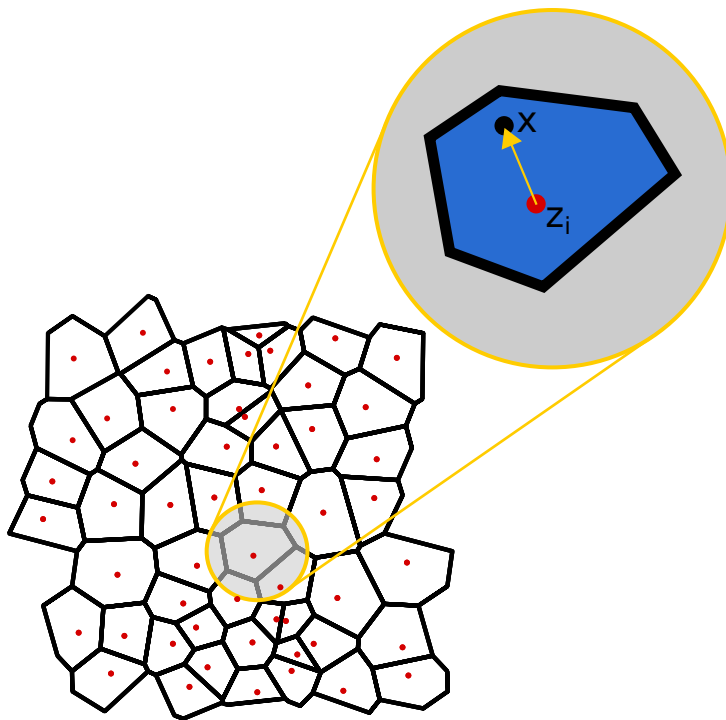
Figure 3.2: The definition of the Quantizer error, for better visualisation in two dimensions. The Voronoi diagram of a point set of generators $\mathbf{z}_i$ is computed, then the quantizer error can be computed according to eq. (3.1). The contribution of each cell to the Quantizer error/energy is the second moment of the mass distribution (i.e., the moment of inertia) with respect to the Voronoi center. A minimal Quantizer error is achieved by most "spherical" and equally sized cells.

More specifically, the Quantizer error is minimised if a Voronoi center $\mathbf{z}$ minimises the functional

$$E(V_i, \mathbf{z}_i) = \int_{V_i} ||\mathbf{x} - \mathbf{z}||^2 d\mathbf{x}, \tag{3.1}$$

where the integral is computed over the entire Voronoi cell V_i. As such, the optimal Quantizer is found for a set of generators $\mathbf{y}_i$ that collectively minimise the Quantizer error

$$E_Q = \sum_i^N E\left(V_i, \mathbf{z}_i\right). \tag{3.2}$$

Equation (3.1) is the second moment of the mass distribution and as such the moment of inertia of the cell. The Quantizer error thus prefers a homogeneous distribution of volumes across all cells, where spherical cell shapes are preferred. The best known global minimum of this energy functional in three dimensions is a point configuration where the $\mathbf{z}_i$ sit at the lattice points of the BCC lattice [Gersho, 1979, Conway and Sloane, 1999].

CVT have been found to minimise the quantizer error [Du et al., 1999, Lu et al., 2012] and as such are local minima to the Quantizer problem [Klatt et al., 2019].

CVTs, and as such the Quantizer problem, find applications in various fields. In data compression, especially image procession, for example, CVTs are used to reduce the number of colors in an image with the least amount of loss of quality [Heckbert, 1982]. Further examples include the meshing of surfaces [Du et al., 2010], grid optimisation [Du and Gunzburger, 2002], description of cell tissue [Honda, 1978, 1983] or approximately model animal territorial behavior [Barlow, 1974, Tanemura and Hasegawa, 1980, Atsuo Suzuki and Masao Iri, 1986].

Lloyd [1982] proposed an algorithm to compute a set of generators that minimise the Quantizer error, that is a CVT. A single iteration of Lloyd's algorithm replaces the centroid $\mathbf{c}$ of each Voronoi cell V_i with its generator $\mathbf{z}$, as visualised in fig (3.3). Since the shape of a single Voronoi cell depends on the locations of all adjacent points, the center of mass of a cell will have moved again after a single Lloyd's iteration. Thus a CVT is achieved by many repetitions of Lloyd's iterations. But also statistical methods has been employed to compute CVTs, such as the "k-means" algorithm [Cam and Neyman, 1967]. In our publication we employ both a Metropolis [Metropolis et al., 1953] Monte Carlo and Molecular Dynamics [Rapaport, 2004] approach to simulate the Quantizer problem in thermal equilibrium; see the "Methods" section of our publication for more details [Hain et al., 2020]. For more details on further methods we refer to the review by Gray and Neuhoff [1998].
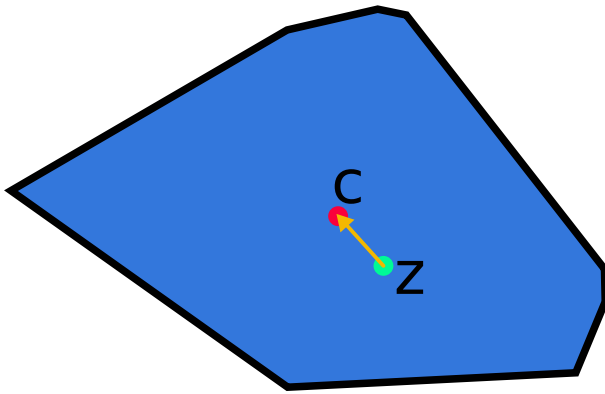
Figure 3.3: An iteration for a single cell in Lloyd's algorithm [Lloyd, 1982]. Lloyd's algorithm converges to a centroidal Voronoi tessellation for an initial point configuration. In each iteration, the generator $\mathbf{z}$ of each cell is moved to the centroid (center of mass) $\mathbf{c}$ of the cell. Repeating these iterations minimises the Quantizer error (eq. (3.2)) of a system.

3.3 The Quantizer as a system of interacting particles

Torquato [2010] reformulated the Quantizer problem as a ground state problem of interacting particles. That is the generators $\mathbf{z}_i$ are considered particles, which interact via a potential derived from the Quantizer error (eq. (3.2)). These interactions are intrinsically multi-body interactions and as such can not be expressed as a superposition of pair-wise interactions, as for example is the case for the Lennard-Jones fluid.

Ruscher et al. [2015] introduced, based on work by Farago et al. [2014], the so-called Voronoi liquid: an ensemble of particles with interactions based on the Quantizer energy. A polarisation vector is defined as $\boldsymbol{\tau}_j = v_j \left(\mathbf{c}_j - \mathbf{z}_j \right)$, where v_j is the volume of the Voronoi cell V_j, $\mathbf{z}_j$ the generator and $\mathbf{c}_j$ the centroid of the j particle. The forces acting on a particle is given as $\mathbf{F}_i = \gamma \boldsymbol{\tau}$ with γ being a constant coefficient. These forces are the gradients of the energy landscape of the Quantizer error; see Du et al. [1999], Liu et al. [2009].

Using this definition, Ruscher et al. [2015] was able to derive a state equation for the Voronoi liquid and investigated dynamical and structural properties such as diffusion and the structure factor of this system. An anomalous sound attenuation in the Voronoi liquid was discovered by Ruscher et al. [2017]. Later this system was extended to the polydisperse Voronoi liquid. Here, a radius is assigned to each particle. This radius is used to compute the weighted Voronoi diagram [Ruscher et al., 2018, 2020]. Hence, particles with a larger radius have larger Voronoi cells than particles with a smaller radius.

In the study of Voronoi liquids, the most relevant result for this thesis was found by Ruscher [2017]. Using Molecular Dynamics simulations, cooling and heating of the monodisperse Voronoi liquid and hence an equilibrium physics approach to the Quantizer problem, was studied. A Liquid-solid/solid-liquid phase transition was found, where the Voronoi liquid crystallised into a BCC lattice. A hysteresis is observed, that is

when cooling the system and subsequently heating it again, the liquid-solid and solid-liquid phase transition occur at different temperatures. These results confirm the BCC configuration to be the (best known) minimiser of the Quantizer system. No disordered, stable states were found or investigated for the monodisperse liquid. However, the bidisperse Voronoi liquid was studied as a glass-former, thus freezing in amorphous states [Ruscher et al., 2018, 2020].

Klatt et al. [2019] used Lloyd's algorithm to compute the CVT for a number of strongly varying initial configurations and found an universal, amorphous but effectively hyperuniform intrinsic structure. Several significantly different initial configurations were used, which all evolved into remarkably similar local minima, instead of finding the best-known global optimum of a BCC structure. Two arguments were put forward why the amorphous state forms: (1) structures emerge which are locally more optimal than the crystalline ground state (2) high energy barriers exist between the amorphous state and two almost degenerate crystalline states.

Lloyd's algorithm is equivalent to a steepest gradient energy minimization [Du et al., 1999], which is effectively a maximally fast quench of the system. Whereas Ruscher [2017] found the Quantizer system to crystallise to its best-known ground state if cooled sufficiently slowly, a fast quench causes the system to get stuck in a local minima. The question remains whether the universal, amorphous *Klatt* structure is a remnant of Lloyd's algorithm or if it is a intrinsic feature of the Quantizer problem, as raised by Klatt et al. [2019]. This open question is addressed in our publication at the end of this chapter.

3.4   Order transitions in cellular media

A well studied cellular model is the vertex model [Hufnagel et al., 2007, Hilgenfeldt et al., 2008, Farhadifar et al., 2007, Manning et al., 2010]. Bi et al. [2016] introduced a self-propelled Voronoi (SPV) model in two dimensions as a model for cells in tissue. It shares many common properties with the Quantizer problem: Its energy functional is defined on the Voronoi tessellation of a set of points and as such is an intrinsic many particle interaction. The energy functional is designed so that each cell strives for an optimal cell area A_0 and perimeter P_0. The forces acting on each particle are the sum of the gradient of the energy landscape combined with a self-propulsion force. Using Molecular Dynamics simulations they found a liquid/solid order transition into a glassy, thus disordered state for a critical value of the parameter $p_0 = P_0/\sqrt{A_0}$. Merkel and Manning [2018] extended the model to three dimensions, where perimeter and area

in the energy functional are replaced by the surface area and cell volume. Using an energy minimisation method a solid/liquid rigidity transition, indicated by a transition of the shear modulus, was found at some critical value of the preferred shape index $s_0 = S_0/\bar{V}^{2/3}$, where S_0 is the preferred surface area and $\bar{V}$ the inverse number density of the system. The authors argue that this transition occurs due to a minimal possible value of average cell surface area $\bar{s}$ in disordered Voronoi tessellations, similar to the maximum packing density in RCP systems. Ordered structures, such as the Kelvin or Weaire-Phelan structures, however, do indeed have smaller $\bar{s}$ values than the reported critical value of the phase transition. However, standard energy minimisation methods fail to reach these ordered states. Furthermore a slight dependence on the energy minimisation protocol are reported. The question whether other methods, such as Molecular dynamics simulations, would be able to reach those ordered minima remains unanswered.

Morse and Corwin [2016] studied order metrics defined on the Voronoi diagrams of a system of jammed packed spheres. In line with the results from the vertex model, the authors find that after the jamming density the surface area reached a plateau where it can only decrease further marginally. Similar results are found in system of densely packed ellipses [Lovrić et al., 2019].

This chapter investigates the question of the influence of the energy minimisation method on the final structure in the Quantizer system. We find that the Quantizer system exhibits both a liquid/solid phase transition into its crystalline ground state, as well as a stable, amorphous state subjected to energy minimisation methods. For more details see the our publication [Hain et al., 2020]. As shown in the example of the Vertex model, the question of whether a systems freezes into a disordered, amorphous local minima over its crystalline ground state is relevant for all cellular, geometrically driven systems.

Here an emphasis lies on polymer melts, since the energy functional of the Quantizer $E\left(V_i, \mathbf{z}_i\right)$ is closely related to the chain stretching contribution F_{st} of the free energy in the SSL. Liquid/solid phase transitions haven been experimentally found in micelle phases in polymer melts [Nicolai et al., 2004] further supporting the validity of this connection. A detailed discussion is provided in chapter 5.

The question of this system being a candidate to form hyperuniform, disordered structures is yet to be addressed and discussed in a later chapter.

3.5   Low-temperature statistical mechanics of the Quantizer problem: Fast quenching and equilibrium cooling of the three-dimensional Voronoi liquid

The following publication aims to contribute towards the understanding of disordered states in amorphous media. Two key aspects are addressed: the stability on the *Klatt* structure and its dependence of the energy minimisation method. We find that the *Klatt* structure seems to be robust against the choice of minimisation methods and find that it forms not only for infinitely fast quenches, but also sufficiently fast out of equilibrium cooling. The article is now reproduced in full from [Hain et al., 2020], with the permission of AIP Publishing.

Low-temperature statistical mechanics of the Quantizer problem: Fast quenching and equilibrium cooling of the three-dimensional Voronoi liquid

Tobias M. Hain,[1,2,3] (ID) Michael A. Klatt,[4,a] (ID) and Gerd E. Schröder-Turk[2,3,5,b] (ID)

AFFILIATIONS

[1] Institut für Mathematik, Universität Potsdam, Karl-Liebknecht-Str. 24-25, D-14476 Potsdam OT Golm, Germany

[2] Physical Chemistry, Center for Chemistry and Chemical Engineering, Lund University, Lund 22100, Sweden

[3] Murdoch University, College of Science, Health, Engineering and Education, Mathematics and Statistics, 90 South St., Murdoch WA 6150, Australia

[4] Department of Physics, Princeton University, Princeton, New Jersey 08544, USA

[5] Department of Food Science, University of Copenhagen, Rolighedsvej 26, 1958 Frederiksberg C, Denmark

[a] Present addresses: Friedrich-Alexander-Universität Erlangen-Nürnberg (FAU), Institut für Theoretische Physik, Staudtstr. 7, 91058 Erlangen, Germany and Department of Experimental Physics, Saarland University, Campus E2 9, 66123 Saarbrücken, Germany.
[b] Author to whom correspondence should be addressed: g.schroeder-turk@murdoch.edu.au

ABSTRACT

The quantizer problem is a tessellation optimization problem where point configurations are identified such that the Voronoi cells minimize the second moment of the volume distribution. While the ground state (optimal state) in 3D is almost certainly the body-centered cubic lattice, disordered and effectively hyperuniform states with energies very close to the ground state exist that result as stable states in an evolution through the geometric Lloyd's algorithm [M. A. Klatt *et al.* Nat. Commun. **10**, 811 (2019)]. When considered as a statistical mechanics problem at finite temperature, the same system has been termed the "Voronoi liquid" by Ruscher, Baschnagel, and Farago [Europhys. Lett. **112**, 66003 (2015)]. Here, we investigate the cooling behavior of the Voronoi liquid with a particular view to the stability of the effectively hyperuniform disordered state. As a confirmation of the results by Ruscher *et al.*, we observe, by both molecular dynamics and Monte Carlo simulations, that upon slow quasi-static equilibrium cooling, the Voronoi liquid crystallizes from a disordered configuration into the body-centered cubic configuration. By contrast, upon sufficiently fast non-equilibrium cooling (and not just in the limit of a maximally fast *quench*), the Voronoi liquid adopts similar states as the effectively hyperuniform inherent structures identified by Klatt *et al.* and prevents the ordering transition into a body-centered cubic ordered structure. This result is in line with the geometric intuition that the geometric Lloyd's algorithm corresponds to a type of fast quench.

Published under license by AIP Publishing. https://doi.org/10.1063/5.0029301

I. INTRODUCTION

Geometric optimization problems of tessellations search for partitions of space into cells with certain optimal geometric properties. Often, these geometric properties can be expressed as energy functionals so that the global optimum corresponds to the ground state of a physical system. Thus, the geometric optimization problem relates fundamental questions in mathematics and physics.

Famous examples in three dimensions (3D) are the Kelvin problem[1,2] (that is, the search for a tessellation with equal-volume cells that have the least surface area) and the Kepler problem[3] (that is, the search for cells with the highest packing fraction of impenetrable spheres).

While global optima correspond to ground states of physical systems, local optima correspond to inherent structures (that is, local minima of complex energy landscapes). At low-temperature,

an equilibrium system will typically be different from a non-equilibrium state that is reached by a quench. Such a fast non-equilibrium cooling often leads to glass-like, highly disordered states. There are, however, also potentials that exhibit disordered ground states and that are hence often highly degenerate. Examples include stealthy potentials where the ground states suppress single scattering up a finite wave number K. The potential suppresses density fluctuations at large scales,[4–6] and as a rigorous consequence, the ground state does not allow for arbitrarily large holes.[7,8] Another class of examples are models of "perfect glass," which involve up to four-body interactions and do not allow for crystalline ground states (but only disordered configurations).[9] Disordered ground states have also been empirically found in vertex models that optimize the isoperimetric ratios of cells (modeling biological tissues).[10,11]

More generally, we are here interested in models with energy landscapes that allow for metastable amorphous states that have energies close to the crystalline ground state.

The geometric optimization problem that we consider here is the *quantizer problem*,[12–17] that is, we optimize the second moment of inertia of each cell. Intuitively speaking, the optimization prefers equal-volume cells with "sphere-like" shapes. It is a prominent problem in computer science, where it is applied, for example, in compression algorithms[18] or mesh generation of two-dimensional manifolds.[19] In recent years, the quantizer problem has attracted attention in physics since it relates to a many-body interaction that results in surprising physical and geometrical properties.[20–23]

Given a configuration of N points in Euclidean space, the Voronoi quantizer (or Voronoi tessellation) assigns to each point z_i a cell C_i that contains all sites in space that are closer to that point than to any other point in the point pattern.[15] The cells subdivide space without overlap. The quantizer energy E_i of a single cell C_i is then defined as the moment of inertia of the cell interpreted as a solid object and measured with respect to the Voronoi center z_i.[17,20,21] More precisely, the total energy E of the system is the sum of the cell energies E_i, defined as follows:

$$E = \sum_{i=1}^{N} E_i, \quad \text{with} \quad E_i = \frac{\gamma}{2} \int_{C_i} \|\mathbf{x} - \mathbf{z}_i\|^2 d\mathbf{x}, \quad (1)$$

where γ is a coefficient to set the dimension of Eq. (1) to an energy and N is the number of points (respectively, cells).

The quantizer problem is defined for a fixed number of points N. Note that this formulation of the quantizer energy is extensive, in contrast to the intensive *quantizer error*, which is the rescaled sum of all single cell energies (see Ref. 23 for more details). The energy functional can also be expressed by the Minkowski tensors[24] of the cell C_i (see below).[23] The quantizer energy functional assigns an energy to each point configuration in Euclidean space. The quantizer problem in computer science has thus been reformulated as a ground state problem in statistical physics.[20]

In 3D, the conjectured optimal solution of the quantizer problem, that is, the ground state, is the body-centered cubic (BCC) lattice.[14] It is closely related to Kelvin's conjectured equal-volume cells with the least surface area,[2,25] a conjecture that was later disproven by the counterexample of Weaire and Phelan.[1] The proof of the Kepler conjecture [that no packing of monodisperse spheres

has a larger packing fraction than the face-centered cubic (FCC) packing] reformulates the problem as an optimization problem of tessellations (including Voronoi cells).[3]

Here, we are interested in disordered inherent structures with energies close to that of the ground state. Following the approach form Ruscher, Baschnagel, and Farago,[21] we study both equilibrium and non-equilibrium dynamics of a many-particle system whose energy is defined by a rescaled quantizer energy, that is, a geometrically driven particle system with many-body interactions. Our focus is on order/disorder transitions, that is, on the degree of structural order and disorder of different states and how it changes during melting, slow cooling, or a quench.

Ruscher *et al.* studied in detail this many-particle system from a thermodynamic point of view[21,22,26] and found intriguing physical behavior like an anomalous sound attenuation.[27] They named the system the *Voronoi liquid*. The distinct difference to the well-established model systems such as the Lennard-Jones fluid is that the interactions in the Voronoi liquid are intrinsically many-body. Ruscher, Baschnagel, and Farago[21] reported theoretical considerations as well as molecular dynamics (MD) simulations that show that the Voronoi liquid in many ways behaves similar to an ordinary fluid, including a scaling law for its free energy and derivated quantities as well as dynamic and structural properties. Furthermore, a melting and a freezing transition when heating and cooling the system are found, showing a metastable state with a hysteresis and under and overcooled states.[22] Ruscher *et al.* studied the Voronoi liquid as a model glass former where crystallization is prevented by the integration of a term corresponding to bidispersity.[26,28] Their work without the polydispersity term,[21] and the results of this paper, shows that the system without polydispersity and defined by Eq. (1) shows a conventional order/disorder transition upon heating or cooling.

Here, we are specifically interested in a better understanding of the inherent structures of the quantizer problem. In a recent study of Klatt *et al.*,[23] the so-called Lloyd's algorithm[13] was applied to a broad range of distinctly different random point patterns to find minimal energy point configurations. At each step of the algorithm, each point is replaced by the center of mass of its Voronoi cell. Klatt *et al.*[23] showed that upon the application of a sufficient number of iterations of Lloyd's algorithm, all initial random point configurations converged to configurations that are amorphous and universal with the same two-point statistics and Minkowski tensors within error bars. Moreover, these final configurations are effectively hyperuniform, that is, they exhibit a strong suppression of large-scale density fluctuations,[29–31] as measured by the hyperuniformity index $H = \lim_{k \to 0} S(k)/\max S(k)$[31,32] with values of $H \lesssim 10^{-4}$. We will here refer to these configurations as the *converged Lloyd state(s)*.

In this article on the quantizer energy, we study both the equilibrium behavior and non-equilibrium quenches. We thus reproduce and confirm the results found by Ruscher, Baschnagel, and Farago.[21] Therefore, we use, besides MD, also Monte Carlo (MC) simulations. Moreover, we vary the cooling rates to study both crystallization and the freezing in inherent structures. We thus further probe the energy landscape of the quantizer problem to address the question of the stability of the disordered, effectively hyperuniform states to which Lloyd's algorithm converges.[23] Since we here study in detail the quantizer problem at finite temperature T, we refer to it as the "QuanTizer problem."

This article is structured as followed: in Sec. II, we give details about our simulations; in Sec. III, we present our results and address the question if a disordered, stable state for the quantizer problem exists, before we give a summary of this article in Sec. IV.

II. METHODS

Three different numerical methods for the evolution of a point pattern are used in this study: Lloyd's algorithm[13] is a purely geometric algorithm used to compute gradient-descent-like quenches as previously described and is used in the same way as in Klatt *et al.*[23] Molecular Dynamics (MD) and Monte Carlo (MC) codes are used to determine statistical properties of quasistatic (slowly cooled or heated) systems. Molecular dynamics is also used to calculate the non-equilibrium evolution of the system when it is quenched, that is, with fast cooling rates.

Throughout this article, we will use reduced units. The unit of length is $\lambda = \rho^{-1/3}$, where ρ is the number density. Thus, we choose $\rho = 1$. Each sample contains $N = 2000$ particles in a cubic simulation box (of side length $2000^{1/3}\lambda \approx 12.6\lambda$) using periodic boundary conditions. The unit of energy is $[E] = \varepsilon = \gamma\lambda^5/1000$, where the factor 1000 is chosen following the work of Ruscher, Baschnagel, and Farago.[21] The unit of temperature is $[T] = \varepsilon/k$, where k is the Boltzmann factor. All particles have the same mass m, which here defines the unit of mass. The arbitrary unit of time for the MD simulation is $[t] = \delta$. (Note that the MC simulation and Lloyd's algorithm have no time scale.)

Monte Carlo method. We use a simple single-step Metropolis algorithm[33] implemented in the software package MOCASINNS:[34,35] a trial move is chosen by selecting a random particle x_i in the system and moving it by a random displacement vector Δx. The energy difference ΔE for this potential new configuration is then computed. The probability of accepting this trial move $p(\Delta E)$ is then given by

$$p(\Delta E) = \begin{cases} 1 & \text{for } \Delta E < 0 \\ \exp\left(-\dfrac{\Delta E}{kT}\right) & \text{for } \Delta E \geq 0 \end{cases} \quad (2)$$

for a given system temperature kT. If the trial move is accepted, the particle is left at its new position, and if the move is declined, it is moved back to its original position. The direction of the random displacement vector Δx is random; its length $\|x\|$ is chosen such as about half of the trial steps are accepted. This is achieved by checking the acceptance ratio in fixed intervals of Monte Carlo steps and doubling the step size if the acceptance ratio is higher than 0.65 or cutting it in half for an acceptance ratio smaller than 0.35. A lookup table was created to quickly find an appropriate step size for a given particle number and temperature.

An essential part of this algorithm is the computation of the energy difference. To improve performance, only the energies of the cells affected by the move are recomputed according to Eq. (1). This definition of the energy is essentially the second moment of the mass distribution of the cell and thus can be expressed as the trace of the Minkowski tensor $W_0^{2,0}$: $E = \text{tr}\left[W_0^{2,0}(C_i)\right]$. Minkowski tensors are a comprehensive set of metrics, describing geometric properties of a body.[24,36]

The computation of the cell energy is carried out in two steps: first, the Voronoi cell of a particle is computed using the *voro++* software package,[37] and the coordinates of the vertices and edges are then parsed into KARAMBOLA,[36] a tool to compute the Minkowski tensors. The cell energy is then obtained by computing $E = \text{tr}\left[W_0^{2,0}(C_i)\right]$. The total energy of a system is just the sum of all individual cell energies.

Molecular dynamics is a method to simulate particle systems by forward integration of Newton's equation of motion $a_i = \frac{F_i}{m_i}$ in time for each particle, thus computing the exact trajectory for each constituent. The essential part of each MD code is thus the computation of the force acting on each particle. We follow Ruscher, Baschnagel, and Farago[21] and define the force on the ith particle as $\mathbf{F}_i = \gamma\tau_i$, where $\tau_i = V_i \cdot (c_i - z_i)$ is the so-called polarization vector, with c_i being the centroid, z_i being the generator, thus the position of the ith particle, and V_i being the volume of the ith cell. The computation of the position of the cell's centroid as well as its volume is done using the software VORO++.[37]

A velocity Verlet integrator coupled with a simple Nosé–Hoover thermostat[38] was used to integrate the equation of motions. The Nosé–Hoover thermostat adds an additional term $\frac{Q}{2}\dot{s}^2 - (f+1)kT_{eq}$ to the Lagrangian of the system to reproduce configurations from the NVT ensemble at a temperature kT. The variable s is associated with the thermostat, f is the number of degrees of freedom of the system, kT_{eq} is the temperature of the NVT ensemble, and Q determines the time scale of the temperature fluctuations introduced by the thermostat. We implemented the formulation by Martyna, Tobias, and Klein.[39] In each integration step, time is advanced by a time step Δt and the positions x_i and velocities $\dot{x}_i$ of each particle as well as the thermostat variable s and its derivative $\dot{s}$ are updated accordingly.

Lloyd's algorithm is a purely geometric algorithm to minimize the quantizer energy. It comprises the reposition of a simple step: move the generator of a cell z_i, thus a particle, to the centroid of its cell c_i.

A typical simulation run, either MD or MC, would consist of the following steps: first, an initial configuration is initialized with a given particle number N and system size.

Initial configurations can be generated as a perfect BCC crystal or as an ideal gas; thus, each component of each particle is chosen uniformly random across the simulation box, corresponding to a binomial point-process. Furthermore, simulation can be initialized with arbitrary point configurations read from simple text files, so a previously saved simulation snapshot can be used as the initial configuration.

The next step is to choose a cooling schedule: a temperature step size $k\Delta T$ as well as a number of temperature steps N_{kT} is set. For each temperature, a set amount of MD or MC steps, called *relax steps*, are performed to get the system to thermodynamic equilibrium. Once these are done, another set of steps, called *measurement steps*, are performed and relevant measurements are taken, the most important being the energy and τ order parameter. After these are done, the system temperature is increased by $k\Delta T$. This is repeated until the final number of temperature increments has been added. In our MD simulations, the cooling rate is defined as $\sigma = \frac{k\Delta T}{\#\text{relax steps}\cdot\Delta t}$ and thus has the units of energy over time. For MD or MC quenches, this cooling schedule would simply consist of a single temperature $kT = 0$.

The measurement used to describe structures in this study are essentially the quantizer energy, the structure factor $S(k)$, and the τ order metric.[4] The structure factor is essentially the scattering intensity of a structure. For a single snapshot of particles in a cubic box of length L with periodic boundary conditions, it is given as[31,40]

$$S(k) = \frac{1}{N}\left|\sum_{i=1}^{N} e^{-i\mathbf{k}\cdot\mathbf{x}_i}\right|^2, \qquad (3)$$

where the sum runs over all particles in the system, $k = \|\mathbf{k}\|$, and $\mathbf{k} \in \left\{\frac{2\pi}{L}(h,k,l) : (h,k,l) \in \mathbb{Z}^3\right\}\{\mathbf{0}\}$.

The τ order metric measures spatial correlations on all length scales and is defined as

$$\tau := \frac{\omega_d}{(2\pi)^d} \int_0^\infty k^{d-1}\left[S(k) - 1\right]^2 dk, \qquad (4)$$

where d is the dimension, in our case $d = 3$, ω_d is the surface area of a unit ball in d dimensions ($\omega_3 = 4\pi$), and $S(k)$ is the structure factor. For a completely disordered, uncorrelated structure, τ vanishes, while it diverges as soon as Bragg peaks appear, i.e., especially for systems with a perfect long range order such as crystals. Since this parameter unites a large amount of information into a single scalar value, it is prone to mainly two errors: small changes in the structure can cause significant change in magnitude of τ; we estimate this error by computing the standard error of multiple runs with identical parameters to $\Delta\tau_{stat} = 0.1\text{--}0.15$, depending on the parameters chosen. Systematic errors caused by the choice of the binning of $S(k)$ as well as an upper integration cutoff k_{max} cannot be avoided. By computing the standard deviation of different binnings of a single system, we estimate these systematic errors to $\Delta\tau_{sys} = 0.9$. Combining both statistical and systematic errors, we assume a total error of $\Delta\tau \approx 1$, which is in line with the previous analysis by Klatt et al.[23]

A detailed list of the parameters used to generate the data in this article is provided in Subsection 3 of the Appendix. Unless stated otherwise, temperature is quantified by kT with the Boltzmann constant k and has units of energy, $[kT] = \varepsilon$. All time steps δt have time unit $[\delta t] = \delta$.

III. RESULTS

Our key results concern the structures obtained by a quench of the system, especially in relation to the converged Lloyd states described by Klatt et al.[23] However, we first describe our reproduction of the findings of Ruscher[22] of an order/disorder transition encountered upon slow equilibrium melting or cooling. Figures 1 and 2 show our results regarding the order/disorder transition upon slow equilibrium cooling or melting.

Figure 1 shows MD simulations essentially of the same system investigated by Ruscher, Baschnagel, and Farago,[21] Ruscher,[22] and Ruscher et al.[27] When a Voronoi liquid of $2 \times 10^3 = 2000$ particles is heated slowly (with a heating rate of $\sigma = 2.5 \times 10^{-4} \varepsilon/\delta$) starting from positions on a BCC lattice at $kT = 0.1$, it undergoes an order/disorder transition; at $kT_{melt} \approx 1.89$, the Voronoi liquid abruptly changes from configurations that represent oscillations around the lattice sites to
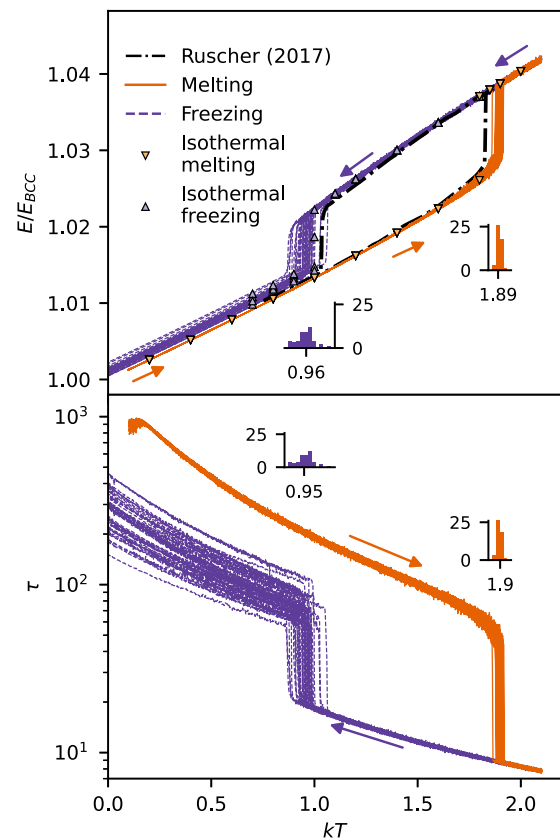
FIG. 1. Molecular dynamics (MD) simulation data of disorder–order (freezing) and order–disorder (melting) phase transitions of the quantizer system observed at melting of a BCC crystal and freezing of an ideal gas, and comparison to earlier data by Ruscher[22] (black dashed-dotted line). Shown is the energy [as per Eq. (1), top panel] and τ order metric [as per Eq. (4), bottom panel] of 48 individual runs for melting and freezing processes. The triangles in the top panel show the mean energy of isothermal systems run over a long time. All runs show a discontinuity in the energy and the τ order metric at the transition temperatures that are different for freezing and melting and which vary slightly from run to run. The insets show the distribution of the transition temperatures. Qualitatively, the hysteresis between the temperature of the phase transition of the disorder/order (freezing) and order/disorder (melting) transitions described by Ruscher[22] is reproduced. The ordered structure obtained by freezing shows variations from the BCC structure, which are most clearly visible in τ and which are indicative of residual defects in the structure. See Subsection 3 of the Appendix for simulation details.

a configuration with no apparent order. Upon further heating, this structure is characterized by the correlations typical for a fluid (for very high temperatures, we expect it to converge to an ideal gas). This transition is evident in the energy E as well as in the structural order parameter τ. In our simulations of 48 systems, the transition temperatures vary slightly, with an average of 1.89 and a standard deviation of 0.01. These transition temperatures are close to but slightly above the observed transition $kT \approx 1.85$ in Refs. 21 and 22. Our curves for the structure factor in the liquid phase agree with those from Ref. 22.
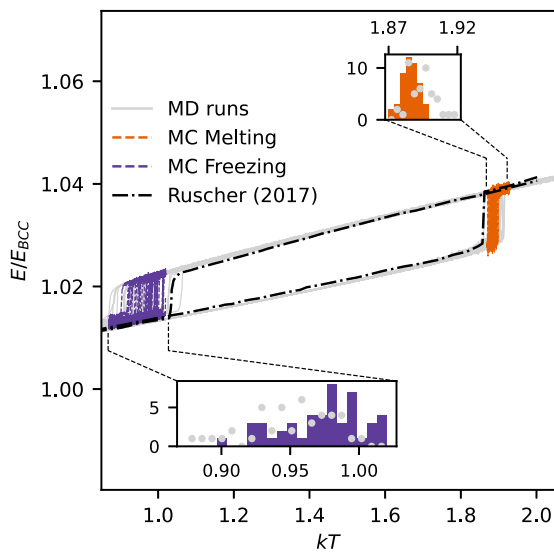
FIG. 2. Monte Carlo (MC) simulation data of disorder–order (freezing) and order–disorder (melting) phase transitions of the quantizer system observed upon heating of a BCC crystal and cooling of an ideal gas. The plot shows 48 individual runs for melting and freezing (dashed, colored lines). The MC data are consistent with the results from MD simulations (see the figure) with slight differences in the variations of the transition temperatures; the MC melting runs show a slightly more narrow distribution of transition temperatures than the MD data, with $kT_m = 1.886 \pm 0.006$ and $kT_f = 0.97 \pm 0.03$, as seen in the insets showing the distribution of transition temperatures in colored bars, and the MD data are indicated by light gray dots. See Subsection 3 of the Appendix for simulation details.

Upon cooling (with the same slow rate as above and starting from an ideal gas configuration at $kT = 2.1$), the system shows the reverse transition from a disordered state to an ordered BCC-like state, at a temperature $kT_{cool} = 0.96 \pm 0.04$ (again close to but slightly below the temperature $kT \approx 1.05$ in Refs. 21 and 22). In line with expectation for the hysteretic behavior of typical first-order ordering transitions, the transition back to the ordered BCC-like state occurs at a temperature lower than the transition upon heating, i.e., $T_{cool} < T_{melt}$. The ordered structures obtained from this cooling process are slightly less ordered than those obtained by slowly heating up an initially perfect BCC lattice; this is evident in a very slight discrepancy in the energy value (which on the interval $kT \in [0.25, 0.8]$ is on average 0.116% higher than the energy values); it is even more evident in the structure factor, which is sensitive to structural detail. The deviations are quantified by the τ order metric and shown on a logarithmic scale in Fig. 1.

The above findings obtained on systems that are cooled down or heated up are supported by "isothermal simulations," that is, simulations at a fixed temperature with significantly longer simulation runs with 8.5×10^5 MD steps (as opposed to the 10^4 MD steps per temperature step in the cooling/melting simulations above).

The mean energies of these isothermal simulations, shown in Fig. 1, support our earlier results. Four independent realizations of the system are simulated for each temperature, as shown in this figure; data labeled "isothermal melting" result from simulating a

system from an initial BCC configuration, whereas "isothermal freezing" refers to a system prepared from an initial ideal gas system; for further simulation details, see Subsection 3 of the Appendix. The mean energy values of the isothermal simulations coincide largely with the energy trajectories of the slow cooling and heating processes, except in a small region around the order/disorder and disorder/order transitions. We thus conclude that the heating and cooling can be assumed a quasi-static process except in the vicinity of the order/disorder and disorder/order transition.

The transitions (discontinuities) in the mean energy of the isothermal simulations are slightly offset from the values of the continuous cooling/heating transitions. The discontinuity of the mean energy of the isothermal heating systems occurs at a slightly lower temperature than all of the slowly heated systems; the discontinuity of the mean energy of the isothermal freezing systems occurs at a slightly higher value than the average transition temperature of the slowly cooled systems. This trend could indicate that our slowly cooled or heated systems are not quite fully equilibrated but fairly close to equilibrium.

We note that the freezing isothermal systems show a similar spread of energy values after the disorder/order transition than the slowly cooled systems, indicating that the residual defects are not caused by too little equilibration time.

Our results (both for slow cooling/heating and for the isothermal simulations) are in good agreement with those from Ruscher's study[22] of the Voronoi liquid. We add three comments in regards to the agreement:

(1) Ruscher's value for the melting temperature ($kT \approx 1.85$) is slightly lower than ours ($kT_m \approx 1.886$), and Ruscher's value for the freezing temperature ($kT_f \approx 1.05$) is slightly higher than ours ($kT \approx 0.96$). These slight differences are probably due to our slightly faster cooling or heating rates, to the different system sizes and to slightly different thermostats and simulation parameters. (We note that as expected for slower cooling rates, Ruscher found a transition temperature for the isothermal melting, which is slightly closer to the isothermal melting system than ours. Within this systematic error due to slight differences in cooling/heating rates, we consider that our results agree with those of Ruscher.)

(2) At the finite size of our simulations ($N = 2000$ particles), we find a distribution for the values of the freezing temperature and the cooling temperatures, which are (average ± standard deviation) $kT_f = 0.96 \pm 0.04$ and $kT_m = 1.89 \pm 0.01$ for the MD simulations (1) and $kT_{freeze} = 0.97 \pm 0.03$ and $kT_{melt} = 1.886 \pm 0.006$ for the MC simulations (2). We understand that Ruscher only presented the data for a single simulation run with about 8000 particles.

(3) In our simulations, the final energy of the freezing curves differs slightly from that of the perfect BCC lattice. Visual examination shows that this is due to residual disordered artifacts in the otherwise ordered lattice. These deviations are more clearly visible in the τ parameter that is sensitive to small deviations from order.

Figure 2 shows Monte Carlo simulation data for the same system, which are consistent with the molecular dynamics simulation data shown in Fig. 1, thereby providing further confirmation of these

results. The quantitative values for the transition temperatures are consistent (within error bars) in MD and MC simulations; however, we observe a narrower spread of transition temperatures for the melting process in our MC simulations as compared to our MD simulations, see Table I.

This concludes our analysis of the quasi-static (slow) equilibrium cooling and heating of the Voronoi liquid. Confirming the results by Ruscher *et al.*, we find the system to behave like a typical first-order order/disorder transition with hysteresis in that limit, with the low-temperature state given by the BCC lattice.

We now turn to a different question, namely, that of what structures the Voronoi liquid adopts upon fast non-equilibrium cooling or a quench. These data are obtained by MD simulations where the system is initialized in equilibrium configurations at high T and then cooled at high cooling rates. The limit of an infinite cooling rate, where the temperature is abruptly set to 0, is here referred to as *quench*. These non-equilibrium final configurations are compared, in particular, to the structures obtained by Lloyd's algorithm, discussed by Klatt *et al.*;[23] Lloyd's algorithm represents a steepest-descent minimization of the energy functional in Eq. (1) and can therefore be regarded as a type of quench.
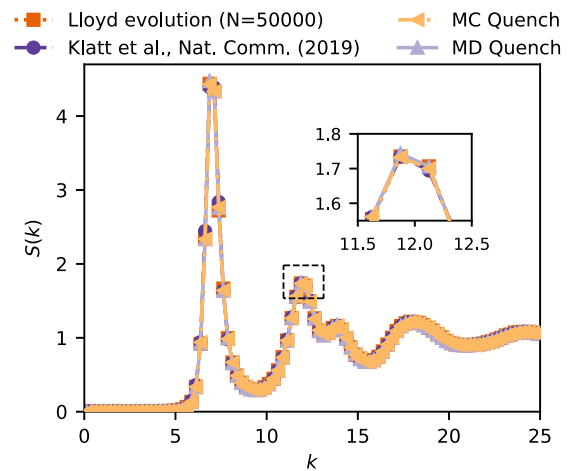
Figure 3 and Table II present our analysis of the structure of the configurations that result from quenching the system, that is, by MD or MC simulations of a system where a high-temperature ideal gas configuration evolves when the temperature is abruptly set to 0. Figure 3 shows the structure factors of the structures thus obtained, and Table II contains the τ order metric calculated from these. See also Subsection 1 of the Appendix for a technical comparison of an MD quench and Lloyd's algorithm.

These final structures are compared to the structures obtained by the application of the (purely geometric) Lloyd's algorithm to the same structures, as suggested by Klatt *et al.*[23] (and also to the data for that same system as reported by Klatt *et al.*[23]). The key result is that to a high degree of accuracy and within the statistical accuracy of our data, structures obtained by MD or MC quenches are indistinguishable from the converged Lloyd states in terms of the structure factor and the derived τ metric (within error bars).

Structural metrics for local order and local packing structure, namely, the Minkowski structure metrics and cell statistics of the Voronoi tessellation, also show good agreement of the final structures of the different quenches. See Subsection 2 of the Appendix for further details. Moreover, we also find a hyperuniformity index H[41] of the order of magnitude 10^{-4}.

FIG. 3. Structure factor $S(k)$ of a quenched ideal gas (binomial point-process) at $kT = 0$ with $N = 2000$ particles and a particle density $\rho = 1$ using molecular dynamics (MD), Monte Carlo (MC), and the gradient-descent-like Lloyd's algorithm. Each structure factor is averaged over 24 individual runs. A detailed description of the processes and parameters are given in Sec. II. All methods evolve into disordered structures with energies and values of the τ order metric equal within measurement uncertainties (see Table II). According to our data, these structures are identical to the universal, amorphous structures previously found by Klatt *et al.*[23] as remarkably stable, disordered minimal energy configurations of the quantizer system. See Subsection 3 of the Appendix for simulation details.

Up to here, we have investigated the two extreme cases being (a) slow quasi-static heating and cooling (which leads to a hysteric order/disorder transition) and (b) quenching as the limit of maximally fast non-equilibrium cooling. We now turn our attention to the intermittent regime of cooling processes that are too fast to be quasi-static yet are not a quench.

The key result of Fig. 4 is that upon rapid non-equilibrium cooling with sufficiently fast but finite cooling rates, the system tends to avoid a transition to an ordered (BCC) structure but instead converges to configurations that are similar in structure (as measured by the structure factor) and similar in energy values to the converged

TABLE I. Transition temperatures T_m for the order/disorder transition (melting) and T_f for the disorder/order (freezing) transition, as computed by molecular dynamics simulations, Monte Carlo simulations, and as reported by Ruscher.[22] The notation is $T \pm \delta T$, where T is the average over all simulation runs and δT is the standard deviation. The values for Ruscher's data are estimates extracted from diagrams in her article.[22]

	kT_f	kT_m
Molecular dynamics	0.96 ± 0.04	1.89 ± 0.01
Monte Carlo	0.97 ± 0.03	1.886 ± 0.006
Ruscher[22]	1.05	1.85

TABLE II. Final energies and τ values of quenched ideal gas systems as described in Fig. 3. The τ order metric measures the degree of order in the system, diverges for crystalline structures, and is zero for complete spatial randomness. The value of the τ order metric from Klatt *et al.*[23] is that for configurations from binomial point-processes (from Table 2 in the supplementary material); here, we added systematic errors discussed both in Ref. 23 and Sec. II. See Subsection 3 of the Appendix for simulation details.

	E/E_{BCC}	τ
MD quench	$1.008\,44 \pm 0.000\,02$	33 ± 1
MC quench	$1.008\,54 \pm 0.000\,03$	33 ± 1
Lloyd's algorithm	$1.008\,52 \pm 0.000\,03$	33 ± 1
Klatt *et al.*[23]	1.008 ± 0.001	32 ± 1
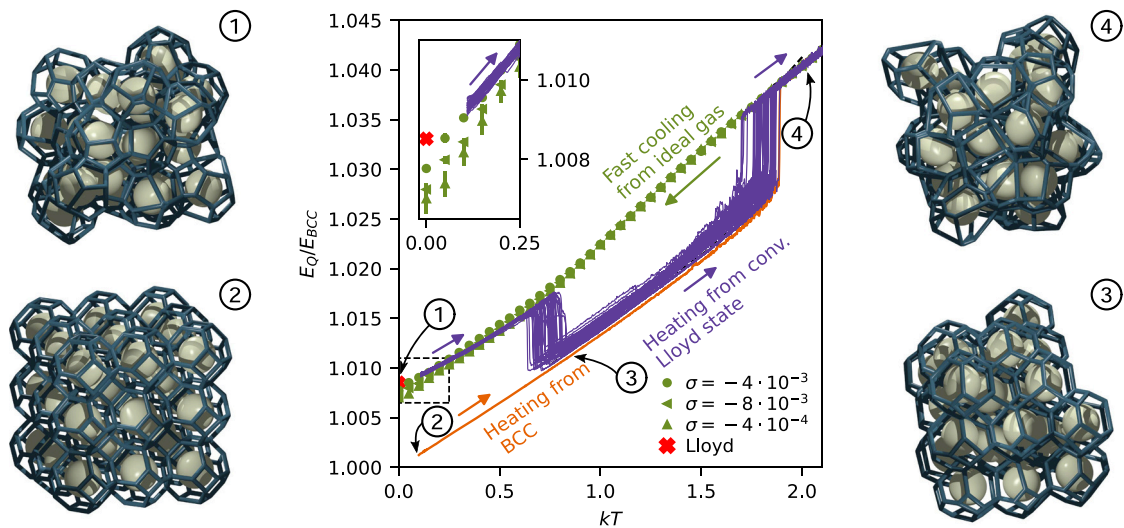
FIG. 4. Non-equilibrium cooling with a fast but finite cooling rate and slow equilibrium heating of the converged Lloyd states of Klatt *et al.*[23] The fast non-equilibrium cooling of a high-temperature ideal gas results in disordered structures very similar to the converged Lloyd states (dotted green curves). The dependence on the cooling rate σ is only weak for $|\sigma| > 4 \cdot 10^{-4} \varepsilon/\delta$ (see the inset). Upon cooling, the energy initially follows the same functional form as for a slow equilibrium cooling; however, it fails to show any sign of the ordering transition (which the slowly cooled systems undergo for $kT_{melt} \approx 0.96$). When, from small T, the converged Lloyd states are heated up slowly at $\sigma = 2.5 \times 10^{-4}$ (purple curves), they initially show at $kT \approx 0.74 \pm 0.05$ a transition to a (softened) BCC configuration, which then melts at a slightly lower phase transition temperature at $kT'_m \approx 1.80 \pm 0.04$. The orange curve represents the slow equilibrium melting transition starting from a low-temperature BCC phase. All data shown here is obtained by molecular dynamics simulations. See Subsection 3 of the Appendix for simulation details. On the left- and right-hand sides, we show the snapshots taken from MD simulations.

Lloyd states. If the cooling is sufficiently fast, the value of the cooling rate only has a minor effect on the final structure that is reached at $kT = 0$; the remaining minor differences in energy are visible in the inset of Fig. 4 and are significantly smaller than the difference between the converged Lloyd states ($E/N = 118.82 \pm 0.02$) and that of the BCC crystal ($E/N = 117.815$).

For the fast cooling rates, the majority of the system do not show a phase transition. At a cooling rate of $-4 \cdot 10^{-3}$, none of the 24 runs showed a phase transition; out of the 24 runs at a cooling rate of $-8 \cdot 10^{-3}$, only one underwent a phase transition, and three out of 24 runs showed a phase transition at a cooling rate of $-4 \cdot 10^{-4}$. (These runs are omitted in the data shown here.)

Finally, we have analyzed the slow quasi-static heating of a system that is prepared at $T = 0$ in converged Lloyd states. When heated slowly, the system energy gradually increases until a certain temperature, following the same (or a very similar) curve to the rapid cooling cycles, in reverse. At a certain temperature (the value of which varies, potentially due to finite size effects), the energy jumps down to almost the energy of a BCC crystal being melted to the same temperature. When heated further, the system behaves similar to that of the melting curve of a system that started from a BCC crystal. There are small remnant differences in the energy (the purple curves in Fig. 4 are slightly above the orange curve), and the eventual transition to a disordered structure occurs at a slightly lower temperature. We do not know the exact nature of these slight differences. The degree of residual randomness in these intermediate BCC-like states appears to facilitate a melting transition at a slightly lower temperature.

The "drop" to a BCC-like state can be avoided when a system prepared as a converged Lloyd state at $T = 0$ is quickly heated. At a heating rate of $\sigma \approx 9.3 \cdot 10^{-3}$, all out of 24 individual runs avoid the intermediate BCC-like state and follow the curve of a quickly cooled system up to the liquid state. With decreasing heating rates, the systems get more likely to fall back into the intermediate states: at a heating rate of $\sigma \approx 4.3 \cdot 10^{-3}$, 6 out of 24 runs return to the BCC-like state. This behavior while heating is analog to the freezing case: here too, the BCC ground state can be avoided if the system is cooled very quickly.

IV. CONCLUSION

We have studied the configuration of the many-particle system that is formed by the many-body interaction of the quantizer energy,[16,17,31] that is, of the Voronoi liquid.[21] We confirmed the freezing and melting transitions found by Ruscher, Baschnagel, and Farago[21] using both MD and MC simulations. A slow cooling in equilibrium leads to the formation of BCC crystallites, as expected, since the conjectured ground state (at $T = 0$) is the BCC lattice.

In contrast, a quench from high temperature states leads to disordered amorphous structures, more similar to the amorphous states found by Lloyd's algorithm.[23] A finite cooling rate results in final energies slightly below that of the final state of Lloyd's algorithm, but as we increase the cooling rate, the final energies increase. A quench at $T = 0$ leads to final states whose energies,

two-point statistics, and local multi-point statistics coincide within our statistical accuracy with those of the converged Lloyd states.

To explain both the similarities and differences between a fast MD quench and Lloyd's algorithm, we derive a limit in which a modified MD quench, where the mass of a particle is given by the volume of its cell, coincides with the iterations of Lloyd's algorithm.

Melting the amorphous converged Lloyd states, we find that the system remains on the amorphous branch for a finite range of temperatures (before the system returns to the crystalline branch), which agrees with the meta-stability of the converged Lloyd states.

In future work, MC simulations of the "QuanTizer problem" (i.e., Voronoi liquid) make it possible to determine the density of states (e.g., using the Wang–Landau algorithm[42]) to further study the intriguing energy landscape of this many-particle interaction.

Lloyd's algorithm is a gradient-descent minimization method tailored to the quantizer problem, in the following sense: The displacement of each point into the direction of the center of mass of its Voronoi cell corresponds to the direction of the negative gradient. Furthermore, the displacement into the center of mass of the Voronoi cell (rather than just in that direction) provides a "local optimum displacement" for the individual cell. The question arises naturally what final structures are obtained when applying other energy minimization methods such as the conjugate gradient-descent method, BFGS, or others. The preliminary results indicate that conjugate gradient methods, steepest descent as well as BFGS minimization methods as implemented in the GSL[43] seem to evolve random initial structures into amorphous structures that are very similar to the inherent structure found by Lloyd's algorithm. (Note that these algorithms were provided with the gradient direction from Lloyd's algorithm as a closed formula for the gradient of the energy functional is not available.) A quantitative statistical analysis needs to include a detailed analysis of the observed cases where the minimization methods get stuck in seemingly shallow local minima and is beyond the scope of this article.

Ultimately, the research presented in this article supports the search for disordered ground states and long-lived inherent structures that offer novel physical properties due to their isotropy (in contrast to their crystalline counter parts). A key question for experimental realizations is the role of long- and short-range interaction in such systems.

APPENDIX: ALGORITHMIC EQUIVALENCY, ADDITIONAL STRUCTURE METRICS, AND SIMULATION DETAILS

1. Lloyd's algorithm as a limit of an MD quench

We showed that a fast MD quench results in a structure similar to the converged Lloyd states. Here, we discuss the conditions under which an MD quench collapses to a "Lloyd quench." MD simulations compute the time evolution of particles, where each step advances time by an increment Δt; thus, the position of the ith particle at time t, given by $\mathbf{r}_i(t)$, is equivalent to $\mathbf{r}_i(n\Delta t) =: \mathbf{r}_{i,n}$.

Since Lloyd's algorithm is missing an intrinsic definition of a time scale, a Lloyd quench can only be compared to an MD quench on a step by step basis. The position of the ith particle at step n is denoted by $\mathbf{r}_{i,n}$. A single Lloyd iteration is then given by $\mathbf{r}_{i,n+1} = \mathbf{c}_{i,n}$, where $\mathbf{c}_{i,n}$ is the centroid of the Voronoi cell associated with the ith particle at step n.

The position of the ith particle after one MD step of time length Δt is given by $\mathbf{r}_{i,n+1} = \mathbf{r}_i(t + \Delta t)$, which can be approximated by its Taylor series,

$$\mathbf{r}_{i,n+1} = \mathbf{r}_{i,n} + \dot{\mathbf{r}}_{i,n}\Delta t + \frac{(\Delta t)^2}{2}\ddot{\mathbf{r}}_{i,n} + \text{higher orders}, \qquad (A1)$$

where a dot denotes the time derivative: $\dot{\mathbf{r}} = \frac{\partial}{\partial t}\mathbf{r}$. The force acting on particle i is given as $\ddot{\mathbf{r}}_i = \frac{\mathbf{F}_i}{m_i} = \gamma\frac{V_i}{m_i}(\mathbf{c}_i - \mathbf{r}_i)$. Substituting this into Eq. (A1) yields

$$\mathbf{r}_{i,n} = \left(1 - \frac{\gamma V_i}{m_i}\frac{(\Delta t)^2}{2}\right)\mathbf{r}_{i,n} + \left(\frac{\gamma V_i}{m_i}\frac{(\Delta t)^2}{2}\right)\mathbf{c}_{i,n} + \dot{\mathbf{r}}_{i,n},$$

where we neglect orders higher than the second derivative. For an MD step being equivalent to a Lloyd iteration, $\mathbf{r}_i(t + \Delta t) = \mathbf{c}_i$ must hold. Thus, the time step Δt must be chosen as

$$\Delta t = \sqrt{\frac{2}{\gamma}\frac{m_i}{V_i}}.$$

For this equation to hold, the masses of all particles must be set equal their volume before each simulation step. The temperatures are set to zero after each simulation step; this acts as a thermostat simulating a quench. In this limit, an MD step is equivalent to a Lloyd iteration.

On the one hand, this limit demonstrates similarities of Lloyd's algorithm and a quench for Voronoi tessellations with energies close to the ground state (with a sharp cell volume distribution). On the other hand, the analysis reveals subtle differences that may lead to a slightly different energies and (global) structures.

2. Local structure metrics

Structures can be locally characterized using the so-called Minkowski metrics.[24,36] These define several scalar, vectorial, and tensorial quantities measuring the shape of a convex body K such as a Voronoi cell. Here, we specifically employ the surface Minkwoski tensors $W_1^{0,s}$ describing the radial distribution of outer normal
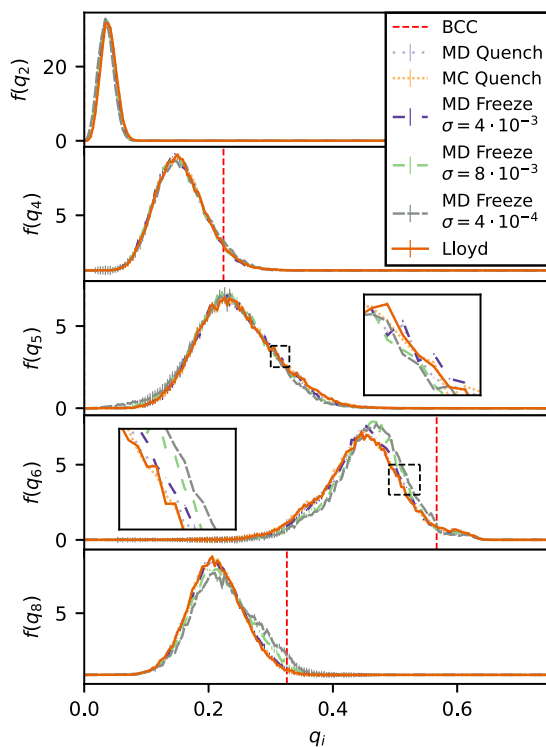
vectors of K.[23] It can be conveniently decomposed into spherical harmonics,

$$\rho_s^m(K) = \sqrt{\frac{4\pi}{2s+1}} \frac{\sum_k A_k Y_s^m(\mathbf{n}_k)}{\sum_k A_k},$$

where A_k are the surface areas of the faces of the body K and $\mathbf{n}_k$ are the outer normal vectors. From this tensor, rotational invariants can be constructed,

$$q_s(K) := \sum_{m=-s}^{s} |\rho_s^m(C)|^2.$$

These q_s describe the shape of a cell independent of its size and orientation and thus can be used as a shape metric. Here, we
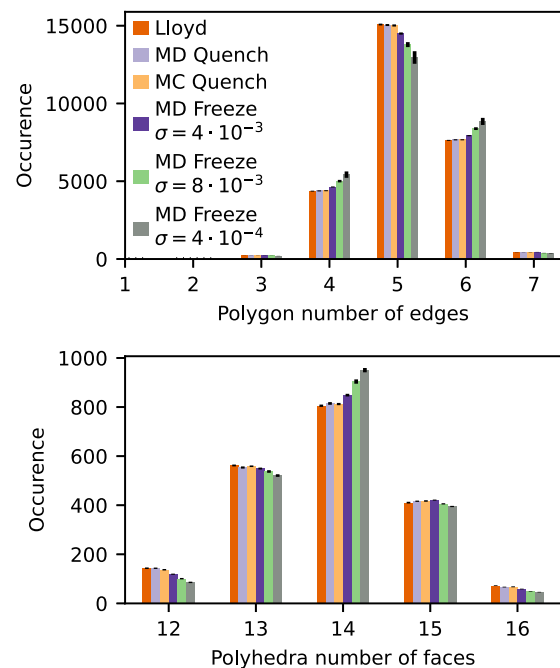
compute the quantities $q_{2,4,5,6,8}$ for each cell in a system and show their normalized distribution.

The distribution of the number of edges of faces as well as the number of faces of each cell in the Voronoi tessellation is presented as a further measurement of the local packing.

Our results are shown in Figs. 5 and 6. We present the shape metrics and Voronoi cell statistics for the final structures obtained from MC, MD, and Lloyd quenches, as well as fast cooling MD simulations. For each quench type, the distribution is averaged over 24 individual simulation runs. The data show good agreement within the statistical limits of the distributions of the MD, MC, and Lloyd quenches. These findings further support the equality of the final structures, as previously indicated by equal energies as well as τ values.

The distributions of the final structures obtained by quickly cooled systems, however, show significant differences compared to the quenched structures. A clear trend is visible: the higher the (absolute value of the) cooling rate, the higher the deviation from the inherent structure. This is visible in the Minkowski structure metrics, but even more in the Voronoi statistics. These results are in line with a similar trend in the final energies, which decrease—hinting toward more optimal structures—with increasing heating rates.

FIG. 5. Local order and structure measures of the final structure obtained by MD, MC, and Lloyd quenches, as well as fast freezing MD simulations. Shown are the rotational invariants $q_{2,4,5,6,8}$ of the face-normal Minkowski tensors. These robust and sensitive measures characterize the shape of single Voronoi cells and thus the local order and structure of the systems. The values of a BCC shaped cell is shown for reference. The data show good agreement of the final structures of MD, MC, and Lloyd quenches within statistical uncertainties, indicating that the final structures of the MD and MC quenches are identical to the ones of the Lloyd quench. The fast freezing MD simulations show good agreement in q_2 and q_4, however, increasing differences in q_5, q_6, and q_8 with increasing cooling rate, indicating a difference in the local order compared to the structures obtained by the quenches. These findings are in line with the decreasing energies of the final structures with increasing cooling rates.

FIG. 6. Cell and face order distributions of the Voronoi cells in the structures obtained by MD, MC, and Lloyd quenches as well as fast freezed MD simulations. Shown is the number of faces with n edges (top) and the number of cells with n faces in the Voronoi tessellation of the final structures. The data show good agreement within statistical limits of the MD, MC, and Lloyd quenches, where as the fast freezing MD runs show significant deviations increasing with the increasing cooling rate.

3. Simulation parameters

Quenches, Fig. 3, Table II: All initial configurations are binomial point-processes (ideal gases) with $N = 2000$ and $\rho = 1$. The structure factors, τ, and energy values of MC, MD, and Lloyd's algorithm runs are averaged over 24 individual runs. **MD**: The MD step size is chosen as $\Delta t = 0.005$, and the initial temperature is set to $kT = 2.1$. An initial set of 5000 MD steps are performed at $kT = 2.1$ to equilibrate the initial configuration, then the temperature is set to $kT = 0$, and the system is run for 6×10^5 MD steps. **MC**: Immediately after initialization, the temperature is set to $kT = 0$, and then, a total of 8.1×10^8 MC steps are run. The step size is adapted every 3×10^7 steps. **Lloyd's algorithm**: A total of 50 000 steps are run. While the τ value in Table II was taken from the supplementary material from Ref. 23, the structure factor shown in Fig. 3 was generated by us from the dataset 3D-FINAL-CONFIGURATION-DERIVED-FROM-BINOMIAL-PP-1.DAT provided by Klatt *et al.*[23] All structure factors are computed with a bin width of 0.25 and a cutoff of $k_{\max} = 25$.

MD melting/freezing, Fig. 1: 48 individual runs for each melting and freezing were run. **Melting** runs were initialized as BCC lattices, with each component of the velocities randomly drawn from a normal distribution to match a system temperature of $kT = 0.1$. The velocities are modified, so the center of mass of the system is at rest. The initial thermostat temperature is set to $kT = 0.1$. **Freezing** runs were initialized as ideal gas; thus, each position component is randomly chosen to uniformly cover the simulation box with random velocities matching an initial temperature of $kT = 2.1$ with the center of mass of the system at rest. For both melting and freezing runs, the thermostat is initialized with $Q = 20$, $s = 1$, and $\dot{s} = 1$, and the MD time step is chosen as $\Delta t = 0.001$. All systems ran a set of 5×10^5 initial relax steps to equilibrate the system and thermostat at the respective initial temperature. Then, 800 (melting)/840 (freezing) temperature steps, each with an increment of $\Delta kT = \pm 2.5 \times 10^{-3}$ are run, resulting in a cooling rate of $\sigma = \frac{2.5 \times 10^{-3} \varepsilon}{10\,000 \cdot 0.001 \delta} = 2.5 \times 10^{-4} \varepsilon/\delta$. For each temperature, 10 000 MD relax steps are run, followed by a measurement phase comprising 1500 MD steps where every 25 steps the energy and structure factor is measured. For the isotherms, four runs at each temperature for each freezing and melting systems are run. The particles in melting systems are initialized on a BCC lattice with velocities drawn from a normal distribution to match their respective temperature with a resting center of mass. The initial positions of the particles in the isothermal freezing systems are uniformly distributed over the simulation box with velocities drawn from a normal distribution to match their respective temperature (ideal gas). Both melting and freezing isothermal systems are then run for $8.5 \cdot 10^5$ steps with a time step of $\Delta t = 0.001$. The thermostat is initialized with $Q = 20$, $s = 1$, and $\dot{s} = 1$. The mean energies are averaged over the last $1.7 \cdot 10^5$ steps.

MC melting/freezing, Fig. 2: Since MD simulations outperforms the MC code by far, we used MD simulations to generate initial configurations very close to the phase transition region and then continued these runs with the MC code. The parameters for the MD runs are identical to the ones mentioned above with these exceptions: no initial relax steps are performed, and the positions of the particles in the systems initialized as ideal gas are identical across all systems; however, they do have randomly chosen velocities. In total, 48 runs were given different initial thermostat settings, where two runs shared one of the combinations between $Q \in \{60, 50, 40, 30, 20, 10\}$ and $(s, \dot{s}) \in \{(0.2, 0), (1, 0.5), (1.5, 1), (4, 3)\}$. Only 500 measure steps were performed at each temperature. The initial configurations for the MC runs were taken after the relax phase at $kT = 1.87$ (melting) and $kT = 1.02$ (freezing). A total of 213 (melting)/320 (freezing) temperature increments each with $\Delta kT = \pm 4.7 \times 10^{-4}$ were simulated. At each temperature, a total of 6×10^6 MC relax steps were performed, followed by 3.8×10^4 measurement steps, with 2000 MC steps in between individual measurements.

Melting of the converged Lloyd states, Fig. 4: The 48 individual MD simulations are initialized with converged Lloyd states; thus, $N = 2000$ and $\rho = 1$. Random temperatures are assigned to match an initial temperature $kT = 0.05$ with the center of mass of the system at rest. 2×10^5 initial relax steps are performed. The thermostat is initialized with $Q = 20$ and $s = \dot{s} = 1$. The MD time step is chosen as $\Delta t = 0.001$. A total of 840 temperature increments with $\Delta kT = 2.5 \times 10^{-3}$ are computed. Each temperature has 10 000 relax steps and 1500 measurements steps with 25 steps in between individual measurements. All data represented by symbols are MD simulations initialized as ideal gas, with random velocities matching their initial temperatures, with the center of mass at rest. All ran a set of initial relax steps of 20 000 MD steps and had 2400 relax and 100 measurement MD steps for each temperature increment, with 25 MD steps between each measurement. The olive circles ("$\sigma = -4 \cdot 10^{-3}$") are combined data from 10 sets, each set consisting of 24 averaged runs, starting at different initial temperatures $kT = (2.5, 2.55, 2.6, 2.65, 2.7, 2.75, 2.8, 2.85, 2.9, 2.95)$. Each set had six temperature increments of $\Delta kT = -0.5$. Combining the interlaced sets yields the curve as shown. The same was done for the olive triangles ("$\sigma = -8 \cdot 10^{-3}$"); however, only two sets (each averaging over 24 runs) started at $kT = (2.1, 2.15)$ and had 22 temperature increments with $\Delta kT = -0.1$. The olive pyramids ("$\sigma = -4 \cdot 10^{-4}$") are a single set averaging over 24 runs starting at $kT = 2.1$ with 43 temperature increments with $\Delta kT = -0.05$.

DATA AVAILABILITY

The data that support the findings of this study and the code used to generate them are available from the corresponding author upon reasonable request.

REFERENCES

[1] D. Weaire and R. Phelan, Philos. Mag. Lett. **69**, 107 (1994).
[2] D. Weaire, *The Kelvin Problem* (Taylor & Francis, London, 1997).
[3] T. Hales, Ann. Math. **162**, 1065 (2005).
[4] S. Torquato, G. Zhang, and F. H. Stillinger, Phys. Rev. X **5**, 021020 (2015).
[5] G. Zhang, F. H. Stillinger, and S. Torquato, Phys. Rev. E **92**, 022119 (2015).
[6] G. Zhang, F. H. Stillinger, and S. Torquato, Phys. Rev. E **92**, 022120 (2015).
[7] G. Zhang, F. H. Stillinger, and S. Torquato, Soft Matter **13**, 6197 (2017).
[8] S. Ghosh and J. L. Lebowitz, Commun. Math. Phys. **363**, 97 (2018).
[9] G. Zhang, F. H. Stillinger, and S. Torquato, Sci. Rep. **6**, 36963 (2016).
[10] D. Bi, J. H. Lopez, J. M. Schwarz, and M. L. Manning, Nat. Phys. **11**, 1074 (2015).
[11] M. Merkel and M. L. Manning, New J. Phys. **20**, 022002 (2018).
[12] A. Gersho, IEEE Trans. Inf. Theory **25**, 373 (1979).
[13] S. Lloyd, IEEE Trans. Inf. Theory **28**, 129 (1982).

[14] J. Conway and N. J. A. Sloane, *Sphere Packings, Lattices and Groups*, Grundlehren Der Mathematischen Wissenschaften, 3rd ed. (Springer-Verlag, New York, 1999).

[15] A. Okabe, B. Boots, K. Sugihara, and S. N. Chiu, *Spatial Tessellations: Concepts and Applications of Voronoi Diagrams*, 2nd ed. (Wiley, Chichester, NY, 2000).

[16] Q. Du and D. Wang, Comput. Math. Appl. **49**, 1355 (2005).

[17] Q. Du, M. Gunzburger, and L. Ju, Numer. Math. Theory, Methods Appl. **3**, 119 (2010).

[18] R. Gray, IEEE ASSP Mag. **1**, 4 (1984).

[19] L. Lu, F. Sun, H. Pan, and W. Wang, IEEE Trans Visualization Comput. Graphics **18**, 1880 (2012).

[20] S. Torquato, Phys. Rev. E **82**, 056109 (2010).

[21] C. Ruscher, J. Baschnagel, and J. Farago, Europhys. Lett. **112**, 66003 (2015).

[22] C. Ruscher, "The Voronoi liquid: A new model to probe the glass transition," Ph.D. thesis, École Doctorale Physique et Chimie-Physique, 2017.

[23] M. A. Klatt, J. Lovrić, D. Chen, S. C. Kapfer, F. M. Schaller, P. W. A. Schönhöfer, B. S. Gardiner, A.-S. Smith, G. E. Schröder-Turk, and S. Torquato, Nat. Commun. **10**, 811 (2019).

[24] G. E. Schröder-Turk, W. Mickel, S. C. Kapfer, M. A. Klatt, F. M. Schaller, M. J. F. Hoffmann, N. Kleppmann, P. Armstrong, A. Inayat, D. Hug, M. Reichelsdorfer, W. Peukert, W. Schwieger, and K. Mecke, Adv. Mater. **23**, 2535 (2011).

[25] W. Thomson, Acta Math. **11**, 121 (1887).

[26] C. Ruscher, J. Baschnagel, and J. Farago, Phys. Rev. E **97**, 032132 (2018).

[27] C. Ruscher, A. N. Semenov, J. Baschnagel, and J. Farago, J. Chem. Phys. **146**, 144502 (2017).

[28] C. Ruscher, S. Ciarella, C. Luo, L. M. C. Janssen, J. Farago, and J. Baschnagel, J. Phys.: Condens. Matter **33**, 064001 (2020).

[29] S. Torquato and F. H. Stillinger, Phys. Rev. E **68**, 041113 (2003).

[30] S. Ghosh and J. L. Lebowitz, Indian J. Pure Appl. Math. **48**, 609 (2017).

[31] S. Torquato, Phys. Rep. **745**, 1 (2018).

[32] S. Atkinson, G. Zhang, A. B. Hopkins, and S. Torquato, Phys. Rev. E **94**, 012902 (2016).

[33] N. Metropolis, A. W. Rosenbluth, M. N. Rosenbluth, A. H. Teller, and E. Teller, J. Chem. Phys. **21**, 1087 (1953).

[34] B. Krüger and J. F. Knauf, Mocasinns, 2016.

[35] B. Krüger, "Simulating triangulations: Graphs, manifolds and (quantum) space-time," Ph.D. thesis, FAU University Press, 2016.

[36] G. E. Schröder-Turk, W. Mickel, S. C. Kapfer, F. M. Schaller, B. Breidenbach, D. Hug, and K. Mecke, New J. Phys. **15**, 083028 (2013).

[37] C. Rycroft, Chaos **19**, 041111 (2009).

[38] S. Nosé, Mol. Phys. **100**, 191 (1983).

[39] G. J. Martyna, D. J. Tobias, and M. L. Klein, J. Chem. Phys. **101**, 4177 (1994).

[40] J.-P. Hansen and I. R. McDonald, *Theory of Simple Liquids: With Applications to Soft Matter*, 4th ed. (Academic Press, Amsterdam, Boston, 2013).

[41] We estimate H by fitting a Gaussian-shaped density to the peak ($6 < k < 7.5$) and by extrapolating a second-degree polynomial $ax^2 + c$ to the origin ($k_{min} < k < 4$). The precise value of H depends on the fit range and functional form.

[42] F. Wang and D. P. Landau, Phys. Rev. Lett. **86**, 2050 (2001).

[43] See https://www.gnu.org/software/gsl/ for details on the implementation of the minimization methods and further information.

Structure identification in soft materials using microscopy images

The first two chapters of this thesis address the structure formation process of cellular media and partitions of space. This chapter forms the second part of the thesis and will present a method to identify structures, called direct template correlative matching (DTC). This method aims to identify the geometrically complex partitions of space, triply periodic minimal surfaces (TPMS), specifically based on transmission electron microscope (TEM) images. This is a challenging task: a two dimensional projection, as available from TEM images, condenses the spatial information of a three dimensional structure into a planar image. Naturally, information is lost during that process. A further layer of complexity is added when parameters of the projection process, such as the viewing angle onto the three dimensional structure, are unknown. DTC was first introduced by Landh [1996] and Deng and Mieczkowski [1998] and found several applications since then [Deng et al., 1999, Almsherqi et al., 2005, 2006].

In this chapter, based on our publication [Hain et al., 2021], we introduce a new open-source software tool, SPIRE, re-implementing and expanding DTC for several reasons. The original software library, first introduced in [Deng and Mieczkowski, 1998] only allowed the generation of entire libraries of projections and thus no interactive matching process and is not accessible for the public anymore. With SPIRE, we developed a software tool, with a focus on an interactive matching process. A screenshot of the user interface illustrating this is shown in fig. (4.1). The influence of structural parameters on the projection can be seen in almost real time, promoting an intuitive

approach to understand DTC. We also added a larger variety of accessible structural parameters, allowing finer control of the projection and new features, such as structural measurements. This latter feature especially provides valuable insight on possible functions of structures. SPIRE is designed to be capable of creating large data sets to train artificial neural networks (ANN) to automate the matching process in the future.
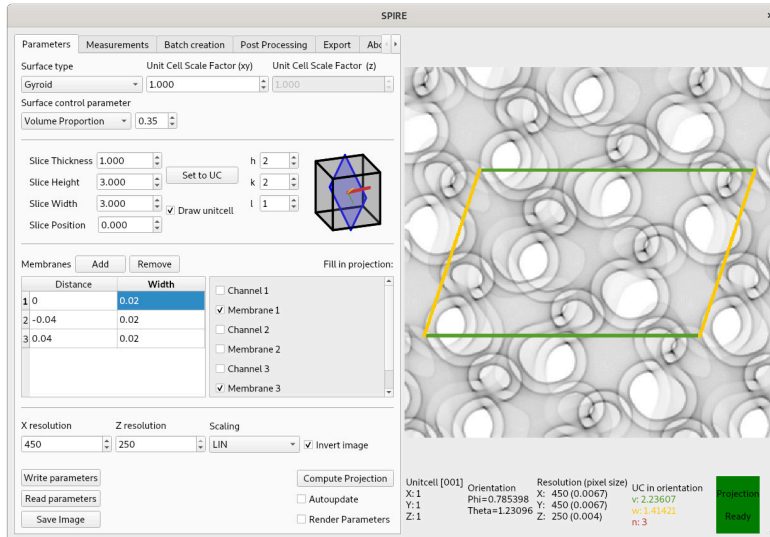
Figure 4.1: The main view of the graphical user interface of SPIRE. All parameters controlling the projection are accessible and the projection is shown almost in real time.

We start by giving a technical introduction to minimal surfaces and TPMSs and their mathematical description, before highlighting their occurrence and significance in biological systems.

4.1 Triply periodic minimal surfaces

To understand minimal surfaces, the term curvature needs to be introduced first. An intuitive explanation was provided in chapter 1, here, we will follow a more quantitative, but yet intuitive approach by Andersson et al. [1988]. The curvature κ of a curve at a point p is the inverse of the radius of the osculating circle which fits the the curve in p most tightly, as shown in fig. (4.2). For a surface, there are infinitely many curvatures along the lines radiating from a point: given the normal vector $\mathbf{n}_P$ to the surface at a point p, the intersection of a plane containing $\mathbf{n}_P$ with the surface yields a curve, with a curvature κ, as illustrated in fig. (4.2). For continuous surfaces, rotating this plane around $\mathbf{n}_P$ then continuously yields different curvatures. The minimum and maximum values of all these curvatures are called the principle curvature κ_1 and κ_2 of the surface. The mean curvature is then $H = \frac{1}{2}(\kappa_1 + \kappa_2)$, where as the Gaussian curvature is defined as $K = \kappa_1 \cdot \kappa_2$. Minimal surfaces are defined by a vanishing mean curvature at each point [Grosse-Brauckmann, 2012, Klinowski et al., 1996b]. This is equivalent to the surfaces minimising their surface area given a fixed boundary [Nitsche, 2011]. As addressed
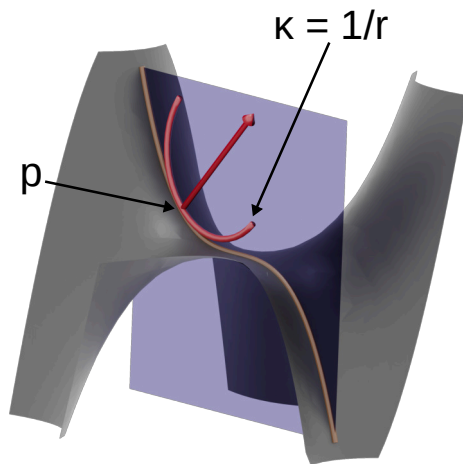
Figure 4.2: The definition of principal curvatures κ of a surface. Shown is a minimal surface, called monkey saddle given as $z = x^3 - 3xy^2$ and a curve created by the intersection of the surface with a plane containing the normal vector onto the surface in a point p. The curve has a curvature of $\kappa = \frac{1}{r}$ in p, with r being the radius of the circle with the best fit to the curve in p. The curvature is a smooth function by rotating the plane containing the normal vector around the latter. The minimum and maximum values are the principal curvatures κ_1 and κ_2 of the surface in p.

in the introduction a familiar example are soap films suspended from wire frames. A close relative to minimal surfaces are constant mean-curvature (CMC) surfaces [Grosse-Brauckmann, 2012, Karcher, 1989]. These have a constant mean curvature across the entire surface, however, the latter is not 0. This is equivalent to minimising the area of a surface given a fixed boundary and volume. Natural examples are soap bubbles: they enclose a fixed amount of air and due to surface tension minimise their surface area.

This chapter focuses on a special class of minimal surfaces with negative Gaussian curvature: the TPMS [Klinowski et al., 1996b], as well as some of their CMC counterparts. The latter can be seen as topologically and symmetrically identical, but geometrically deformed surfaces at a distance to the original TPMS [Anderson et al., 1990, Grosse-Brauckmann, 2012, Karcher, 1989, Han and Che, 2018].

One characteristic property of TPMS (and of their corresponding companions [Grosse-Brauckmann, 1997]) is that they are periodic in each spatial dimension, i.e. they are invariant under a translation along the coordinate axes [Grosse-Brauckmann, 2012]. The first TPMS were studied by Schwarz [1890] and Neovius [1883], who found the primitive (P) and diamond (D) by solving Plateau's problem for suitable fundamental, asymmetrical patches with fixed boundaries. As discussed in the context of tilings in the introduction, repeatedly applying appropriate symmetries on the fundamental patch then yields infinite, periodic, highly symmetric minimal surfaces. The boundaries of both P and D surfaces are straight lines or have mirror planes. The symmetries of the surfaces are described using crystallographic space groups [Hahn, 2005]. For the P surface it is (SG229) and for the D surface $Pn\bar{3}m$ (SG224) [Han and Che, 2018]. Another important surface, the Gyroid (G) surface with the space group $Ia\bar{3}d$, was later found by Schoen [1970]. In contrast to the P and D surfaces, the latter is chiral and does not contain straight lines or mirror planes [Grosse-Brauckmann, 1997, Han and Che, 2018]. Visualisations of the surfaces and their medial skeletons are shown in fig. (4.3). An

(a) Primitive (P)   **(b)** Diamond (D)   **(c)** Gyroid (G)
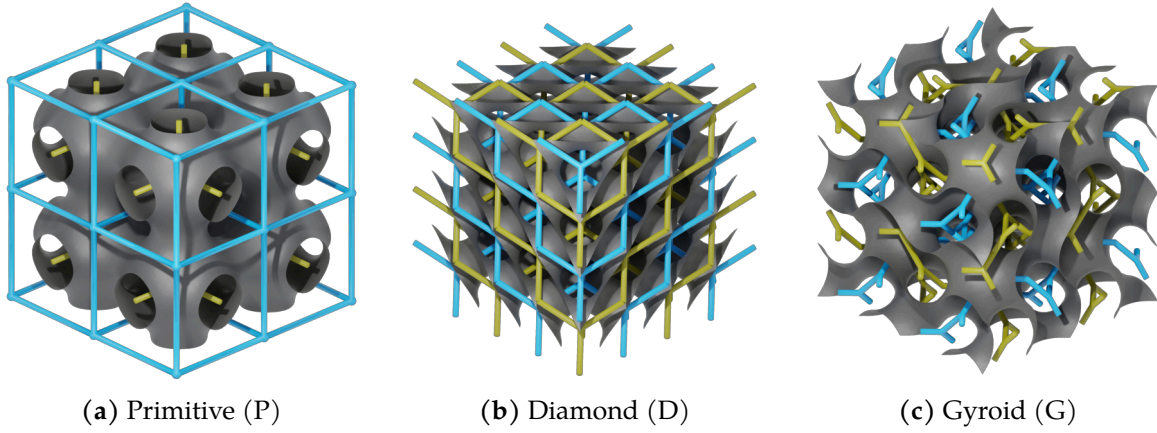
Figure 4.3: Three common triply periodic minimal surfaces (TPMS) with their corresponding medial skeleton. TPMS are minimal surfaces, i.e. surfaces with zero mean curvature everywhere and a negative Gaussian curvature. See main text for details. These three TPMS divide the space into two intertwined, open but disconnected subvolumes. The medial skeleton of the latter is often used to describe the topology and structure of the channel.

exact parameterisation of these three surfaces is given by the Weierstrass representation [Gandy et al., 1999, Gandy and Klinowski, 2000a,b]. This is a set of three complex integrals providing a way to compute the surfaces in Cartesian coordinates [Andersson et al., 1988, Hyde et al., 1996, Nitsche, 2011]. A more accessible description of TPMS is the so-called nodal representation [Klinowski et al., 1996b, Gandy et al., 2001]. von Schnering and Nesper [1991] developed the latter based on a Fourier expansion of the structure factor of a structure. Using only a few terms of the Fourier series yields an approximation of these surfaces. For the P, D and G surface these so-called nodal representations read

$$
\begin{aligned}
F_P(x, y, z) &= \cos(X) + \cos(Y) + \cos(Z) \\
F_D(x, y, z) &= \cos(X)\cos(Y)\cos(Z) - \sin(X)\sin(Y)\sin(Z) \\
F_G(x, y, z) &= \sin(X)\cos(Y) + \sin(Y)\cos(Z) + \cos(X)\sin(Z)
\end{aligned}
$$

where $X = \frac{2\pi}{a}$ with a being the periodicity of the surface in each spatial dimension. For $F(x, y, z) = 0$ this implicit formula describes a surface which approximates the minimal surface with a high accuracy [Gandy et al., 2001], where as parameters $F(x, y, z) = c \neq 0$ yield approximations of symmetrically and topologically identical CMC companions of the TPMS for small enough values c. Following the original DTC tool by Deng and Mieczkowski [1998], SPIRE uses the nodal representation to compute voxelised TPMS or CMC companions thereof [Hain et al., 2021].

TPMS separate space into two separated, intertwined but completely open channels [Andersson et al., 1984, Feng et al., 2019, Schröder-Turk et al., 2007, 2006, Schröder

et al., 2004, 2003]. In biological contexts the term bicontinuous phases is used frequently, referring to the presence of two infinite channels. Whereas the two channels of the P and D surface are identical, the two channels of the Gyroid are identical down to an inversion. Here the CMC companions play an important role, since they separate two channels of different volumes, see fig. (4.4). However, also TPMS, such as the I-WF surface exists, which separate two non-identical channels of different volumes [Hyde et al., 1996]. A new feature introduced in SPIRE is the computation of the volumes of the channels of the three dimensional structure, which projection is matched to a TEM image. We refer to our publication [Hain et al., 2021] for more details. The geometry

(a)   (b)   (c)
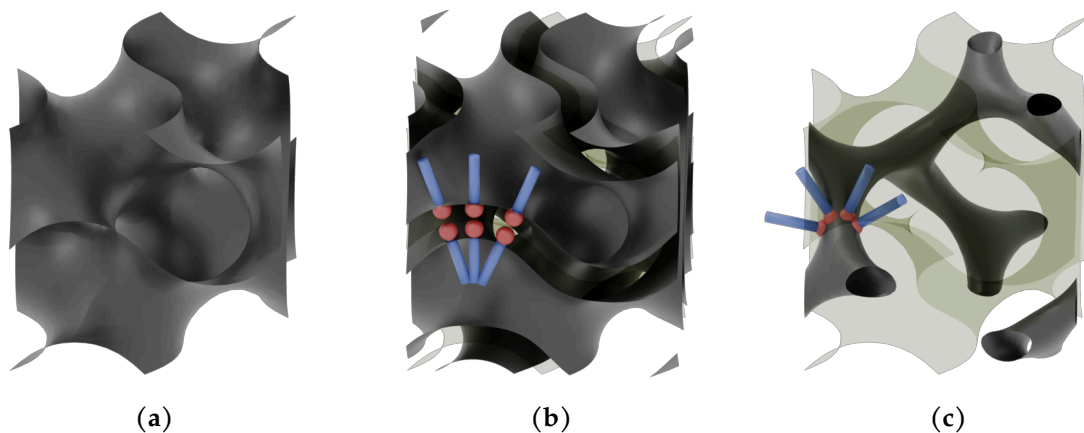
Figure 4.4: Constant mean curvature companions of the Gyroid surface. (a) A unit cell of the Gyroid minimal surface (b) Two CMC companion surfaces of the Gyroid, centered around the minimal surface Gyroid (indicated as transparent surface). The structure has two continuous channels of equal volumes. These can model, for example, a lipid bi-layer membrane with a finite thickness or polymer melts in solution, where the head group (red spheres) or the minority part of the polymer is in-between the two surfaces. (c) A single CMC surface separating two channels of different volumes. These structures are found e.g. in polymer melts or protein based structures with one solid channel, filled by protein or the minority part of the polymers, and one larger volume occupied by a solvent like water or the majority part of the polymer. These solid channels are follow the medial skeleton of the structures.

and structure of the surface and its channels is often described by the medial skeleton of their channels. This is a network of rods placed in the center of the channels. These networks are often relevant, since they are self-assembled by for example polymers, as we will address further below.

The skeleton of the D surface is the atomic structure of a diamond, i.e. has 4-connected vertices, where as the skeleton of the P surface consists of 6-connected vertices placed on a simple cubic lattice [Han and Che, 2018, Cui et al., 2020]. The skeleton of the Gyroid is the srs net [O'Keeffe et al., 2008], a chiral network without straight lines based on the atomic structure of $SrSi_2$ [Pringle, 1972].

Some of the fundamental minimal surfaces are connected by the Bonnet trans-

formation. The latter transforms the D and G surface continuously without changing the curvature of the surface. This is a significant result since it helped identifying the coexistence of these structures in lipid-water systems [Andersson et al., 1988, Hyde et al., 1984].

4.2   Occurrence and significance of TPMS in natural and artificial systems

Self-assembled complex bicontinuous structures occur often in natural and artificial systems. The intriguing shapes have long been of interest and were eventually identified as one of three fundamental TPMS, the Gyroid, Primitive and Diamond surface. As
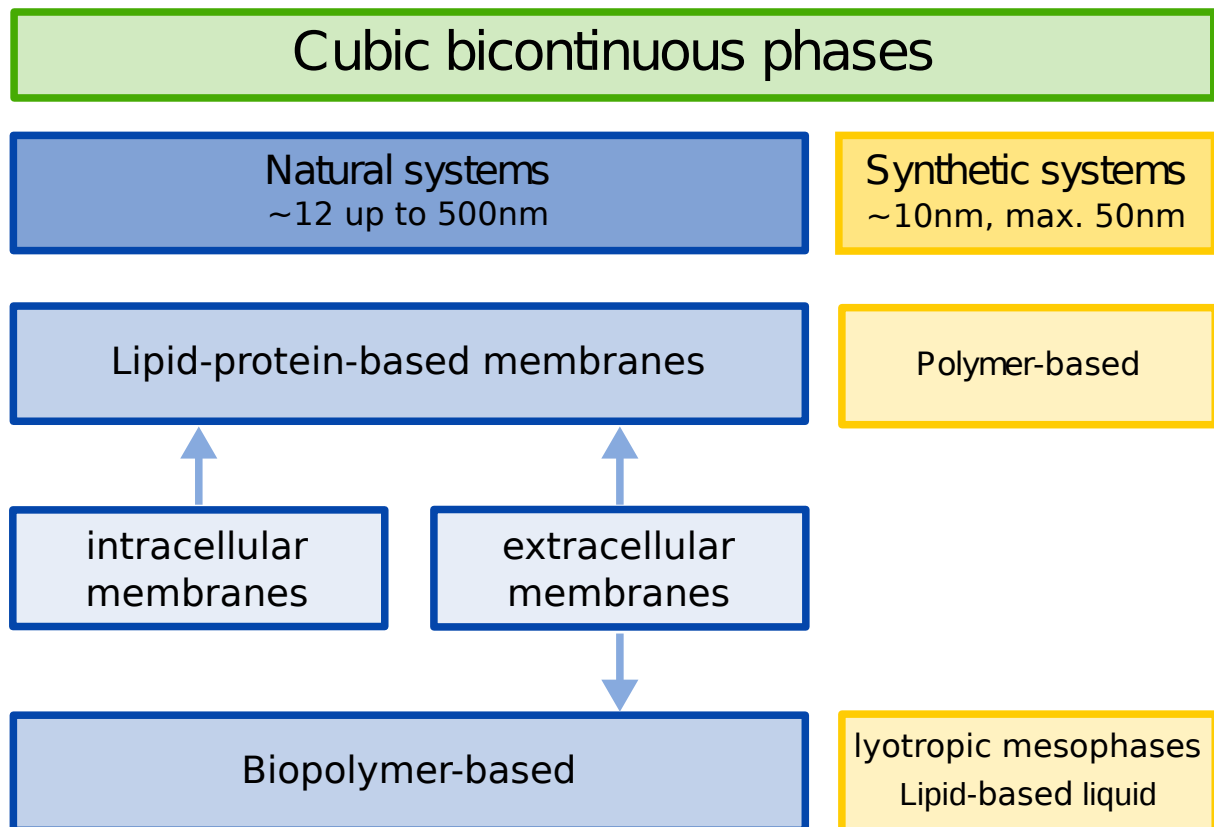
Figure 4.5: A selection of synthetic and natural systems forming cubic phases. The most important difference between synthetic and artificial systems are the length scales of the assembled structures, as indicated with in the figure. The length scales play an important role in the choice of method to analyse the morphology of the structures. For references see the main text.

fig. (4.5) suggests cubic, bicontinuous phases, i.e. TPMSs or CMCs, can be differentiated between naturally occurring or synthetic structures. There are two main differences between artificial and synthetic (membrane)systems. First, unlike artificial systems, natural occurring membrane structures are not purely built from lipids, but include

more complex molecules like proteins, which influence their self-organisation [Han and Che, 2018, Cui et al., 2020, Mezzenga et al., 2019, Hyde et al., 1996]. Second, the typical unit cell sizes differ substantially. Where as lyotropic liquid crystals are only of a few nanometers in size, natural membrane structures can be as large as several hundreds nanometers [Cui et al., 2020]. This difference in size is not only relevant for the functionality of the structures, but also for the analysis and identification of the latter.

Notable synthetic systems include, but are not limited to, polymer self-assemblies [Bates, 2005, Meuler et al., 2009, Stefik et al., 2015], both as melt and in solution, and lyotropic liquid crystals, such as a lipid/water systems [Hyde et al., 1996, Mezzenga et al., 2019]. Naturally occurring systems may be grouped into intracellular and extracellular membranes.

The driving force of both synthetic and natural lipidic, as well as biopolymeric self-assembly is similar to the already addressed polymer melts: the reduction of unfavourable contacts of the immiscible entities, e.g. polar and fatty or hydrophilic and hydrophobic components [Chandler, 2005]. In a lipid/water system the polar head groups of the lipids aggregate to avoid water contacts, where as the apolar tails reach into the water phase. Depending on the type of lipid and conditions in the system, different structures, including lamellar phases, inverse hexagonal phases, inverse micellar and bicontinuous cubic phases, emerge [Hyde, 2002, Mezzenga et al., 2019]. There are two possibilities to form a bicontinuous structure: (1) a bi-layer membrane, where the heads of the lipids aggregate on both sides of a TPMS (see fig. (4.4b)), separating two channels filled with solvent or (2) a structure with one CMC surface, where one channel is filled solid with the biopolymer (see fig. (4.4c)). Polymers in solution behave analogously, where the minority block of the chain is equivalent to the head group, where as in melts the membrane or solid assembles in a matrix made up by the majority part of the polymer molecule.

Bicontinuous cubic phases with a network-like structure in soft matter systems has been reported by Luzzati et al. [1968]. The authors identified these phases in lipid/water systems using X-ray diffraction. The proposed structure is described as two interwoven but disconnected networks of three-connected rods on a body-centered cubic lattice. This network can be thought of a CMC companion of a TPMS, where one channel is of smaller volume than the other and filled with the head groups of the lipids, where as the other channel is filled with water into which the tails of the lipid extend (see fig. (4.4c)). The size of the unit cell of the lattice varies on the specific lipid, but in all cases is reported to be less than $10\,nm$. Scriven [1976] proposed that bicontinuous minimal surfaces, partitioning space into two continuous subvolumes, called channels,

can occur in fluids such as micellar solutions, lyotropic crystals or colloid structures. Here the two channels can have different volumes with different compositions of matter and as such need to be described using CMC rather than TPMS. Lindblom et al. [1979] report lipid bi-layer membranes, continuous in all three spatial directions, and Larsson et al. [1980] proposed that these membranes take the shape of TPMS as described by Schoen [1970]. Longley and McIntosh [1983] and Larsson [1983] report two cubic phases with a primitive and a body-centered lattice, where bi-layer membranes in the shape of minimal surfaces separate two water-filled channels. Hyde et al. [1984] presents proof that the membranes with a body-centered lattice have the shape of the Gyroid surface. These cubic phases are also found in self-assembled nanoparticles, then called cubosomes [Garg et al., 2007]. Their internal structure provides them with unique properties, applicable in e.g. drug delivery.

Much work since then has been devoted to further study minimal surfaces in lipid systems and their significance, which are summarised in a number of reviews and articles [Larsson, 1989, Larsson and Tiberg, 2005, Hyde et al., 1996, Larsson, 1986, Luzzati, 1997, Cui et al., 2020, Landh, 1996, Mezzenga et al., 2005, 2019]. The P, D and G surfaces have been found to be the principal minimal surfaces of the bicontinuous surfaces found in lipid/water systems [Larsson and Tiberg, 2005]. Differential geometry has been established as the preferred method to handle not only the geometry and description of cubic phases, but also the connection between the mathematical minimal surfaces and their biological features [Andersson et al., 1984, 1988, Hyde et al., 1996].

Bicontinuous phases are also assembled in synthetic polymer systems, either as melt or in solution. Thomas et al. [1986] identified a cubic phase in a star block co-polymer melt. Here, one block of the polymers formed a bicontinuous network of rods (see fig. (4.4c)) with the structure of a double diamond cubic lattice. The structure was recognised using a combination of small-angle X-ray scattering (SAXS) methods and direct TEM imaging. A double diamond network structure was also found in a system of copolymers in solution by Hasegawa et al. [1987]. A finite thickness Gyroid membrane (see fig. (4.4b)) was found in diblock copolymer melts by Hajduk et al. [1994] and were identified using SAXS methods and comparing TEM images with computer generated images. Unit cell sizes between 35 and 50 nm are suggested. Further Gyroid surfaces were found in experiments and theory in ABC triblock copolymers by Matsushita et al. [1998]. Fischer et al. [2014] found a new tricontinous phase in ABC star polymers with an extended core. A number of reviews about network like phases and bicontinuous phases in copolymer systems exists [Bates, 2005, Meuler et al., 2009, Stefik et al., 2015].

As already addressed in fig. (4.5), naturally occurring bicontinuous phases can be grouped into biopolymer and lipid-protein based structures.

Biopolymer based, solid bicontinuous structures include for example the skeleton of echinoderms [Donnay and Pawson, 1969]. A Gyroid structure is reported in the wing scales of the butterfly (*Callophrys rubi*), where one of the channels is filled solid with chitin [Saranathan et al., 2010, Schröder-Turk et al., 2011b]. This structure acts as a photonic crystal providing green color. A similar example is provided by Wilts et al. [2012a,b], where a single diamond structure is found in a diamond weevil (*Entimus imperialis*).

Lipid based bicontinuous liquid-crystalline structures can be found for example in milk: Salentinig et al. [2015] analysed the digestion of breast milk, an oil-in-water emulsion, by human infants. The authors found Im3m-type bicontinuous phases formed inside the oil droplets. This structure formation is reported to be linked with the digestion process of breast milk. Pham et al. [2020] report the same cubic bicontinuous phases in goat and bovine milk, however, at different stages of the digestion process.

An example for intracellular membranes which has been of interest for some time now are the prolamellar bodies (PLB) of plant etioplasts. These structures are at the center of this chapter's publication [Hain et al., 2021]. Latest research suggest that PLBs act as an efficient lipid storage for the transition to chloroplasts [Armarego-Marriott et al., 2019, Pipitone et al., 2021]. The structure of PLBs has been long debated: Gunning [1965] found a hyperbolic membrane structure in PLBs which was identified to be of the p-type. Ikeda [1968], however, report the structure to have four-connected vertices, contradicting previous observations. With further structures proposed [Gunning, 2001, Menke, 1963, Landh, 1996], the exact geometric shape of the surface is still unknown. An open question, which is addressed using SPIRE in [Hain et al., 2021].

Further bicontinuous membrane structures in cells and cell compartments have been reported [Gunning, 1965, Deng and Mieczkowski, 1998, Deng et al., 1999, Almsherqi et al., 2006, 2009, Mezzenga et al., 2019, Foelix et al., 1987]. Apart from single bi-layer membranes, structures with up to 12 bi-layer membranes were found (reviewed in [Almsherqi et al., 2012]). Several reviews summarise occurrences and functions of bicontinuous membrane structures [Hyde et al., 1996, Almsherqi et al., 2009, Mezzenga et al., 2019]. Functions include for example transport and controlled release of nutrients or control structural properties. For many of these cubic phases, however, the functions are elusive.

Nature's ability to build functional structures on large length scales (compare membranes found in amoeba with unit cell sizes around $200\,\text{nm}$ to synthetic lipid or polymer systems with $\approx 5\,\text{nm}$ lattice parameters) is unparalleled by artificial bottom-up assemblies. Studying natural structures in order to mimic their formation processes

provides blueprints for a powerful tool to construct materials [Han and Che, 2018]. An important step of these investigations is of course the identification of the assembled structures. In the presented examples, essentially three methods were used for that purpose: X-ray scattering, especially SAXS, electron tomography or direct imaging using transmission (TEM) or scanning electron microscopy (SEM) [Weiner et al., 2021]. SPIRE is designed to identify structures based on images obtained by microscopy.

SAXS methods provide scattering intensities which allow the identification of the symmetries, i.e. the crystallographic space group, of structures with length scales from 1 to 100 nm [Willis and Carlile, 2017, Impéror-Clerc, 2012]. The exact microstructure determination is not straight forward and requires considerable effort [Hajduk et al., 1994, Impéror-Clerc, 2012] since many structures share the same space group.

3D electron microscopy has been used to reconstruct three dimensional structures, see e.g. [Kowalewska et al., 2016, 2019] and allows a direct visualisation of the three dimensional structure. However, these methods are very time and money-consuming and thus limited in their application [Neumüller, 2018].

Next to the just introduced methods of structure identification, DTC has established itself as a reliable and efficient method to identify cubic phases on all length scales. (Electron)Microscopy allows direct visualisation of structures, however, only provides a planar projection or cross section of the structure, making the identification of the underlying three dimensional structure challenging. This is emphasised by several structures, such as the PLBs, being mis-identified in the past. The standard method of identifying structures is to compare electron microscopy images with computer generated projections of possible candidate structures.

Although this method has been used to identify structures before (see e.g. [Thomas et al., 1986, Hasegawa et al., 1987] and references above), Deng and Mieczkowski [1998] were the first, to our knowledge, to made a systematic approach by creating large libraries of artificial projections with varying parameters. TEM image are then matched against this library. By finding a match from the library, the structure can be identified.

4.3   SPIRE—a software tool for bicontinuous phase recognition: application for plastid cubic membranes

In the paper, we expand on the projection matching method by Deng and Mieczkowski [1998], Deng et al. [1999] by introducing a new open-source tool, called SPIRE (Surface

Projection Image Recognition Environment). SPIRE generates projections of cubic bicontinuous structures and allows an intuitive and easy-to-use interactive matching and thus identification process. Our results can be found in Hain et al. [2021] and in the following section. A video tutorial on the usage can be found online[1]. Using SPIRE, we were able to identify the structure of the PLBs to be a diamond structure with unequal channel sizes.

---

[1]`http://chloroplast.pl/spire`

Plant Physiology®

Breakthrough Tech

SPIRE—a software tool for bicontinuous phase recognition: application for plastid cubic membranes

Tobias M. Hain [1,2,3] Michał Bykowski,[4] Matthias Saba,[5] Myfanwy E. Evans [1]
Gerd E. Schröder-Turk[2,6,†] and Łucja Kowalewska [4,*,†]

1 Institute of Mathematics, University of Potsdam, Potsdam D-14476, Germany
2 College of Science, Health, Engineering and Education, Mathematics and Statistics, Murdoch University, Murdoch WA 6150, Australia
3 Physical Chemistry, Center for Chemistry and Chemical Engineering, Lund University, Lund 22100, Sweden
4 Department of Plant Anatomy and Cytology, Faculty of Biology, Institute of Experimental Plant Biology and Biotechnology, University of Warsaw, Warsaw, Poland
5 Adolphe Merkle Institute, University of Fribourg, Fribourg CH-1700, Switzerland
6 Department of Applied Mathematics, The Australian National University, Research School of Physics, Canberra 2601, Australia

*Author for communication: lucja.kowalewska@uw.edu.pl
†Senior authors.

T.H., M.B., G.E.S.T., and Ł.K. wrote the original draft; T.H., M.B., M.S., M.E., G.E.S.T., and Ł.K. edited and review the manuscript; T.H. and M.B. designed the software; T.H. implemented the software; T.H. and M.S. designed computational solutions; Ł.K. provided resources (TEM images); M.E., G.E.S.T., and Ł.K. supervised the project, M.B. and Ł.K. performed experiments; M.B. performed image analysis; T.H., M.B., and Ł.K. prepared figures; G.E.S.T. proposed the research; T.H., M.B., G.E.S.T., and Ł.K. provided conception of the project.

The author responsible for distribution of materials integral to the findings presented in this article in accordance with the policy described in the Instructions for Authors (https://academic.oup.com/plphys/pages/general-instructions) is Łucja Kowalewska (lucja.kowalewska@uw.edu.pl).

Abstract

Bicontinuous membranes in cell organelles epitomize nature's ability to create complex functional nanostructures. Like their synthetic counterparts, these membranes are characterized by continuous membrane sheets draped onto topologically complex saddle-shaped surfaces with a periodic network-like structure. Their structure sizes, (around 50–500 nm), and fluid nature make transmission electron microscopy (TEM) the analysis method of choice to decipher their nanostructural features. Here we present a tool, Surface Projection Image Recognition Environment (SPIRE), to identify bicontinuous structures from TEM sections through interactive identification by comparison to mathematical "nodal surface" models. The prolamellar body (PLB) of plant etioplasts is a bicontinuous membrane structure with a key physiological role in chloroplast biogenesis. However, the determination of its spatial structural features has been held back by the lack of tools enabling the identification and quantitative analysis of symmetric membrane conformations. Using our SPIRE tool, we achieved a robust identification of the bicontinuous diamond surface as the dominant PLB geometry in angiosperm etioplasts in contrast to earlier long-standing assertions in the literature. Our data also provide insights into membrane storage capacities of PLBs with different volume proportions and hint at the limited role of a plastid ribosome localization directly inside the PLB grid for its proper functioning. This represents an important step in understanding their as yet elusive structure–function relationship.

Open Access

Introduction

Biological membranes, dynamic yet stable unique assemblies of lipids and proteins, are selective barriers and enzymatically active regions playing a crucial role in orchestrated cells' functioning. From a structural point of view, they are described mainly as flat sheets or small folded isolated entities called vesicles. Interestingly, in specific cases, almost all types of cellular membranes can form symmetrical, bicontinuous configurations called "cubic membranes" (Almsherqi et al., 2006, 2009). These are characterized by a spatial structure based on a periodic network or labyrinth-like geometry, defined by uninterrupted negatively curved membranes and with high symmetry (often cubic; Luzzati, 1997). These can be modeled by negatively curved surfaces as the spatial model for the bilayer membrane. Note, that herein the phrase "cubic membrane" is used synonymously for any bicontinuous membranes with two membrane-separated aqueous channels and with a cubic or otherwise highly symmetric spatial structure.

Cubic membranes are observed in cells of different organisms, from protozoa to mammals. They can self-organize from almost all types of membranes, including, for example, endoplasmic reticulum, plasma membrane, mitochondria and plastid inner membranes, and inner nuclear membrane (reviewed in Almsherqi et al., 2009). Due to the length scale of such structures with typical periodicities between 50 and 500 nm, our knowledge about cubic membrane arrangements is almost exclusively obtained from electron microscopy data. Note that this is in contrast to bicontinuous soft matter phases, with much smaller periodicity and homogeneous nature of samples, where X-ray and neutron scattering have been traditionally used to identify structures.

Although the highly regular nature of the membrane arrangements has been noted by many authors, structure identification remains difficult, due to a lack of widely available image processing tools for this purpose. As a result, many of these structures have been inaccurately identified as, for example, tubular inclusions, undulating membranes, or cisternal systems (for the review of this issue, see Almsherqi et al., 2006, 2009; Cui et al., 2020), instead of associating them correctly with cubic phases. The deep understanding of the factors governing the formation of such complex amphiphilic arrangements is still not established, partially due to the scattered nature and incorrect annotations of reported data. On the other hand, considerable advancement in recognition of intrinsic and extrinsic factors playing a role in elementary membrane bending and curvature sensing has been made, forming a solid foundation for further studies in understanding how the complex architecture of cubic membranes controls cellular traffic (Kozlov et al., 2014; Jarsch et al., 2016; Lou et al., 2018; Simunovic et al., 2019; Callens et al., 2020).

Recently, there is a growing interest in the possibility of obtaining nature-inspired and, therefore, stable, large length-scaled cubic systems (>50 nm) to develop concepts to tackle different multidisciplinary issues and healthcare problems (reviewed in Mezzenga et al., 2019). The potential application of inducible cubic membranes in plant synthetic biology has also been raised (Sandor et al., 2021). However, such broad interdisciplinary interest in bicontinuous systems has not yet been addressed by recent fundamental research on naturally occurring cubic membranes. Key factors constraining advances in this field are the recognition and spatial analysis of observed membrane arrangements. Such data are crucial to establishing a model system for further biochemical studies and, finally, to discover the shape-dependent role of cubic membranes. This generates a great demand for methods to recognize and measure 3D properties of periodic assemblies.

In terms of topology and geometry, cubic membrane structures can be described using triply periodic minimal surfaces (TPMSs). Minimal surfaces are surfaces that locally minimize their surface area based on some global constraint (e.g. a surface between a given boundary). As a consequence of this minimization, they have a mean curvature of zero at all points on the surface. TPMSs are minimal surfaces with a crystalline, symmetric structure where they repeat in three independent translation directions in space. A wide array of TPMSs has been described mathematically with different crystallographic symmetries. However, three particular TPMSs with cubic symmetry are most commonly observed in biological cubic membranes. Primitive and diamond types were characterized by Schwarz in 1865 and the so-called gyroid recognized by Schoen (1970) almost a hundred years later (1970) (reviewed in Hyde et al., 1996). TPMSs divide inner space into two separated, intertwining yet open channels. In terms of cubic membranes, the presence of such isolated regions of given sizes might have tremendous consequences in constraining molecular motion.

One of the examples of extensively studied cubic membrane assemblies is a prolamellar body (PLB) of plant etioplasts, see Figure 1. The PLB is a direct precursor of the chloroplast thylakoid network, and their lipid–pigment–protein composition shares some similarities (for the review of PLB composition, see Adam et al., 2011; Pribil et al., 2014; Kowalewska et al., 2019). The PLB is considered as a lipid reservoir during tubular–lamellar transition increasing the efficiency of grana formation (Armarego-Marriott et al., 2019; Pipitone et al., 2021). The number of PLB building blocks plays a crucial role in maintaining its structure, including the protochlorophyllide:light-dependent protochlorophyllide oxidoreductase:NADPH complex as well as particular galactolipids and carotenoids (Sperling et al., 1998; Fujii et al., 2019; Bykowski et al., 2020; Cazzonelli et al., 2020; Floris and Kuhlbrandt, 2021; Nguyen et al., 2021). Although the role of light-dependent protochlorophyllide oxidoreductase in membrane tubulation was proven recently using electron cryo-tomography techniques (Floris and Kuhlbrandt, 2021; Nguyen et al., 2021), factors governing the transition of tubular arrangements into cubic configuration remain elusive (Wietrzynski and Engel, 2021). PLBs are rare examples of cubic membranes which can be modeled using imbalanced
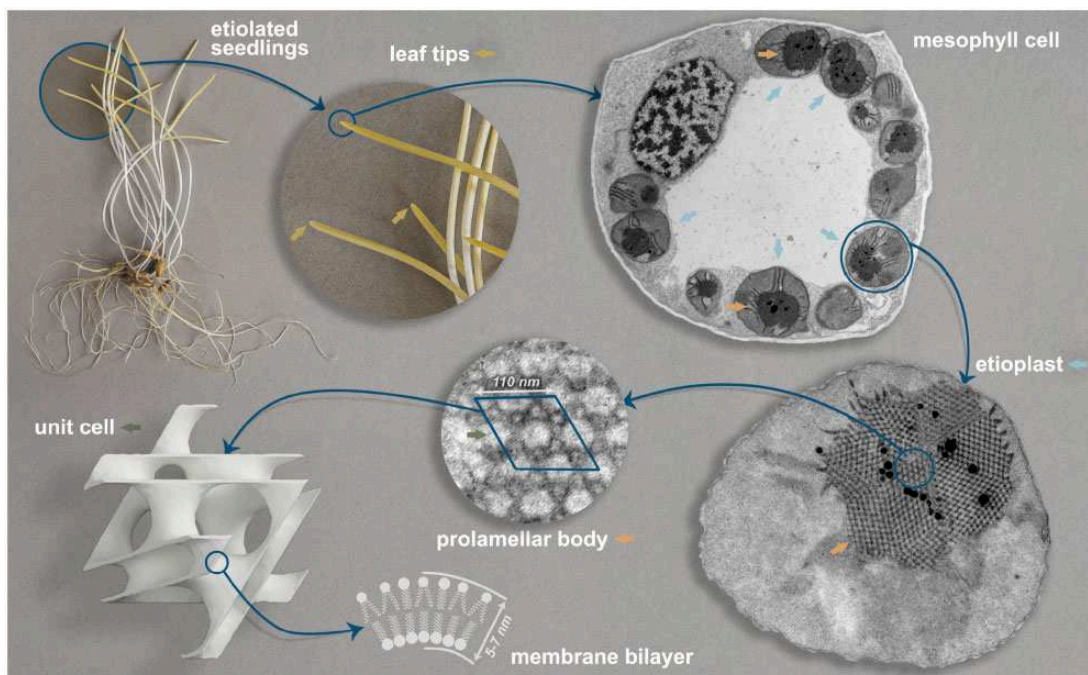
Figure 1 Cellular localization of cubic membrane assembly—PLB in etiolated seedlings of oat. Cubic structure of PLBs located in etiolated seedlings of angiosperms—here exemplified by growing for 7 d in complete darkness. PLBs develop in etioplasts present in developing leaves' mesophyll cells (yellow parts of the seedling visible above white part of the shoot). The cubic arrangement of the PLB is characterized by a single membrane separating two water channels of different volumes (referred to as being imbalanced, with volume proportions different from 50%) and a relatively small length scale compared to other naturally occurring cubic membranes. Note that recent results indicated that PLB membranes are densely decorated with light-dependent protochlorophyllide oxidoreductase protein, whose role in membrane tubulation has been proven in *in vitro* studies (Floris and Kuhlbrandt, 2021; Nguyen et al., 2021). Apart from marked elements, the presented photographs, and electron micrographs are not shown to scale; mesophyll cell and etioplast are free-form selected manually from TEM images of etiolated oat leaves.

TPMS, that is, the two channels separated by the membrane are geometrically different such that one has a smaller volume. In relation to the PLB, this means the volumes of the two aqueous channels differ substantially—beyond natural fluctuations—from each other. The smaller channel is a direct precursor of thylakoid lumen of chloroplasts (Kowalewska et al., 2016). In early studies, PLB structures were most frequently referred to as zinc sulfide crystal forms of wurtzite (lonsdaleite) and zincblende type, both based on tetrahedral units forming complex hexagonal networks and as such with hexagonal instead of cubic symmetry. The primitive, face-centered diamond and double diamond cubic membrane types were also proposed (Menke, 1963; Ikeda, 1968; Gunning and Steer, 1975; Landh, 1996). These variable structural annotations were made based on the analyses of randomly cut PLB sections visible in 2D transmission electron microscopy (TEM) micrographs via their comparison with 3D models (physical or rendered) of the mentioned structures. However, even comparing many 2D projections of a 3D structure (TEM specimen) at different viewing angles with an actual 3D model is not directly verifiable and probably led to such inconsistency in the identification of the most abundant spatial PLB configuration.

There are two main methods for analyzing the 3D structure of PLB and other cubic membrane arrangements. Both methods are based on the assumption that cubic membrane structures correspond directly to mathematically well-defined TPMSs. The first approach consists of the visualization of cubic membranes using electron tomography, further segmentation, modeling the periodic arrangement, and finally, its direct comparison to the rendered 3D model of different bicontinuous structures with variable surface parameters and length scales (Chong and Deng, 2012; Demurtas et al., 2015; Kowalewska et al., 2016). Such a method is time, money, and computational power-consuming due to the operation on the 3D objects. It is also limited to the cubic membrane structures of particular length scales. Moreover, it should be stressed that manual segmentation of cubic membranes is complicated, and automated methods, while sufficient to estimate general structural parameters (e.g. channel volume or surface area), fail in terms of precise shape visualization.

Alternatively, the second method is performed using 2D TEM images of cubic membranes and their direct comparison with a simulation of a 2D TPMS projection of given parameters. The idea of the "template matching" method for cubic structure recognition was initially introduced by Mark Mieczkowski and Yuru Deng (Deng and Mieczkowski, 1998; Deng et al., 1999). It was successfully implemented to recognize the surface type of several membrane arrangements, for example, in mitochondria of starved *Chaos carolinensis* (Deng et al., 1999) or chloroplasts of green alga

Zygnema sp. in the log phase of growth ([Zhan et al., 2017](#)) using the developed software called cubic membrane simulation program (QMSP). The QMSP tool enabled the generation of a library of projection images for structures of primitive, double diamond, and gyroid surfaces; the user could manipulate the direction of the projection, number of visualized unit cells (UCs), and thickness of the projected TPMS region. The tool is not publicly available and has limited functionalities in projection scaling, surface types, channel balance, and measurement properties.

Inspired by [Deng and Mieczkowski (1998)](#), we introduce Surface Projection Image Recognition Environment (SPIRE), an open-source tool to simulate TEM images of TPMSs. It addresses the aforementioned issues, vastly extends and improves the structure identification process by focusing on interactive matching, and lays the foundation for an automated identification process.

The SPIRE tool focuses on the interactive matching of TEM images, with access to a large range of parameters and metrics of the structure. It is broadly applicable to reliably recognize and analyze structural, spatial properties of bicontinuous arrangements visualized in electron microscopy. A widespread representation of cubic membranes in living organisms highlights the importance of our tool for a large community of biologists. The intuitive SPIRE graphical user interface (GUI) can be used by a broad group of scientists, including those with no explicit knowledge of the geometrical description of cubic structures.

Although we developed SPIRE to investigate cellular cubic membranes visualized in TEM images, it is also a suitable tool for analyzing microscopy images of any highly symmetric arrangement such as cuboids or polymer assemblies. In the latter, we see similar geometries to those found in the biological cubic membranes ([Bates, 2005](#); [Kirkensgaard et al., 2011](#); [Han et al., 2020](#)) or cubic rod packings ([O'Keeffe et al., 2001](#)). The latter is used to model the keratin microstructure in skin cells, a geometry that is closely related to—and likely coexistent with—a gyroid surface ([Norlen and Al-Amoudi, 2004](#); [Evans and Hyde, 2011](#); [Evans and Roth, 2014](#)). Synthetic cubic structures are mainly analyzed using scattering methods, but in nonuniform samples, additional microscopy analyses are required.

This article first describes the main concepts and algorithms of the software, followed by a detailed walkthrough of a structure identification process using the PLB arrangements in etiolated seedlings as an example.

Results

Numerical procedures

[Figure 2](#) illustrates the major steps in the simulation process used in SPIRE: the simulation of TEM images of ultrathin sections of biological samples, which are essentially planar projections, thus 2D images, of the 3D structures inside the sample. The TEM image of a 3D structure encodes the amount of beam attenuating material along its path that generates the microscope image: whereas dark regions
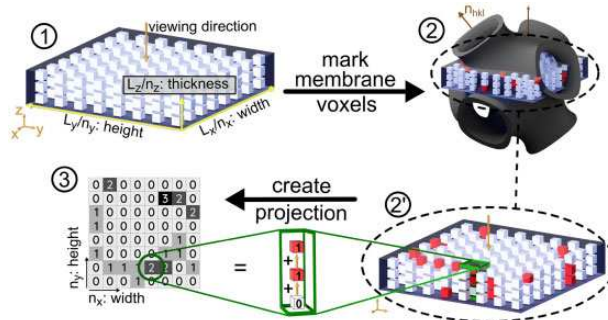
Figure 2 The basic steps in the process of computing a planar projection (1) Schematic representation of the rectangular simulation box (called slice) with the dimensions (L_x, L_y, L_z), filled with a grid of $n_x \cdot n_y \cdot n_z$ voxels of size (L_x/n_x, L_y/n_y, L_z/n_z). The viewing direction is perpendicular to the L_xL_y plane. Note that the space between voxels is just for visualization and is not existent in the simulation. (2) All voxels are evaluated using the mathematical model of the surface structure: the slice is superimposed in the oriented membrane structure; a voxel is marked if located within a membrane (2') The projection is computed by adding the values of voxels with identical x and y coordinates, that is, all voxels congruent in viewing direction. Each marked voxel is valued as "1," whereas unmarked voxels do not contribute (3). The simulated planar projection, a pixel image where each pixel brightness holds the number of marked, thus membrane, voxels. Its resolution is determined by the number of voxels (n_x, n_y) in the initial slice.

in the image represent areas of a large amount of material along the beam path, brighter regions present less material.

To simulate those projections, a model of the sample is created by using one or multiple membranes, modeled as minimal or negatively curved surfaces. A discrete grid of points, where each point is either marked as "attenuating," or not marked, that is "translucent," is then used to compute the planar projection. In this section, details on the underlying processes and methods are presented.

Mathematical modeling of bicontinous membranes

The so-called nodal representation is used to describe membrane geometries. In this model, the true TPMSs are approximated by implicit functions $f(x, y, z) : E^3 \rightarrow R$, the so-called nodal functions ([von Schnering and Nesper, 1991](#); [Klinowski et al., 1996](#)). Surfaces are then defined using so-called level set parametrization: the surface is the set of all points where $f(x, y, z) = c$, with c being an arbitrary constant. Different values of c yield different surfaces.

SPIRE contains nodal representations for several surfaces as well as rod packings. Three surfaces with cubic symmetries are included: the gyroid, diamond, and primitive surface. The nodal representations of the latter are taken from [von Schnering and Nesper (1991)](#). We computed the nodal representation of the lonsdaleite ("hexagonal diamond") surface from its corresponding spacegroup (SG194) and its structure factor (similar to [Wohlgemuth et al., 2001](#), and references therein). The leading term only representation reads

$$f(x,y,z) = -\cos(2Z) + \cos(X) + \cos(Y) + \cos(X-Y)$$
$$+ \sin(Z)[-\sin(X) + \sin(Y) + \sin(X-Y)]$$

with

$$(X, Y, Z) = 2\pi A^{-1}.(x,y,z)^\top$$

and **A** being the matrix comprising the three canonical lattice vectors of a structure with hexagonal symmetry:

$$a_1 = (1,0,0)^\top, \quad a_2 = \left(-\frac{1}{2}, \frac{\sqrt{3}}{2}, 0\right)^\top, \quad a_3 = \left(0, 0, \sqrt{\frac{8}{3}}\right)^\top$$

and the dot denoting the matrix product (see section "Crystallographic nature of highly symmetricmembranes" for more details). Note, that due to their repeating nature, all representations of triply periodic surfaces can be expressed solely using periodic trigonometric functions. Although the presented formula yields a surface with a topology and geometry equivalent to the lonsdaleite structure, it is not a minimal surface. For the implementation in SPIRE, we therefore used a numerically optimized version. A triangulated, minimal lonsdaleite surface was created using an input file by Ken Brakke for the surface evolver (Brakke, 1992). A voxelized version of the surface was created by marking points on a rectangular grid as "1" on one side of the surface and "−1" on the other side. This discrete, 3D test function is approximated by a Fourier series $f(x,y,z)$. The latter has a root everywhere on the surface, thus $f(x,y,z)$ is a nodal representation of the surface. The same numerical protocol was used to compute nodal representations of two cubic rod packings, namely the β-Mn and Σ^+ rod packings. The original input was generated by placing cylinders of a given radius along the invariant axes of the rods, as described in O'Keeffe et al. (2001). Note that for convenience, in this implementation, instead of using the canonical choice of lattice vectors for a hexagonal symmetry, we use orthogonal lattice vectors with a rhomboidal symmetry. Please refer to Supplemental Figure S1 and Supplemental Table S1 in the supplementary material for detailed information.

All TPMSs divide space into two intertwining channels. Here, the nodal representation is chosen such as $f(x,y,z) = 0$ yields the balanced case: the membrane separates two channels of equal volume. Membranes at $f(x,y,z) = c$ with arbitrary c, separate two channels with unequal volumes. The constant c is thus a measure of the proportion of volumes of the two channels. SPIRE allows to choose the position of the membrane either based on the constant c ("level set") or the volume proportion of the two channels. Note, however, that only for membranes where $f(x,y,z,) = 0$ the nodal representation does approximate a true minimal surface! Whereas the surface $f(x,y,z) = 0$ will converge toward the true minimal surface by adding more terms to the series expansion, this is not the case for surfaces with $f(x,y,z) = c$ where c0. The latter, however, are topologically equivalent (within a symmetric interval of c values) nonminimal, triply periodic surfaces.

Obtained models can only be matched to actual samples within a margin of error due to various reasons such as quality of TEM images, fluctuations in the biological sample, etc. Once matched, however, the model is intrinsically well defined and exact, which means all model parameters are without error margins. Only when using the model to describe the actual sample variability error margins are relevant.

Discretization of structure models

For the discretization of the structure models, an approach combining level sets of the nodal representations with a distance map is employed as follows. The process begins by computing the value of the nodal representation $f(p_x, p_y, p_z)$ for each voxel at position (p_x, p_y, p_z) in the simulation box. As shown in Figure 2, a voxel is marked, if $c - \lambda f <, \; f(p_x, p_y, p_z) < +\lambda$, where λ is a constant with the meaning of the width of the membrane. In a naive implementation, visually speaking a voxel is marked if it is located within the space bounded by the two level-set surfaces given by $f(x,y,z) = c + \lambda$ and $f(x,y,z) = c - \lambda$. Note that these two surfaces bounding the membrane are not necessarily parallel and thus would create a membrane with varying width. To resolve this issue, the following procedure is used: the parameter λ is chosen very small, such that ideally the resulting membrane width is only a single voxel. A so-called Euclidean distance map (EDM) (Felzenszwalb and Huttenlocher, 2012) is then computed. This function EDM(p_x, p_y, p_z) assigns each voxel in the slice the value of the distance (in length units) of the current voxel to the closest marked one, thus the closest membrane voxel. All voxels inside one channel are assigned a positive distance, whereas voxels in the other channel have negative distances to the membrane. The membrane with the desired width is then obtained by marking all voxels where the value EDM(p_x, p_y, p_z) is smaller than or equal to half of the membrane width.

Although less common, more complicated geometries such as double bilayer membranes occur in nature (Deng and Mieczkowski, 1998). To model such systems, SPIRE allows for multiple membranes. The positions of additional membranes are given as a distance to the initial, positioned by the level-set membrane, whereas additional parameters control the width of each membrane (see Supplemental Figure S2). Voxels of additional membranes are marked using the EDM computed before: for each membrane i of width w_i and distance d_i all voxels for which $d_i - (w_i/2)$ EDM(p_x, p_y, p_z) $d_i + (w_i/2)$ holds are marked.

Whereas a single bilayer membrane separates space into two channels, each additional membrane will add a further domain (called "channel" in the software; meaning the space between two parallel membranes). Since membranes have a finite width and thus a volume, this software internally considers the latter as channels, too. Channels are labeled with increasing integers starting at "1" with the innermost channel (containing the center of the UC), the innermost

membrane then has the channel number "2," etc. Also see Supplemental Figure S2 for more information.

So far, only systems related to the double "gyroid" (or other "double phases") where a membrane (modeled as absorbing) separates two aqueous channels (modeled as translucent) were considered. Several examples in nature, such as a gyroid surface in the wing scales of the butterfly (Schroder-Turk et al., 2011) have been reported with a single surface separating two intertwining channels, where one of the two is filled by a solid material. To account for such systems, the software allows to mark all voxels inside a channel, thus models it as opaque.

Crystallographic nature of highly symmetric membranes

After introducing the mathematical description of the TPMSs and their geometries, this description is now used to create synthetic images corresponding to the membrane structure in voxelized (3D pixel) form.

The simulation process starts with the initialization of the simulation box, a cuboid with dimensions L_x, L_y, and L_z, where each edge is aligned with its corresponding axes of the canonical base, see Figure 2. The simulation box will be called "slice" and represents the region of interest (L_x and L_y) as well as physical thickness (L_z) of the ultrathin section of tissue captured by the TEM image, and will be filled with a discretized version of the membrane structure. To store the latter, the simulation box is fitted with a regular, rectangular grid of a total of $n_x \cdot n_y \cdot n_z$ sites, see part 1 in Figure 2. On each site, a small cuboid with dimensions (dx, dy, dz), a so-called voxel, is placed, such as there is no overlap or space between two adjacent voxels. Each of these voxels can be "unmarked," that is, translucent, or "marked," that is, opaque. In Figure 2, this property is represented by the color "white" and "red" and will be assigned in a later step.

The slice dimension (L_x, L_y, L_z) is an important parameter to match the simulated projection to the size of the TEM image. That is, the slice dimensions should be chosen to correspond to the size of the TEM image of the section considered. The number of voxels in the slice can be tuned by providing the number of voxels in x (n_x) and z (n_z) direction. To obtain voxels with a square footprint ($dx \approx dy$) the number of voxels in y direction is then computed to $n_y = L_x/L_y \cdot n_x$ (or nearest integer). The voxel dimensions are computed automatically. The number of voxels determines the resolution and hence the quality of the projection, in line with the resolution of the TEM image.

The software focuses on the modeling of periodic membrane structures. The latter is characterized by the fact that the entire information of a periodic structure is stored in a translational UC and three replication directions, called lattice vectors u, v, and w. We conveniently choose these vectors as the bounding edges of the UC (see Figure 3), although other choices exist and may be more fitting for different purposes. As a consequence, the size and shape of the UC is, apart from the structure itself, solely determined
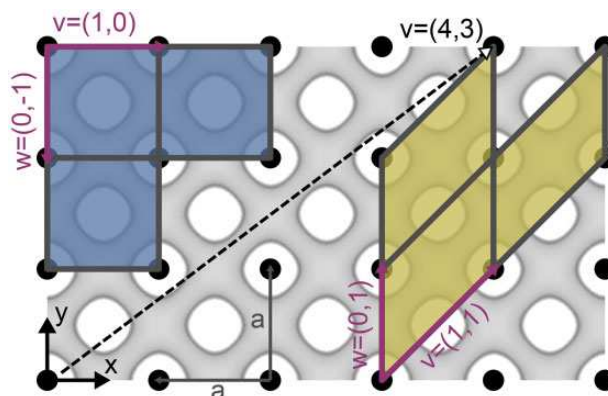

Figure 3 The definition of a UC and its base vectors. An example of a 2D, periodic structure with two choices of lattice vectors and resulting UCs: the fundamental UC (smallest UC with least amount of information to fully replicate the infinite structure while being cubic or rectangular) and an inclination UC (see main text for definition). The black dots are a choice of lattice points and represent geometrically identical, since repeating locations in the structure. The choice of lattice vectors and thus UCs is arbitrary and the size of the UC depends on the choice of lattice vectors: for $v = (1, 0)$ and $w = (0, -1)$ the UC is square with an edge length of a (lattice constant), whereas for $v = (1, 1)$ and $w = (0, 1)$ the UC is a parallelogram with edge lengths $v = \sqrt{2}a$ and $w = a$. The dashed vector v demonstrates that lattice vectors (and thus the UC) can get very long for odd directions.

by a choice of the three lattice vectors u, v, and w, that is the replication directions. An infinitely large, continuous structure can be constructed by repeating the UC along the replication directions. Due to this repeating nature, points with identical geometry but different spatial coordinates, here called lattice points, can be identified. The black dots in Figure 3 represent a possible choice of lattice points.

Given a periodic structure, there is no unique choice of a UC: the lattice vectors and thus the UC can be chosen arbitrarily. We introduce a distinct choice of the UC, the herein called fundamental UC. The latter is the cubic (for the surfaces with cubic symmetries, for example, the primitive, diamond, and gyroid surface) or rectangular (for rectangular symmetries, as the Lonsdaleite) UC which among all choices has the smallest volume and content possible (in Figure 3 exactly one lattice point) while still containing all information needed to reproduce the entire structure. In the case of cubic or rectangular TPMSs the lattice vectors u, v, and w, with $u = c$, $v = a$ and $w = b$, of the fundamental UC can be conveniently aligned with the Cartesian coordinate axes x, y, and z. Any UC with a different shape or choice of lattice vectors, especially rotated versions of the fundamental UC, will herein be called inclination UC. The Supplemental Figure S3 lists all fundamental UCs of the structures built into the software.

Whereas in real samples the orientations of the TPMS structures are in most cases random and thus unknown (there are cases, where structures grown onto substrates may exhibit preferred orientations, see Winter et al., 2015; Yoshioka et al., 2014), simulations provide the ability to generate projections with identified orientations. The fixed
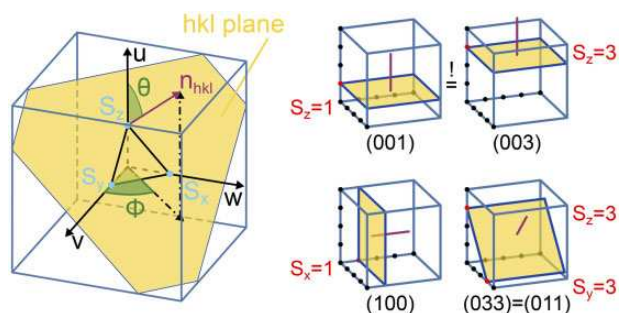
Figure 4 Definition of Miller indices and orientation denotation (left) Formally h, k, and l are defined by $h = p/S_x$, $k = p/S_y$ and $l = p/S_z$ where p is the smallest integer, for which (hkl) is a triplet of integers without a common divisor. S_x, S_y, and S_z are the points, given in terms of the lattice vectors v, w, and u, where the plane, denoted by the Miller indices (hkl), intersects the x, y, and z axes (for detailed description of Miller indices principles, see Kittel, 2004). Thus the Miller indices define a plane fixed by three points in space. An index value of 0 means the plane is parallel to the respective axis. For structures with cubic or rectangular fundamental UCs (i.e. all structures implemented in the tool), the normal vector n_{hkl} on the (hkl) plane—and thus a direction—can be written in terms of the Miller indices: $n_{hkl} = ((1/a) \cdot h, (1/b) \cdot k, (1/c) \cdot l)^\top$. The polar angle Φ is the angle between the x-axis and the projection of n_{hkl} onto the xy-plane, the azimuthal angle Θ is the angle between the z-axis and n_{hkl}. (right). Examples of planes denoted by different values of Miller indices. The red line denotes the normal vector on the plane, whose coordinates, in the case of cubic symmetry, are given by the Miller indices. The black dots denote the coordinate grid spanned by the lattice vectors; each dot represents a symmetrically equivalent position. As a result, although at different positions and with different Miller indices, the two planes in the upper row are equivalent.

viewing direction onto the sample is reflected in SPIRE by fixing the viewing direction on to the 3D slice arbitrarily but conveniently to the negative z-direction, that is, perpendicular to the $L_x L_y$ plane of the slice, as shown in panel 1 in Figure 2.

The orientation of the membrane structure within the slice is described using the so-called Miller indices (hkl) (Kittel, 2004), a triplet of integer numbers denoting the orientation of a lattice plane and its normal vector n_{hkl}, see Figure 4 for more details. Note that due to the choice of using a rectangular fundamental UC for cubic structures and the hexagonal Lonsdaleite alike, the (hkl) values do not correspond to the expected direction in the crystallographic convention and extra care needs to be taken when specifying the inclination. Supplemental Table S1 lists the exact dimensions and choice of lattice vectors of all fundamental UCs in the software. Internally, the orientation of the normal vector given as Miller indices is converted in two angles, the polar angle Φ, and the azimuthal angle Θ, as defined in Figure 4.

In SPIRE, the orientation of the fundamental UC, where v, w, and u align with the coordinate axes, is assigned the "neutral" orientation (001) with $n_{001} = z$, that is, the orientational normal vector n_{hkl} aligns with the positive z direction. The two orientation angles then are $\Phi = 0$ and $\Theta = 0$.

In the software, a triplet of Miller indices indicates the desired viewing angle on the structure as a vector n_{hkl}.

However, since the viewing angle in the tool is fixed to the z axis, the vector n_{hkl}—and with it the structure—needs to be aligned with the z-axis, as described in Figure 5.

After the alignment, the structure can still be rotated around the z axis without changing the orientation determined by n_{hkl}. This remaining rotation is related to the choice of in-plane base vectors v and w. The software first chooses the two lattice vectors v and w in the plane denoted by (hkl), and thus perpendicular to n_{hkl}, so that both vectors are as short and as orthogonal to each other as possible (see the blue cell in comparison with the yellow one in Figure 3). Then the surface is rotated around the z-axis until the longer of the two vectors v or w is aligned with the x-axis. Since the lattice in the plane, that is, the pattern of the points in Figure 3, is dependent on the orientation of the plane, the choice of the base vectors differs for each choice of viewing directions n_{hkl}.

Note that for odd combinations of large Miller indices, the UC vectors v, w, and u—and with it, the inclination UC—can get very large (many multiples of the size of the fundamental UC). Figure 3 shows an example vector v, which is long compared to the size of the fundamental UC. This behavior directly translates to three dimensions.

Having the orientation fixed, the last step is to fix the translational degrees of freedom. This can be imagined as the oriented slice being a stencil, cutting a rectangular piece out of the infinite, periodic membrane structure at different locations. Moving a stencil along a periodic structure does not substantially change its content, given the stencil is at least the size of an inclination UC: the slice will in most cases contain one or multiple copies of the UC. As most biological samples will be ultra-thin slices, that is, have a much larger base than thickness, this caveat is met in most cases in the v and w direction of the sample, that is, its width and height, but not the u direction, the viewing direction. Thus, whereas translating the slice through the membrane structure in v and w direction does barely affect the projection, moving it along the u direction will impact the projection substantially, since different parts of the structure are contained in the slice.

SPIRE always centers the slice around the origin, however, allows translation along the normal vector n_{hkl}. In the case of a slice thickness smaller than the size of the inclination UC in the normal direction, this provides the ability to scan through different parts of the UC.

Synthetic microscopy images as projections of the discretized membrane model

The planar projection of a virtual membrane structure is a pixel image, thus an array of $n_x \times n_y$ pixels, each with a value indicating the brightness of the pixel. In the biological sample, a dark pixel in a TEM image indicates that much of the brightness of the incident beam has been lost due to a large amount of attenuation with matter, that is, much electron-dense material is located along the path of the beam corresponding to that particular pixel.
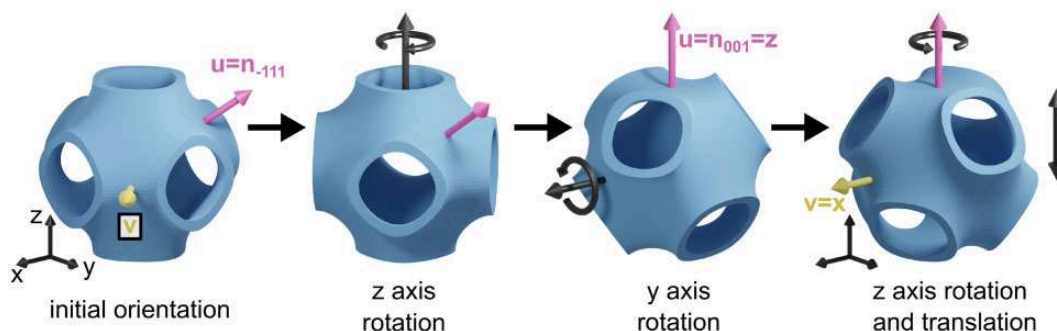
Figure 5 Orienting the membrane structure in the virtual sample. To simulate a projection with the desired viewing angle, the structure needs to be aligned accordingly inside the slice. Starting at the orientation of the fundamental UC, the structure is first rotated around the z-axis by the polar angle Φ, rotating the vector u into the yz-plane, and subsequently around the y-axis by the azimuthal angle Θ, aligning u with the z-axis and thus the viewing direction. The last rotation around the z-axis aligns the in-plane vector v with the x-axis, such that the inclination UC has minimal volume given the normal vector n_{hkl}. In a last step, the structure can be translated along the z-axis to choose the termination.

This behavior is imitated in SPIRE: each voxel marked as being inside a membrane is assigned a numerical value of "1," whereas all unmarked pixels, thus representing aqueous phases, are assigned a value of "0." A value of "1" means that a membrane, therefore attenuating material, is located at that voxel. Adding all voxel values along a given direction yields the total amount of material interaction along that particular path. The values for each pixel at position (i, j) are computed by choosing a path along the viewing direction, thus normal to the $L_x L_y$ plane, where the path is located such that it intersects all voxels with identical x and y positions at $p_x = i \cdot dx$ and $p_y = j \cdot dy$, as shown in Figure 2. As a result, the final resolution of the projection is determined by the resolution of the voxel grid in the simulation box.

To avoid different brightnesses of projections due to varying numbers of voxels, all pixel values in the planar projection images are rescaled to an integer in the range between 0 and 255. This scaling allows for a linear or a logarithmic scale, which depending on the membrane structure may reveal more details in the projection.

Additional structural properties
On demand, the software can compute the channel volume, the surface area of the membranes, and the percolation threshold of all channels as described below.

Channel volume
Each voxel occupies a volume of $V_v = dx \cdot dy \cdot dz$, thus the total volume of a channel is just the number of all voxels associated to that channel multiplied with the volume of a single voxel. While there are discretization errors, these are small and decay quickly when voxel sizes are small.

Membrane surface area
The surface area of the membranes is computed using a triangulation of the membrane surface. The triangulation is computed by an algorithm called "Advancing front surface reconstruction," implemented in the computational geometry algorithms library (CGAL) (Da and Cohen-Steiner, 2020; The CGAL Project, 2020), applied to the surface voxels of the

membranes. The total surface area of the membrane is the sum of the areas of all triangles in the triangulation. The quality of the approximation of the membrane surface by the triangulation, and thus the accuracy of the surface area, increases with an increasing number of voxels in the simulation box.

Percolation threshold
Percolation theory is an area in mathematics, statistical physics, and material science considering basic global connectivity properties of networks and graphs (Stauffer and Aharony, 1992). A network is said to percolate if a path through this network from a defined starting and end point can be found. Removing elements of such a percolating network can cause the connecting path to be cut and thus renders the network nonpercolating.

This software uses percolation analysis to compute the percolation threshold of a channel, that is the maximum diameter of a body (e.g. a sphere or molecule) which can move freely through a channel of the entire structure without getting stuck at narrow passages (Mickel et al., 2008). This measurement is found by increasing the width of the membranes enclosing a channel step by step and checking if the channel is still percolating. The width at which the channel stops to percolate is called the percolation threshold, and denotes the most narrow diameter in the channel. A Hoshen–Kopelmann (Hoshen and Kopelman, 1976) algorithm is used to perform a cluster analysis of all voxels in a channel, that is, all connected nodes of the network are grouped into a single object. The channel is percolating if only a single cluster is found during said analysis, that is each node (and thus voxel) in the channel can be reached from any other node in the same channel. A number of two or more clusters means that the channel has been separated.

Identification of the structure of prolamellar bodies

Structure identification process
Here, we present the essential SPIRE features exemplified by matching TEM images of etioplast PLBs with software-

generated projections. A video tutorial is provided, proposing an efficient workflow to recognize surface types with proper structural parameters visible on TEM images (http://chloroplast.pl/spire). The appearance of a 3D structure in a 2D projection depends mostly on (1) the scale of a structure regarding its magnification, (2) the thickness of the visualized section, and (3) the orientation of a structure in the TEM sample. We discuss how to use these parameters for proper and efficient matching.

Since the size of the TEM sample is known, the first parameters which can easily be fixed to start the matching are the slice height, width, and thickness. While the height and width only extend or reduce the size of the simulated sample, the thickness does influence the projection, as visualized in Supplemental Figure S4. Two examples of plastid cubic membranes varying in UC size and volume proportion of the two aqueous channels are provided: a gyroid membrane with a large UC and balanced channel volumes present in *Zygnema* sp. chloroplasts (Zhan et al., 2017) and a diamond membrane with a relatively small UC and imbalanced channel volumes found in runner bean (*Phaseolus coccineus*) etioplasts (Kowalewska et al., 2016). Drastic differences in the image characteristics point to the crucial role of the proper identification of scale and channel volume proportion of observed structures. All these properties can be easily calculated directly from the TEM micrographs using standard image analysis tools (e.g. ImageJ).

The next step is to make an initial (educated) guess for the structure type and orientation. A small gallery of all implemented surface types of different UC scales, volume proportions, and orientations are presented in Supplemental Figure S5, which can be used to facilitate this step. Using the bulk creation functions in SPIRE, a user can also create their own, more refined, and suitable galleries to provide better options for an initial guess. In the next step, the user can finely tune all parameters—with direct visual feedback—to further match the simulated projection to the TEM image.

If the slice thickness is not equal to the size of the inclination UC, that is, it contains a fraction of an inclination UC (the UC in orientation), the projection differs depending on which parts of the inclination UC are contained in the sample. In the software, the UC region is chosen by the slice position parameter. Figure 6 shows three serial sections of the same PLB structure. Selected regions marked with different colors are matched with the following slices, taking into account the slice's progressing position. The slight inaccuracies in the (hkl) values for the same regions in the subsequent slices are probably due to the sample warping during its visualization in TEM; note that neither the UC size nor the channel volume proportion was disturbed.

If possible, the identification of the structure should be confirmed by performing the matching procedure on several different regions of the sample with different orientations. These might be taken from different images or from a single image of a polycrystalline sample. PLBs often have a polycrystalline-like structure providing views of several projections of different orientations within one etioplast on a single micrograph; for details see Figure 7.

The user can directly extract different structural features of identified surfaces from the measurement tab of SPIRE. Therefore, it is possible to automatically calculate variable 3D features of a recognized surface based on a 2D TEM image of the structure. Such information is particularly valuable from a biological point of view. Due to the lack of control over the direction of cubic membrane sectioning during sample preparation, recognition of surface type is based on different (hkl) projections. Calculations of channel diameters and UC sizes from 2D data are reliable only in cases of specific projections and in terms of primitive surface type also only in the exact depth of the slice. Therefore, the measurement functions of SPIRE, enabling calculations of the 3D features of the recognized structure, bring reliable information about, for example, the membrane area, the volume of the aqueous channels, and the penetrability of the network by molecules of a given sizes; see percolation limit definition above.

Diamond as the predominant geometry in angiosperm PLBs

Using SPIRE and the described matching process, we identified the diamond surface type to be a dominating form of PLB cubic structures in the plethora of angiosperm species representing hypo- and epigeal germination as well as mono and dicotyledonous plants (oat (*Avena sativa*): Figures 6–8; pea (*Pisum sativum*), runner bean, cucumber (*Cucumis sativus*), *Arabidopsis thaliana*, and maize (*Zea mays*): Figure 8). Although in all analyzed examples the PLBs matched the diamond surface, the UC size and volume proportion of both aqueous channels varied between 73.5–90.5 nm and 0.2–0.3, respectively (see Supplemental Table S1). It was reported before that, in particular species or growing conditions, PLBs can also adopt an unusual structural type described as an "open PLB" (Gunning, 2001; Rudowska et al., 2012; Skupien et al., 2017). Among all registered PLB micrographs of analyzed plants (100–300/species), we observed such geometry only in <2% of visualized oat PLBs. We also showed that other network structural parameters were very similar both within one seedling (Supplemental Figure S6) and in different plants of the same species identically grown (see network parameters for oat in Figures 6–10). Note, however, that the etiolation period can influence PLB structural parameters. We detected that extended time of etiolation resulted in the increase of PLB UC size in oat etioplasts, from 80 nm registered in 1-week etiolated plants up to ∼87.3 after 2 weeks of skotomorphogenesis (Figures 6–10; Supplemental Figure S6).

In specific cases, the PLB can adopt a—within matching accuracy—geometrically balanced diamond structure with a volume proportion reaching 0.5. Such a configuration has been so far identified in mutant plants with a disturbed composition of the PLB membranes only; for example,
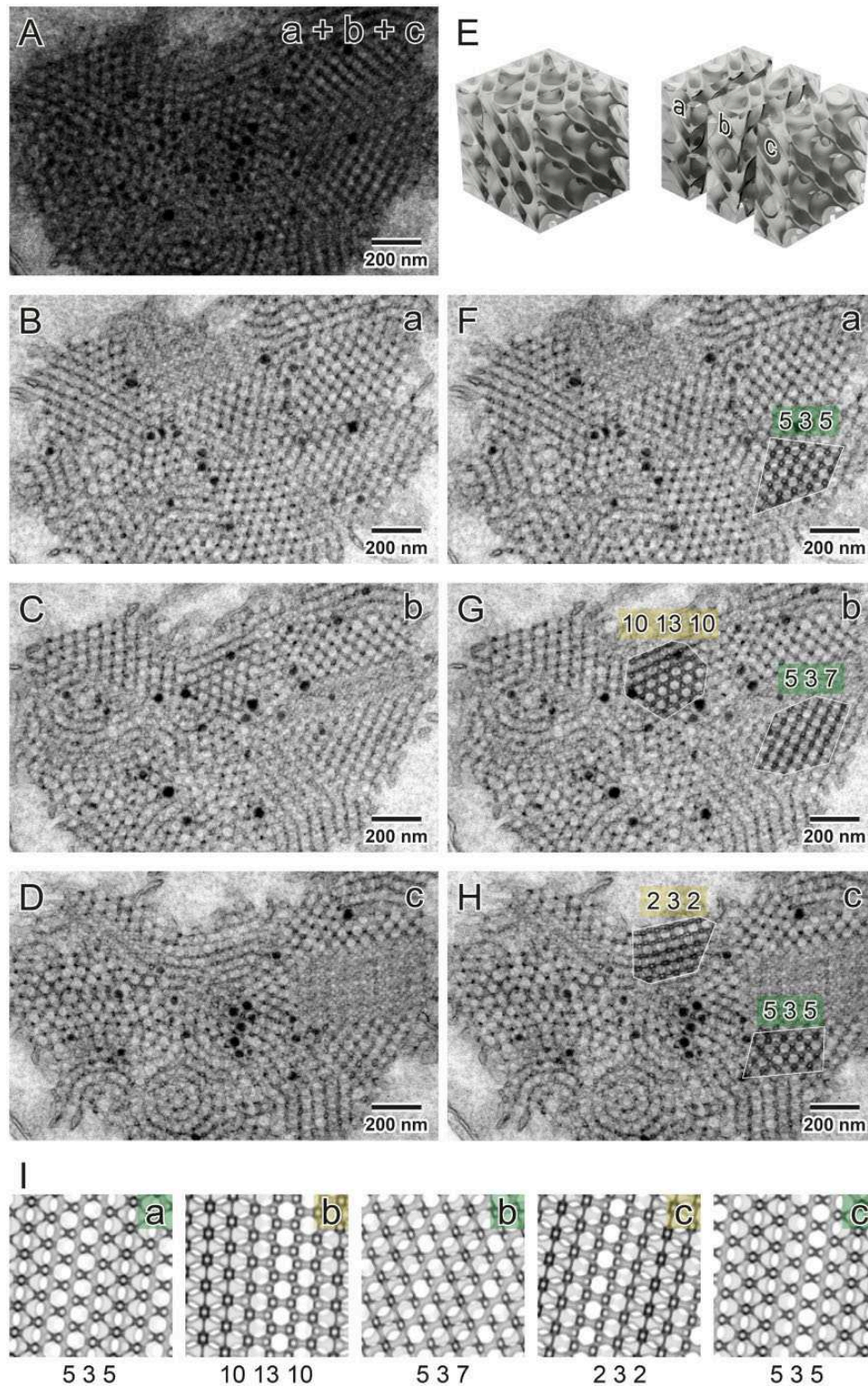
Figure 6 Surface type recognition in particular regions of oat PLB shown in serial TEM sections. Superimposed TEM images (a + b + c) showing PLB projections of a given thickness (70 nm) simulating a thick TEM specimen (210 nm) (A). Serial sectioning of a leaf sample enables visualization of subsequent regions of the PLB cubic structure (B–D); see an exemplary 3D model of the cubic surface presenting the idea of parallel cutting of the specimen block (E). In principle, in selected regions (marked with yellow and green) of subsequent slices (a–c) matched projections should be the same (identical (hkl) values) but localized in the different depth of the structure. Such expected depth shift is observed in recognized projections (I) of a diamond surface type; however, matched projections are similar but not always identical in subsequent slices. Such an effect is probably due to the thin TEM sample's warping during its visualization in the TEM chamber. Accuracy of projection matching is confirmed by superposition of computed projection and TEM image using multiply blend mode (F–H; regions marked with white border); all parameters used to generate projections are listed in Supplemental Table S1.
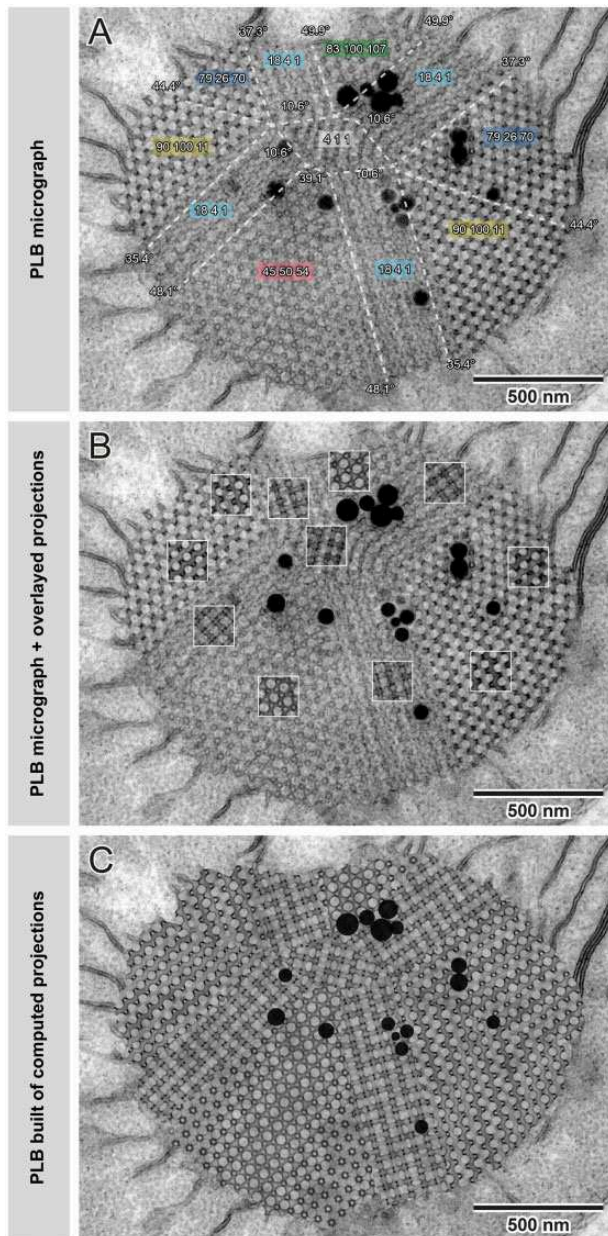
Figure 7 Construction of simulated oat PLB image built of computed projections. In many cases, PLBs and other naturally occurring cubic membranes are composed of several connected regions of bicontinuous surfaces at different orientations, forming "polycrystalline" arrangements (A). For a high confidence identification of the surface type, all different regions should be matched and analyzed. (A; same color indicates identical projections visible in PLB regions connected at different angles). To confirm the consistency of a match, the simulated projections can be superimposed on top of the TEM images (B; regions marked with white squares). To visualize the high accuracy of matches, we constructed an entirely simulated PLB built of particular computed projections (C) connected in the areas marked with white dashed lines visible on (A). Note that random noise was overlaid on computed projections to simulate the typical appearance of the TEM image; black dots added on top of composed projections (C) indicate the position of plastoglobules visible on the TEM micrograph (A, B); all parameters used to generate projections are listed in Supplemental Table S1.
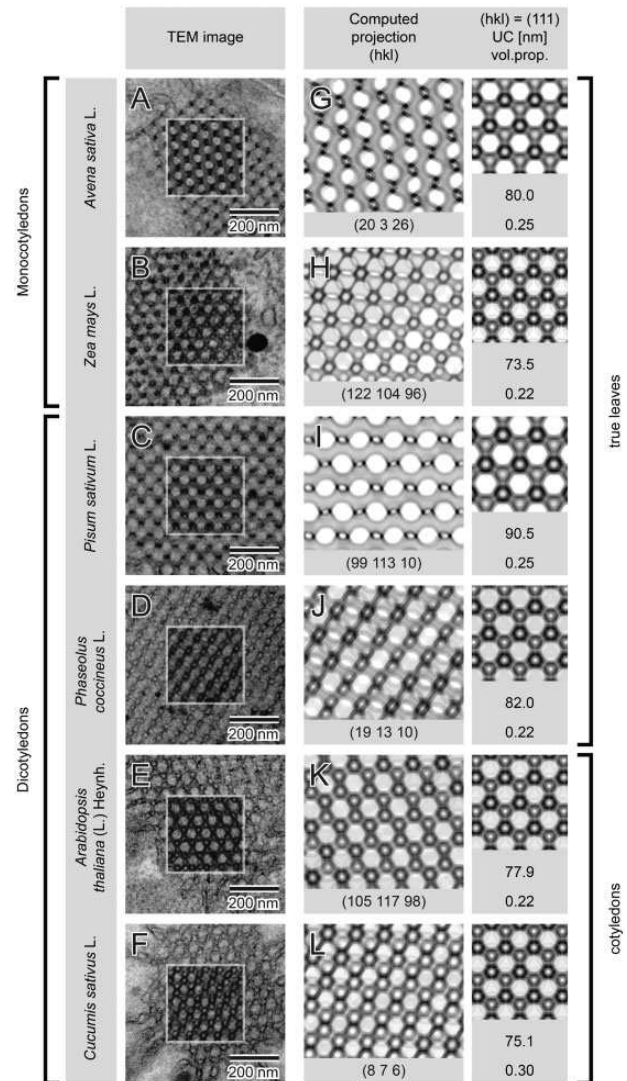

Figure 8 Diamond surface type—a dominating form of the PLB structure in etioplasts of angiosperms. Ultrastructure of the PLB in etiolated seedlings of several species from monocots (A and B) and dicots (C–F) exhibiting hypogeal (A–D) and epigeal (E and F) germination show the diamond type of cubic structure. Regions marked with rectangles present superposition of computed projections and TEM images using multiply blend mode (A–F). Matched computed projections are shown together with insets presenting 111 orientations of particular surfaces (G–L); all parameters used to generate projections are listed in Supplemental Table S1.

PHYTOCHROME-INTERACTING FACTOR 1 mutant plants (*pif1*) over-accumulating chlorophyll precursor (protochlorophyllide) (Bykowski et al., 2020; Figure 9). Note that a substantial increase in volume proportion alone, without changes in UC size, causes a rise in the membrane area packed in a given volume (Figure 9). Therefore, when the PLB size is maintained between different genotypes, such a geometrically balanced PLB network might store significantly larger amounts of membrane components, including enzymatic proteins and galactolipids crucial for efficient etioplast–chloroplast transition.
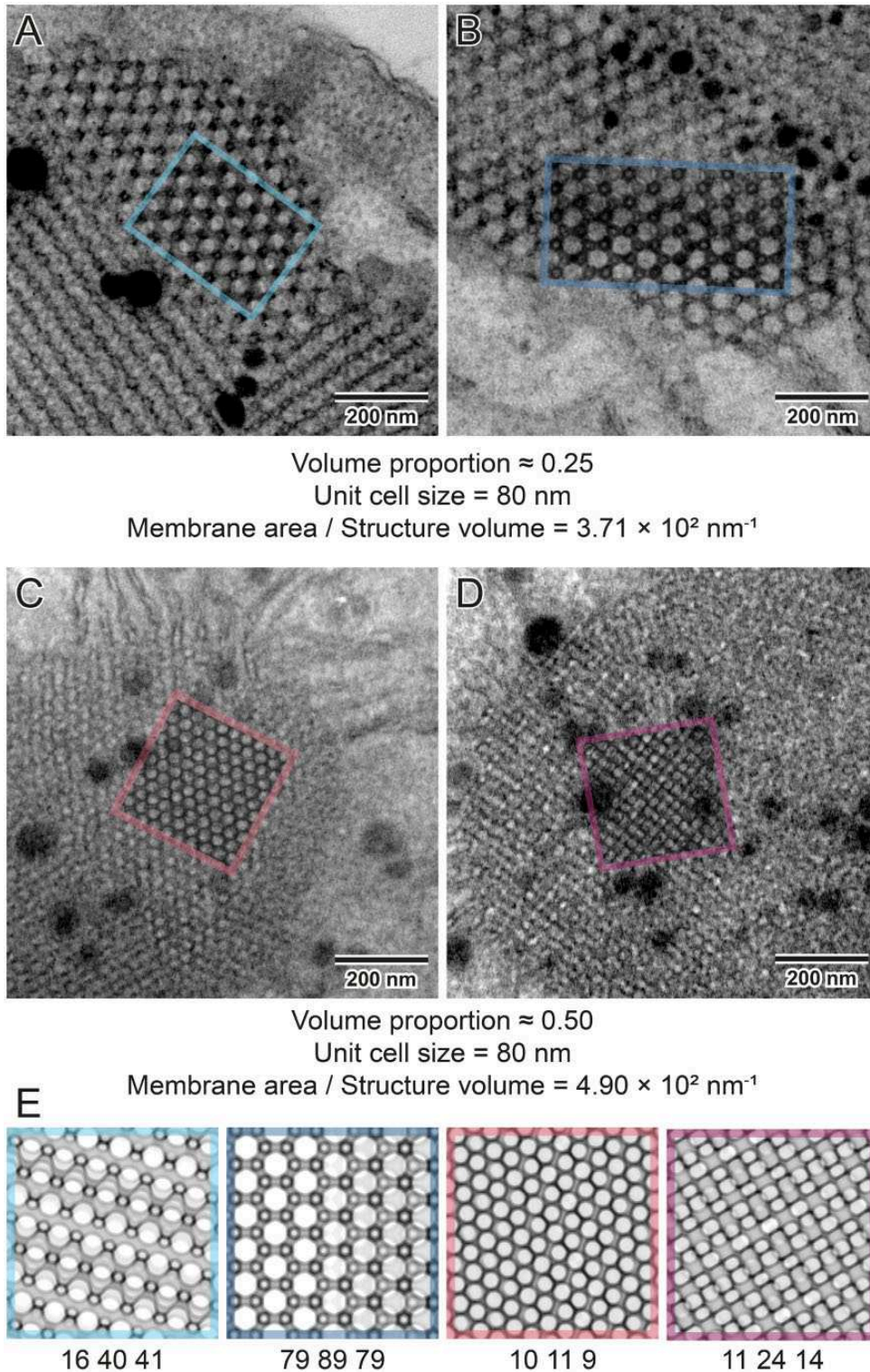
Figure 9 Imbalanced versus balanced nature of PLB cubic membranes. PLBs are cubic membranes of diamond configuration characterized by an imbalanced structure in which two aqueous channels are geometrically different (A and B); regions marked with colored rectangles show a super-position of computed projections and TEM images using multiply blend mode. Changes in the volume proportion resulting in geometrically balanced PLB structure without disturbances in the UC size are observed in plants over accumulating protochlorophyllide (*pif1* mutants of Arabidopsis)—a primary precursor pigment of etioplasts (C and D). Computed projections show differences in the observed patterns of networks that structurally differ only in the volume proportion ratio (E). This variability also influences the structure's membrane packaging potential; geometrically balanced PLBs can accumulate more membrane components in the given volume; all parameters used to generate projections are listed in Supplemental Table S1.
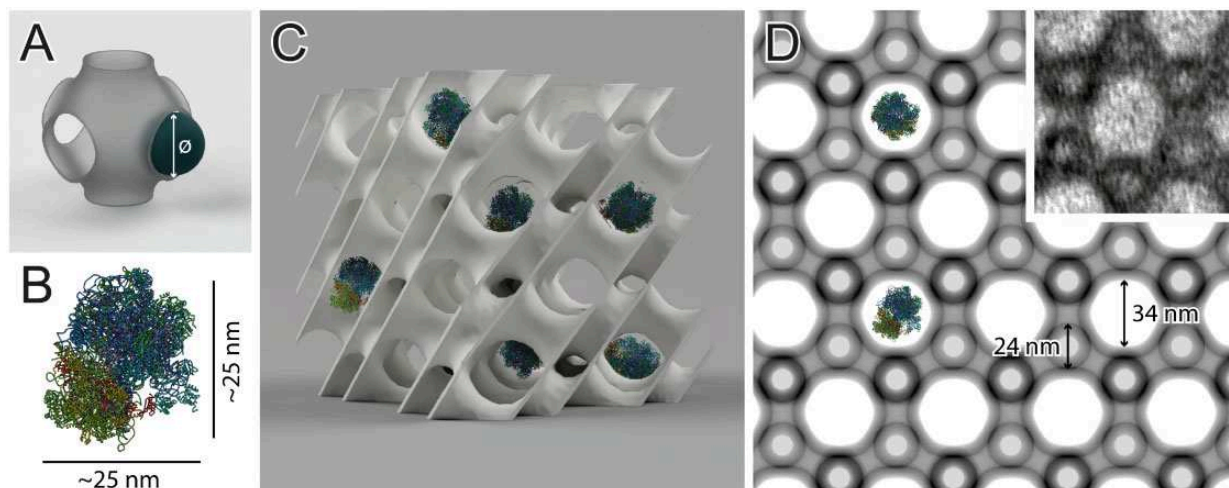
Figure 10 Penetrability of the 3D prolamellar network—combining ultrastructural and molecular data. To estimate the maximum diameter of a sphere that can freely penetrate through a channel of the entire structure, the "percolation threshold" implemented in SPIRE can be computed (A). Here we used an example of plastid ribosome (B, PDB 5MMM, spinach (*Spinacia oleracea*) 70S chloroplast ribosome modeled using Chimera software) whose size is comparable with diameters of the oat PLB channels. Using the percolation threshold function, it is possible to estimate whether a molecule whose spatial structure is already revealed could move freely through the channels of a particular cubic surface (C). The percolation threshold (31.57 nm) of a given network (UC size 80 nm, volume proportion 0.25), identified by a structure's projection (D), can be calculated in SPIRE. The diamond network of oat PLB in (111) direction is presented with ribosomes in the same scale, the region marked with a white square presents superposition of computed projection and TEM image using multiply blend mode. Note that proper calculations are also provided for the surfaces recognized by projections in which the channel's maximal diameter (40.11 nm) is not visible. In this example, ribosome size is smaller than the oat PLB's percolation limit, which indicates that this molecule can move freely through the larger aqueous channel of the PLB network (stroma) of oat, hypothetically fulfilling its biological function directly inside the cubic structure; all parameters used to generate projection are listed in Supplemental Table S1.

In Figure 10, we present the exemplary utilization of the percolation threshold function. The obtained values indicate that the oat PLB structure enables a free flow of chloroplast ribosome particles through a larger aqueous network channel. Our percolation limit calculation stays in line with recent experimental electron cryo-tomography data, which confirmed the presence of fully assembled ribosomes at a stromal side of a ruptured pea etioplast PLB (Floris and Kuhlbrandt, 2021). However, it should be stressed that in both cases the size of the ribosome and the channel diameter are similar. Therefore, in PLBs of smaller UC size or varying volume proportion registered in different species, such mobility will be blocked. This suggests that ribosome presence in the PLB network may not be crucial for its proper functioning.

Discussion

In this work, we introduced a software tool (SPIRE), which, based on "nodal surface" models, generates synthetic microscopy images of cubic membranes, bicontinuous phases and other structures. This tool enables the stereological identification of 3D structures based on their 2D projections, a key element in understanding structure–function relationships. We have demonstrated the basic concepts and workflow of SPIRE with a novel application to one of the common examples of cubic membranes occurring in nature—etioplast prolamellar bodies. We revealed that PLB configurations resemble a diamond surface type and, despite earlier assumptions, is not based on a lonsdaleite (wurtzite) structure, at least for the plants analyzed here. Moreover, this work serves as a reference paper for the open-source SPIRE tool.

The development of the interdisciplinary field of naturally occurring cubic structures relies on the availability of tools to analyze observed structures; tools which can be robustly used without a need for an in-depth understanding of the mathematical background.

At this stage, much of the experimental work of biologists does not contribute to the field and might even pass unnoticed due to the lack of a common recognition of cubic arrangements. This is particularly regrettable given that biological bicontinuous structures have achieved a property that remains largely elusive in synthetic cubic phases: structure sizes (lattice parameters) > 50 nm.

By expanding the pioneering work by Deng and Mieczkowski (1998), SPIRE fills a gap in the field of surface type identification of cubic membranes, which has only been partially covered by previous methods.

In future work, we aim to improve and extend SPIRE capabilities. A prime target is to automate the matching process of the simulated projection with the actual TEM image. Here the toolbox of image analysis and classification can be employed. A very promising approach here is deep neural networks, specifically convolutional neural networks, which have been proven to efficiently classify images (Krizhevsky et al., 2012; Rawat and Wang, 2017). Having several

projections of a structure at different orientations available (as is the case for the samples presented here) could significantly increase the matching accuracy. SPIRE is ideally suited to generate training data sets of nearly arbitrary size for these purposes.

An anticipated broad interest in periodic structure recognition in biological samples enabled by SPIRE will lead to the proper identification of many naturally occurring bicontinuous structures, including geometric measurements computed by the tool. Starting with and extending the tables and data of cubic membrane occurrence in biological systems provided by Almsherqi et al. (2009), Landh (1996) and further literature, this could be the start for a new repository, connecting geometric structures with their natural or synthetic occurrence and functions. Such a database would open opportunities for the meta-analyses of geometric arrangements occurrence in the contexts of their, for example, composition, evolutionary background, developmental importance, and biological meaning, and thus pave the way for insights on broader scales.

In most of the studies, the cubic membranes' appearance is reported without further interpretation of neither the data nor their numerical analyses. SPIRE could help to re-evaluate and properly annotate numerous already published structures. SPIRE enables acquiring several spatial parameters of the network, which might also be interpreted in the context of other experimental data, for example, percolation limit with the mobility of molecules of given sizes whose presence in the aqueous environment of the network has been confirmed in biochemical studies.

SPIRE is a key tool to accelerate the dynamic field combining actual biological data, computer modeling, and finally, obtaining synthetic periodic structures based on natural ones. Therefore, SPIRE has the potential to broaden our understanding of cellular cubic membranes, their biological role, and their relevance in designing nature-inspired artificial bicontinuous phases of comprehensive utilization.

Materials and methods

Implementation details
The tool (https://sourceforge.net/projects/spire-tool/) as well as the source code (https://github.com/tohain/SPIRE) and all dependencies are open source and thus freely and openly available. The software was entirely written in C++ providing an intuitive GUI, shown in Supplemental Figure S7, implemented using the QT libraries (https://doc.qt.io/). Several libraries are used in this tool: integer math library (https://cs.uwaterloo.ca/~astorjoh/iml.html), openblas (https://www.openblas.net/), gnu multiprecision library (https://gmplib.org/), and gnu multiple precision floating point reliable library (https://www.mpfr.org/) are used to compute minimal UCs, zlib (https://www.zlib.net/), and libpng (http://www.libpng.org/pub/png/libpng.html) are used to output projections to the .png image format, the (CGAL (https://www.cgal.org/) is used to reconstruct surfaces to measure their area. Furthermore the algorithms from (Felzenszwalb and Huttenlocher, 2012)

are implemented to compute the EDM and the Hoshen and Kopelman (1976) algorithm is used to compute the percolation threshold.

A separation of the computational core code and the interface code allows the use as a library to incorporate into further projects. A simple command line interface for the creation of large batches of projections as an example is included.

The code is designed to allow an easy implementation of further surface types, given in the form of an implicit level-set equation.

Plant material and growth conditions
Oat (*A. sativa* L.), maize (*Z. mays* L.), pea (*P. sativum* L.), runner bean (*P. coccineus* L.), and cucumber (*C. sativus* L.) dark-germinated seedlings were etiolated for 1 week in high closed glass containers on wet paper moistened with nutrient solution containing 3 mM $Ca(NO_3)_2$, 1.5 mM KNO_3, 1.2 mM $MgSO_4$, 1.1 mM KH_2PO_4, 0.1 mM $C_{10}H_{12}N_2O_8FeNa$, 5 μM $CuSO_4$, 2 μM $MnSO_4 \cdot 5H_2O$, 2 μM $ZnSO_4 \cdot 7H_2O$, and 15 nM $(NH_4)6Mo_7O_{24} \cdot 4H_2O$, pH 6.0–6.5, room temperature (RT). An additional week of etiolation was applied for oat seedlings used in particular experiments. Seeds of *A. thaliana* Col-0 (N1092) and mutant *pif1* (N66041; Huq et al., 2004) were obtained from The European Arabidopsis Stock Center. Seeds were stratified in 4°C for 24 h, and 4 h illumination (120 μmol photons m^{-2} s^{-1} 23°C) was applied to induce germination. Seedlings were etiolated for 5 d in Petri dishes on Murashige and Skoog Basal Medium supplemented with Gamborg B5 vitamin mixture (M0231; Duchefa Biochemie, Haarlem, Netherlands) and 0.8% (w/v) Phytagel (P8169; Sigma-Aldrich, St Louis, MO, USA) in 23°C. Leaf and cotyledon samples were collected under photomorphogenetically inactive dim green light.

TEM
Leaf specimens were fixed in 2.5% (v/v) glutaraldehyde in 0.05 M cacodylate buffer, pH 7.4 (prepared using 25% v/v glutaraldehyde solution G5882, Sigma-Aldrich; sodium cacodylate trihydrate C0250, Sigma-Aldrich; pH adjusted with 0.1 M HCl) for 2 h, washed, and postfixed in 2% (w/v) OsO_4 in 0.05 M cacodylate buffer, pH 7.4 (prepared using 4% w/v OsO_4 solution R1023; Agar Scientific, Essex, UK) at 4°C over-night. Samples were dehydrated in a graded series of acetone and embedded in epoxy resin (AGR1031 Agar 100 Resin Kit, Agar Scientific). The material was cut on a Leica UCT ultramicrotome into 70 nm sections. Samples were analyzed in a JEM 1400 electron microscope (Jeol) equipped with a Morada G2 CCD camera (EMSIS GmbH, Münster, Germany) in the Laboratory of Electron Microscopy, Nencki Institute of Experimental Biology of Polish Academy of Sciences, Warsaw, Poland. The PLB ultrastructural features were measured with the help of ImageJ software (Abramoff et al., 2004). The periodicity of 2D sections was calculated based on averaged values obtained from Fast Fourier Transform of PLB cross-sections. PLB tubule diameters were

measured manually based on each tubule's outer limits in particular orientations of PLB cross-sections.

In silico image generation and manipulation

Projections obtained using SPIRE were superimposed on TEM micrographs (where applicable) using multiply blend mode in Adobe Photoshop. In Figure 7C, the image was obtained using Adobe Photoshop by deleting a portion of the TEM micrograph and substituting it with projections generated using SPIRE. Random noise was added using Add Noise filter with Gaussian Distribution and Monochromatic settings on a uniform gray image (RGB 127 127 127), blurred using Gaussian blur filter, and superimposed on the image using multiply blend mode. Meshes of 3D models were generated in Houdini using the level-set representation of the surfaces and rendered using Autodesk Fusion 360 software. The 70S chloroplast ribosome was obtained from RCSB PDB (accession number 5MMM) and rendered using UCSF Chimera software (Pettersen et al., 2004).

Supplemental data

The following materials are available in the online version of this article.

Supplemental Figure S1. Choice of lattice vectors of the fundamental UC of the lonsdaleite surface.

Supplemental Figure S2. Multi-layer membrane structures and channel enumeration.

Supplemental Figure S3. Renderings of the fundamental UCs of the built-in structures.

Supplemental Figure S4. Diamond and gyroid type surfaces and computer simulation of TEM images of respective structures cut into sections of variable thickness (40–250 nm).

Supplemental Figure S5. Gallery of selected hkl projections of four different surface types implemented in the software.

Supplemental Figure S6. PLB network structural parameters are stable in etioplasts of the same seedling.

Supplemental Figure S7. Screenshot of the GUI of SPIRE.

Supplemental Table S1. Choice of lattice vectors for fundamental UCs.

Supplemental Table S2. Parameters used to generate projections.

Acknowledgments

Funding

References

Abramoff MD, Magalhaes PJ, Ram SJ (2004) Image processing with ImageJ. Biophotonics Int **11**: 36–42

Adam Z, Charuvi D, Tsabari O, Knopf RR, Reich Z (2011) Biogenesis of thylakoid networks in angiosperms: knowns and unknowns. Plant Mol Biol **76**: 221–234

Almsherqi ZA, Kohlwein SD, Deng Y (2006) Cubic membranes: a legend beyond the Flatland of cell membrane organization. J Cell Biol **173**: 839–844

Almsherqi ZA, Landh T, Kohlwein SD, Deng Y (2009) Chapter 6- Cubic membranes: the missing dimension of cell membrane organization. International Review of Cell and Molecular Biology, volume of International Review of Cell and Molecular Biology, Academic Press, Cambridge, MA, pp 275–342

Armarego-Marriott T, Kowalewska Ł, Burgos A, Fischer A, Thiele W, Erban A, Strand D, Kahlau S, Hertle A, Kopka J, et al. (2019) Highly resolved systems biology to dissect the etioplast-to-chloroplast transition in tobacco leaves. Plant Physiol **180**: 654–681

Bates FS (2005) Network phases in block copolymer melts. MRS Bull **30**: 525–532

Brakke KA (1992) The surface evolver. Exp Math **1**: 141–165

Bykowski M, Mazur R, Buszewicz D, Szach J, Mostowska A, Kowalewska L (2020) Spatial nano-morphology of the prolamellar body in etiolated *Arabidopsis thaliana* plants with disturbed pigment and polyprenol composition. Front Cell Dev Biol **8**: 586628

Callens SJP, Uyttendaele RJC, Fratila-Apachitei LE, Zadpoor AA (2020) Substrate curvature as a cue to guide spatiotemporal cell and tissue organization. Biomaterials **232**: 119739

Cazzonelli CI, Hou X, Alagoz Y, Rivers J, Dhami N, Lee J, Marri S, Pogson BJ (2020) A cis-carotene derived apocarotenoid regulates etioplast and chloroplast development. eLife **9**: e45310

Chong K, Deng Y (2012) Chapter 15 - The three dimensionality of cell membranes: lamellar to cubic membrane transition as investigated by electron microscopy. *In* G Di Paolo, MR Wenk, eds, Methods in Cell Biology, Vol. 108 of Lipids, Academic Press, Cambridge, MA, pp 317–343.

Cui C, Deng Y, Han L (2020) Bicontinuous cubic phases in biological and artificial self-assembled systems. Sci China Mater **63**: 686–702

Da TKF, Cohen-Steiner D (2020) Advancing Front Surface Reconstruction. CGAL Editorial Board, Ed 5.2

Demurtas D, Guichard P, Martiel I, Mezzenga R, H'ebert C, Sagalowicz L (2015) Direct visualization of dispersed lipid bicontinuous cubic phases by cryo-electron tomography. Nat Commun **6**: 8915

Deng Y, Mieczkowski M (1998) Three-dimensional periodic cubic membrane structure in the mitochondria of amoebae *Chaos carolinensis*. Protoplasma **203**: 16–25

Deng Y, Marko M, Buttle KF, Leith A, Mieczkowski M, Mannella CA (1999) Cubic membrane structure in Amoeba (*Chaos carolinensis*) mitochondria determined by electron microscopic tomography. J Struct Biol **127**: 231–239

Evans ME, Hyde ST (2011) From three-dimensional weavings to swollen corneocytes. J Royal Soc Interface **8**: 1274–1280

Evans ME, Roth R (2014) Shaping the skin: the interplay of mesoscale geometry and corneocyte swelling. Phys Rev Lett **112**: 038102

Felzenszwalb PF, Huttenlocher DP (2012) Distance transforms of sampled functions. Theory Comput 8: 415–428

Floris D, Kuhlbrandt W (2021) Molecular landscape of etioplast inner membranes in higher plants. Nat Plants 7: 514–523

Fujii S, Nagata N, Masuda T, Wada H, Kobayashi K (2019) Galactolipids are essential for internal 617 membrane transformation during etioplast-to-chloroplast differentiation. Plant Cell Physiol 60: 1224–1238

Gunning BE, Steer MW (1975) Ultrastructure and the Biology of Plant Cells, Arnold, London

Gunning BES (2001) Membrane geometry of" open" prolamellar bodies. Protoplasma 215: 4–15

Han L, Fujita N, Chen H, Jin C, Terasaki O, Che S (2020) Crystal twinning of bicontinuous cubic structures. IUCrJ 7: 228–237

Hoshen J, Kopelman R (1976) Percolation and cluster distribution. I. Cluster multiple labeling technique and critical concentration algorithm. Phys Rev B 14: 3438–3445

Huq E, Al-Sady B, Hudson M, Kim C, Apel K, Quail PH (2004) PHYTOCHROME-INTERACTING FACTOR 1 is a critical bHLH regulator of chlorophyll biosynthesis. Science 305: 1937–1941

Hyde S, Blum Z, Landh T, Lidin S, Ninham BW, Andersson S, Larsson K (1996) The Language of Shape: The Role of Curvature in Condensed Matter: Physics, Chemistry and Biology, Ed 1, Elsevier Science, Amsterdam, Netherlands; New York, NY

Ikeda T (1968) Analytical studies on structure of prolamellar body. Bot Mag.-TOKYO 81: 517

Jarsch IK, Daste F, Gallop JL (2016) Membrane curvature in cell biology: an integration of molecular mechanisms. J Cell Biol 214: 375–387

Kirkensgaard JJK, Fragouli P, Hadjichristidis N, Mortensen K (2011) Perforated lamellae morphology in novel P2VP(PDMS-b-PI-b-PS)2 3-miktoarm star qarterpolymer. Macromolecules 44: 575–582

Kittel C (2004) Introduction to Solid State Physics, Ed 8, Wiley, Hoboken, NJ

Klinowski J, Mackay AL, Terrones H, Klinowski J, Mackay AL (1996) Curved surfaces in chemical structure. Philos Trans Royal Soc Lond A Mathe Phys Eng Sci 354: 1975–1987

Kowalewska Ł, Mazur R, Suski S, Garstka M, Mostowska A (2016) Three-dimensional visualization of the tubular-lamellar transformation of the internal plastid membrane network during runner bean chloroplast biogenesis. Plant Cell 28: 875–891

Kowalewska Ł, Bykowski M, Mostowska A (2019) Spatial organization of thylakoid network in higher plants. Bot Lett 166: 326–343

Kozlov MM, Campelo F, Liska N, Chernomordik LV, Marrink SJ, McMahon HT (2014) Mechanisms shaping cell membranes. Curr Opin Cell Biol 29: 53–60

Krizhevsky A, Sutskever I, Hinton GE (2012) ImageNet classification with deep convolutional neural networks. Proceedings of the 25th International Conference on Neural Information Processing Systems, Vol. 1, NIPS'12, Curran Associates Inc., Red Hook, NY, pp 1097–1105

Landh T (1996) Cubic cell membrane architectures. Taking another look at membrane bound cell spaces. PhD thesis. Department of Food Technology, Lund University, Lund, Sweden

Lou HY, Zhao W, Zeng Y, Cui B (2018) The role of membrane curvature in nanoscale topography- induced intracellular signaling. Account Chem Res 51: 1046–1053

Luzzati V (1997) Biological significance of lipid polymorphism: the cubic phases. Curr Opin Struct Biol 7: 661–668

Menke W (1963) Zur Stereometrie der Heitz-Leyonschen Kristalle von Chlorophytum comosum. Z Für Naturforsch B 18: 821–826

Mezzenga R, Seddon JM, Drummond CJ, Boyd BJ, Schröder-Turk GE, Sagalowicz L (2019) Nature-inspired design and application of lipidic lyotropic liquid crystals. Adv Mater 31: 1900818

Mickel W, Munster S, Jawerth LM, Vader DA, Weitz DA, Sheppard AP, Mecke K, Fabry B, Schroder-Turk GE (2008) Robust pore size analysis of filamentous networks from three-dimensional confocal microscopy. Biophys J 95: 6072–6080

Nguyen HC, Melo AA, Kruk J, Frost A, Gabruk M (2021) Photocatalytic LPOR forms helical lattices that shape membranes for chlorophyll synthesis. Nat Plants 7: 437–444

Norlen L, Al-Amoudi A (2004) Stratum corneum keratin structure, function, and formation: the cubic rod-packing and membrane templating model. J Invest Dermatol 123: 715–732

O'Keeffe M, Plevert J, Teshima Y, Watanabe Y, Ogama T (2001) The invariant cubic rod (cylinder) packings: symmetries and coordinates. Acta Cryst A 57: 110–111

Pettersen EF, Goddard TD, Huang CC, Couch GS, Greenblatt DM, Meng EC, Ferrin TE (2004) UCSF Chimera—A visualization system for exploratory research and analysis. J Comput Chem 25: 1605–1612

Pipitone R, Eicke S, Pfister B, Glauser G, Falconet D, Uwizeye C, Pralon T, Zeeman SC, Kessler F, Demarsy E (2021) A multifaceted analysis reveals two distinct phases of chloroplast biogenesis during de-etiolation in Arabidopsis. eLife 10: e62709

Pribil M, Labs M, Leister D (2014) Structure and dynamics of thylakoids in land plants. J Exp Bot 65: 1955–1972

Rawat W, Wang Z (2017) Deep convolutional neural networks for image classification: a comprehensive review. Neural Comput 29: 2352–2449

Rudowska Ł, Gieczewska K, Mazur R, Garstka M, Mostowska A (2012) Chloroplast biogenesis correlation between structure and function. Biochim Biophys Acta 1817: 1380–1387

Sandor A, Fricker MD, Kriechbaumer V, Sweetlove LJ (2021) IntERResting structures: formation and applications of organised smooth endoplasmic reticulum in plant cells. Plant Physiol 185: 550–561

Schoen AH (1970) Infinite periodic minimal surfaces without self-intersections. NASA Technical Note, NASA TN D-5541. National Aeronautics and Space Administration, Springfield, VA

Schroder-Turk GE, Wickham S, Averdunk H, Brink F, Fitz Gerald JD, Poladian L, Large MCJ, Hyde ST (2011) The chiral structure of porous chitin within the wing-scales of Callophrys rubi. J Struct Biol 174: 290–295

Simunovic M, Evergren E, Callan-Jones A, Bassereau P (2019) Curving cells inside and out: roles of BAR domain proteins in membrane shaping and its cellular implications. Annu Rev Cell Dev Biol 35: 111–129

Skupień J, Wójtowicz J, Kowalewska Ł, Mazur R, Garstka M, Gieczewska K, Mostowska A (2017) 714 Dark-chilling induces substantial structural changes and modifies galactolipid and carotenoid composition during chloroplast biogenesis in cucumber (Cucumis sativus l.) cotyledons. Plant Physiol Biochem 111: 107–118

Sperling U, Franck F, van Cleve B, Frick G, Apel K, Armstrong GA (1998) Etioplast differentiation in Arabidopsis: both PORA and PORB restore the prolamellar body and photoactive protochlorophyllide–F655 to the cop1 photomorphogenic mutant. Plant Cell 10: 283–296

Stauffer D, Aharony A (1992) Introduction To Percolation Theory, Ed 2, Taylor & Francis, London

The CGAL Project (2020) CGAL User and Reference Manual. CGAL Editorial Board, Ed 5.2

von Schnering HG, Nesper R (1991) Nodal surfaces of Fourier series: fundamental invariants of structured matter. Z Physik B – Condensed Matter 83: 407–412 doi: 10.1007/BF01313411

Wietrzynski W, Engel BD (2021) Chlorophyll biogenesis sees the light. Nat Plants 7: 380–381

Winter B, Butz B, Dieker C, Schroder-Turk GE, Mecke K, Spiecker E (2015) Coexistence of both gyroid chiralities in individual butterfly wing scales of Callophrys rubi. Proc Natl Acad Sci USA 112: 12911–12916

Wohlgemuth M, Yufa N, Hoffman J, Thomas EL (2001) Triply periodic bicontinuous cubic microdomain morphologies by symmetries. Macromolecules 34: 6083–6089

Yoshioka S, Fujita H, Kinoshita S, Matsuhana B (2014) Alignment of crystal orientations of the multi-domain photonic crystals in Parides sesostris wing scales. J Royal Soc Interface 11: 20131029

Zhan T, Lv W, Deng Y (2017) Multilayer gyroid cubic membrane organization in green alga Zygnema. Protoplasma 254: 1923–1930

Supplementary Material for SPIRE, a software tool for bicontinuous phase recognition: application for plastid cubic membranes

Tobias M. Hain[1,2,3], Michał Bykowski[4], Matthias Saba[5], Myfanwy E. Evans[1], Gerd E. Schröder-Turk[2,6], Łucja Kowalewska[4]

[1]Institute of Mathematics, University of Potsdam, Karl-Liebknecht-Str. 24-25, D-14476 Potsdam OT Golm, Germany

[2]Murdoch University, College of Science, Health, Engineering and Education, Mathematics and Statistics, 90 South St., Murdoch, WA 6150, Australia

[3]Physical Chemistry, Center for Chemistry and Chemical Engineering, Lund University, Lund 22100, Sweden

[4]Department of Plant Anatomy and Cytology, Institute of Experimental Plant Biology and Biotechnology, Faculty of Biology, University of Warsaw, Warsaw, Poland

[5]Adolphe Merkle Institute, University of Fribourg, Chemin des Verdiers 4, CH-1700 Fribourg, Switzerland

[6]The Australian National University, Research School of Physics, Department of Applied Mathematics, Canberra Acton ACT 2601, Australia

1

.1 Supplementary figures
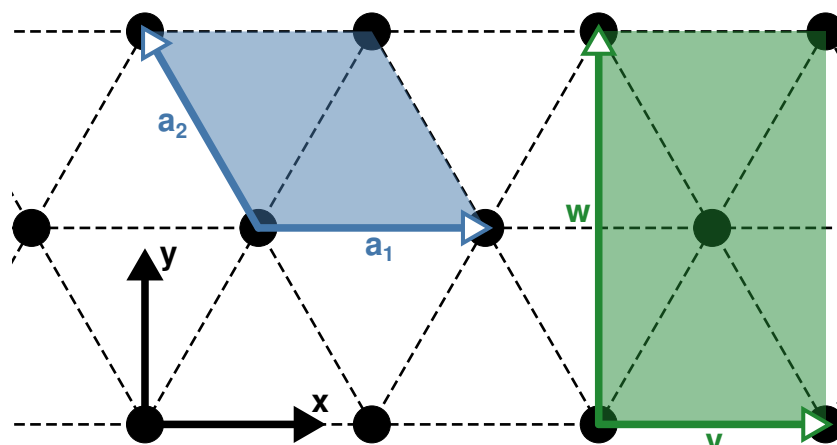
Supplemental Figure S1: **Choice of lattice vectors of the fundamental unit cell of the lonsdaleite surface.** Shown is a top-down view of a hexagonal structure with the canonical choice of the unit cell (lattice vectors a_1 and a_2) and a rectangular unit cell (lattice vectors v and w). For convenience, we chose the rectangular unit cell over the canonical choice. The exact dimensions of the fundamental unit cell are provided in Table S1
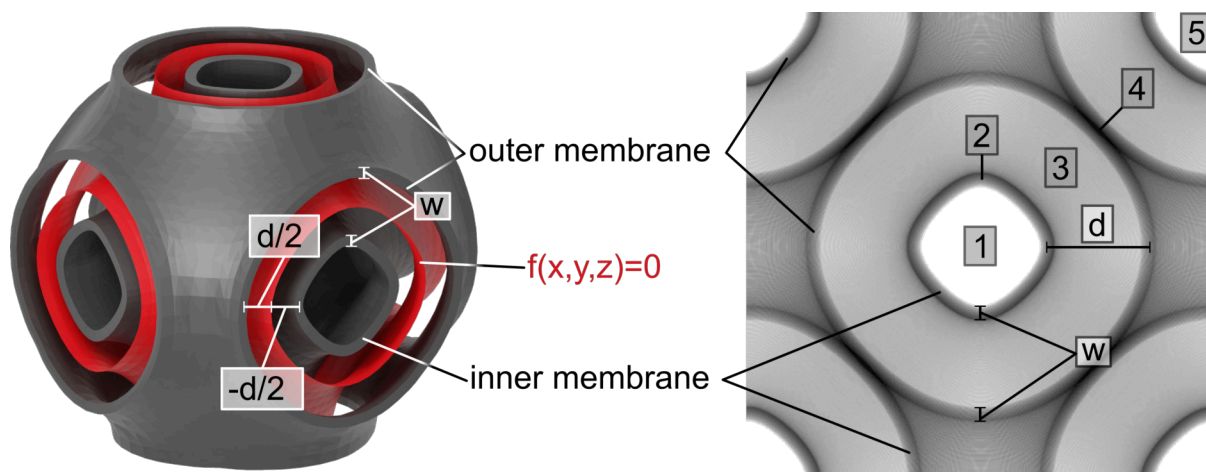
Supplemental Figure S2: **Multi-layer membrane structures and channel enumeration** A primitive surface multi-layer membrane system and its 2D projection in (100) orientation with two membranes of width w at a distance of d computed as parallel surfaces from the level-set membrane, the minimal surface at $f(x, y, z) = 0$, shown in red. The latter is only computed internally and does not show in the projection. The inner membrane is inside of the level-set membrane, therefore has a negative distance. The numbers denote the channel numbers of a total of 5 channels, of which 3 are "true" channels and 2 are membranes, also considered as channels internally.
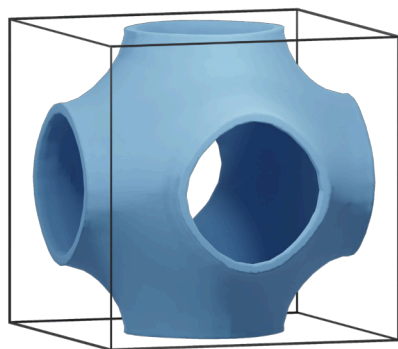
Primitive
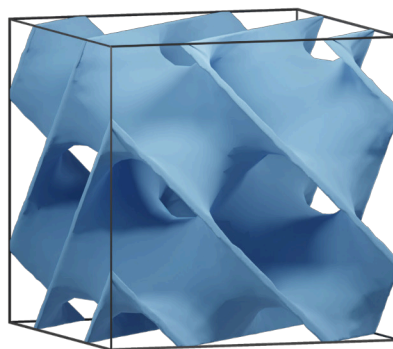
Diamond
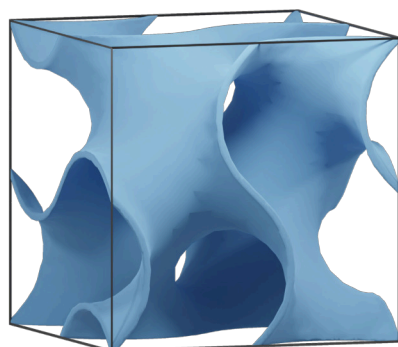
Gyroid

Lonsdaleite

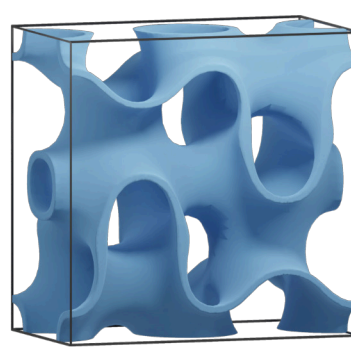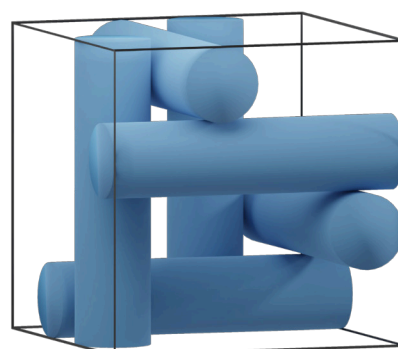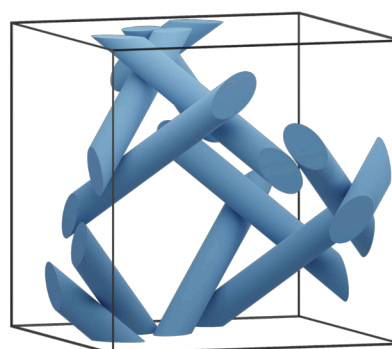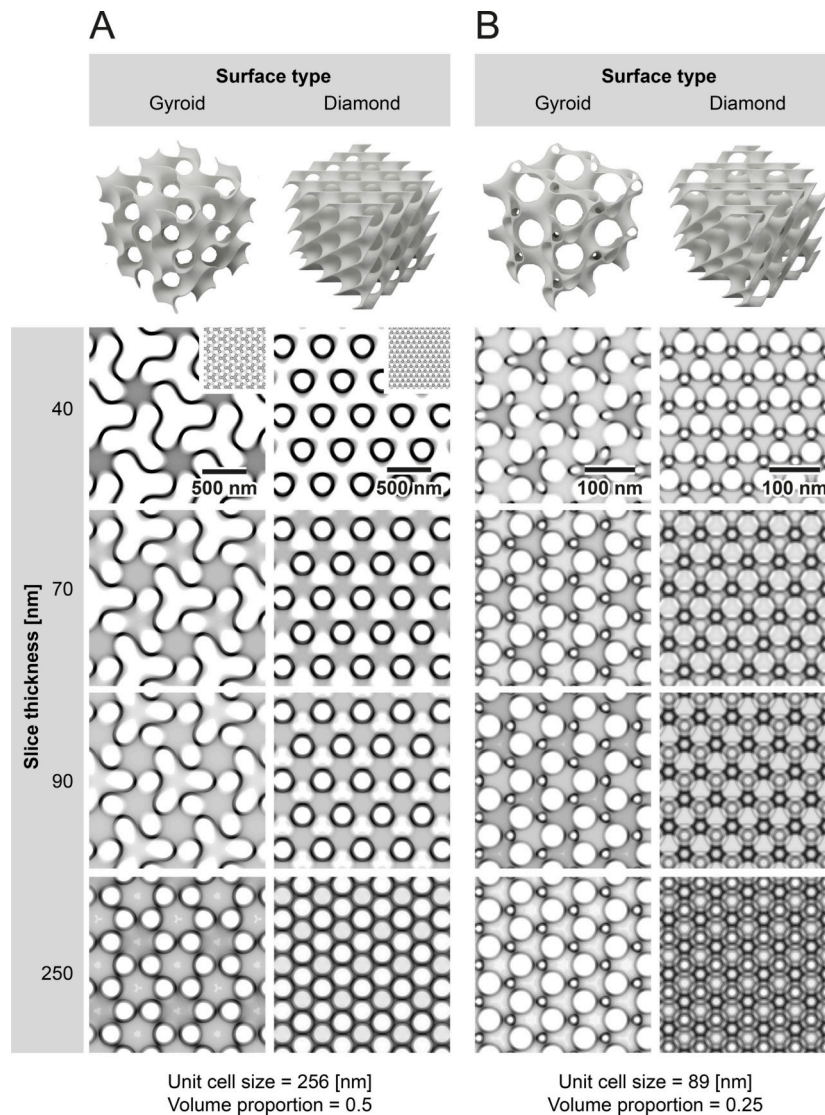β-Mn rod packing

Σ^+ rod packing

Supplemental Figure S3: **Renderings of the fundamental unit cells of the built-in structures**

3

Supplemental Figure S4: **Diamond and gyroid type surfaces and computer simulation of Transmission Electron Microscopy (TEM) images of respective structures cut into sections of variable thickness (40–250 nm)** The first row presents three-dimensional (3D) models of eight unit cells (UCs) of gyroid and diamond surfaces with balanced (**A**) and imbalanced (**B**) channel proportion. Computer simulations of TEM images are based on structural parameters (UC size and volume proportion – see bottom of the image) of cubic membranes recognized in (**A**) – gyroid of *Zygnema* sp. chloroplasts (Zhan et al., 2017) and (**B**) – diamond of bean *P. coccineus* etioplasts (Kowalewska et al., 2016). Note that for a better comparison, both surface types are simulated using the same structural parameters and are presented in (111) direction only. The figure shows how the slice thickness (subsequent rows) and structure scale (large (**A**) vs. small (**B**)) influence the pattern observed in computer simulations and, therefore, actual TEM images of such structures. Insets visible in the upper right corners of the second row of panel (**A**) present projections from panel (**B**) scaled equally; all parameters used to generate projections are listed in Table S2.
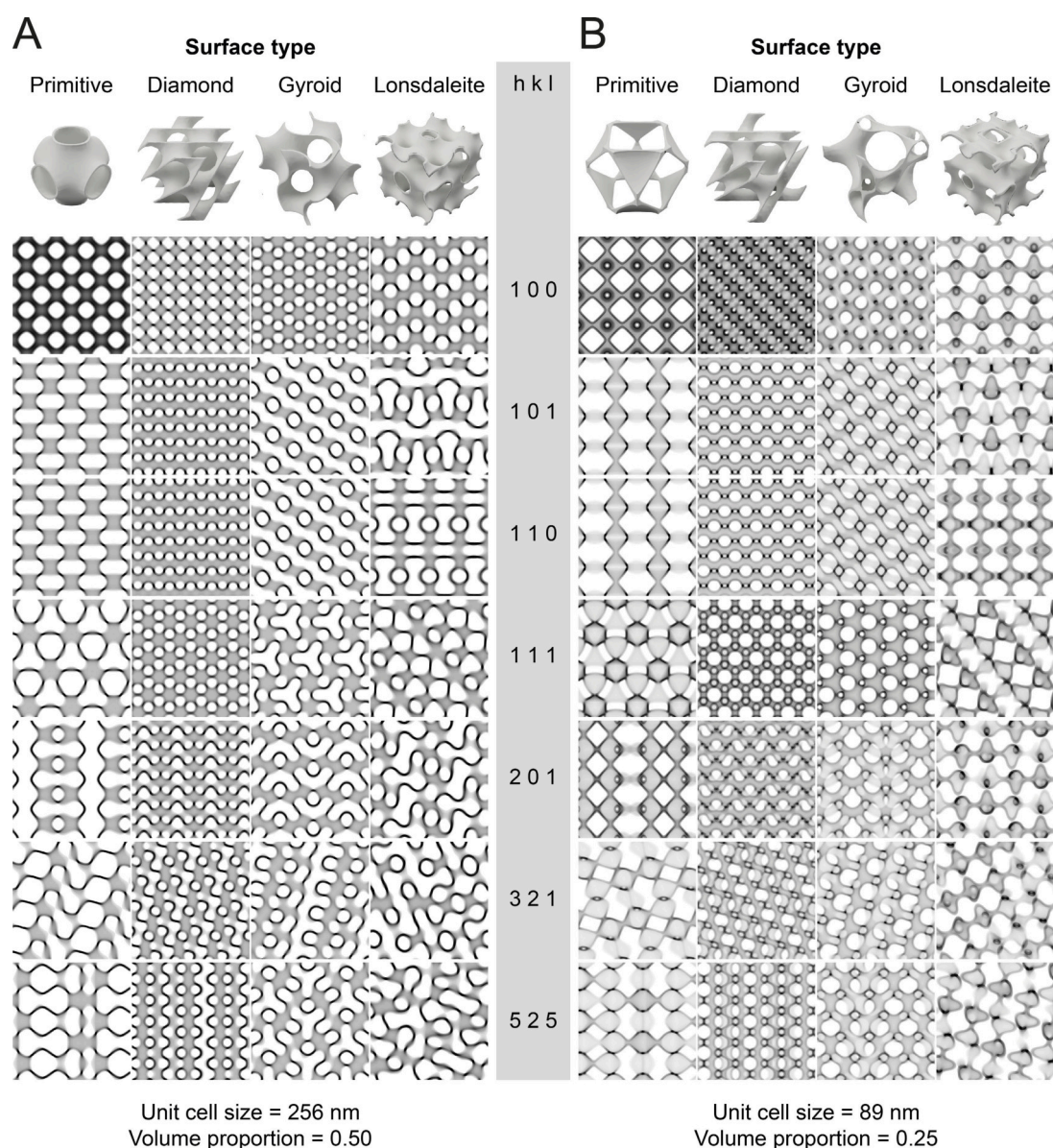
4

Supplemental Figure S5: **Gallery of selected** (hkl) **projections of four different surface types implemented in the software.** The efficient process of surface matching is preceded by obtaining structural parameters such as unit cell (UC) size and volume proportion estimated directly from Transmission Electron Microscopy (TEM) images. The second step is completed by selecting a proper surface type and recognizing the structure's orientation on the particular micrograph. For this purpose, a basic gallery showing variable (hkl) projections of different surface types, based on the idea provided by (Deng and Mieczkowski, 1998), computed for balanced/imbalanced and large/small length scaled structures is a good starting point. Custom, more tailored galleries can be created by the user with the bulk creation function of the tool. Note that projections were computed to simulated TEM samples of 70 nm thickness for membrane structural parameters (UC size and volume proportion), same as in Figure S4 on panels (**A**) and (**B**), respectively. three-dimensional (3D) models of periodic surfaces (first row) are presented for a single UC of all surface types; computed projections of TEM images are scaled to show the same number of UC despite the structure's length scale; all parameters used to generate projections are listed in Table S2.

5
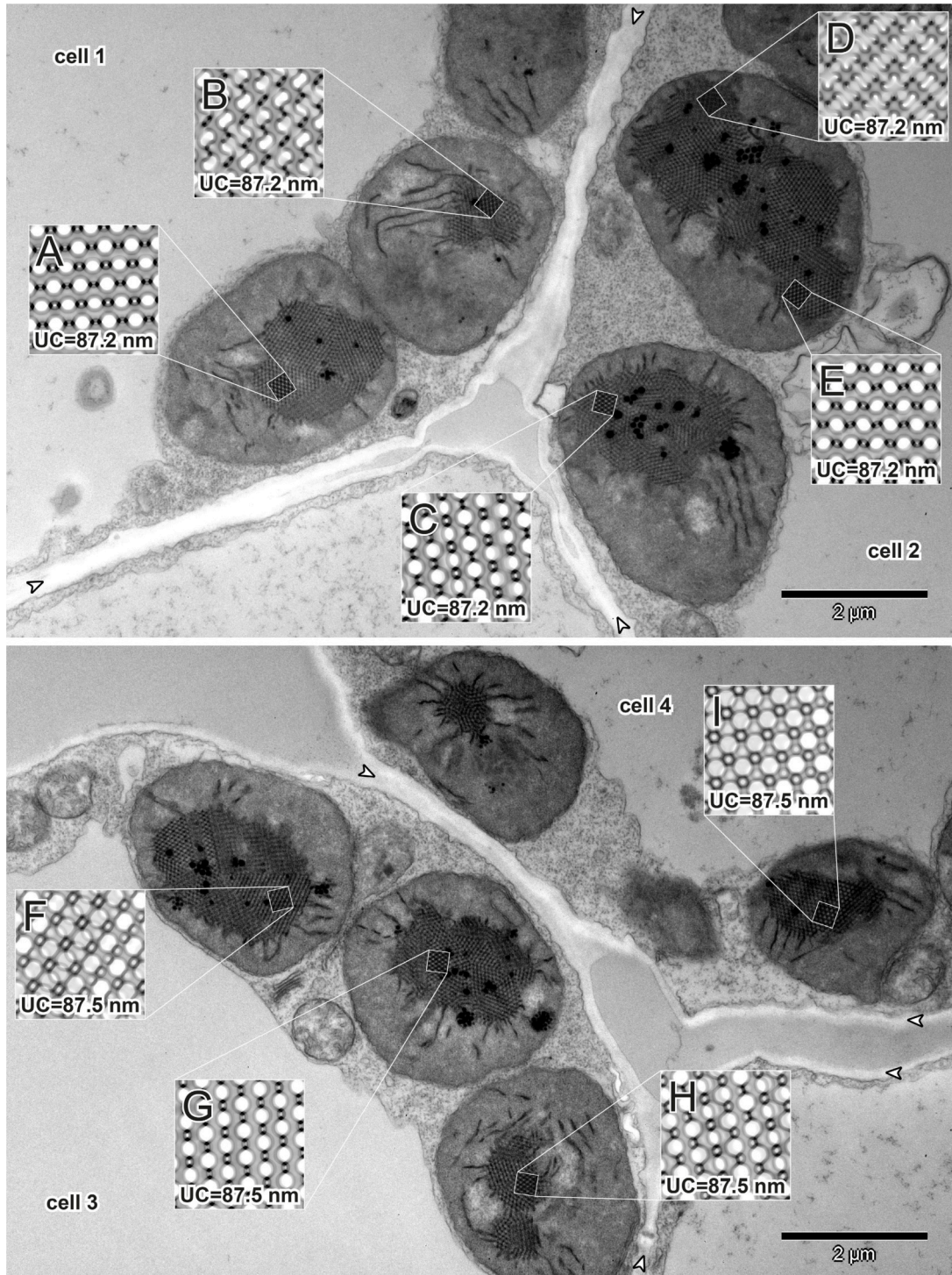
Supplemental Figure S6: **Prolamellar body (PLB) network structural parameters are stable in etioplasts of the same seedling.** Electron micrographs of mesophyll cells in two-week etiolated oat seedlings (same plant) showing etioplasts with diamond-type PLBs (**A**–**H**). PLB surface type was recognized via matching with computed projections of diamond surface type. Regions marked with rectangles present superposition of computed projections and TEM images using multiply blend mode; Regions marked with rectangles present superposition of computed projections and TEM images using multiply blend mode.

6
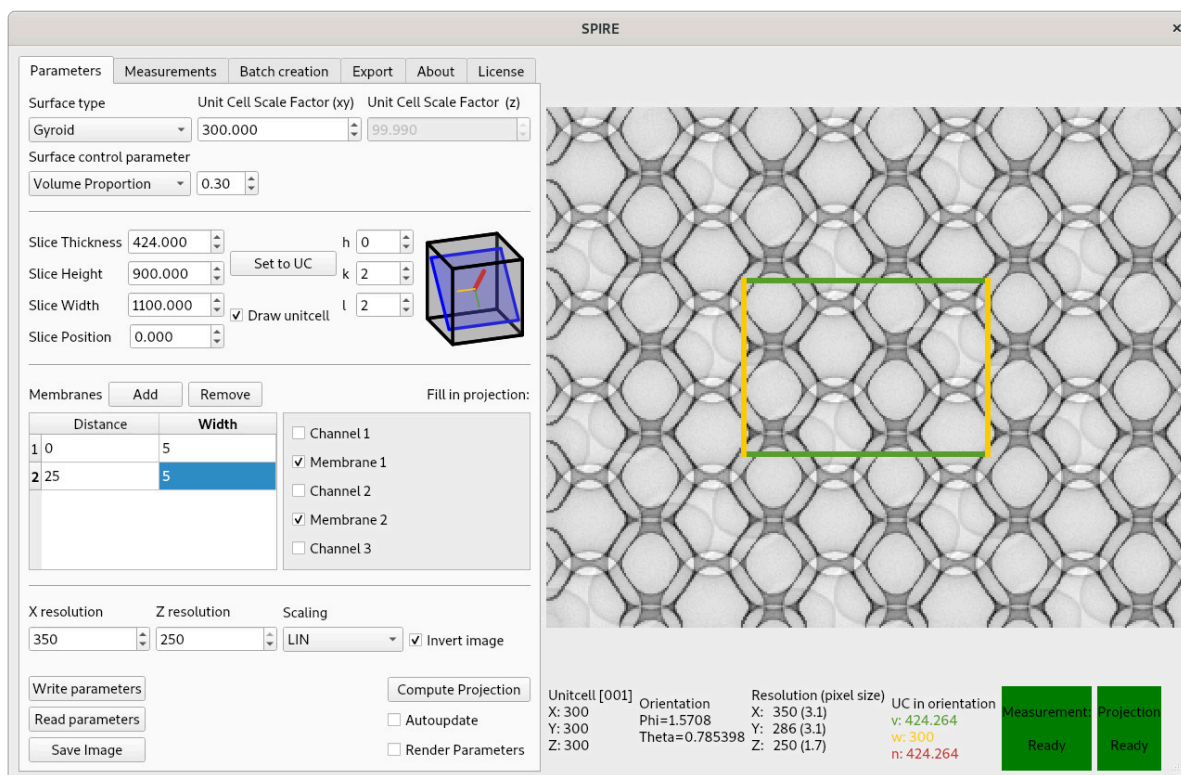
Supplemental Figure S7: **Screenshot of the Graphical User Interface (GUI) of SPIRE**

7

.2 Supplementary tables

Supplemental Table S1: Choice of lattice vectors for fundamental unit cells

Primitive	$a_1 = (1,0,0)^\mathsf{T}$, $a_2 = (0,1,0)^\mathsf{T}$, $a_3 = (0,0,1)^\mathsf{T}$
Diamond	$a_1 = (1,0,0)^\mathsf{T}$, $a_2 = (0,1,0)^\mathsf{T}$, $a_3 = (0,0,1)^\mathsf{T}$
Gyroid	$a_1 = (1,0,0)^\mathsf{T}$, $a_2 = (0,1,0)^\mathsf{T}$, $a_3 = (0,0,1)^\mathsf{T}$
Lonsdaleite	$a_1 = (1,0,0)^\mathsf{T}$, $a_2 = (0,\sqrt{3},0)^\mathsf{T}$, $a_3 = (0,0,1.732692)^\mathsf{T}$
Beta rod packing	$a_1 = (1,0,0)^\mathsf{T}$, $a_2 = (0,1,0)^\mathsf{T}$, $a_3 = (0,0,1)^\mathsf{T}$
Sigma rod packing	$a_1 = (1,0,0)^\mathsf{T}$, $a_2 = (0,1,0)^\mathsf{T}$, $a_3 = (0,0,1)^\mathsf{T}$

Supplemental Table S2: Parameters used to generate projections shown across the article including those matching actual TEM biological data.

Structure type	UC Scale	Vol. prop.	Slice dimensions [nm]	Slice position [nm]	Orientation	Membrane width [nm]
			Figure 6 F			
Diamond	80	0.25	350 x 350 x 70	200	(5 3 5)	7
			Figure 6 G			
Diamond	80	0.25	350 x 350 x 70	140	(10 13 10)	7
	80	0.25	350 x 350 x 70	140	(5 3 7)	7
			Figure 6 H			
Diamond	80	0.25	350 x 350 x 70	60	(5 3 5)	7
	80	0.25	350 x 350 x 70	60	(2 3 2)	7
			Figure 7 B, C			
Diamond	80	0.25	350 x 350 x 40	190	(18 4 1)	5
	80	0.25	350 x 350 x 40	190	(83 100 107)	5
	80	0.25	350 x 350 x 40	190	(18 4 1)	5
	80	0.25	350 x 350 x 40	190	(79 26 70)	5
	80	0.25	350 x 350 x 40	190	(90 100 11)	5
	80	0.25	350 x 350 x 40	190	(18 4 1)	5
	80	0.25	350 x 350 x 40	190	(45 50 54)	5
	80	0.25	350 x 350 x 40	190	(18 4 1)	5
	80	0.25	350 x 350 x 40	190	(90 100 11)	5
	80	0.25	350 x 350 x 40	190	(79 26 70)	5
	80	0.25	350 x 350 x 40	190	(4 1 1)	5
			Figure 8 A, G			
Diamond	80	0.25	300 x 300 x 80	0	(20 3 26)	7
			Figure 8 B, H			
Diamond	73.5	0.22	300 x 300 x 80	313	(122 104 96)	8
			Figure 8 C, I			
Diamond	90.5	0.25	300 x 300 x 70	275	(99 113 10)	8
			Figure 8 D, J			
Diamond	82	0.22	300 x 300 x 80	55	(19 13 10)	8

8

			Figure 8 E, K			
Diamond	77.9	0.22	300 x 300 x 80	50	(105 117 98)	8
			Figure 8 F, L			
Diamond	75.1	0.3	300 x 300 x 80	50	(8 7 6)	8
			Figure 9 A			
Diamond	80	0.25	350 x 350 x 70	57	(16 40 41)	5
			Figure 9 B			
Diamond	80	0.22	350 x 350 x 70	58	(79 89 79)	5
			Figure 9 C			
Diamond	80	0.48	350 x 350 x 70	50	(10 11 9)	5
			Figure 9 D			
Diamond	80	0.45	350 x 350 x 70	50	(11 24 14)	5
			Figure 10 D			
Diamond	80	0.25	120 x 240 x 60	195	(1 1 1)	5
			Figure S4 A			
Gyroid	256	0.5	800 x 800 x 40	400	(1 1 1)	15
	256	0.5	800 x 800 x 70	400	(1 1 1)	15
	256	0.5	800 x 800 x 90	400	(1 1 1)	15
	256	0.5	800 x 800 x 250	400	(1 1 1)	15
Diamond	256	0.5	800 x 800 x 40	400	(1 1 1)	15
	256	0.5	800 x 800 x 70	400	(1 1 1)	15
	256	0.5	800 x 800 x 90	400	(1 1 1)	15
	256	0.5	800 x 800 x 250	400	(1 1 1)	15
			Figure S4 B			
Gyroid	89	0.25	350 x 350 x 40	175	(1 1 1)	5
	89	0.25	350 x 350 x 70	175	(1 1 1)	5
	89	0.25	350 x 350 x 90	175	(1 1 1)	5
	89	0.25	350 x 350 x 250	175	(1 1 1)	5
Diamond	89	0.25	350 x 350 x 40	175	(1 1 1)	5
	89	0.25	350 x 350 x 70	175	(1 1 1)	5
	89	0.25	350 x 350 x 90	175	(1 1 1)	5
	89	0.25	350 x 350 x 250	175	(1 1 1)	5
			Figure S5 A			
Primitive	256	0.5	1006 x 1006 x 70	60	(1 0 0)	15
	256	0.5	1006 x 1006 x 70	60	(1 0 1)	15
	256	0.5	1006 x 1006 x 70	60	(1 1 0)	15
	256	0.5	1006 x 1006 x 70	60	(1 1 1)	15
	256	0.5	1006 x 1006 x 70	60	(2 0 1)	15
	256	0.5	1006 x 1006 x 70	60	(3 2 1)	15
	256	0.5	1006 x 1006 x 70	60	(5 2 5)	15
Diamond	256	0.5	1006 x 1006 x 70	60	(1 0 0)	15
	256	0.5	1006 x 1006 x 70	60	(1 0 1)	15
	256	0.5	1006 x 1006 x 70	60	(1 1 0)	15
	256	0.5	1006 x 1006 x 70	60	(1 1 1)	15
	256	0.5	1006 x 1006 x 70	60	(2 0 1)	15

9

	256	0.5	1006 x 1006 x 70	60	(3 2 1)	15
	256	0.5	1006 x 1006 x 70	60	(5 2 5)	15
Gyroid	256	0.5	1006 x 1006 x 70	60	(1 0 0)	15
	256	0.5	1006 x 1006 x 70	60	(1 0 1)	15
	256	0.5	1006 x 1006 x 70	60	(1 1 0)	15
	256	0.5	1006 x 1006 x 70	60	(1 1 1)	15
	256	0.5	1006 x 1006 x 70	60	(2 0 1)	15
	256	0.5	1006 x 1006 x 70	60	(3 2 1)	15
	256	0.5	1006 x 1006 x 70	60	(5 2 5)	15
Lonsdaleite	256	0.5	1006 x 1006 x 70	60	(1 0 0)	15
	256	0.5	1006 x 1006 x 70	60	(1 0 1)	15
	256	0.5	1006 x 1006 x 70	60	(1 1 0)	15
	256	0.5	1006 x 1006 x 70	60	(1 1 1)	15
	256	0.5	1006 x 1006 x 70	60	(2 0 1)	15
	256	0.5	1006 x 1006 x 70	60	(3 2 1)	15
	256	0.5	1006 x 1006 x 70	60	(5 2 5)	15

Figure S5 B

Primitive	89	0.25	350 x 350 x 70	60	(1 0 0)	5
	89	0.25	350 x 350 x 70	60	(1 0 1)	5
	89	0.25	350 x 350 x 70	60	(1 1 0)	5
	89	0.25	350 x 350 x 70	60	(1 1 1)	5
	89	0.25	350 x 350 x 70	60	(2 0 1)	5
	89	0.25	350 x 350 x 70	60	(3 2 1)	5
	89	0.25	350 x 350 x 70	60	(5 2 5)	5
Diamond	89	0.25	350 x 350 x 70	60	(1 0 0)	5
	89	0.25	350 x 350 x 70	60	(1 0 1)	5
	89	0.25	350 x 350 x 70	60	(1 1 0)	5
	89	0.25	350 x 350 x 70	60	(1 1 1)	5
	89	0.25	350 x 350 x 70	60	(2 0 1)	5
	89	0.25	350 x 350 x 70	60	(3 2 1)	5
	89	0.25	350 x 350 x 70	60	(5 2 5)	5
Gyroid	89	0.25	350 x 350 x 70	60	(1 0 0)	5
	89	0.25	350 x 350 x 70	60	(1 0 1)	5
	89	0.25	350 x 350 x 70	60	(1 1 0)	5
	89	0.25	350 x 350 x 70	60	(1 1 1)	5
	89	0.25	350 x 350 x 70	60	(2 0 1)	5
	89	0.25	350 x 350 x 70	60	(3 2 1)	5
	89	0.25	350 x 350 x 70	60	(5 2 5)	5
Lonsdaleite	89	0.25	350 x 350 x 70	60	(1 0 0)	5
	89	0.25	350 x 350 x 70	60	(1 0 1)	5
	89	0.25	350 x 350 x 70	60	(1 1 0)	5
	89	0.25	350 x 350 x 70	60	(1 1 1)	5
	89	0.25	350 x 350 x 70	60	(2 0 1)	5
	89	0.25	350 x 350 x 70	60	(3 2 1)	5
	89	0.25	350 x 350 x 70	60	(5 2 5)	5

Figure S6 A

Diamond	87.2	0.25	300 x 300 x 70	25	(91 13 92)	7

Figure S6 B

Diamond	87.2	0.25	300 x 300 x 70	25	(18 3 7)	7

Figure S6 C

10

Diamond	87.2	0.25	300 x 300 x 70	25	(71 19 72)	7

<div align="center">Figure S6 D</div>

Diamond	87.2	0.25	300 x 300 x 70	25	(181 25 11)	7

<div align="center">Figure S6 E</div>

Diamond	87.2	0.25	300 x 300 x 70	25	(90 111 7)	7

<div align="center">Figure S6 F</div>

Diamond	87.5	0.25	300 x 300 x 70	25	(33 19 22)	7

<div align="center">Figure S6 G</div>

Diamond	87.5	0.25	300 x 300 x 70	25	(78 9 75)	7

<div align="center">Figure S6 H</div>

Diamond	87.5	0.25	300 x 300 x 70	25	(81 28 74)	7

<div align="center">Figure S6 I</div>

Diamond	87.5	0.25	300 x 300 x 70	25	(89 89 76)	7

11

Conclusion and outlook: geometrically driven functional materials

In this thesis we have addressed geometrically driven soft matter systems. Our contribution is of special interest in regards to what we refer to as functional geometry: the functionality of a system or tissue is provided through its geometric structure. Examples include dynamical processes like the swelling of skin under prolonged exposure to water [Evans and Roth, 2014], "static" properties like water repelling surfaces [Darmanin and Guittard, 2015], structural color [Schröder-Turk et al., 2011b, Wilts et al., 2012a,b] or biological membranes with a vast variety of functions (reviewed e.g. in [Almsherqi et al., 2009, Mezzenga et al., 2019, Cui et al., 2020]). However, often the functionality of structures stay elusive.

Many of the aforementioned systems, especially biological systems, are self-assembled, i.e. constituents arrange without external influences solely due to internal forces. Using this process, nature's ability to build highly functional structures on larger length scales ($> 150 \, \text{nm}$) is unparalleled. A complete knowledge and understanding of these structures thus would provide powerful blueprints for the engineering of nano materials with a vast variety of functions. Two important aspects of this field are addressed by this thesis: the identification and formation of self-assembled structures.

In this concluding chapter we recap our results and put them in context with existing and ongoing research to emphasize our contribution to the field of self-assembly and structures in soft matter.

5.1   Self-assembly of geometrically optimal cellular materials

Chapter 2 addressed quasi-planar micelles in copolymer melts. When such a system is exposed to curvature the ground state shifts from a hexagonal honeycomb pattern in bulk systems to solutions of the Thomson problems on spherical surfaces. By tuning the radius of the spherical substrate the number of micelles, and thus tiles in the tiling, can be controlled. While introducing a color constraint does not change the general behavior of this system, we find a number of non-Thomson solutions, i.e. configurations corresponding to local minima in the energy landscape. We argue that introducing the color-constraint increases the complexity of the energy landscape and a simple quench as employed here can not reliably find the global minima. In this first section, we address three different approaches on how to interpret our results.

The first perspective from which our research can be seen is from the study of the defect structure of a three-colored, planar, hexagonal tiling forced onto a topologically incompatible curved surface. For single-colored tilings this is a well studied problem, both using polymeric self-assembly as well as other methods (see chapter 2 and our publication [Hain et al., 2019] for details and references). Our approach of using three-armed star polymers to generate three-colored tilings to study the defect structure on spherical surfaces is to our knowledge new in the literature.

Our fine-grained approach using Molecular Dynamics simulations and set-Voronoi diagrams allows a detailed analysis of the shapes of the tiles, compared to a purely topological study of the tiling. Here, further studies could investigate possible influences of the color constraint on the shape of the tiles. First steps towards these studies has been implemented and carried out in the supplement of our first publication. A difference of the radius of gyration of the polymers in ABB and ABC systems, i.e. systems with and without color constraint, has been found. The shape of tiles has been analysed using the tensor of inertia. Comparing non-Thomson to Thomson solutions did not yield significant differences, however, comparing ABB to ABC systems is a promising approach. For finer shape analysis, the Minkowski tensors used in the Quantizer chapter could be employed. Due to the high computational effort of the Molecular Dynamics approach, the system sizes were kept moderately small, meaning the radius of the spherical substrate is relative small compared to the size of the patches. A careful consideration if possible shape differences are due to the color constraint or the relatively small system sizes has to be made, for example by studying trends in increasing substrate radii.

A natural extension to our study is to use more complex, confining geometries,

especially surfaces with negative Gaussian curvature, such as capillary bridges studied by Irvine et al. [2010, 2012], Kusumaatmaja and Wales [2013]. Patterns and tilings on hyperbolic surfaces has been studied before [Nesper and Leoni, 2001, Robins et al., 2004, Ramsden et al., 2009, Dotera et al., 2012, Kirkensgaard, 2012b, Evans et al., 2013a, Kolbe and Evans, 2021], for example by projecting tilings of the two-dimensional hyperbolic plane onto TPMS [Evans et al., 2013a]. However, the investigation of polymeric self-assembly on hyperbolic surfaces, especially with the implication of generating three-colored tilings, seems to be lacking in the literature.

The second interpretation of our results is that we present a process to create spherical substrates whose surface structure is controlled by its radius. As addressed in the final section of our publication [Hain et al., 2019], we propose to make use of this fact to create spherical nano particles with controlled surface structures.

Nano particles self-assembled from diblock copolymers with internal structures have been extensively studied before [Jeon et al., 2007, Ku et al., 2019, Cui et al., 2019, Wong et al., 2020, Shin et al., 2020, Ku, 2021, Higuchi et al., 2008a,b]. The internal structure, size or anisotropy of these particles could be controlled by, among other factors, the composition of the polymers. ABC star polymers, which we used for our studies, have also been used to prepare nano particles [Xu et al., 2015], however, with a focus on the internal structure as well as the size of the particles, not the surface structure as proposed here.

Nano particles with a controlled surface structure have also been studied in the context of patchy particles [Pons-Siepermann and Glotzer, 2012a,b]. The latter were assembled by surfactants adsorbed onto gold nano particles. This approach is analog to our simulation setup, where polymers are forced into a spherical shell.

In sum, self-assembled nano particles with a focus on controlling their internal structure have been studied, as well as nano particles with controlled surface structure, however, on a predefined substrate. Here we propose to merge those two approaches: create self-assembled nano particles with a controlled surface structure.

To create nano particles without the need of a substrate, we propose to use $ABBD$ and $ABCD$ star polymers in a solvent. The A, B and C blocks are chosen soluble where as the D block is insoluble. A spherical substrate forming the core of the nano particle is then assembled by the D blocks, covered by the other blocks to avoid contact of the D blocks and the solvent. Using DPD simulations as described in our publication [Hain et al., 2019], we were able to show that this approach of creating nano particles works, and spherical micelles, as shown in fig. (5.1a), with a core indeed assemble.

(a) Internal structure of micelles in solution

(b) Self-assembled Janus-Particle as the Thomson solution for $N = 2$ with $ABBD$ star polymers
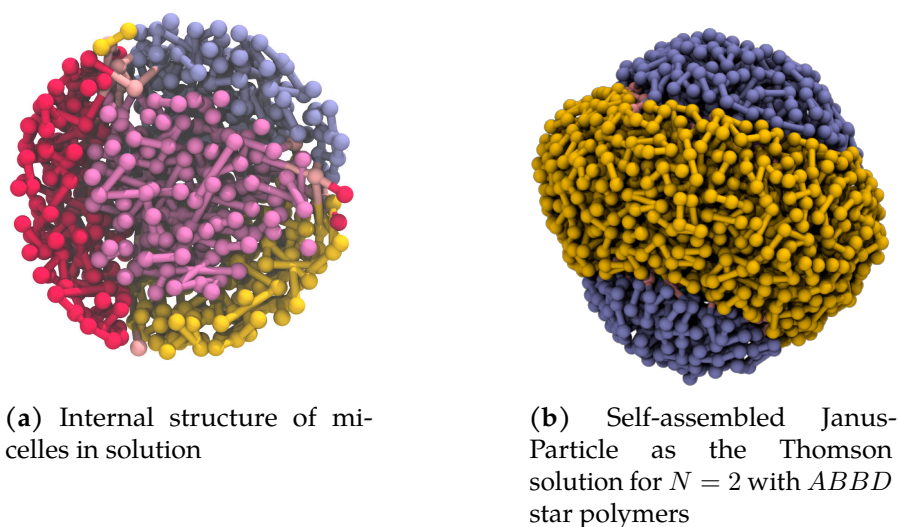
Figure 5.1: A micelle assembled from four-armed star copolymers in solution (not shown). A long arm (pink) forms the core of the micelle and acts as a substrate. The remaining three arms will assemble the tilings found in this thesis on the substrate.

As we find in our publication [Hain et al., 2019], the surface of the structure of the nano particles is given by Thomson problem solution configurations. The number of tiles, and thus the surface structure, can be tuned by varying the length of the D block, which controls the radius of the core. An exemplary $N = 2$ solution for $ABBD$ stars is shown in fig. (5.1b).

We argue that nano particles as proposed here, that is polymer micelles with a defined surface structure, can act as patchy particles: patches of the same block type on the surface of the particles are effectively attractive when put in an appropriate solvent and can act as connectors between particles. This way patchy particles can self-organise into larger structures [Zhang and Glotzer, 2004, Walther and Müller, 2013]. As such our results form a key building block for hierarchical self-assembly [Gröschel and Müller, 2015], where macroscopic structures could self-assemble from $ABCD$ star copolymers, analogous to previous work with ABC linear triblocks [Gröschel et al., 2012, Löbling et al., 2016].

As a last remark to the first article, we suggest that our project can contribute towards the field of so-called "soft granular media": these are e.g. systems consisting of bubbles of gas which are tightly packed in an emulsion [Giustiniani et al., 2016, 2018] and are driven by interface tension and bubble-bubble interactions. Since these bubbles can deform, packings of the latter stand in contrast to "hard", non-deformable granular media. These systems has been introduced briefly in chapter 1, examples include hard sphere and bead packings, both in bulk or on curved surfaces, [Giarritta et al., 1992, 1993, Burke et al., 2015, Mascioli et al., 2017, Dotera et al., 2012, Lovrić et al., 2019, Giarritta

et al., 1992, 1993], soft sphere packings [Miller and Cacciuto, 2011b, Mughal, 2014] or optimization problems such as the Kepler problem [de Gennes, 1999, Szpiro, 2003]. Our polymer system can be seen as a packing of soft, deformable and interacting bubbles, very similar to a soap froth. The significant differences are an additional stretching term in the energy functional and that the geometry of the interface is not constraint by Plateau's laws. As such, our polymer system might be transferable to the field of "soft granular media" and packings on curved surfaces. The concept of a "polymer foam" has been raised before, and will be discussed in the following section.

Our second publication [Hain et al., 2020] investigates the Quantizer system as a statistical mechanics problem at finite temperatures, which was previously introduced as the so-called *Voronoi liquid* [Farago et al., 2014, Ruscher et al., 2015]. In our work we confirm a liquid/solid order transition into its BCC ground state when a Quantizer system is cooled quasi-statically [Ruscher, 2017]. Whereas Ruscher [2017] used Molecular Dynamics, we implemented a new Monte Carlo Metropolis algorithm of the Voronoi liquid.

Our key finding, however, is related to a previously found universal, amorphous inherent structure, which is formed when the system is subjected to a maximally fast quench [Klatt et al., 2019]. We are able to reproduce (within statistical limits) this previously found structure using fast quenches of Molecular Dynamics and Monte Carlo simulations. This addresses a particular question raised in [Klatt et al., 2019]: does the local minima depend on the method of energy minimization - thus quenching? Although a definite answer could not be given, our results strongly supports the universality of the structure.

Furthermore we show that the inherent structure is not only stable when subjected to a maximally fast quench, but also when cooled sufficiently fast enough. In this case the system does not undergo a phase transition, but stays amorphous. This result on its own sheds more light on the complex energy landscape of the Quantizer problem, such as the height and origins of energy barriers around local minima. For example, Royall et al. [2015] investigated the role of locally favored structures, that is local clusters which have a lower energy than the global minimum, as reasons for systems to stay amorphous. Such studies could be especially fruitful if put in context with similar findings from other cellular systems, such as the vertex model [Bi et al., 2016, Merkel and Manning, 2018] introduced in chapter 3.

So far, we only ran simulations of the Quantizer system at fixed density. Extending the simulation code to allow for varying densities, i.e. systems at a fixed pressure, would allow us to address following questions: Would the system collapse at zero temperature?

Could this potential collapse be stabilized by entropic effects at finite temperatures? Would this allow coexistence of the crystalline ground state and the amorphous local minima?

The stability of the inherent structure is especially interesting from the point of view of established, geometric optimization problems, as introduced in chapter 3, specifically in fig. (3.1). Here the hypothesis was raised that the inherent structure found by Klatt et al. [2019] could be an equivalent "characteristic", amorphous local minima of the Quantizer problem, analog to Plateau's foams of the Kelvin, and RCP packings of the Kepler problem. This hypothesis is supported by our findings strengthening the universality of the inherent structure.

Our Quantizer implementation builds the base for the study of the so-called diblock foam model (DFM) [Reddy et al., 2018], modelling micelle phases in diblock copolymers. For the latter, an interface energy term is added to the Quantizer energy functional, modelling the immiscibility of the two different blocks of the polymer chains. Such a model has been proposed earlier by Ziherl and Kamien [2000] for general micelle systems. Our implementation of the DFM can be interpreted from two points of view: (1) as introduced by Reddy et al. [2018] this new energy functional represents a Voronoi based, coarse grained, particulate model of micelle phases in diblock copolymer melts and (2) enables the study of "mixed" optimisation problems, in this case a combination of the Kelvin and the Quantizer problem. These two interpretations are strongly connected, as a polymer melt is a natural implementation of the aforementioned combination of Kelvin and Quantizer problem. The particulate model interpretation thus allows to study micelle structures in polymer melts at different temperatures. The "mixed" optimization problem approach allows fine control over the strength of the interface contribution, allowing us to study the influence of the interfacial term on the ground state and possible local minima.

Using our Monte Carlo implementation of the DFM, we briefly present two case studies: a quasi static cooling of systems with a small number of particles, respective micelles, and a fast quench. These two are representative of the two interpretations mentioned above.

The slow cooling of the Quantizer system investigates the ground state of the DFM and thus minimal energy micelle configurations in the polymer melt at $kT = 0$. Previous work predicted the Frank-Kasper A15 phase to be stable, using the DFM [Reddy et al., 2018]. Later Bates et al. [2019] gave experimental proof for the existence of the $A15$ phase, where as [Bates et al., 2020] found the σ Frank-Kasper phases in AB_n copolymers. Kim et al. [2017] found both σ and A15 phases in systems of micelles of surfactants.

According to eq. (2.3) and (2.4), the chain stretching term of the polymeric free energy scales with $F_{st} \propto r^5$ whereas the interface term scales with $F_{int} \propto r^2$. In both terms r is the radius of the micelle. The "amount" of surface tension can thus be controlled by tuning the micelle size. The free energy of different possible groundstates at different micelle sizes ρ^{-1} are shown in fig. (5.2). The data shows that for large micelles, where the chain stretching (Quantizer) term dominates, the ground state is a BCC lattice. For small, interface tension dominated micelles an A15 lattice is the optimal configuration. At the minimum of the free energy, i.e. the micelle size that would form in real samples, the optimal structure is A15 which is in line with theoretical and experimental earlier results [Reddy et al., 2018, Bates et al., 2019]. Monte Carlo simulations of systems slowly cooled are in line with these results. The stable A15 phase indicates that the polymer melt is indeed behaving like a foam: the best-known minimiser for purely interfacially driven soap froths is the Weaire-Phelan structure which is the Voronoi cells of points sitting on an A15 lattice.
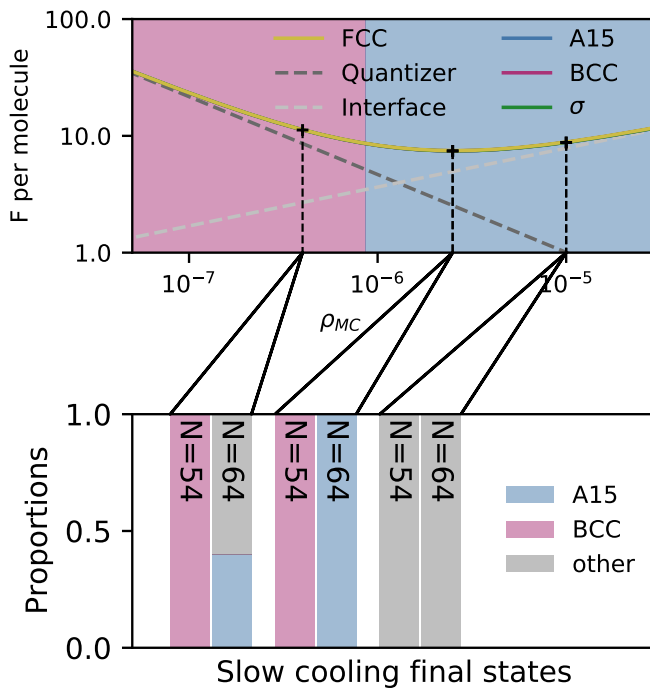
Figure 5.2: Micelle phases in diblock copolymers studied using the diblock foam model (DFM). *top panel:* The free energy per polymer molecule as a function of average micelle size for four different lattices. The background color indicates the structure with the lowest energy. In the case of large micelles, the chain stretching energy dominates, and the system is essentially the Quantizer problem with a BCC ground state. With decreasing micelle size, the interfacial contribution gains weight and the ground states shifts from BCC to A15. These results are confirmed by Monte Carlo simulations (bottom panel). Systems with $N = 54$ and $N = 64$ at three different micelle sizes ρ^{-1} are cooled quasi-statically to $kT = 0$. BCC configurations are only found in the Quantizer driven and intermediate regime, where Quantizer and interface energy are competing. The A15 structure is only formed reliably in the intermediate regime. At smaller micelle sizes, signs of different Frank-Kasper phases are found.

Apart from the ground state analysis, our Monte Carlo implementation also provides the ability to investigate the dynamics of the cooling process, as we did in the

publication [Hain et al., 2020] about the Quantizer problem. Here, we find that the DFM has a liquid/solid phase transition, analogous to the Quantizer problem. Similar phase transitions have been found experimentally [Nicolai et al., 2004] which supports the validity of the DFM model.

A shortcoming of this model as presented is that it only models systems at fixed density and thus micelle size. In real experiments though, the micelle size is not fixed, but depends on the chemical and architectural properties of the polymers. This can be modeled by running the system at variable density or variable particle (micelle) number. This is especially interesting in conjunction with above mentioned variable-density experiments of the Quantizer problem. A different approach would be to use weighted Voronoi tessellations, thus assigning each particle a variable radius that is tuned throughout the simulations.

The results of the DFM model subjected to a fast quench are shown in fig (5.3). The preliminary data shows the statistically different structure factors of inherent, "characteristic" structures of the Kepler and Quantizer problem in comparison to the quenched structure of the DFM. Given these results, we propose to address two questions. The first one considers polymer melts as natural, real implementations of the DFM: can the structural signature, such as the structure factor, of an amorphous micelle configuration of the DFM be found in real systems, such as studied by Nicolai et al. [2004]? The second question is based on the assumption of having access to a structural signature of an amorphous micelle configuration. Can a geometrical interaction driving the system be deduced solely based on the structural signature of a system?
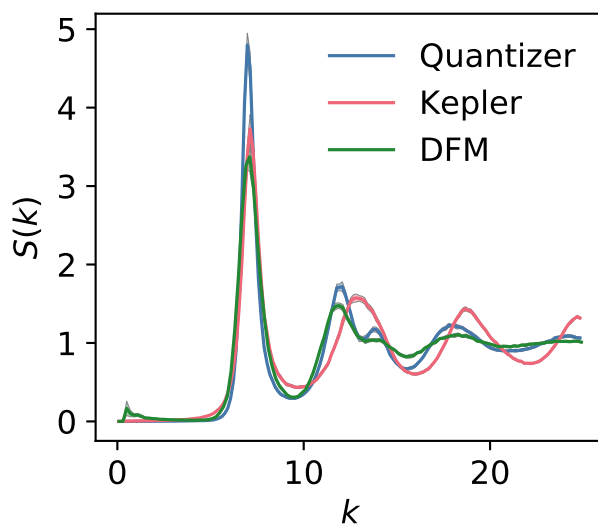
Figure 5.3: Structure factors of inherent structures, i.e. local minima, of different optimisation problems: the Quantizer problem (Klatt structure) [Klatt et al., 2019], Kepler problem (random closed packing) [Torquato and Stillinger, 2010] and a quench of the diblock foam model computed using our Monte Carlo model. The preliminary data shows a statistically significant difference between the inherent structures of the pure Quantizer problem and the DFM model due to the added interface tension.

Although, the first experiments with our DFM model implementation seems to be in good agreement with existing results on micelle phases in polymer melts and

lyotropic liquid crystals, more work is needed to assess its validity of being a model of micelle phases in polymer melts. Regardless, the presented DFM model proves to be valuable for the study of ground states and inherent structures of geometrical optimization problems.

To conclude this first part, we argue that both of our publications [Hain et al., 2019, 2020] address geometrical optimization problems: the Quantizer problem minimising the Quantizer error and the polymers minimising the free energy, which is essentially the Quantizer error extended by an interface tension term. We investigate the assembly process of structures representing both ground states and local minima of the geometric energy functionals with different methodologies. In this section we have shown how our results have a broad range of implications for future work.

5.2 Structure identification: automated direct template matching

The second part of this thesis introduced a software tool facilitating structure identification. As stated in chapter 4, three methods are primarily used to identify three dimensional structures: small-angle X-ray scattering, 3D electron microscopy and template matching based on electron microscope images. Due to the comparably easy access to microscope images from soft materials, template matching has became an important standard. Our work contributes by significantly extending the existing matching processes and publishing an open-source software tool facilitating the structure identification process based on microscope images. Since its publication, a first study used the tool successfully to identify structures, highlighting SPIRES' potential in the field [Sandoval-Ibáñez et al., 2021].

In the current state, however, the matching process is still manually and involves the testing of many hundreds of parameter combinations to fit the generated projection to the TEM images. Many of those can be eliminated by educated guesses and previous information about the structure e.g. the symmetry group from SAXS experiments.

This drawback of the current identification process is addressed in ongoing research. We aim to automate the matching process, without any need of previous knowledge or manual parameter testing. Our choice of tools are Deep Convolutional Neural Networks (CNN) [Goodfellow et al., 2016], which have been used successfully for image classification [Krizhevsky et al., 2012] before. These deep learning models also guided image classification in biological applications [Moen et al., 2019] and specifically

feature recognition on TEM images [Horwath et al., 2020].

In image classification, a CNN is a model taking an image as input and outputting a vector of probabilities, where the vector has as many entries as possible classes there are. The highest probability indicates the predicted structure. A CNN is essentially a mathematical model capable of training its parameters to maximise a fitness function. For this training a large set of labelled images is needed, i.e. images whose classes are known [Goodfellow et al., 2016]. The biggest challenge hereby is to collect and label said training data set.

(a)　　　　　　　　　　　　　　　　　　**(b)**
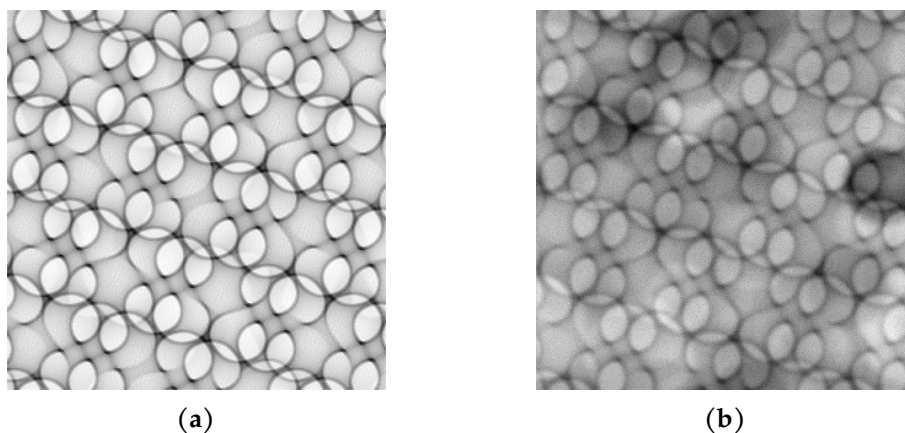
Figure 5.4: A clean (a) and noisy (b) projection in (221) direction of a Gyroid minimal surface. The artificial noise is to mimic real TEM images and provide more realistic training data set for deep learning.

Thus we propose to use an artificial training data set, generated by SPIRE. Since the images are generated from known parameters, the labelling process is automated. For this purpose the tool includes a so-called batch creation functionality, allowing to generate a large set of projections with different parameters. Functions to create artificial, "noisy" data are provided to create a more realistic training data set, as shown in fig. (5.4).

The quality of the trained model greatly depends on the size and quality of the data set. The size of the data set needs to be chosen to avoid under- or overfitting. Furthermore it should cover all parameter ranges which are expected to be encountered in the images to be classified. Our choices of parameter ranges are oriented on existing biological systems, such as the PLBs introduced in chapter 4. As possible structures, we included projections from Gyroid, Diamond, Primitive and Lonsdaleite surfaces. Each input image is thus classified as one of those four possible structures. We also included images with a varying level of artificial noise, so the model is trained to handle different qualities of electron microscope images.

An additional measurement to expand the data set is so-called data augmentation. Here, images are modified and then reused for training. Typical image modifications include rotation and cropping. A rotation can be interpreted as changing the in-plane orientation of the biological sample shown in the image, whereas cropping an image is equivalent to reducing the sample size.

A CNN can be considered to consist of two parts: the convolutional layers and some fully connected layers. Whereas the convolutional layers extract geometric patterns present in the input images and create so-called feature maps, the fully connected layers pieces these future maps together and predicts the structure [Goodfellow et al., 2016].

We also make use of the fact, that many biological samples are poly-crystalline. Poly-crystallinity occurs when different regions in the structure are grown in different orientations, providing projections of the same structure from different perspectives. This provides microscope images from the same structure, but different orientations. There exists several approaches to deal with so-called multi-view input [Seeland and Mäder, 2021]. One includes fusing the feature maps of all input images with different views and pass them through merging layers. The second, and somewhat easier approach fuses only the prediction scores, i.e. the vector of probabilities for each class.

For preliminary results, we created a training data set of about 1000 images with artificial noise for each of the four considered structure types. The multi-view approach is not considered for now. A test data set was created in the same way. First results using standard architectures of CNN for image classification show good accuracies: around $90\,\%$ of artificial projections are identified as the correct structure. By including the multi-view approach, the accuracy is increased by about 4 % points.

To truly validate the network, a test data set of real, labelled microscope images is needed. The latter is still being collected, so no assumption about the true accuracy of this automated matching approach can be made yet.

Although the validation of our model with real data is still missing, our SPIRE-enabled approach using CNN to automate the structure identification process looks promising. Especially the connection between geometric structure identification and the thriving field of AI research proves to be fruitful and interesting.

Bibliography

M. D. Abramoff, Paulo J. Magalhães, and Sunanda J. Ram. Image processing with ImageJ. *Biophotonics Int.*, 11:36–42, 2004.

Zach Adam, Dana Charuvi, Onie Tsabari, Ronit Rimon Knopf, and Ziv Reich. Biogenesis of thylakoid networks in angiosperms: Knowns and unknowns. *Plant Mol Biol*, 76: 221–234, 2011. doi:10.1007/s11103-010-9693-5.

Zakaria Almsherqi, Felix Margadant, and Yuru Deng. A look through 'lens' cubic mitochondria. *Interface Focus*, 2:539–545, 2012. doi:10.1098/rsfs.2011.0120.

Zakaria A. Almsherqi, Craig S. McLachlan, Peter Mossop, Kèvin Knoops, and Yuru Deng. Direct template matching reveals a host subcellular membrane gyroid cubic structure that is associated with SARS virus. *Redox Rep.*, 10:167–171, 2005. doi:10.1179/135100005X57373.

Zakaria A. Almsherqi, Sepp D. Kohlwein, and Yuru Deng. Cubic membranes: A legend beyond the Flatland* of cell membrane organization. *Journal of Cell Biology*, 173: 839–844, 2006. doi:10.1083/jcb.200603055.

Zakaria A. Almsherqi, Tomas Landh, Sepp D. Kohlwein, and Yuru Deng. Chapter 6 Cubic Membranes: The Missing Dimension of Cell Membrane Organization. In *International Review of Cell and Molecular Biology*, volume 274 of *International Review of Cell and Molecular Biology*, pages 275–342. Academic Press, 2009. doi:10.1016/S1937-6448(08)02006-6.

Jens Als-Nielsen and Des McMorrow. *Elements of Modern X-ray Physics*. John Wiley & Sons, 2011a.

Jens Als-Nielsen and Des McMorrow. Kinematical scattering I: Non-crystalline materials. In *Elements of Modern X-ray Physics*, chapter 4, pages 113–146. John Wiley & Sons, Ltd, 2011b. doi:10.1002/9781119998365.ch4.

Eric Lewin Altschuler, Timothy J. Williams, Edward R. Ratner, Farid Dowla, and Frederick Wooten. Method of constrained global optimization. *Phys. Rev. Lett.*, 72:2671–2674, 1994. doi:10.1103/PhysRevLett.72.2671.

Eric Lewin Altschuler, Timothy J. Williams, Edward R. Ratner, Robert Tipton, Richard Stong, Farid Dowla, and Frederick Wooten. Possible global minimum lattice configurations for thomson's problem of charges on a sphere. *Phys. Rev. Lett.*, 78:2681–2685, 1997. doi:10.1103/PhysRevLett.78.2681.

D. M. Anderson, H. T. Davis, L. E. Scriven, and J. C. C. Nitsche. Periodic Surfaces of Prescribed Mean Curvature. In *Advances in Chemical Physics*, pages 337–396. John Wiley & Sons, Ltd, 1990. doi:10.1002/9780470141267.ch6.

Joshua A. Anderson, Chris D. Lorenz, and A. Travesset. General purpose molecular dynamics simulations fully implemented on graphics processing units. *Journal of Computational Physics*, 227(10):5342 – 5359, 2008. ISSN 0021-9991. doi:https://doi.org/10.1016/j.jcp.2008.01.047. URL http://www.sciencedirect.com/science/article/pii/S0021999108000818.

Sten Andersson, S. T. Hyde, and Von Hans Georg Schnering. The intrinsic curvature of solids. *Z. Für Krist. - Cryst. Mater.*, 168:1–18, 1984. doi:10.1524/zkri.1984.168.14.1.

Sten Andersson, S. T. Hyde, Kare Larsson, and Sven Lidin. Minimal surfaces and structures: From inorganic and metal crystals to cell membranes and biopolymers. *Chem. Rev.*, 88:221–242, 1988. doi:10.1021/cr00083a011.

K. Appel and W. Haken. Every planar map is four colorable. Part I: Discharging. *Ill. J. Math.*, 21:429–490, 1977. doi:10.1215/ijm/1256049011.

K. Appel, W. Haken, and J. Koch. Every planar map is four colorable. Part II: Reducibility. *Ill. J. Math.*, 21:491–567, 1977. doi:10.1215/ijm/1256049012.

Tegan Armarego-Marriott, Łucja Kowalewska, Asdrubal Burgos, Axel Fischer, Wolfram Thiele, Alexander Erban, Deserah Strand, Sabine Kahlau, Alexander Hertle, Joachim Kopka, Dirk Walther, Ziv Reich, Mark Aurel Schöttler, and Ralph Bock. Highly Resolved Systems Biology to Dissect the Etioplast-to-Chloroplast Transition in Tobacco Leaves. *Plant Physiology*, 180:654–681, 2019. doi:10.1104/pp.18.01432.

Akash Arora, Jian Qin, David C. Morse, Kris T. Delaney, Glenn H. Fredrickson, Frank S. Bates, and Kevin D. Dorfman. Broadly Accessible Self-Consistent Field Theory for Block Polymer Materials Discovery. *Macromolecules*, 49:4675–4690, 2016. doi:10.1021/acs.macromol.6b00107.

Hans Arwin, Roger Magnusson, Jan Landin, and Kenneth Järrendahl. Chirality-induced polarization effects in the cuticle of scarab beetles: 100 years after Michelson. *Philos. Mag.*, 92:1583–1599, 2012. doi:10.1080/14786435.2011.648228.

Neil W. Ashcroft, AshcroftNeil W, il W. Ashcroft, and N. David Mermin. *Solid State Physics*. Holt, Rinehart and Winston, 1976.

Steven Atkinson, Ge Zhang, Adam B. Hopkins, and Salvatore Torquato. Critical slowing down and hyperuniformity on approach to jamming. *Phys. Rev. E*, 94:012902, 2016. doi:10.1103/PhysRevE.94.012902.

Atsuo Suzuki and Masao Iri. Approximation Of A Tessellation Of The Plane By A Voronoi Diagram. *J. Oper. Res. Soc. OfJapan*, 29:69–97, 1986. doi:10.15807/jorsj.29.69.

Franz Aurenhammer. Voronoi diagrams - a survey of a fundamental geometric data structure. *ACM Comput. Surv.*, 23:345–405, 1991. doi:10.1145/116873.116880.

Franz Aurenhammer, Rolf Klein, and Der-tsai Lee. *Voronoi Diagrams And Delaunay Triangulations*. World Scientific Publishing Company, 2013.

George W. Barlow. Hexagonal territories. *Animal Behaviour*, 22:876–IN1, 1974. doi:10.1016/0003-3472(74)90010-4.

David Barnette. *Map Coloring, Polyhedra, and the Four-color Problem*. Mathematical Association of America, 1983.

Christopher M. Bates and Frank S. Bates. 50th Anniversary Perspective: Block Polymers—Pure Potential. *Macromolecules*, 50:3–22, 2017. doi:10.1021/acs.macromol.6b02355.

Frank S. Bates. Network phases in block copolymer melts. *MRS Bull.*, 30:525–532, 2005. doi:10.1557/mrs2005.145.

Frank S. Bates and Glenn H. Frederickson. Block copolymers - designer soft materials. *Phys. Today*, 52:32, 1999. doi:10.1063/1.882522.

Frank S. Bates and Glenn H. Fredrickson. Block copolymer thermodynamics: Theory and experiment. *Annu. Rev. Phys. Chem.*, 41:525–557, 1990. doi:10.1146/annurev.pc.41.100190.002521.

Frank S. Bates, Mark F. Schulz, Ashish K. Khandpur, Stephan Forster, Jeffrey H. Rosedale, Kristoffer Almdal, and Kell Mortensen. Fluctuations, conformational asymmetry and block copolymer phase behaviour. *Faraday Discuss.*, 98:7–18, 1994. doi:10.1039/FD9949800007.

Morgan W. Bates, Joshua Lequieu, Stephanie M. Barbon, Ronald M. Lewis, Kris T. Delaney, Athina Anastasaki, Craig J. Hawker, Glenn H. Fredrickson, and Christopher M. Bates. Stability of the A15 phase in diblock copolymer melts. *PNAS*, 116:13194–13199, 2019. doi:10.1073/pnas.1900121116.

Morgan W. Bates, Stephanie M. Barbon, Adam E. Levi, Ronald M. Lewis, Haley K. Beech, Kasper M. Vonk, Cheng Zhang, Glenn H. Fredrickson, Craig J. Hawker, and Christopher M. Bates. Synthesis and Self-Assembly of ABn Miktoarm Star Polymers. *ACS Macro Lett.*, 9:396–403, 2020. doi:10.1021/acsmacrolett.0c00061.

A. R. Bausch, M. J. Bowick, A. Cacciuto, A. D. Dinsmore, M. F. Hsu, D. R. Nelson, M. G. Nikolaides, A. Travesset, and D. A. Weitz. Grain boundary scars and spherical crystallography. *Science*, 299:1716–1718, 2003.

Bonnie Berger, Peter W. Shor, Lisa Tucker-Kellogg, and Jonathan King. Local rule-based theory of virus shell assembly. *Proc. Natl. Acad. Sci. U. S. A.*, 91:7732–7736, 1994.

J. D. Bernal and J. Mason. Packing of Spheres: Co-ordination of Randomly Packed Spheres. *Nature*, 188:910–911, 1960. doi:10.1038/188910a0.

Serge Berthier, Magali Thomé, and Priscilla Simonis. Circular Polarization in Nature: Factual, Theoretical and Experimental Summary. *Materials Today: Proceedings*, 1: 145–154, 2014. doi:10.1016/j.matpr.2014.09.015.

Dapeng Bi, J. H. Lopez, J. M. Schwarz, and M. Lisa Manning. A density-independent rigidity transition in biological tissues. *Nature Phys*, 11:1074–1079, 2015. doi:10.1038/nphys3471.

Dapeng Bi, Xingbo Yang, M. Cristina Marchetti, and M. Lisa Manning. Motility-Driven Glass and Jamming Transitions in Biological Tissues. *Phys. Rev. X*, 6:021011, 2016. doi:10.1103/PhysRevX.6.021011.

Viktor Blåsjö. The Isoperimetric Problem. *Am. Math. Mon.*, 112:526–566, 2005. doi:10.2307/30037526.

A N Bondarenko, M N Karchevskiy, and L A Kozinkin. The structure of metastable states in the thomson problem. *J. Phys. Conf. Ser.*, 643:012103, 2015.

M. Bowick, A. Cacciuto, D. R. Nelson, and A. Travesset. Crystalline Order on a Sphere and the Generalized Thomson Problem. *Phys. Rev. Lett.*, 89:185502, 2002. doi:10.1103/PhysRevLett.89.185502.

Mark J. Bowick and Luca Giomi. Two-dimensional matter: order, curvature and defects. *Advances in Physics*, 58(5):449–563, 2009. doi:10.1080/00018730903043166. URL `https://doi.org/10.1080/00018730903043166`.

Mark J. Bowick and Zhenwei Yao. Crystalline order on catenoidal capillary bridges. *EPL Europhys. Lett.*, 93:36001, 2011.

Mark J. Bowick, David R. Nelson, and Alex Travesset. Interacting topological defects on frozen topographies. *Phys. Rev. B*, 62:8738–8751, Oct 2000. doi:10.1103/PhysRevB.62.8738. URL `https://link.aps.org/doi/10.1103/PhysRevB.62.8738`.

Mark J. Bowick, Angelo Cacciuto, David R. Nelson, and Alex Travesset. Crystalline particle packings on a sphere with long-range power-law potentials. *Phys. Rev. B*, 73:024115, 2006. doi:10.1103/PhysRevB.73.024115.

Kenneth A. Brakke. The Surface Evolver. *Exp. Math.*, 1:141–165, 1992. doi:10.1080/10586458.1992.10504253.

Christopher J. Burke, Badel L. Mbanga, Zengyi Wei, Patrick T. Spicer, and Timothy J. Atherton. The role of curvature anisotropy in the ordering of spheres on an ellipsoid. *Soft Matter*, 11:5872–5882, 2015. doi:10.1039/C5SM01118C.

Michał Bykowski, Radosław Mazur, Daniel Buszewicz, Joanna Szach, Agnieszka Mostowska, and Łucja Kowalewska. Spatial Nano-Morphology of the Prolamellar Body in Etiolated Arabidopsis thaliana Plants With Disturbed Pigment and Polyprenol Composition. *Front. Cell Dev. Biol.*, 8, 2020. doi:10.3389/fcell.2020.586628.

Sebastien J. P. Callens, Rafael J. C. Uyttendaele, Lidy E. Fratila-Apachitei, and Amir A. Zadpoor. Substrate curvature as a cue to guide spatiotemporal cell and tissue organization. *Biomaterials*, 232:119739, 2020. doi:10.1016/j.biomaterials.2019.119739.

Lucien Marie Le Cam and Jerzy Neyman. *Proceedings of the Fifth Berkeley Symposium on Mathematical Statistics and Probability: Weather Modification*. University of California Press, 1967.

C Casagrande, P Fabre, E Raphaël, and M Veyssié. "janus beads": Realization and behaviour at water/oil interfaces. *Europhysics Letters (EPL)*, 9(3):251–255, jun 1989. doi:10.1209/0295-5075/9/3/011. URL `https://doi.org/10.1209%2F0295-5075%2F9%2F3%2F011`.

D. L. D. Caspar and A. Klug. Physical principles in the construction of regular viruses. *Cold Spring Harb. Symp. Quant. Biol.*, 27:1–24, 1962. doi:10.1101/SQB.1962.027.001.005.

Christopher I Cazzonelli, Xin Hou, Yagiz Alagoz, John Rivers, Namraj Dhami, Jiwon Lee, Shashikanth Marri, and Barry J Pogson. A cis-carotene derived apocarotenoid regulates etioplast and chloroplast development. *eLife*, 9:e45310, 2020. doi:10.7554/eLife.45310.

Hector D. Ceniceros and Glenn H. Fredrickson. Numerical Solution of Polymer Self-Consistent Field Theory. *Multiscale Model. Simul.*, 2:452–474, 2004. doi:10.1137/030601338.

David Chandler. Interfaces and the driving force of hydrophobic assembly. *Nature*, 437:640–647, 2005. doi:10.1038/nature04162.

Tanya L. Chantawansri, August W. Bosse, Alexander Hexemer, Hector D. Ceniceros, Carlos J. García-Cervera, Edward J. Kramer, and Glenn H. Fredrickson. Self-consistent field theory simulations of block copolymer assembly on a sphere. *Phys. Rev. E*, 75:031802, 2007. doi:10.1103/PhysRevE.75.031802.

Ketpin Chong and Yuru Deng. Chapter 15 - The Three Dimensionality of Cell Membranes: Lamellar to Cubic Membrane Transition as Investigated by Electron Microscopy. In Gilbert Di Paolo and Markus R Wenk, editors, *Methods in Cell Biology*, volume 108 of *Lipids*, pages 317–343. Academic Press, 2012. doi:10.1016/B978-0-12-386487-1.00015-8.

Maxime Clusel, Eric I. Corwin, Alexander O. N. Siemens, and Jasna Brujić. A 'granocentric' model for random packing of jammed emulsions. *Nature*, 460:611–615, 2009. doi:10.1038/nature08158.

W. L. Coggshall and R. A. Morse. Beeswax: Production, harvesting, processing and products. *Beeswax Prod. Harvest. Process. Prod.*, 1984.

Henry Cohn and Noam Elkies. New Upper Bounds on Sphere Packings I. *Ann. Math.*, 157:689–714, 2003.

John Conway and Neil J. A. Sloane. *Sphere Packings, Lattices and Groups*. Grundlehren Der Mathematischen Wissenschaften. Springer-Verlag, New York, third edition, 1999. doi:10.1007/978-1-4757-6568-7.

John H. Conway, Heidi Burgiel, and Chaim Goodman-Strauss. *The Symmetries of Things*. CRC Press, 2016.

H. S. M. Coxeter, M. S. Longuet-Higgins, and J. C. P. Miller. Uniform Polyhedra. *Philos. Trans. R. Soc. Lond. Ser. Math. Phys. Sci.*, 246:401–450, 1954.

Congcong Cui, Yuru Deng, and Lu Han. Bicontinuous cubic phases in biological and artificial self-assembled systems. *Sci. China Mater.*, 63:686–702, 2020. doi:10.1007/s40843-019-1261-1.

Tingting Cui, Xingye Li, Bin Dong, Xiang Li, Mengxue Guo, Lixin Wu, Baohui Li, and Haolong Li. Janus onions of block copolymers via confined self-assembly. *Polymer*, 174:70–76, 2019. doi:10.1016/j.polymer.2019.04.062.

Thierry Darmanin and Frédéric Guittard. Superhydrophobic and superoleophobic properties in nature. *Materials Today*, 18:273–285, 2015. doi:10.1016/j.mattod.2015.01.001.

Liliana de Campo, Trond Varslot, Minoo J. Moghaddam, Jacob J. K. Kirkensgaard, Kell Mortensen, and Stephen T. Hyde. A novel lyotropic liquid crystal formed by triphilic star-polyphiles: Hydrophilic/oleophilic/fluorophilic rods arranged in a 12.6.4. tiling. *Phys. Chem. Chem. Phys.*, 13:3139–3152, 2011. doi:10.1039/C0CP01201G.

P. G. de Gennes. Granular matter: A tentative view. *Rev. Mod. Phys.*, 71:S374–S382, 1999. doi:10.1103/RevModPhys.71.S374.

Davide Demurtas, Paul Guichard, Isabelle Martiel, Raffaele Mezzenga, Cécile Hébert, and Laurent Sagalowicz. Direct visualization of dispersed lipid bicontinuous cubic phases by cryo-electron tomography. *Nat. Commun.*, 6:8915, 2015. doi:10.1038/ncomms9915.

Yuru Deng and Mark Mieczkowski. Three-dimensional periodic cubic membrane structure in the mitochondria of amoebae Chaos carolinensis. *Protoplasma*, 203:16–25, 1998. doi:10.1007/BF01280583.

Yuru Deng, Michael Marko, Karolyn F. Buttle, ArDean Leith, Mark Mieczkowski, and Carmen A. Mannella. Cubic Membrane Structure in Amoeba (Chaos carolinensis) Mitochondria Determined by Electron Microscopic Tomography. *Journal of Structural Biology*, 127:231–239, 1999. doi:10.1006/jsbi.1999.4147.

Marjolein Dijkstra and René van Roij. Entropic wetting in colloidal suspensions. *J. Phys.: Condens. Matter*, 17:S3507–S3514, 2005. doi:10.1088/0953-8984/17/45/041.

G. Lejeune Dirichlet. Über die Reduction der positiven quadratischen Formen mit drei unbestimmten ganzen Zahlen. *J. Für Reine Angew. Math. Crelles J.*, 1850:209–227, 1850. doi:10.1515/crll.1850.40.209.

Gabrielle Donnay and David L. Pawson. X-ray Diffraction Studies of Echinoderm Plates. *Science*, 166:1147–1150, 1969. doi:10.1126/science.166.3909.1147.

Tomonari Dotera and Akira Hatano. The diagonal bond method: A new lattice polymer model for simulation study of block copolymers. *J. Chem. Phys.*, 105:8413–8427, 1996. doi:10.1063/1.472696.

Tomonari Dotera, Masakiyo Kimoto, and Junichi Matsuzawa. Hard spheres on the gyroid surface. *Interface Focus*, 2:575–581, 2012. doi:10.1098/rsfs.2011.0092.

W. Drenckhan, S. J. Cox, G. Delaney, H. Holste, D. Weaire, and N. Kern. Rheology of ordered foams—on the way to Discrete Microfluidics. *Colloids and Surfaces A: Physicochemical and Engineering Aspects*, 263:52–64, 2005. doi:10.1016/j.colsurfa.2005.01.005.

Wiebke Drenckhan and Dominique Langevin. Monodisperse foams in one to three dimensions. *Current Opinion in Colloid & Interface Science*, 15:341–358, 2010. doi:10.1016/j.cocis.2010.06.002.

Qiang Du and Max Gunzburger. Grid generation and optimization based on centroidal Voronoi tessellations. *Applied Mathematics and Computation*, 133:591–607, 2002. doi:10.1016/S0096-3003(01)00260-0.

Qiang Du and Desheng Wang. The optimal centroidal Voronoi tessellations and the gersho's conjecture in the three-dimensional space. *Comput. Math. Appl.*, 49:1355–1373, 2005. doi:10.1016/j.camwa.2004.12.008.

Qiang Du, Vance Faber, and Max Gunzburger. Centroidal Voronoi Tessellations: Applications and Algorithms. *SIAM Rev.*, 41:637–676, 1999. doi:10.1137/S0036144599352836.

Qiang Du, Max Gunzburger, and Lili Ju. Advances in Studies and Applications of Centroidal Voronoi Tessellations. *Numer. Math. Theor. Meth. Appl.*, 3:119–142, 2010. doi:10.4208/nmtma.2010.32s.1.

Thomas Einert, Peter Lipowsky, Jörg Schilling, Mark J. Bowick, and Andreas R. Bausch. Grain boundary scars on spherical crystals. *Langmuir*, 21:12076–12079, 2005. doi:10.1021/la0517383.

L. J. Ellison, D. J. Michel, F. Barmes, and D. J. Cleaver. Entropy-Driven Formation of the Gyroid Cubic Phase. *Phys. Rev. Lett.*, 97:237801, 2006. doi:10.1103/PhysRevLett.97.237801.

S. Enders and B.A. Wolf. *Polymer Thermodynamics: Liquid Polymer-Containing Mixtures*. Advances in Polymer Science. Springer Berlin Heidelberg, 2011.

T Erber and G M Hockney. Equilibrium configurations of N equal charges on a sphere. *J. Phys. Math. Gen.*, 24:L1369, 1991.

P. Español and P. Warren. Statistical Mechanics of Dissipative Particle Dynamics. *EPL*, 30:191–196, 1995. doi:10.1209/0295-5075/30/4/001.

Pep Español and Patrick B. Warren. Perspective: Dissipative particle dynamics. *J. Chem. Phys.*, 146:150901, 2017. doi:10.1063/1.4979514.

M. E. Evans, V. Robins, and S. T. Hyde. Periodic entanglement I: Networks from hyperbolic reticulations. *Acta Cryst A*, 69:241–261, 2013a. doi:10.1107/S0108767313001670.

Myfanwy E. Evans and Stephen T. Hyde. From three-dimensional weavings to swollen corneocytes. *J. R. Soc. Interface*, 8:1274–1280, 2011. doi:10.1098/rsif.2010.0722.

Myfanwy E. Evans and Roland Roth. Shaping the Skin: The Interplay of Mesoscale Geometry and Corneocyte Swelling. *Phys. Rev. Lett.*, 112:038102, 2014. doi:10.1103/PhysRevLett.112.038102.

Myfanwy E. Evans, Johannes Zirkelbach, Gerd E. Schröder-Turk, Andrew M. Kraynik, and Klaus Mecke. Deformation of Platonic foam cells: Effect on growth rate. *Phys. Rev. E*, 85:061401, 2012. doi:10.1103/PhysRevE.85.061401.

Myfanwy E. Evans, Andrew M. Kraynik, Douglas A. Reinelt, Klaus Mecke, and Gerd E. Schröder-Turk. Networklike Propagation of Cell-Level Stress in Sheared Random Foams. *Phys. Rev. Lett.*, 111:138301, 2013b. doi:10.1103/PhysRevLett.111.138301.

Myfanwy E. Evans, Gerd E. Schröder-Turk, and Andrew M. Kraynik. A geometric exploration of stress in deformed liquid foams. *J. Phys.: Condens. Matter*, 29:124004, 2017. doi:10.1088/1361-648X/aa57c7.

Jean Farago, Alexander Semenov, Stefan Frey, and Jörg Baschnagel. New conserved structural fields for supercooled liquids. *Eur. Phys. J. E*, 37:46, 2014. doi:10.1140/epje/i2014-14046-9.

Reza Farhadifar, Jens-Christian Röper, Benoit Aigouy, Suzanne Eaton, and Frank Jülicher. The Influence of Cell Mechanics, Cell-Cell Interactions, and Proliferation on Epithelial Packing. *Current Biology*, 17:2095–2104, 2007. doi:10.1016/j.cub.2007.11.049.

Pedro F. Felzenszwalb and Daniel P. Huttenlocher. Distance Transforms of Sampled Functions. *Theory Comput.*, 8:415–428, 2012. doi:10.4086/toc.2012.v008a019.

Xueyan Feng, Christopher J. Burke, Mujin Zhuo, Hua Guo, Kaiqi Yang, Abhiram Reddy, Ishan Prasad, Rong-Ming Ho, Apostolos Avgeropoulos, Gregory M. Grason, and Edwin L. Thomas. Seeing mesoatomic distortions in soft-matter crystals of a double-gyroid block copolymer. *Nature*, 575:175–179, 2019. doi:10.1038/s41586-019-1706-1.

John L. Finney. Bernal's road to random packing and the structure of liquids. *Philos. Mag.*, 93:3940–3969, 2013. doi:10.1080/14786435.2013.770179.

Michael G. Fischer, Liliana de Campo, Jacob J. K. Kirkensgaard, Stephen T. Hyde, and Gerd E. Schröder-Turk. The Tricontinuous 3ths(5) Phase: A New Morphology in Copolymer Melts. *Macromolecules*, 47:7424–7430, 2014. doi:10.1021/ma5016352.

Marshall Fixman. Radius of gyration of polymer chains. *J. Chem. Phys.*, 36:306–310, 1962. doi:10.1063/1.1732501.

S. Jane Flint, Vincent R. Racaniello, Glenn F. Rall, and Anna Marie Skalka. *Principles of Virology, Volume 2: Pathogenesis and Control*. Wiley, 2015.

Davide Floris and Werner Kühlbrandt. Molecular landscape of etioplast inner membranes in higher plants. *Nat. Plants*, 7:514–523, 2021. doi:10.1038/s41477-021-00896-z.

Paul J. Flory. Thermodynamics of high polymer solutions. *J. Chem. Phys.*, 10:51–61, 1942. doi:10.1063/1.1723621.

Paul J. Flory. Thermodynamics of heterogeneous polymers and their solutions. *J. Chem. Phys.*, 12:425–438, 1944. doi:10.1063/1.1723887.

Rainer F. Foelix, R. Kretz, and G. Rager. Structure and postnatal development of photoreceptors and their synapses in the retina of the tree shrew (Tupaia belangen). *Cell Tissue Res.*, 247:287–297, 1987. doi:10.1007/BF00218310.

Stephan Foerster, Ashish K. Khandpur, Jin Zhao, Frank S. Bates, Ian W. Hamley, Anthony J. Ryan, and Wim Bras. Complex phase behavior of polyisoprene-polystyrene diblock copolymers near the order-disorder transition. *Macromolecules*, 27:6922–6935, 1994. doi:10.1021/ma00101a033.

Glenn H. Fredrickson, Venkat Ganesan, and François Drolet. Field-Theoretic Computer Simulation Methods for Polymers and Complex Fluids. *Macromolecules*, 35:16–39, 2002. doi:10.1021/ma011515t.

Sho Fujii, Noriko Nagata, Tatsuru Masuda, Hajime Wada, and Koichi Kobayashi. Galactolipids Are Essential for Internal Membrane Transformation during Etioplast-to-Chloroplast Differentiation. *Plant Cell Physiol.*, 60:1224–1238, 2019. doi:10.1093/pcp/pcz041.

Paul J. F. Gandy and Jacek Klinowski. Exact computation of the triply periodic Schwarz P minimal surface. *Chemical Physics Letters*, 322:579–586, 2000a. doi:10.1016/S0009-2614(00)00453-X.

Paul J. F Gandy and Jacek Klinowski. Exact computation of the triply periodic G ('Gyroid') minimal surface. *Chemical Physics Letters*, 321:363–371, 2000b. doi:10.1016/S0009-2614(00)00373-0.

Paul J. F. Gandy, Djurdje Cvijović, Alan L. Mackay, and Jacek Klinowski. Exact computation of the triply periodic D ('diamond') minimal surface. *Chemical Physics Letters*, 314:543–551, 1999. doi:10.1016/S0009-2614(99)01000-3.

Paul J. F. Gandy, Sonny Bardhan, Alan L. Mackay, and Jacek Klinowski. Nodal surface approximations to the P,G,D and I-WP triply periodic minimal surfaces. *Chemical Physics Letters*, 336:187–195, 2001. doi:10.1016/S0009-2614(00)01418-4.

Győző Garab. Self-assembly and structural–functional flexibility of oxygenic photosynthetic machineries: Personal perspectives. *Photosynth Res*, 127:131–150, 2016. doi:10.1007/s11120-015-0192-z.

Gopal Garg, Shailendra Saraf, and Swarnlata Saraf. Cubosomes: An Overview. *Biol. Pharm. Bull.*, 30:350–353, 2007. doi:10.1248/bpb.30.350.

U.W. Gedde. *Polymer Physics*. Springer Netherlands, 2013.

Tohru Gemma, Akira Hatano, and Tomonari Dotera. Monte Carlo Simulations of the Morphology of ABC Star Polymers Using the Diagonal Bond Method. *Macromolecules*, 35:3225–3237, 2002. doi:10.1021/ma001040q.

Allen Gersho. Asymptotically optimal block quantization. *IEEE Trans. Inf. Theory*, 25:373–380, 1979.

Subhroshekhar Ghosh and Joel L. Lebowitz. Fluctuations, large deviations and rigidity in hyperuniform systems: A brief survey. *Indian J. Pure Appl. Math.*, 48:609–631, 2017. doi:10.1007/s13226-017-0248-1.

Subhroshekhar Ghosh and Joel L. Lebowitz. Generalized Stealthy Hyperuniform Processes: Maximal Rigidity and the Bounded Holes Conjecture. *Commun. Math. Phys.*, 363:97–110, 2018. doi:10.1007/s00220-018-3226-5.

S. Prestipino Giarritta, M. Ferrario, and P. V. Giaquinta. Statistical geometry of hard particles on a sphere. *Phys. Stat. Mech. Its Appl.*, 187:456–474, 1992. doi:10.1016/0378-4371(92)90005-B.

S. Prestipino Giarritta, M. Ferrario, and P. V. Giaquinta. Statistical geometry of hard particles on a sphere: Analysis of defects at high density. *Phys. Stat. Mech. Its Appl.*, 201:649–665, 1993. doi:10.1016/0378-4371(93)90134-P.

Anaïs Giustiniani, Philippe Guégan, Manon Marchand, Christophe Poulard, and Wiebke Drenckhan. Generation of Silicone Poly-HIPEs with Controlled Pore Sizes via Reactive Emulsion Stabilization. *Macromol. Rapid Commun.*, 37:1527–1532, 2016. doi:10.1002/marc.201600281.

Anaïs Giustiniani, Simon Weis, Christophe Poulard, Paul H. Kamm, Francisco García-Moreno, Matthias Schröter, and Wiebke Drenckhan. Skinny emulsions take on granular matter. *Soft Matter*, 14:7310–7323, 2018. doi:10.1039/C8SM00830B.

Jens Glaser, Trung Dac Nguyen, Joshua A. Anderson, Pak Lui, Filippo Spiga, Jaime A. Millan, David C. Morse, and Sharon C. Glotzer. Strong scaling of general-purpose molecular dynamics simulations on gpus. *Computer Physics Communications*, 192: 97 – 107, 2015. ISSN 0010-4655. doi:https://doi.org/10.1016/j.cpc.2015.02.028. URL `http://www.sciencedirect.com/science/article/pii/S0010465515000867`.

Ian Goodfellow, Yoshua Bengio, and Aaron Courville. *Deep Learning*. MIT Press, 2016.

Marc De Graef and Michael E. McHenry. Structure of Materials: An Introduction to Crystallography, Diffraction and Symmetry, 2012.

Gregory M. Grason. The packing of soft materials: Molecular asymmetry, geometric frustration and optimal lattices in block copolymer melts. *Physics Reports*, 433:1–64, 2006. doi:10.1016/j.physrep.2006.08.001.

Gregory M. Grason. Perspective: Geometrically frustrated assemblies. *J. Chem. Phys.*, 145:110901, 2016. doi:10.1063/1.4962629.

Gregory M. Grason and Randall D. Kamien. Interfaces in Diblocks: A Study of Miktoarm Star Copolymers. *Macromolecules*, 37:7371–7380, 2004. doi:10.1021/ma049255d.

Gregory M. Grason, B. A. DiDonna, and Randall D. Kamien. Geometric Theory of Diblock Copolymer Phases. *Phys. Rev. Lett.*, 91:058304, 2003. doi:10.1103/PhysRevLett.91.058304.

R.M. Gray and D.L. Neuhoff. Quantization. *IEEE Trans. Inf. Theory*, 44:2325–2383, 1998. doi:10.1109/18.720541.

Robert D. Groot and Timothy J. Madden. Dynamic simulation of diblock copolymer microphase separation. *J. Chem. Phys.*, 108:8713–8724, 1998. doi:10.1063/1.476300.

André H. Gröschel and Axel H. E. Müller. Self-assembly concepts for multicompartment nanostructures. *Nanoscale*, 7:11841–11876, 2015. doi:10.1039/C5NR02448J.

André H. Gröschel, Felix H. Schacher, Holger Schmalz, Oleg V. Borisov, Ekaterina B. Zhulina, Andreas Walther, and Axel H. E. Müller. Precise hierarchical self-assembly of multicompartment micelles. *Nat Commun*, 3:710, 2012. doi:10.1038/ncomms1707.

Karsten Grosse-Brauckmann. On Gyroid Interfaces. *Journal of Colloid and Interface Science*, 187:418–428, 1997. doi:10.1006/jcis.1996.4720.

Karsten Grosse-Brauckmann. Triply periodic minimal and constant mean curvature surfaces. *Interface Focus*, 2:582–588, 2012. doi:10.1098/rsfs.2011.0096.

Branko Grünbaum and G. C. Shephard. Spherical Tilings with Transitivity Properties. In Chandler Davis, Branko Grünbaum, and F. A. Sherk, editors, *The Geometric Vein*, pages 65–98, New York, NY, 1981. Springer. doi:10.1007/978-1-4612-5648-9_4.

Branko Grünbaum and G. C. Shephard. *Tilings and Patterns*. Dover Publications, Incorporated, 2013.

Rodrigo E. Guerra, Colm P. Kelleher, Andrew D. Hollingsworth, and Paul M. Chaikin. Freezing on a sphere. *Nature*, 554:346, 2018. doi:10.1038/nature25468.

B. E. S. Gunning. The greening process in plastids. *Protoplasma*, 60:111–130, 1965. doi:10.1007/BF01248133.

B. E. S. Gunning. Membrane geometry of "open" prolamellar bodies. *Protoplasma*, 215: 4–15, 2001. doi:10.1007/BF01280299.

Brian ES Gunning and Martin W. Steer. *Ultrastructure and the Biology of Plant Cells*. Arnold, 1975.

Zuojun Guo, Guojie Zhang, Feng Qiu, Hongdong Zhang, Yuliang Yang, and An-Chang Shi. Discovering Ordered Phases of Block Copolymers: New Results from a Generic Fourier-Space Approach. *Phys. Rev. Lett.*, 101:028301, 2008. doi:10.1103/PhysRevLett.101.028301.

Theo Hahn. *International Tables for Crystallography, Space-Group Symmetry*. Wiley, 2005.

Tobias M. Hain, Gerd E. Schröder-Turk, and Jacob J. K. Kirkensgaard. Patchy particles by self-assembly of star copolymers on a spherical substrate: Thomson solutions in a geometric problem with a color constraint. *Soft Matter*, 15:9394–9404, 2019. doi:10.1039/C9SM01460H.

Tobias M. Hain, Michael A. Klatt, and Gerd E. Schröder-Turk. Low-temperature statistical mechanics of the Quantizer problem: Fast quenching and equilibrium cooling of the three-dimensional Voronoi liquid. *J. Chem. Phys.*, 153:234505, 2020. doi:10.1063/5.0029301.

Tobias M Hain, Michał Bykowski, Matthias Saba, Myfanwy E Evans, Gerd E Schröder-Turk, and Łucja Kowalewska. SPIRE—a software tool for bicontinuous phase recognition: Application for plastid cubic membranes. *Plant Physiology*, 2021. doi:10.1093/plphys/kiab476.

Damian A. Hajduk, Paul E. Harper, Sol M. Gruner, Christian C. Honeker, Gia Kim, Edwin L. Thomas, and Lewis J. Fetters. The Gyroid: A New Equilibrium Morphology in Weakly Segregated Diblock Copolymers. *Macromolecules*, 27:4063–4075, 1994. doi:10.1021/ma00093a006.

T. C. Hales. The Honeycomb Conjecture. *Discrete Comput Geom*, 25:1–22, 2001. doi:10.1007/s004540010071.

Thomas Hales. A proof of the Kepler conjecture. *Ann. Math.*, 162:1065–1185, 2005. doi:10.4007/annals.2005.162.1065.

Thomas C. Hales. Historical Overview of the Kepler Conjecture. *Discrete Comput Geom*, 36:5–20, 2006. doi:10.1007/s00454-005-1210-2.

Türkan Haliloğlu and Wayne L. Mattice. Monte Carlo Simulation of Self-Assembly in Macro-Molecular Systems. In Stephen E. Webber, Petr Munk, and Zdenek Tuzar, editors, *Solvents and Self-Organization of Polymers*, NATO ASI Series, pages 167–196. Springer Netherlands, Dordrecht, 1996. doi:10.1007/978-94-009-0333-3_9.

Ian W. Hamley. *The Physics of Block Copolymers*. Oxford University Press, 1998.

L. Han, N. Fujita, H. Chen, C. Jin, O. Terasaki, and S. Che. Crystal twinning of bicontinuous cubic structures. *IUCrJ*, 7:228–237, 2020. doi:10.1107/S2052252519017287.

Lu Han and Shunai Che. An Overview of Materials with Triply Periodic Minimal Surfaces and Related Geometry: From Biological Structures to Self-Assembled Systems. *Adv. Mater.*, 30:1705708, 2018. doi:10.1002/adma.201705708.

Wenchi Han, Ping Tang, Xuan Li, Feng Qiu, Hongdong Zhang, and Yuliang Yang. Self-Assembly of Star ABC Triblock Copolymer Thin Films: Self-Consistent Field Theory. *J. Phys. Chem. B*, 112:13738–13748, 2008. doi:10.1021/jp801675z.

Jean-Pierre Hansen and Ian R. McDonald. *Theory of Simple Liquids: With Applications to Soft Matter*. Academic Press, Amsterdam; Boston, fourth edition, 2013.

Jenny Harrison and Harrison Pugh. Plateau's Problem. In Jr. Nash, John Forbes and Michael Th. Rassias, editors, *Open Problems in Mathematics*, pages 273–302. Springer International Publishing, Cham, 2016. doi:10.1007/978-3-319-32162-2_7.

Hirokazu Hasegawa, Hideaki Tanaka, Komei Yamasaki, and Takeji Hashimoto. Bicontinuous microdomain morphology of block copolymers. 1. Tetrapod-network structure of polystyrene-polyisoprene diblock polymers. *Macromolecules*, 20:1651–1662, 1987. doi:10.1021/ma00173a036.

Kenichi Hayashida, Wataru Kawashima, Atsushi Takano, Yuya Shinohara, Yoshiyuki Amemiya, Yoshinobu Nozue, and Yushu Matsushita. Archimedean Tiling Patterns of ABC Star-Shaped Terpolymers Studied by Microbeam Small-Angle X-ray Scattering. *Macromolecules*, 39:4869–4872, 2006. doi:10.1021/ma060647p.

Kenichi Hayashida, Tomonari Dotera, Atsushi Takano, and Yushu Matsushita. Polymeric Quasicrystal: Mesoscopic Quasicrystalline Tiling in ABC Star Polymers. *Phys. Rev. Lett.*, 98:195502, 2007. doi:10.1103/PhysRevLett.98.195502.

A F Hebard. Buckminsterfullerene. *Annu. Rev. Mater. Sci.*, 23:159–191, 1993. doi:10.1146/annurev.ms.23.080193.001111.

Paul Heckbert. Color image quantization for frame buffer display. *SIGGRAPH Comput. Graph.*, 16:297–307, 1982. doi:10.1145/965145.801294.

Eugene Helfand. Theory of inhomogeneous polymers: Fundamentals of the Gaussian random-walk model. *J. Chem. Phys.*, 62:999–1005, 1975. doi:10.1063/1.430517.

Eugene Helfand and Anne Marie Sapse. Theory of unsymmetric polymer–polymer interfaces. *J. Chem. Phys.*, 62:1327–1331, 1975. doi:10.1063/1.430632.

Eugene Helfand and Yukiko Tagami. Theory of the interface between immiscible polymers. *J. Polym. Sci. [B]*, 9:741–746, 1971. doi:10.1002/pol.1971.110091006.

Eugene Helfand and Yukiko Tagami. Theory of the Interface between Immiscible Polymers. II. *J. Chem. Phys.*, 56:3592–3601, 1972. doi:10.1063/1.1677735.

Eugene Helfand and Z. R. Wasserman. Block Copolymer Theory. 4. Narrow Interphase Approximation. *Macromolecules*, 9:879–888, 1976. doi:10.1021/ma60054a001.

Takeshi Higuchi, Atsunori Tajima, Kiwamu Motoyoshi, Hiroshi Yabu, and Masatsugu Shimomura. Frustrated Phases of Block Copolymers in Nanoparticles. *Angew. Chem. Int. Ed.*, 47:8044–8046, 2008a. doi:10.1002/anie.200803003.

Takeshi Higuchi, Atsunori Tajima, Hiroshi Yabu, and Masatsugu Shimomura. Spontaneous formation of polymer nanoparticles with inner micro-phase separation structures. *Soft Matter*, 4:1302–1305, 2008b. doi:10.1039/B800904J.

Sascha Hilgenfeldt, Sinem Erisken, and Richard W. Carthew. Physical modeling of cell geometric order in an epithelial tissue. *Proc Natl Acad Sci U S A*, 105:907–911, 2008. doi:10.1073/pnas.0711077105.

Alexander Hoffmann, Jens-Uwe Sommer, and Alexander Blumen. Statics and dynamics of dense copolymer melts: A Monte Carlo simulation study. *J. Chem. Phys.*, 106: 6709–6721, 1997. doi:10.1063/1.473668.

Hisao Honda. Description of cellular patterns by Dirichlet domains: The two-dimensional case. *Journal of Theoretical Biology*, 72:523–543, 1978. doi:10.1016/0022-5193(78)90315-6.

Hisao Honda. Geometrical Models for Cells in Tissues. In G. H. Bourne, J. F. Danielli, and K. W. Jeon, editors, *International Review of Cytology*, volume 81, pages 191–248. Academic Press, 1983. doi:10.1016/S0074-7696(08)62339-6.

P. J. Hoogerbrugge and J. M. V. A. Koelman. Simulating Microscopic Hydrodynamic Phenomena with Dissipative Particle Dynamics. *EPL*, 19:155–160, 1992. doi:10.1209/0295-5075/19/3/001.

C. E. Horne. *Geometric Symmetry in Patterns and Tilings*. Elsevier, 2000.

James P. Horwath, Dmitri N. Zakharov, Rémi Mégret, and Eric A. Stach. Understanding important features of deep learning models for segmentation of high-resolution transmission electron microscopy images. *npj Comput Mater*, 6:1–9, 2020. doi:10.1038/s41524-020-00363-x.

J. Hoshen and R. Kopelman. Percolation and cluster distribution. I. Cluster multiple labeling technique and critical concentration algorithm. *Phys. Rev. B*, 14:3438–3445, 1976. doi:10.1103/PhysRevB.14.3438.

Ching-I. Huang and Hsu-Tung Yu. Microphase separation and molecular conformation of AB2 miktoarm star copolymers by dissipative particle dynamics. *Polymer*, 48: 4537–4546, 2007. doi:10.1016/j.polymer.2007.06.002.

Lars Hufnagel, Aurelio A. Teleman, Hervé Rouault, Stephen M. Cohen, and Boris I. Shraiman. On the mechanism of wing size determination in fly development. *PNAS*, 104:3835–3840, 2007. doi:10.1073/pnas.0607134104.

Maurice L. Huggins. Thermodynamic Properties of Solutions of Long-Chain Compounds. *Ann. N. Y. Acad. Sci.*, 43:1–32, 1942. doi:10.1111/j.1749-6632.1942.tb47940.x.

William Humphrey, Andrew Dalke, and Klaus Schulten. VMD – Visual Molecular Dynamics. *Journal of Molecular Graphics*, 14:33–38, 1996.

Enamul Huq, Bassem Al-Sady, Matthew Hudson, Chanhong Kim, Klaus Apel, and Peter H. Quail. PHYTOCHROME-INTERACTING FACTOR 1 Is a Critical bHLH Regulator of Chlorophyll Biosynthesis. *Science*, 305:1937–1941, 2004. doi:10.1126/science.1099728.

S. Hyde, Z. Blum, T. Landh, S. Lidin, B. W. Ninham, S. Andersson, and K. Larsson. *The Language of Shape: The Role of Curvature in Condensed Matter: Physics, Chemistry and Biology*. Elsevier, 1996.

S. T. Hyde, Sten Andersson, Bodil Ericsson, and Kåre Larsson. A cubic structure consisting of a lipid bilayer forming an infinite periodic minimum surface of the gyroid type in the glycerolmonooleat-water system. *Z. Für Krist. - Cryst. Mater.*, 168:213–220, 1984. doi:10.1524/zkri.1984.168.14.213.

Stephen T. Hyde. Identification of Lyotropic Liquid Crystalline Mesophases. In *Handbook of Applied Surface and Colloid Chemistry*, volume 2, pages 299–332. JOHN WILEY & SONS, LTD, 1st edition, 2002.

Taiji Ikeda. Analytical Studies on the Structure of Prolamellar Body. *Shokubutsugaku Zasshi*, 81:517–527, 1968. doi:10.15281/jplantres1887.81.517.

Marianne Impéror-Clerc. Three-dimensional periodic complex structures in soft matter: Investigation using scattering methods. *Interface Focus*, 2:589–601, 2012. doi:10.1098/rsfs.2011.0081.

William T. M. Irvine, Vincenzo Vitelli, and Paul M. Chaikin. Pleats in crystals on curved surfaces. *Nature*, 468:947, 2010. doi:10.1038/nature09620.

William T. M. Irvine, Mark J. Bowick, and Paul M. Chaikin. Fractionalization of interstitials in curved colloidal crystals. *Nat. Mater.*, 11:948–51, 2012.

Lyle Isaacs, Donovan N. Chin, Ned Bowden, Younan Xia, and George M. Whitesides. Self-Assembling Systems on Scales from Nanometers to Millimeters: Design and Discovery. In *Perspectives in Supramolecular Chemistry*, pages 1–46. John Wiley & Sons, Ltd, 1999. doi:10.1002/9780470511497.ch1.

Cyril Isenberg. *The Science of Soap Films and Soap Bubbles*. Dover Publications, 1992.

Iris K. Jarsch, Frederic Daste, and Jennifer L. Gallop. Membrane curvature in cell biology: An integration of molecular mechanisms. *J. Cell Biol.*, 214:375–387, 2016. doi:10.1083/jcb.201604003.

Seog-Jin Jeon, Gi-Ra Yi, Chong Min Koo, and Seung-Man Yang. Nanostructures Inside Colloidal Particles of Block Copolymer/Homopolymer Blends. *Macromolecules*, 40: 8430–8439, 2007. doi:10.1021/ma0712302.

S. A. Jewell, P. Vukusic, and N. W. Roberts. Circularly polarized colour reflection from helicoidal structures in the beetlePlusiotis boucardi. *New J. Phys.*, 9:99–99, 2007. doi:10.1088/1367-2630/9/4/099.

John D. Joannopoulos, Steven G. Johnson, Joshua N. Winn, and Robert D. Meade. *Photonic Crystals: Molding the Flow of Light - Second Edition*. Princeton University Press, 2011. doi:10.1515/9781400828241.

R.A.L. Jones and R.W. Richards. *Polymers at Surfaces and Interfaces*. Polymers at Surfaces and Interfaces. Cambridge University Press, 1999.

Randall D. Kamien. The geometry of soft materials: A primer. *Rev. Mod. Phys.*, 74: 953–971, 2002. doi:10.1103/RevModPhys.74.953.

Hermann Karcher. The triply periodic minimal surfaces of Alan Schoen and their constant mean curvature companions. *Manuscripta Math*, 64:291–357, 1989. doi:10.1007/BF01165824.

G. Katgert and M. van Hecke. Jamming and geometry of two-dimensional foams. *EPL*, 92:34002, 2010. doi:10.1209/0295-5075/92/34002.

Ashish K. Khandpur, Stephan Foerster, Frank S. Bates, Ian W. Hamley, Anthony J. Ryan, Wim Bras, Kristoffer Almdal, and Kell Mortensen. Polyisoprene-Polystyrene Diblock Copolymer Phase Diagram near the Order-Disorder Transition. *Macromolecules*, 28: 8796–8806, 1995. doi:10.1021/ma00130a012.

Sung A. Kim, Kyeong-Jun Jeong, Arun Yethiraj, and Mahesh K. Mahanthappa. Low-symmetry sphere packings of simple surfactant micelles induced by ionic sphericity. *PNAS*, 114:4072–4077, 2017. doi:10.1073/pnas.1701608114.

Jacob J. K. Kirkensgaard, Martin C. Pedersen, and Stephen T. Hyde. Tiling patterns from ABC star molecules: 3-colored foams? *Soft Matter*, 10:7182–7194, 2014. doi:10.1039/C4SM01052C.

Jacob Judas Kain Kirkensgaard. Systematic progressions of core-shell polygon containing tiling patterns in melts of 2nd generation dendritic miktoarm star copolymers. *Soft Matter*, 7:10756, 2011.

Jacob Judas Kain Kirkensgaard. Kaleidoscopic tilings, networks and hierarchical structures in blends of 3-miktoarm star terpolymers. *Interface Focus*, 2:602–607, 2012a. doi:10.1098/rsfs.2011.0093.

Jacob Judas Kain Kirkensgaard. Striped networks and other hierarchical structures in $A_mB_mC_n$ $(2m + n)$-miktoarm star terpolymer melts. *Phys. Rev. E*, 85:031802, 2012b. doi:10.1103/PhysRevE.85.031802.

Charlse Kittel. *Introduction to Solid State Physics*. Wiley, eighth edition, 2004.

Michael A. Klatt, Jakov Lovrić, Duyu Chen, Sebastian C. Kapfer, Fabian M. Schaller, Philipp W. A. Schönhöfer, Bruce S. Gardiner, Ana-Sunčana Smith, Gerd E. Schröder-Turk, and Salvatore Torquato. Universal hidden order in amorphous cellular geometries. *Nat. Commun.*, 10:811, 2019. doi:10.1038/s41467-019-08360-5.

Jacek Klinowski, Alan Lindsay Mackay, Humberto Terrones, Jacek Klinowski, and Alan Lindsay Mackay. Curved surfaces in chemical structure. *Philos. Trans. R. Soc. Lond. Ser. Math. Phys. Eng. Sci.*, 354:1975–1987, 1996a. doi:10.1098/rsta.1996.0086.

Jacek Klinowski, Alan Lindsay Mackay, Humberto Terrones, Jacek Klinowski, and Alan Lindsay Mackay. Curved surfaces in chemical structure. *Philos. Trans. R. Soc. Lond. Ser. Math. Phys. Eng. Sci.*, 354:1975–1987, 1996b. doi:10.1098/rsta.1996.0086.

Moon Bae Ko and Wayne L. Mattice. Monte Carlo simulation of concentrated diblock copolymers in a selective solvent: Anisotropy of the diffusion. *Macromolecules*, 28:6871–6877, 1995. doi:10.1021/ma00124a024.

Benedikt Kolbe and Myfanwy E. Evans. Isotopic tiling theory for hyperbolic surfaces. *Geom Dedicata*, 212:177–204, 2021. doi:10.1007/s10711-020-00554-2.

O. V. Konevtsova, S. B. Rochal, and V. L. Lorman. Chiral quasicrystalline order and dodecahedral geometry in exceptional families of viruses. *Phys. Rev. Lett.*, 108:038102, 2012. doi:10.1103/PhysRevLett.108.038102.

Łucja Kowalewska, Radosław Mazur, Szymon Suski, Maciej Garstka, and Agnieszka Mostowska. Three-Dimensional Visualization of the Tubular-Lamellar Transformation of the Internal Plastid Membrane Network during Runner Bean Chloroplast Biogenesis. *The Plant Cell*, 28:875–891, 2016. doi:10.1105/tpc.15.01053.

Łucja Kowalewska, Michał Bykowski, and Agnieszka Mostowska. Spatial organization of thylakoid network in higher plants. *Bot. Lett.*, 166:326–343, 2019. doi:10.1080/23818107.2019.1619195.

Michael M Kozlov, Felix Campelo, Nicole Liska, Leonid V Chernomordik, Siewert J Marrink, and Harvey T McMahon. Mechanisms shaping cell membranes. *Curr. Opin. Cell Biol.*, 29:53–60, 2014. doi:10.1016/j.ceb.2014.03.006.

A. M. Kraynik. The Structure of Random Foam. *Adv. Eng. Mater.*, 8:900–906, 2006. doi:10.1002/adem.200600167.

Andrew M. Kraynik, Douglas A. Reinelt, and Frank van Swol. Structure of Random Foam. *Phys. Rev. Lett.*, 93:208301, 2004. doi:10.1103/PhysRevLett.93.208301.

Alex Krizhevsky, Ilya Sutskever, and Geoffrey E Hinton. ImageNet Classification with Deep Convolutional Neural Networks. In *Advances in Neural Information Processing Systems*, volume 25. Curran Associates, Inc., 2012.

Benedikt Krüger. *Simulating Triangulations: Graphs, Manifolds and (Quantum) Spacetime*. Doctoralthesis, FAU University Press, 2016.

Kang Hee Ku. Responsive Nanostructured Polymer Particles. *Polymers*, 13:273, 2021. doi:10.3390/polym13020273.

Kang Hee Ku, Young Jun Lee, YongJoo Kim, and Bumjoon J. Kim. Shape-Anisotropic Diblock Copolymer Particles from Evaporative Emulsions: Experiment and Theory. *Macromolecules*, 52:1150–1157, 2019. doi:10.1021/acs.macromol.8b02465.

Halim Kusumaatmaja and David J. Wales. Defect Motifs for Constant Mean Curvature Surfaces. *Phys. Rev. Lett.*, 110:165502, 2013. doi:10.1103/PhysRevLett.110.165502.

Tomas Landh. *Cubic Cell Membrane Architectures. Taking Another Look at Membrane Bound Cell Spaces*. PhD thesis, Department of Food Technology, Lund University, 1996.

R. G. Larson. Self-assembly of surfactant liquid crystalline phases by Monte Carlo simulation. *J. Chem. Phys.*, 91:2479–2488, 1989. doi:10.1063/1.457007.

K. Larsson. Two cubic phases in monoolein–water system. *Nature*, 304:664–664, 1983. doi:10.1038/304664c0.

K. Larsson. Cubic lipid-water phases: Structures and biomembrane aspects. *J. Phys. Chem.*, 93:7304–7314, 1989. doi:10.1021/j100358a010.

K. Larsson, K. Fontell, and N. Krog. Structural relationships between lamellar, cubic and hexagonal phases in monoglyceride-water systems. possibility of cubic structures in biological systems. *Chemistry and Physics of Lipids*, 27:321–328, 1980. doi:10.1016/0009-3084(80)90026-2.

Kåre Larsson. Periodic minimal surface structures of cubic phases formed by lipids and surfactants. *Journal of Colloid and Interface Science*, 113:299–300, 1986. doi:10.1016/0021-9797(86)90232-8.

Kåre Larsson and Fredrik Tiberg. Periodic minimal surface structures in bicontinuous lipid–water phases and nanoparticles. *Current Opinion in Colloid & Interface Science*, 9: 365–369, 2005. doi:10.1016/j.cocis.2004.12.002.

Ludwik Leibler. Theory of microphase separation in block copolymers. *Macromolecules*, 13:1602–1617, 1980. doi:10.1021/ma60078a047.

Shiben Li, Ying Jiang, and Jeff Z. Y. Chen. Morphologies and phase diagrams of ABC star triblock copolymers confined in a spherical cavity. *Soft Matter*, 9:4843–4854, 2013. doi:10.1039/C3SM27770D.

Alexey E. Likhtman and Alexander N. Semenov. Stability of the OBDD Structure for Diblock Copolymer Melts in the Strong Segregation Limit. *Macromolecules*, 27:3103–3106, 1994. doi:10.1021/ma00089a030.

Bo Lin, Hongdong Zhang, Feng Qiu, and Yuliang Yang. Self-Assembly of ABC Star Triblock Copolymer Thin Films Confined with a Preferential Surface: A Self-Consistent Mean Field Theory. *Langmuir*, 26:19033–19044, 2010. doi:10.1021/la102519f.

Goeran Lindblom, Kaare Larsson, Lennart Johansson, Krister Fontell, and Sture Forsen. The cubic phase of monoglyceride-water systems. Arguments for a structure based upon lamellar bilayer units. *J. Am. Chem. Soc.*, 101:5465–5470, 1979. doi:10.1021/ja00513a002.

Peter Lipowsky, Mark J. Bowick, Jan H. Meinke, David R. Nelson, and Andreas R. Bausch. Direct visualization of dislocation dynamics in grain-boundary scars. *Nat. Mater.*, 4:407–11, 2005.

Yang Liu, Wenping Wang, Bruno Lévy, Feng Sun, Dong-Ming Yan, Lin Lu, and Chenglei Yang. On centroidal voronoi tessellation—energy smoothness and fast computation. *ACM Trans. Graph.*, 28:101:1–101:17, 2009. doi:10.1145/1559755.1559758.

S. Lloyd. Least squares quantization in PCM. *IEEE Trans. Inf. Theory*, 28:129–137, 1982. doi:10.1109/TIT.1982.1056489.

Tina I. Löbling, Oleg Borisov, Johannes S. Haataja, Olli Ikkala, André H. Gröschel, and Axel H. E. Müller. Rational design of ABC triblock terpolymer solution nanostructures with controlled patch morphology. *Nat Commun*, 7:12097, 2016. doi:10.1038/ncomms12097.

William Longley and Thomas J. McIntosh. A bicontinuous tetrahedral structure in a liquid-crystalline lipid. *Nature*, 303:612–614, 1983. doi:10.1038/303612a0.

Hsin-Ya Lou, Wenting Zhao, Yongpeng Zeng, and Bianxiao Cui. The Role of Membrane Curvature in Nanoscale Topography-Induced Intracellular Signaling. *Acc. Chem. Res.*, 51:1046–1053, 2018. doi:10.1021/acs.accounts.7b00594.

Jean-Christophe Loudet, Philippe Barois, and Philippe Poulin. Colloidal ordering from phase separation in a liquid- crystalline continuous phase. *Nature*, 407:611–613, 2000. doi:10.1038/35036539.

Jakov Lovrić, Sara Kaliman, Wolfram Barfuss, Gerd E. Schröder-Turk, and Ana-Sunčana Smith. Geometric effects in random assemblies of ellipses. *Soft Matter*, 15:8566–8577, 2019. doi:10.1039/C9SM01067J.

Lin Lu, Feng Sun, Hao Pan, and Wenping Wang. Global Optimization of Centroidal Voronoi Tessellation with Monte Carlo Approach. *IEEE Trans. Vis. Comput. Graph.*, 18: 1880–1890, 2012. doi:10.1109/TVCG.2012.28.

Xinjiang Lü and James T. Kindt. Monte Carlo simulation of the self-assembly and phase behavior of semiflexible equilibrium polymers. *J. Chem. Phys.*, 120:10328–10338, 2004. doi:10.1063/1.1729855.

Vittorio Luzzati. Biological significance of lipid polymorphism: The cubic phases. *Current Opinion in Structural Biology*, 7:661–668, 1997. doi:10.1016/S0959-440X(97)80075-9.

Vittorio Luzzati, A. Tardieu, T. Gulik-Krzywicki, E. Rivas, and F. Reiss-Husson. Structure of the Cubic Phases of Lipid–Water Systems. *Nature*, 220:485–488, 1968. doi:10.1038/220485a0.

Zhaoyan Lv, Ji Wu, Wenchang Lang, Xianghong Wang, and Shiben Li. Self-assembly of tiling-forming ABC star triblock copolymers in cylindrical nanotubes: A study of self-consistent field theory. *Journal of the Taiwan Institute of Chemical Engineers*, 65: 565–573, 2016. doi:10.1016/j.jtice.2016.05.051.

Ranjan V. Mannige and Charles L. Brooks. Tilable nature of virus capsids and the role of topological constraints in natural capsid design. *Phys. Rev. E*, 77:051902, 2008. doi:10.1103/PhysRevE.77.051902.

M. Lisa Manning, Ramsey A. Foty, Malcolm S. Steinberg, and Eva-Maria Schoetz. Coaction of intercellular adhesion and cortical tension specifies tissue surface tension. *PNAS*, 107:12517–12522, 2010. doi:10.1073/pnas.1003743107.

Glenn J. Martyna, Douglas J. Tobias, and Michael L. Klein. Constant pressure molecular dynamics algorithms. *J. Chem. Phys.*, 101:4177–4189, 1994. doi:10.1063/1.467468.

Andrew M. Mascioli, Christopher J. Burke, Mathew Q. Giso, and Timothy J. Atherton. Defect structure and percolation in the packing of bidispersed particles on a sphere. *Soft Matter*, 13:7090–7097, 2017. doi:10.1039/C7SM00179G.

M W Matsen. The standard Gaussian model for block copolymer melts. *J. Phys. Condens. Matter*, 14:R21, 2002.

M. W. Matsen and F. S. Bates. Unifying weak- and strong-segregation block copolymer theories. *Macromolecules*, 29:1091–1098, 1996. doi:10.1021/ma951138i.

M. W. Matsen and M. Schick. Stable and unstable phases of a diblock copolymer melt. *Phys. Rev. Lett.*, 72:2660–2663, 1994. doi:10.1103/PhysRevLett.72.2660.

Mark W. Matsen. Self consistent field theory and its applications. In *Soft Matter*, chapter 2, pages 87–178. Wiley-Blackwell, 2007. doi:10.1002/9783527617050.ch2.

Yushu Matsushita. Creation of Hierarchically Ordered Nanophase Structures in Block Polymers Having Various Competing Interactions. *Macromolecules*, 40:771–776, 2007. doi:10.1021/ma062266h.

Yushu Matsushita, Jiro Suzuki, and Motohiro Seki. Surfaces of tricontinuous structure formed by an ABC triblock copolymer in bulk. *Physica B: Condensed Matter*, 248:238–242, 1998. doi:10.1016/S0921-4526(98)00239-7.

Edwin B. Matzke. The Three-Dimensional Shape of Bubbles in Foam—an Analysis of the Rôle of Surface Forces in Three-Dimensional Cell Shape Determination. *Am. J. Bot.*, 33:58–80, 1946. doi:10.1002/j.1537-2197.1946.tb10347.x.

Anita Mehta. *Granular Matter: An Interdisciplinary Approach.* Springer Science & Business Media, 2012.

Wilhelm Menke. Zur Stereometrie der Heitz-Leyonschen Kristalle vonChlorophytum comosum. *Z. Für Naturforschung B*, 18:821–826, 1963. doi:10.1515/znb-1963-1007.

Matthias Merkel and M. Lisa Manning. A geometrically controlled rigidity transition in a model for confluent 3D tissues. *New J. Phys.*, 20:022002, 2018. doi:10.1088/1367-2630/aaaa13.

Nicholas Metropolis, Arianna W. Rosenbluth, Marshall N. Rosenbluth, Augusta H. Teller, and Edward Teller. Equation of State Calculations by Fast Computing Machines. *J. Chem. Phys.*, 21:1087–1092, 1953. doi:10.1063/1.1699114.

Adam J. Meuler, Marc A. Hillmyer, and Frank S. Bates. Ordered Network Mesostructures in Block Polymer Materials. *Macromolecules*, 42:7221–7250, 2009. doi:10.1021/ma9009593.

Raffaele Mezzenga, Peter Schurtenberger, Adam Burbidge, and Martin Michel. Understanding foods as soft materials. *Nature Mater*, 4:729–740, 2005. doi:10.1038/nmat1496.

Raffaele Mezzenga, John M. Seddon, Calum J. Drummond, Ben J. Boyd, Gerd E. Schröder-Turk, and Laurent Sagalowicz. Nature-Inspired Design and Application of Lipidic Lyotropic Liquid Crystals. *Adv. Mater.*, 31:1900818, 2019. doi:10.1002/adma.201900818.

A.A. Michelson. LXI. On metallic colouring in birds and insects. *Lond. Edinb. Dublin Philos. Mag. J. Sci.*, 21:554–567, 1911. doi:10.1080/14786440408637061.

Uwe Micka and Kurt Binder. Unusual finite size effects in the Monte Carlo simulation of microphase formation of block copolymer melts. *Macromol. Theory Simul.*, 4:419–447, 1995. doi:10.1002/mats.1995.040040303.

Walter Mickel, Stefan Münster, Louise M. Jawerth, David A. Vader, David A. Weitz, Adrian P. Sheppard, Klaus Mecke, Ben Fabry, and Gerd E. Schröder-Turk. Robust Pore Size Analysis of Filamentous Networks from Three-Dimensional Confocal Microscopy. *Biophys. J.*, 95:6072–6080, 2008. doi:10.1529/biophysj.108.135939.

William L. Miller and Angelo Cacciuto. Two-dimensional packing of soft particles and the soft generalized Thomson problem. *Soft Matter*, 7:7552–7559, 2011a. doi:10.1039/C1SM05731F.

William L. Miller and Angelo Cacciuto. Two-dimensional packing of soft particles and the soft generalized Thomson problem. *Soft Matter*, 7:7552–7559, 2011b. doi:10.1039/C1SM05731F.

Richard S. Millman. *Elements of Differential Geometry*. Prentice-Hall Inc., Upper Saddle River, NJ, 1977.

Richard S. Millman and George D. Parker. *Elements of Differential Geometry*. Prentice-Hall, Englewood Cliffs, NJ, 1977.

Erick Moen, Dylan Bannon, Takamasa Kudo, William Graf, Markus Covert, and David Van Valen. Deep learning for cellular image analysis. *Nat Methods*, 16:1233–1246, 2019. doi:10.1038/s41592-019-0403-1.

Peter K. Morse and Eric I. Corwin. Geometric order parameters derived from the Voronoi tessellation show signatures of the jamming transition. *Soft Matter*, 12:1248–1255, 2016. doi:10.1039/C5SM02575C.

A. Mughal, S. J. Cox, and G. E. Schröder-Turk. Curvature driven motion of a bubble in a toroidal Hele-Shaw cell. *Interface Focus*, 7:20160106, 2017a. doi:10.1098/rsfs.2016.0106.

A. Mughal, T. Libertiny, and G. E. Schröder-Turk. How bees and foams respond to curved confinement: Level set boundary representations in the Surface Evolver. *Colloids and Surfaces A: Physicochemical and Engineering Aspects*, 534:94–104, 2017b. doi:10.1016/j.colsurfa.2017.02.090.

Adil Mughal. Packing of Softly Repulsive Particles in a Spherical Box—A Generalised Thomson Problem. *Forma*, 2014. doi:10.5047/forma.2014.003.

Edvard Rudolf Neovius. Bestimmung zweier speciellen periodischen Minimalflächen, auf welchen unendlich viele gerade Linien und unendlich viele ebene geodätische Linien liegen. 1883.

Reinhard Nesper and Stefano Leoni. On Tilings and Patterns on Hyperbolic Surfaces and Their Relation to Structural Chemistry. *ChemPhysChem*, 2:413–422, 2001. doi:10.1002/1439-7641(20010716)2:7<413::AID-CPHC413>3.0.CO;2-V.

Josef Neumüller. Electron tomography—a tool for ultrastructural 3D visualization in cell biology and histology. *Wien Med Wochenschr*, 168:322–329, 2018. doi:10.1007/s10354-018-0646-y.

Henry C. Nguyen, Arthur A. Melo, Jerzy Kruk, Adam Frost, and Michal Gabruk. Photocatalytic LPOR forms helical lattices that shape membranes for chlorophyll synthesis. *Nat. Plants*, 7:437–444, 2021. doi:10.1038/s41477-021-00885-2.

Taco Nicolai, Fabrice Laflèche, and Alain Gibaud. Jamming and Crystallization of Polymeric Micelles. *Macromolecules*, 37:8066–8071, 2004. doi:10.1021/ma049101y.

Johannes C. C. Nitsche. *Lectures on Minimal Surfaces: Volume 1, Introduction, Fundamentals, Geometry and Basic Boundary Value Problems*. Cambridge University Press, 2011.

Lars Norlén and Ashraf Al-Amoudi. Stratum Corneum Keratin Structure, Function, and Formation: The Cubic Rod-Packing and Membrane Templating Model. *J Invest Dermatol*, 123:715–732, 2004. doi:10.1111/j.0022-202X.2004.23213.x.

Shūichi Nosé. A molecular dynamics method for simulations in the canonical ensemble. *Mol. Phys.*, 100:191–198, 1983. doi:10.1080/00268970110089108.

Atsuyuki Okabe, Barry Boots, Kokichi Sugihara, and Sung Nok Chiu. *Spatial Tessellations: Concepts and Applications of Voronoi Diagrams*. Wiley, Chichester; New York, second edition, 2000.

Shigeru Okamoto, Hirokazu Hasegawa, Takeji Hashimoto, Teruo Fujimoto, Hongmin Zhang, Takeo Kazama, Atsushi Takano, and Yoshinobu Isono. Morphology of model three-component three-arm star-shaped copolymers. *Polymer*, 38(21):5275 – 5281, 1997. ISSN 0032-3861. doi:https://doi.org/10.1016/S0032-3861(97)00089-X. URL `http://www.sciencedirect.com/science/article/pii/S003238619700089X`.

M. O'Keeffe, J. Plévert, Y. Teshima, Y. Watanabe, and T. Ogama. The invariant cubic rod (cylinder) packings: Symmetries and coordinates. *Acta Cryst A*, 57:110–111, 2001. doi:10.1107/S010876730001151X.

Michael O'Keeffe, Maxim A. Peskov, Stuart J. Ramsden, and Omar M. Yaghi. The Reticular Chemistry Structure Resource (RCSR) Database of, and Symbols for, Crystal Nets. *Acc. Chem. Res.*, 41:1782–1789, 2008. doi:10.1021/ar800124u.

Peter D. Olmsted and Scott T. Milner. Strong-segregation theory of bicontinuous phases in block copolymers. *Phys. Rev. Lett.*, 72:936–939, 1994. doi:10.1103/PhysRevLett.72.936.

Peter D. Olmsted and Scott T. Milner. Strong Segregation Theory of Bicontinuous Phases in Block Copolymers. *Macromolecules*, 31:4011–4022, 1998. doi:10.1021/ma980043o.

Monica Olvera de la Cruz and Isaac C. Sanchez. Theory of microphase separation in graft and star copolymers. *Macromolecules*, 19:2501–2508, 1986. doi:10.1021/ma00164a008.

Joseph O'Rourke, Olin Professor of Computer Science Joseph O'Rourke, and Associate Professor of Computer Science Joseph O'Rourke. *Computational Geometry in C.* Cambridge University Press, 1998.

A. Pérez-Garrido, M. J. W. Dodgson, and M. A. Moore. Influence of dislocations in thomson's problem. *Phys. Rev. B*, 56:3640–3643, Aug 1997. doi:10.1103/PhysRevB.56.3640. URL https://link.aps.org/doi/10.1103/PhysRevB.56.3640.

S. Perkowitz and Sidney Perkowitz. *Universal Foam: From Cappuccino to the Cosmos.* Walker & Company, 2000.

Eric F. Pettersen, Thomas D. Goddard, Conrad C. Huang, Gregory S. Couch, Daniel M. Greenblatt, Elaine C. Meng, and Thomas E. Ferrin. UCSF Chimera—A visualization system for exploratory research and analysis. *J. Comput. Chem.*, 25:1605–1612, 2004. doi:10.1002/jcc.20084.

Anna C. Pham, Kang-Yu Peng, Malinda Salim, Gisela Ramirez, Adrian Hawley, Andrew J. Clulow, and Ben J. Boyd. Correlating Digestion-Driven Self-Assembly in Milk and Infant Formulas with Changes in Lipid Composition. *ACS Appl. Bio Mater.*, 3:3087–3098, 2020. doi:10.1021/acsabm.0c00131.

Carolyn L. Phillips, Joshua A. Anderson, and Sharon C. Glotzer. Pseudo-random number generation for brownian dynamics and dissipative particle dynamics simulations on gpu devices. *Journal of Computational Physics*, 230(19):7191 – 7201, 2011. ISSN 0021-9991. doi:https://doi.org/10.1016/j.jcp.2011.05.021. URL http://www.sciencedirect.com/science/article/pii/S0021999111003329.

Douglas Philp and J. Fraser Stoddart. Self-Assembly in Natural and Unnatural Systems. *Angew. Chem. Int. Ed. Engl.*, 35:1154–1196, 1996. doi:10.1002/anie.199611541.

Rosa Pipitone, Simona Eicke, Barbara Pfister, Gaetan Glauser, Denis Falconet, Clarisse Uwizeye, Thibaut Pralon, Samuel C Zeeman, Felix Kessler, and Emilie Demarsy. A multifaceted analysis reveals two distinct phases of chloroplast biogenesis during de-etiolation in Arabidopsis. *eLife*, 10:e62709, 2021. doi:10.7554/eLife.62709.

Joseph Plateau. *Statique expérimentale et théorique des liquides soumis aux seules forces moléculaires*. Gauthier-Villars, 1873.

George Polymeropoulos, George Zapsas, Konstantinos Ntetsikas, Panayiotis Bilalis, Yves Gnanou, and Nikos Hadjichristidis. 50th anniversary perspective: Polymers with complex architectures. *Macromolecules*, 50:1253–1290, 2017. doi:10.1021/acs.macromol.6b02569.

Inés C. Pons-Siepermann and Sharon C. Glotzer. Design of patchy particles using ternary self-assembled monolayers. *Soft Matter*, 8:6226–6231, 2012a. doi:10.1039/C2SM00014H.

Ines C. Pons-Siepermann and Sharon C. Glotzer. Design of Patchy Particles Using Quaternary Self-Assembled Monolayers. *ACS Nano*, 6:3919–3924, 2012b. doi:10.1021/nn300059x.

Mathias Pribil, Mathias Labs, and Dario Leister. Structure and dynamics of thylakoids in land plants. *J. Exp. Bot.*, 65:1955–1972, 2014. doi:10.1093/jxb/eru090.

G. E. Pringle. The structure of SrSI2: A crystal of class O (432). *Acta Cryst B*, 28:2326–2328, 1972. doi:10.1107/S0567740872006053.

S. J. Ramsden, V. Robins, and S. T. Hyde. Three-dimensional Euclidean nets from two-dimensional hyperbolic tilings: Kaleidoscopic examples. *Acta Cryst A*, 65:81–108, 2009. doi:10.1107/S0108767308040592.

D. C. Rapaport. *The Art of Molecular Dynamics Simulation*. Cambridge University Press, Cambridge, second edition, 2004. doi:10.1017/CBO9780511816581.

Waseem Rawat and Zenghui Wang. Deep Convolutional Neural Networks for Image Classification: A Comprehensive Review. *Neural Comput.*, 29:2352–2449, 2017. doi:10.1162/neco_a_00990.

Abhiram Reddy, Michael B. Buckley, Akash Arora, Frank S. Bates, Kevin D. Dorfman, and Gregory M. Grason. Stable Frank–Kasper phases of self-assembled, soft matter spheres. *PNAS*, 115:10233–10238, 2018. doi:10.1073/pnas.1809655115.

Abhiram Reddy, Xueyan Feng, Edwin L. Thomas, and Gregory M. Grason. Block Copolymers beneath the Surface: Measuring and Modeling Complex Morphology at the Subdomain Scale. *Macromolecules*, 54:9223–9257, 2021. doi:10.1021/acs.macromol.1c00958.

P. Richard, L. Oger, J.P. Troadec, and A. Gervois. A model of binary assemblies of spheres. *Eur. Phys. J. E*, 6:295–303, 2001. doi:10.1007/s10189-001-8044-6.

V. Robins, S. J. Ramsden, and S. T. Hyde. 2D hyperbolic groups induce three-periodic Euclidean reticulations. *Eur. Phys. J. B*, 39:365–375, 2004. doi:10.1140/epjb/e2004-00202-2.

M. Robinson, I. Suarez-Martinez, and N. A. Marks. Generalized method for constructing the atomic coordinates of nanotube caps. *Phys. Rev. B*, 87:155430, Apr 2013. doi:10.1103/PhysRevB.87.155430. URL https://link.aps.org/doi/10.1103/PhysRevB.87.155430.

S. B. Rochal, O. V. Konevtsova, A. E. Myasnikova, and V. L. Lorman. Hidden symmetry of small spherical viruses and organization principles in "anomalous" and double-shelled capsid nanoassemblies. *Nanoscale*, 8:16976–16988, 2016. doi:10.1039/C6NR04930C. URL http://dx.doi.org/10.1039/C6NR04930C.

A. E. Roth, C. D. Jones, and D. J. Durian. Coarsening of a two-dimensional foam on a dome. *Phys. Rev. E*, 86:021402, 2012. doi:10.1103/PhysRevE.86.021402.

C. Patrick Royall, Alex Malins, Andrew J. Dunleavy, and Rhiannon Pinney. Strong geometric frustration in model glassformers. *Journal of Non-Crystalline Solids*, 407:34–43, 2015. doi:10.1016/j.jnoncrysol.2014.08.017.

C. Ruscher, J. Baschnagel, and J. Farago. The Voronoi liquid. *EPL*, 112:66003, 2015. doi:10.1209/0295-5075/112/66003.

C. Ruscher, A. N. Semenov, J. Baschnagel, and J. Farago. Anomalous sound attenuation in Voronoi liquid. *J. Chem. Phys.*, 146:144502, 2017. doi:10.1063/1.4979720.

C. Ruscher, J. Baschnagel, and J. Farago. Voronoi glass-forming liquids: A structural study. *Phys. Rev. E*, 97:032132, 2018. doi:10.1103/PhysRevE.97.032132.

C. Ruscher, S. Ciarella, C. Luo, L. M. C. Janssen, J. Farago, and J. Baschnagel. Glassy dynamics of a binary Voronoi fluid: A mode-coupling analysis. *J. Phys.: Condens. Matter*, 33:064001, 2020. doi:10.1088/1361-648X/abc4cc.

Céline Ruscher. *The Voronoi Liquid : A New Model to Probe the Glass Transition*. PhD thesis, École doctorale Physique et chimie-physique, 2017.

Shawn D. Ryan, Xiaoyu Zheng, and Peter Palffy-Muhoray. Curvature-driven foam coarsening on a sphere: A computer simulation. *Phys. Rev. E*, 93:053301, 2016. doi:10.1103/PhysRevE.93.053301.

Chris H. Rycroft. VORO++: A three-dimensional Voronoi cell library in C++. *Chaos*, 19:041111, 2009. doi:10.1063/1.3215722.

Jean-François Sadoc and Rémy Mosseri. *Geometrical Frustration*. Collection Alea-Saclay: Monographs and Texts in Statistical Physics. Cambridge University Press, Cambridge, 1999. doi:10.1017/CBO9780511599934.

Stefan Salentinig, Stephanie Phan, Adrian Hawley, and Ben J. Boyd. Self-Assembly Structure Formation during the Digestion of Human Breast Milk. *Angew. Chem. Int. Ed.*, 54:1600–1603, 2015. doi:10.1002/anie.201408320.

Andras Sandor, Mark David Fricker, Verena Kriechbaumer, and Lee J. Sweetlove. IntEResting structures: Formation and applications of organised smooth endoplasmic reticulum in plant cells. *Plant Physiol.*, 185:550–561, 2021. doi:10.1104/pp.20.00719.

Omar Sandoval-Ibáñez, Anurag Sharma, Michał Bykowski, Guillem Borràs-Gas, James B. Y. H. Behrendorff, Silas Mellor, Klaus Qvortrup, Julian C. Verdonk, Ralph Bock, Łucja Kowalewska, and Mathias Pribil. Curvature thylakoid 1 proteins modulate prolamellar body morphology and promote organized thylakoid biogenesis in Arabidopsis thaliana. *PNAS*, 118, 2021. doi:10.1073/pnas.2113934118.

Donald Sands. *Introduction to Crystallography*. New York : Dover, 1993.

Vinodkumar Saranathan, Chinedum O. Osuji, Simon G. J. Mochrie, Heeso Noh, Suresh Narayanan, Alec Sandy, Eric R. Dufresne, and Richard O. Prum. Structure, function, and self-assembly of single network gyroid (I4132) photonic crystals in butterfly wing scales. *PNAS*, 107:11676–11681, 2010. doi:10.1073/pnas.0909616107.

W. Schaertl and H. Sillescu. Brownian dynamics of polydisperse colloidal hard spheres: Equilibrium structures and random close packings. *J Stat Phys*, 77:1007–1025, 1994. doi:10.1007/BF02183148.

Fabian M. Schaller, Sebastian C. Kapfer, Myfanwy E. Evans, Matthias J.F. Hoffmann, Tomaso Aste, Mohammad Saadatfar, Klaus Mecke, Gary W. Delaney, and Gerd E. Schröder-Turk. Set Voronoi diagrams of 3D assemblies of aspherical particles. *Philos. Mag.*, 93:3993–4017, 2013. doi:10.1080/14786435.2013.834389.

F. Schmid. Self-consistent-field theories for complex fluids. *J. Phys.: Condens. Matter*, 10: 8105–8138, 1998a. doi:10.1088/0953-8984/10/37/002.

F. Schmid. Self-consistent-field theories for complex fluids. *J. Phys.: Condens. Matter*, 10: 8105–8138, 1998b. doi:10.1088/0953-8984/10/37/002.

Alan H. Schoen. *Infinite Periodic Minimal Surfaces without Self-Intersections*. NASA Technical Note, NASA TN D-5541. National Aeronautics and Space Administration; [for sale by the Clearinghouse for Federal Scientific and Technical Information, Springfield, Va.], Washington, 1970.

Philipp W. A. Schönhöfer, Laurence J. Ellison, Matthieu Marechal, Douglas J. Cleaver, and Gerd E. Schröder-Turk. Purely entropic self-assembly of the bicontinuous Ia3d gyroid phase in equilibrium hard-pear systems. *Interface Focus*, 7, 2017. doi:10.1098/rsfs.2016.0161.

G. E. Schröder, S. J. Ramsden, A. G. Christy, and S. T. Hyde. Medial surfaces of hyperbolic structures. *Eur. Phys. J. B*, 35:551–564, 2003. doi:10.1140/epjb/e2003-00308-y.

G. E. Schröder, S. J. Ramsden, A. Fogden, and S. T. Hyde. A rhombohedral family of minimal surfaces as a pathway between the P and D cubic mesophases. *Physica A: Statistical Mechanics and its Applications*, 339:137–144, 2004. doi:10.1016/j.physa.2004.03.056.

G. E. Schröder-Turk, A. Fogden, and S. T. Hyde. Bicontinuous geometries and molecular self-assembly: Comparison of local curvature and global packing variations in genus-three cubic, tetragonal and rhombohedral surfaces. *Eur. Phys. J. B*, 54:509–524, 2006. doi:10.1140/epjb/e2007-00025-7.

G. E. Schröder-Turk, A. Fogden, and S. T. Hyde. Local v/a variations as a measure of structural packing frustration in bicontinuous mesophases, and geometric arguments for an alternating ${\rm Im}\overline{{\mathsf3}}{\rm m}$(I-WP) phase in block-copolymers with polydispersity. *Eur. Phys. J. B*, 59:115–126, 2007. doi:10.1140/epjb/e2007-00272-6.

G. E. Schröder-Turk, W. Mickel, S. C. Kapfer, M. A. Klatt, F. M. Schaller, M. J. F. Hoffmann, N. Kleppmann, P. Armstrong, A. Inayat, D. Hug, M. Reichelsdorfer, W. Peukert, W. Schwieger, and K. Mecke. Minkowski Tensor Shape Analysis of Cellular, Granular and Porous Structures. *Adv. Mater.*, 23:2535–2553, 2011a. doi:10.1002/adma.201100562.

G. E. Schröder-Turk, S. Wickham, H. Averdunk, F. Brink, J. D. Fitz Gerald, L. Poladian, M. C. J. Large, and S. T. Hyde. The chiral structure of porous chitin within the wing-scales of Callophrys rubi. *Journal of Structural Biology*, 174:290–295, 2011b. doi:10.1016/j.jsb.2011.01.004.

G. E. Schröder-Turk, W. Mickel, S. C. Kapfer, F. M. Schaller, B. Breidenbach, D. Hug, and K. Mecke. Minkowski tensors of anisotropic spatial structure. *New J. Phys.*, 15:083028, 2013. doi:10.1088/1367-2630/15/8/083028.

H. A. Schwarz. Fortgesetzte Untersuchungen über specielle Minimalflächen. In H. A. Schwarz, editor, *Gesammelte Mathematische Abhandlungen: Erster Band*, pages 126–148. Springer, Berlin, Heidelberg, 1890. doi:10.1007/978-3-642-50665-9_4.

L. E. Scriven. Equilibrium bicontinuous structure. *Nature*, 263:123–125, 1976. doi:10.1038/263123a0.

Marco Seeland and Patrick Mäder. Multi-view classification with convolutional neural networks. *PLOS ONE*, 16:e0245230, 2021. doi:10.1371/journal.pone.0245230.

A.N. Semenov. Contribution to the theory of microphase layering in block-copolymer melts. *J. Exp. Theor. Physic*, 61:744, 1985.

Vivek Sharma, Matija Crne, Jung Ok Park, and Mohan Srinivasarao. Bouligand Structures Underlie Circularly Polarized Iridescence of Scarab Beetles: A Closer View. *Materials Today: Proceedings*, 1:161–171, 2014. doi:10.1016/j.matpr.2014.09.019.

Jaeman J. Shin, Eun Ji Kim, Kang Hee Ku, Young Jun Lee, Craig J. Hawker, and Bumjoon J. Kim. 100th Anniversary of Macromolecular Science Viewpoint: Block Copolymer Particles: Tuning Shape, Interfaces, and Morphology. *ACS Macro Lett.*, 9:306–317, 2020. doi:10.1021/acsmacrolett.0c00020.

Mijo Simunovic, Emma Evergren, Andrew Callan-Jones, and Patricia Bassereau. Curving Cells Inside and Out: Roles of BAR Domain Proteins in Membrane Shaping and Its Cellular Implications. *Annu. Rev. Cell Dev. Biol.*, 35:111–129, 2019. doi:10.1146/annurev-cellbio-100617-060558.

Sir William Thomson. LXIII. On the division of space with minimum partitional area. *Lond. Edinb. Dublin Philos. Mag. J. Sci.*, 24:503–514, 1887. doi:10.1080/14786448708628135.

Ulrich Sperling, Fabrice Franck, Barbara van Cleve, Geneviève Frick, Klaus Apel, and Gregory A. Armstrong. Etioplast Differentiation in Arabidopsis: Both PORA and PORB Restore the Prolamellar Body and Photoactive Protochlorophyllide–F655 to the cop1 Photomorphogenic Mutant. *Plant Cell*, 10:283–296, 1998. doi:10.1105/tpc.10.2.283.

Dietrich Stauffer and Ammon Aharony. *Introduction To Percolation Theory : Second Edition*. Taylor & Francis, London, second edition, 1992. doi:10.1201/9781315274386.

Morgan Stefik, Stefan Guldin, Silvia Vignolini, Ulrich Wiesner, and Ullrich Steiner. Block copolymer self-assembly for nanophotonics. *Chem. Soc. Rev.*, 44:5076–5091, 2015. doi:10.1039/C4CS00517A.

Paul Stevenson. *Foam Engineering: Fundamentals and Applications*. John Wiley & Sons, 2012.

John Stone. *An Efficient Library for Parallel Ray Tracing and Animation*. Master's thesis, Computer Science Department, University of Missouri-Rolla, April 1998.

George G. Szpiro. *Kepler's Conjecture*. John Wiley & Sons, Inc., Hoboken, New Jersey, 2003.

Nevill Gonzalez Szwacki and Teresa Szwacka. *Basic Elements of Crystallography*. CRC Press, 2016.

A. Takano, S. Wada, S. Sato, T. Araki, K. Hirahara, T. Kazama, S. Kawahara, Y. Isono, A. Ohno, N. Tanaka, and Y. Matsushita. Observation of Cylinder-Based Microphase-Separated Structures from ABC Star-Shaped Terpolymers Investigated by Electron Computerized Tomography. *Macromolecules*, 37:9941–9946, 2004. doi:10.1021/ma048893t.

A. Takano, W. Kawashima, A. Noro, Y. Isono, N. Tanaka, T. Dotera, and Y. Matsushita. A mesoscopic Archimedean tiling having a new complexity in an ABC star polymer. *J. Polym. Sci. Part B Polym. Phys.*, 43:2427–2432, 2005. doi:10.1002/polb.20537.

Masaharu Tanemura and Masami Hasegawa. Geometrical models of territory I. Models for synchronous and asynchronous settlement of territories. *Journal of Theoretical Biology*, 82:477–496, 1980. doi:10.1016/0022-5193(80)90251-9.

Ping Tang, Feng Qiu, Hongdong Zhang, and Yuliang Yang. Morphology and Phase Diagram of Complex Block Copolymers: ABC Star Triblock Copolymers. *J. Phys. Chem. B*, 108:8434–8438, 2004. doi:10.1021/jp037911q.

Ping Tang, Feng Qiu, Hongdong Zhang, and Yuliang Yang. Phase separation patterns for diblock copolymers on spherical surfaces: A finite volume method. *Phys. Rev. E*, 72:016710, 2005. doi:10.1103/PhysRevE.72.016710.

Edwin L. Thomas, David B. Alward, David J. Kinning, David C. Martin, Dale L. Handlin, and Lewis J. Fetters. Ordered bicontinuous double-diamond structure of star block copolymers: A new equilibrium microdomain morphology. *Macromolecules*, 19:2197–2202, 1986. doi:10.1021/ma00162a016.

Joseph John Thomson. XXIV. On the structure of the atom: An investigation of the stability and periods of oscillation of a number of corpuscles arranged at equal intervals around the circumference of a circle; with application of the results to the theory of atomic structure. *Lond. Edinb. Dublin Philos. Mag. J. Sci.*, 7:237–265, 1904. doi:10.1080/14786440409463107.

S. Torquato. Reformulation of the covering and quantizer problems as ground states of interacting particles. *Phys. Rev. E*, 82, 2010. doi:10.1103/PhysRevE.82.056109.

S. Torquato and F. H. Stillinger. Jammed hard-particle packings: From Kepler to Bernal and beyond. *Rev. Mod. Phys.*, 82:2633–2672, 2010. doi:10.1103/RevModPhys.82.2633.

S. Torquato, G. Zhang, and F. H. Stillinger. Ensemble Theory for Stealthy Hyperuniform Disordered Ground States. *Phys. Rev. X*, 5:021020, 2015. doi:10.1103/PhysRevX.5.021020.

Salvatore Torquato. Monodisperse Spheres. In Salvatore Torquato, editor, *Random Heterogeneous Materials: Microstructure and Macroscopic Properties*, Interdisciplinary Applied Mathematics, pages 119–159. Springer, New York, NY, 2002. doi:10.1007/978-1-4757-6355-3_5.

Salvatore Torquato. Hyperuniformity and its generalizations. *Phys. Rev. E*, 94:022122, 2016. doi:10.1103/PhysRevE.94.022122.

Salvatore Torquato. Hyperuniform states of matter. *Physics Reports*, 745:1–95, 2018. doi:10.1016/j.physrep.2018.03.001.

Salvatore Torquato and Frank H. Stillinger. Local density fluctuations, hyperuniformity, and order metrics. *Phys. Rev. E*, 68:041113, 2003. doi:10.1103/PhysRevE.68.041113.

L. Fejes Tóth. What the bees know and what they do not know. *Bull. Am. Math. Soc.*, 70: 468–481, 1964.

László Fejes Tóth. Lagerungs- und Überdeckungsprobleme in der Ebene. In László Fejes Tóth, editor, *Lagerungen in der Ebene auf der Kugel und im Raum*, Die Grundlehren der mathematischen Wissenschaften, pages 55–99. Springer, Berlin, Heidelberg, 1972. doi:10.1007/978-3-642-65234-9_3.

Christopher A. Tyler, Jian Qin, Frank S. Bates, and David C. Morse. SCFT Study of Nonfrustrated ABC Triblock Copolymer Melts. *Macromolecules*, 40:4654–4668, 2007. doi:10.1021/ma062778w.

Marcus Terentius Varro. *On Agriculture*. Loeb Classical Library, 1934.

Peter H. Verdier and W. H. Stockmayer. Monte Carlo Calculations on the Dynamics of Polymers in Dilute Solution. *J. Chem. Phys.*, 36:227–235, 1962. doi:10.1063/1.1732301.

Vincenzo Vitelli, J. B. Lucks, and D. R. Nelson. Crystallography on curved surfaces. *Proc. Natl. Acad. Sci. U. S. A.*, 103:12323–12328, 2006.

H. G. von Schnering and R. Nesper. Nodal surfaces of Fourier series: Fundamental invariants of structured matter. *Z. Physik B - Condensed Matter*, 83:407–412, 1991. doi:10.1007/BF01313411.

Georges Voronoi. Nouvelles applications des paramètres continus à la théorie des formes quadratiques. Premier mémoire. Sur quelques propriétés des formes quadratiques positives parfaites. *J. Für Reine Angew. Math.*, 133:97–178, 1908.

Bart Vorselaars, Jaeup U. Kim, Tanya L. Chantawansri, Glenn H. Fredrickson, and Mark W. Matsen. Self-consistent field theory for diblock copolymers grafted to a sphere. *Soft Matter*, 7:5128–5137, 2011. doi:10.1039/C0SM01242D.

Pete Vukusic and J. Roy Sambles. Photonic structures in biology. *Nature*, 424:852–855, 2003. doi:10.1038/nature01941.

David Wales and Wales. *Energy Landscapes: Applications to Clusters, Biomolecules and Glasses*. Cambridge University Press, 2003.

David J. Wales and Sidika Ulker. Structure and dynamics of spherical crystals characterized for the Thomson problem. *Phys. Rev. B*, 74:212101, 2006. doi:10.1103/PhysRevB.74.212101.

David J. Wales, Hayley McKay, and Eric L. Altschuler. Defect motifs for spherical topologies. *Phys. Rev. B*, 79:224115, Jun 2009. doi:10.1103/PhysRevB.79.224115. URL `https://link.aps.org/doi/10.1103/PhysRevB.79.224115`.

Andreas Walther and Axel H. E. Müller. Janus Particles: Synthesis, Self-Assembly, Physical Properties, and Applications. *Chem. Rev.*, 113:5194–5261, 2013. doi:10.1021/cr300089t.

Fugao Wang and D. P. Landau. Efficient, Multiple-Range Random Walk Algorithm to Calculate the Density of States. *Phys. Rev. Lett.*, 86:2050–2053, 2001. doi:10.1103/PhysRevLett.86.2050.

Jihao Wang, Yufen Han, Zhiyang Xu, Xiaozhen Yang, Seeram Ramakrishna, and Yong Liu. Dissipative Particle Dynamics Simulation: A Review on Investigating Mesoscale Properties of Polymer Systems. *Macromol. Mater. Eng.*, 306:2000724, 2021. doi:10.1002/mame.202000724.

D. Weaire and R. Phelan. A counter-example to Kelvin's conjecture on minimal surfaces. *Philos. Mag. Lett.*, 69:107–110, 1994. doi:10.1080/09500839408241577.

D. L. Weaire and Stefan Hutzler. *The Physics of Foams*. Clarendon Press, 2001.

Denis Weaire. *The Kelvin Problem*. CRC Press, 1997.

Denis Weaire and Tomaso Aste. *The Pursuit of Perfect Packing*. CRC Press, Boca Raton, second edition, 2008. doi:10.1201/9781420068184.

Ethan Weiner, Justine M Pinskey, Daniela Nicastro, and Marisa S Otegui. Electron microscopy for imaging organelles in plants and algae. *Plant Physiology*, 2021. doi:10.1093/plphys/kiab449.

Simon Weis, Philipp W. A. Schönhöfer, Fabian M. Schaller, Matthias Schröter, and Gerd E. Schröder-Turk. Pomelo, a tool for computing Generic Set Voronoi Diagrams of Aspherical Particles of Arbitrary Shape. *EPJ Web Conf.*, 140:06007, 2017. doi:10.1051/epjconf/201714006007.

George M. Whitesides and Bartosz Grzybowski. Self-Assembly at All Scales. *Science*, 2002.

M. D. Whitmore and J. D. Vavasour. Self-consistent field theory of block copolymers and block copolymer blends. *Acta Polym.*, 46:341–360, 1995. doi:10.1002/actp.1995.010460501.

Wojciech Wietrzynski and Benjamin D. Engel. Chlorophyll biogenesis sees the light. *Nat. Plants*, 7:380–381, 2021. doi:10.1038/s41477-021-00900-6.

B. T. M. Willis and C. J. Carlile. *Experimental Neutron Scattering*. Oxford University Press, 2017.

Ashley J. Wilson. *Foams: Physics, Chemistry and Structure*. Springer, 2014.

Bodo D. Wilts, Kristel Michielsen, Hans De Raedt, and Doekele G. Stavenga. Hemispherical Brillouin zone imaging of a diamond-type biological photonic crystal. *J. R. Soc. Interface*, 9:1609–1614, 2012a. doi:10.1098/rsif.2011.0730.

Bodo D. Wilts, Kristel Michielsen, Jeroen Kuipers, Hans De Raedt, and Doekele G. Stavenga. Brilliant camouflage: Photonic crystals in the diamond weevil, Entimus imperialis. *Proceedings of the Royal Society B: Biological Sciences*, 279:2524–2530, 2012b. doi:10.1098/rspb.2011.2651.

Bodo D. Wilts, Benjamin Apeleo Zubiri, Michael A. Klatt, Benjamin Butz, Michael G. Fischer, Stephen T. Kelly, Erdmann Spiecker, Ullrich Steiner, and Gerd E. Schröder-Turk. Butterfly gyroid nanostructures as a time-frozen glimpse of intracellular membrane development. *Sci. Adv.*, 3, 2017. doi:10.1126/sciadv.1603119.

Benjamin Winter, Benjamin Butz, Christel Dieker, Gerd E. Schröder-Turk, Klaus Mecke, and Erdmann Spiecker. Coexistence of both gyroid chiralities in individual butterfly wing scales of Callophrys rubi. *PNAS*, 112:12911–12916, 2015. doi:10.1073/pnas.1511354112.

Meinhard Wohlgemuth, Nataliya Yufa, James Hoffman, and Edwin L. Thomas. Triply Periodic Bicontinuous Cubic Microdomain Morphologies by Symmetries. *Macromolecules*, 34:6083–6089, 2001. doi:10.1021/ma0019499.

Chin Ken Wong, Xiaolian Qiang, Axel H. E. Müller, and André H. Gröschel. Self-Assembly of block copolymers into internally ordered microparticles. *Progress in Polymer Science*, 102:101211, 2020. doi:10.1016/j.progpolymsci.2020.101211.

Hans Wynberg, E. W. Meijer, J. C. Hummelen, H. P. J. M. Dekkers, P. H. Schippers, and A. D. Carlson. Circular polarization observed in bioluminescence. *Nature*, 286:641–642, 1980. doi:10.1038/286641a0.

Jiangping Xu, Ke Wang, Jingyi Li, Huamin Zhou, Xiaolin Xie, and Jintao Zhu. ABC Triblock Copolymer Particles with Tunable Shape and Internal Structure through 3D Confined Assembly. *Macromolecules*, 48:2628–2636, 2015. doi:10.1021/acs.macromol.5b00335.

Yuci Xu, Weihua Li, Feng Qiu, Yuliang Yang, and An-Chang Shi. Self-Assembly of ABC Star Triblock Copolymers under a Cylindrical Confinement. *J. Phys. Chem. B*, 113: 11153–11159, 2009. doi:10.1021/jp9043896.

Xianggui Ye, Tongfei Shi, Zhongyuan Lu, Chengxiang Zhang, Zhaoyan Sun, and Lijia An. Study of Morphology and Phase Diagram of π-Shaped ABC Block Copolymers Using Self-Consistent-Field Theory. *Macromolecules*, 38:8853–8857, 2005. doi:10.1021/ma051303m.

S. Yoshioka, H. Fujita, S. Kinoshita, and B. Matsuhana. Alignment of crystal orientations of the multi-domain photonic crystals in Parides sesostris wing scales. *J. R. Soc. Interface*, 11:20131029, 2014. doi:10.1098/rsif.2013.1029.

Bin Yu, Baohui Li, Qinghua Jin, Datong Ding, and An-Chang Shi. Self-Assembly of Symmetric Diblock Copolymers Confined in Spherical Nanopores. *Macromolecules*, 40:9133–9142, 2007. doi:10.1021/ma071624t.

Ting Zhan, Wenhua Lv, and Yuru Deng. Multilayer gyroid cubic membrane organization in green alga Zygnema. *Protoplasma*, 254:1923–1930, 2017. doi:10.1007/s00709-017-1083-2.

G. Zhang, F. H. Stillinger, and S. Torquato. Ground states of stealthy hyperuniform potentials: I. Entropically favored configurations. *Phys. Rev. E*, 92:022119, 2015a. doi:10.1103/PhysRevE.92.022119.

G. Zhang, F. H. Stillinger, and S. Torquato. Ground states of stealthy hyperuniform potentials. II. Stacked-slider phases. *Phys. Rev. E*, 92:022120, 2015b. doi:10.1103/PhysRevE.92.022120.

G. Zhang, F. H. Stillinger, and S. Torquato. The Perfect Glass Paradigm: Disordered Hyperuniform Glasses Down to Absolute Zero. *Sci. Rep.*, 6:36963, 2016. doi:10.1038/srep36963.

G. Zhang, F. H. Stillinger, and S. Torquato. Can exotic disordered "stealthy" particle configurations tolerate arbitrarily large holes? *Soft Matter*, 13:6197–6207, 2017. doi:10.1039/C7SM01028A.

Guojie Zhang, Feng Qiu, Hongdong Zhang, Yuliang Yang, and An-Chang Shi. SCFT Study of Tiling Patterns in ABC Star Terpolymers. *Macromolecules*, 43:2981–2989, 2010. doi:10.1021/ma902735t.

Liangshun Zhang, Liquan Wang, and Jiaping Lin. Defect structures and ordering behaviours of diblock copolymers self-assembling on spherical substrates. *Soft Matter*, 10:6713–6721, 2014. doi:10.1039/C4SM01180E.

Zhenli Zhang and Sharon C. Glotzer. Self-Assembly of Patchy Particles. *Nano Lett.*, 4: 1407–1413, 2004. doi:10.1021/nl0493500.

Jin Zhao, Biswaroop Majumdar, Mark F. Schulz, Frank S. Bates, Kristoffer Almdal, Kell Mortensen, Damian A. Hajduk, and Sol M. Gruner. Phase Behavior of Pure Diblocks and Binary Diblock Blends of Poly(ethylene)-Poly(ethylethylene). *Macromolecules*, 29: 1204–1215, 1996. doi:10.1021/ma9507251.

P. Ziherl and Randall D. Kamien. Soap Froths and Crystal Structures. *Phys. Rev. Lett.*, 85: 3528–3531, 2000. doi:10.1103/PhysRevLett.85.3528.

Acknowledgements

Finally, my PhD journey of just over four years is coming to an end, cumulating into this piece of writing. One of the most important lessons I learned over the course of the past years is that nothing of this remarkable time (and maybe achievement) in my life could have been done without the help and support of a large number of persons, to whom I would like to offer my deepest gratitude.

I want to begin with my principal supervisor Associate Professor Gerd Schröder-Turk at Murdoch University. He ignited my passion for geometry, soft matter, computer simulations and visualisation over seven years ago when I pursued my Bachelor thesis in his group in Klaus Mecke's "Theorie I" at the Friedrich-Alexander Universität Erlangen-Nürnberg. Since then he has accompanied my academic career, especially when entrusting me with this amazing opportunity to pursue a PhD in Australia. I am truly grateful for all the guidance, encouragement, motivation, enthusiasm, beers, travels and so much more which made our research and my stay in Perth so much fun and (in my opinion) successful. Thank you for the patience and quick responses, when a couple of deadlines were about to get stretched. Gerd never failed to live up to the highest moral standards and integrity, not only in research, but in everything he stands for. His unfailing will to stand up for the right cause even under the harshest conditions is truly inspiring and makes me especially proud to have him as my supervisor, mentor and friend.

Next, I want to thank my second principal supervisor Professor Myfanwy Evans at Potsdam University. Our paths crossed also when I started my Bachelor thesis with her, back then in Gerd's group in Erlangen. I am grateful to Myf for accepting me as a PhD

But at last I want to thank my family and parents for their unfailing (although occasional headshakingly) emotional and financial support for whatever crazy plans and ideas I had in life. You have made me the person who I am, I cannot ever thank you enough for that.